

# Characterization of the High Frequency Response of LASER Interferometer Gravitational Wave Detectors

by

William E. Butler

Submitted in Partial Fulfillment  
of the  
Requirements for the Degree  
Doctor of Philosophy

Supervised by

Professor Adrian C. Melissinos

Department of Physics and Astronomy  
The College  
Arts & Sciences

University of Rochester  
Rochester, New York

2004



## **Dedication**

I wish to dedicate this to the memory of my grandfather Alfred Bisbee Butler and my great uncle Don Stratton. My grandfather put my feet on the path to physics at an early age by doing everything from providing me with switches to flip to “see what they do”, to explaining instantaneous visual vector analysis and its implications in a game of running catch. My great uncle, whom I only really got to know once I started graduate school, inspired me with the tales of his success and his personal quirks which bear such an astonishing similarity to my own, that I felt instantly at home with him.



## Curriculum Vitae

The author was born in Olympia, WA on September 1, 1975. He attended Eastern Washington University from 1993 to 1998, and graduated *cum laude* with a Bachelor of Science degree in Physics and a Bachelor of Science degree in Computer Science. He began his graduate research with the University of Rochester at Fermi National Accelerator Laboratory, just outside Chicago, during the Summer of 1998, and started classwork in Rochester in the Fall of 1998. He pursued his research in physics under the direction of Professor Adrian Melissinos, and received the Master of Arts degree from the University of Rochester in 2000. The research involved work at the Laboratory for LASER Energetics at the University, and the LIGO Hanford Observatory in Washington State.



## Acknowledgments

First I must thank the LIGO collaboration and the LSC for allowing me to use their instrument, without which there would be no data to analyze. In particular I am grateful to those people who helped me at the lab: Doug Cook, Mike Landry, Tom Mahood, Greg Mendell, Josh Myers, Daniel Sigg and the rest of the staff of LHO. I also thank Fred Raab, who agreed to be my on site adviser.

Foremost I would like to express my heartfelt gratitude to Adrian Melissinos, my thesis adviser, for all his help throughout my graduate career. Throughout changing research topics, times of indecision and remote locations he has always been encouraging and helpful. The one decision that I never regretted was my choice of research adviser!

Thank you to Janet Fogg, Connie Jones, Judy Mack, Diane Pickersgill and Barbara Warren from Rochester for support and kindness. Also a thank you to those with whom I worked on all of my non-thesis projects, and learned from: Sean Bentley, Todd Blalock, Bob Boyd and Michael Fitch in particular.

I survived the good times in Rochester with the help of more friends than I can name, and my time spent in Richland passed with the help of even more. Special thanks to my parents, who, besides dealing with a son in graduate school, also managed to help me through my fight with cancer. I can attribute a great deal of my sanity to the support of my Great Aunt Concha Stratton.





## **Abstract**

This thesis describes a search for a stochastic background of gravitational waves at high frequency, 37.52 kHz. At this frequency, the separation between distant detectors precludes the use of a correlation technique. Instead I rely on the spectral response of the LASER interferometer (IFO) to isolate a possible signal from the underlying noise. This research was carried out at the LIGO (LASER Interferometer Gravitational Observatory) located in Hanford, WA and within the LIGO Scientific Collaboration (LSC).[20]

Chapter 1 serves as a general introduction to the present state of the search for gravitational waves (GW). I discuss the indirect observation of gravitational radiation as well as the expected sources of GW and their characteristics. I also discuss possible future developments, in particular the Advanced LIGO instruments and the LASER Interferometer Space Antenna (LISA). The characteristics of the large LASER interferometers, layout, terminology and analytic formulae are developed in Chapter 2.

To carry out the proposed search, it is essential that the frequency response of the interferometer be thoroughly understood, including all possible noise sources. This was the subject of a series of experimental investigations using sideband injection and mirror excitations to characterize the IFO response in the region of the characteristic frequency of the optical system (free spectral range) at 37.52 kHz. The results of these experiments as well as the theoretical modeling are presented in Chapter 3. Contributions to the spectrum from mechanical noise

are investigated in Chapter 4, and compared to the expected contribution due to thermal excitation.

The results of my search are based on data obtained during the third science run of LIGO (S3) and are presented in Chapter 5. I show that a signal such as expected from a stochastic gravitational wave background is manifest in the data and compare it to the expected noise. This allows me to set a limit on a possible stochastic background of GW. I also discuss possible future higher sensitivity measurements at these frequencies.

# Contents

Dedication . . . . .	iii
Curriculum Vitae . . . . .	v
Acknowledgments . . . . .	vii
Abstract . . . . .	ix
<b>1 Introduction</b>	<b>1</b>
1.1 General Relativity . . . . .	3
1.2 Binary Pulsar Evidence for GW . . . . .	5
1.3 Detectors . . . . .	8
1.3.1 Resonant Bars . . . . .	8
1.3.2 LASER Interferometers (IFOs) . . . . .	9
1.4 Expected Sources of Gravitational Waves . . . . .	11
1.5 Future Detectors . . . . .	17
1.5.1 Advanced LIGO . . . . .	17
1.5.2 LISA . . . . .	21
<b>2 The LIGO IFOs</b>	<b>25</b>
2.1 LIGO Layout . . . . .	25
2.2 The mirror equations . . . . .	30
2.2.1 Simple Fabry-Perot . . . . .	31
2.2.2 Interferometer with Fabry-Perot Arms . . . . .	33
2.2.3 Power Recycled Interferometer . . . . .	36
2.2.4 A Perfect Interferometer . . . . .	38
<b>3 Characterization of the Instrument</b>	<b>47</b>
3.1 Sideband Injection . . . . .	47
3.1.1 Calculation of Fields . . . . .	49
3.1.2 Response to sideband injection at $f_{\text{fsr}}$ and $2f_{\text{fsr}}$ . . . . .	53
3.1.3 Response to sideband injection at $\frac{1}{2}f_{\text{fsr}}$ and $\frac{3}{2}f_{\text{fsr}}$ . . . . .	65
3.1.4 Transverse Modes . . . . .	71

3.2	Parametric Conversion . . . . .	76
3.2.1	Modulation and Demodulation . . . . .	78
3.2.2	Field Calculation Methods . . . . .	82
3.2.3	Data Fits . . . . .	85
3.2.4	Calibration and Normalization . . . . .	90
3.3	Sensitivity @ 37.52 kHz . . . . .	99
<b>4</b>	<b>Mechanical Noise</b>	<b>103</b>
4.1	Active Measurements . . . . .	103
4.1.1	Test Mass Internal Resonances . . . . .	104
4.2	Passive Measurements . . . . .	108
4.2.1	Up-converted Seismic and Suspension Noise . . . . .	108
4.2.2	Test Mass Internal Resonances . . . . .	113
4.3	Test Mass Resonance Comparison with Theory . . . . .	127
4.3.1	Contributions to FSR Signal . . . . .	127
4.3.2	Calibration and Coupling . . . . .	128
<b>5</b>	<b>Stochastic Gravitational Wave Signal</b>	<b>133</b>
5.1	Present Limits . . . . .	134
5.2	Correlation Technique . . . . .	137
5.3	Free Spectral Range (FSR) Technique . . . . .	138
5.4	FSR Search Method . . . . .	140
5.5	FSR Search Results . . . . .	143
5.6	Calibration of FSR Data . . . . .	152
5.7	Sensitivity of Future Measurements . . . . .	155
	<b>Bibliography</b>	<b>157</b>
<b>A</b>	<b>“Strain Calibration in LIGO”</b>	<b>167</b>
A.1	GW Interaction with an IFO Detector . . . . .	167
A.1.1	The Coordinate System . . . . .	167
A.1.2	Round-Trip Phase Change . . . . .	168
A.1.3	Higher Frequency Response . . . . .	171
<b>B</b>	<b>MATLAB functions and scripts</b>	<b>175</b>
B.1	General Functions . . . . .	176
B.1.1	Bode Plot . . . . .	176
B.1.2	Gaussian Curve Generation . . . . .	176
B.1.3	Mechanical Resonance Curve Generation . . . . .	180
B.1.4	Step Function . . . . .	182

B.1.5	Index Locator . . . . .	183
B.2	Simple Fabry-Perot Cavity Calculations . . . . .	184
B.2.1	Reflectivity . . . . .	184
B.2.2	Demodulation Parameter Calculation . . . . .	185
B.2.3	Demodulated Signal . . . . .	186
B.2.4	Data Fitting . . . . .	187
B.2.5	Shaking Response . . . . .	191
B.2.6	Shaking Demodulation Parameters . . . . .	192
B.2.7	Shaking Demodulation Functions . . . . .	193
B.3	Power Recycled Interferometer . . . . .	194
B.3.1	Arm Cavity Reflection . . . . .	194
B.3.2	Demodulation Parameters . . . . .	195
B.3.3	Demodulation Functions . . . . .	196
B.3.4	Arm Cavity Shaking Response . . . . .	197
B.3.5	Shaking Demodulation Parameters . . . . .	197
B.3.6	Shaking Demodulation Outputs . . . . .	198
B.4	Matrix Method Calculations . . . . .	199
B.4.1	FP Matrix Code . . . . .	199
B.4.2	FP Demodulation Parameters . . . . .	203
B.4.3	FP Demodulation Functions . . . . .	206
B.4.4	AS Matrix Code . . . . .	207
B.4.5	AS Demodulation Parameters . . . . .	214
B.4.6	AS Demodulation Functions . . . . .	216
B.5	Frame Data Analysis . . . . .	217
B.5.1	Reading in the Data . . . . .	218
B.5.2	Pre-analysis Manipulation . . . . .	225
B.5.3	Data Analysis . . . . .	227
B.5.4	Example Data Analysis . . . . .	231



# List of Tables

2.1	Nominal Parameters for WA 2k Interferometer . . . . .	44
2.2	Build-up Factors for Carrier and Resonant Sidebands for the 2k Recycled Interferometer as calculated by the Algebraic method. . . . .	45
2.3	Build-up Factors for Carrier and Resonant Sidebands in the 4k Recycled Interferometer as calculated by the Numerical method of Sec. 3.2.2 . . . . .	45
3.1	Nominal Parameters for WA 4k Interferometer . . . . .	88
3.2	Output Attenuation . . . . .	97
4.1	Test Mass Internal Resonances . . . . .	107
4.2	Overall Fit Parameters . . . . .	107
4.3	Up-converted Noise . . . . .	114
4.4	Test Mass Modes prediction [22] . . . . .	123
4.5	Parameters for Passively Measured Mechanical Resonances. . . . .	124
4.6	Measured Parameters used for Mechanical Resonance Characterization . . . . .	126
4.7	Parameters used for Mechanical Resonance Characterization, Normalized to 1 Frame per FFT . . . . .	127
4.8	Measured Resonance Parameters . . . . .	131
5.1	Summary of upper limits on $\Omega_0 h_{100}^2$ over a large range of frequency bands (from [21]). . . . .	136
5.2	Fit Coefficients . . . . .	145
5.3	Results of Differential Motion Signal Injection through software. . . . .	152





# List of Figures

1.1	Graphical simulation of Gravitational Wave Polarizations . . . . .	5
1.2	The orbital period of any body around another decreases because of the energy lost to gravitational radiation. That effect is strongest in highly relativistic systems such as the binary pulsar PSR1913+16. . . . .	7
1.3	Resonant Bar Gravitational Wave Antenna . . . . .	9
1.4	Schematic layout of the Interferometer showing mirror suspensions	10
1.5	LIGO Detectors in Richland, WA (LHO) and Livingston, LA (LLO)	12
1.6	Measurement of GW source by inter-collaboration correlation measurements . . . . .	12
1.7	LIGO Sensitivity to Periodic Sources, estimated 1989 [70] . . . . .	14
1.8	LIGO Sensitivity to Burst Sources, estimated 1989 [70] . . . . .	15
1.9	LIGO Sensitivity to Stochastic Sources, estimated 1989 [70] . . . . .	18
1.10	LIGO S1 calibrated strain measurements as of Sept. 2002, for the L1 = Livingston 4k IFO, H1 = Hanford 4k IFO and H2 = Hanford 2k IFO. Also shown is the design sensitivity, and two stochastic GW background levels for comparison . . . . .	19
1.11	Orbital Schematic of LISA: LASER Interferometer Space Antenna	21
1.12	Cutaway of LISA's instrument. The actual spacecraft will be protected with a cover. Image from LISA webpage [19]. . . . .	22
1.13	LISA Instrument . . . . .	23
2.1	2k Hanford LIGO Schematic . . . . .	26
2.2	HAM Chamber and its seismic isolation . . . . .	27
2.3	BSC Chamber and its seismic isolation . . . . .	28
2.4	Simple Fabry-Perot Cavity . . . . .	32
2.5	Michelson Interferometer with Fabry-Perot Arms . . . . .	34
2.6	Michelson Interferometer . . . . .	35
2.7	Power Recycled Michelson Interferometer . . . . .	36

3.1	X-arm 1 FSR . . . . .	54
3.2	X-arm 2 FSR . . . . .	55
3.3	Typical chi squared fit for IFO arm length . . . . .	58
3.4	Y-arm FSR, I-phase . . . . .	59
3.5	Y-arm FSR, Q-phase . . . . .	60
3.6	Y-arm 2 FSR, I-phase . . . . .	61
3.7	Full-IFO Sideband Injection Response, Q-phase . . . . .	63
3.8	Full-IFO Sideband Injection Response, I-phase . . . . .	64
3.9	$\frac{1}{2}$ FSR, I-phase . . . . .	67
3.10	$\frac{1}{2}$ FSR, Q-phase . . . . .	68
3.11	$\frac{3}{2}$ FSR, I-phase . . . . .	69
3.12	$\frac{3}{2}$ FSR, Q-phase . . . . .	70
3.13	Sideband Injection Sweep for Transverse Mode Characterization . . . . .	72
3.14	Transverse Mode Frequency variance with Yaw . . . . .	74
3.15	Transverse Mode Frequency variance with Pitch . . . . .	75
3.16	FFT of X-arm signal with no excitation . . . . .	77
3.17	Simple Fabry-Perot Cavity . . . . .	83
3.18	X-arm Shake Response . . . . .	91
3.19	Full-IFO Mirror Excitation Response, Q-phase October . . . . .	92
3.20	Full-IFO Mirror Excitation Response, I and Q phase . . . . .	93
3.21	Full-IFO Mirror Excitation Response, I-phase . . . . .	94
3.22	Full-IFO Mirror Excitation Response, Q-phase . . . . .	95
3.23	FFT of AS_I with mass excitation of $1V_{pk}$ @ 37.52 kHz . . . . .	101
3.24	Response of the IFO to ITM excitation at varying magnitudes in both I and Q quadratures. . . . .	102
4.1	Swept Sine Response to ITM excitation in full PRIFO configuration. . . . .	106
4.2	FFT of AS_I with mass excitation of $0.5V_{pk}$ @ 37.52 kHz taken in December of 2002. A) Linear frequency; B) Log frequency away from 37.52 kHz plotted vs. magnitude . . . . .	110
4.3	FFT of AS_I with mass excitation of $1.0V_{pk}$ @ 37.52 kHz taken in December of 2002. A) Linear frequency; B) Log frequency away from 37.52 kHz plotted vs. magnitude . . . . .	111
4.4	FFT of AS_I with a 2V excitation @ 37.52 kHz taken in October of 2002 (at this time the drive was not calibrated). A) Linear frequency; B) Log frequency away from 37.52 kHz plotted vs. magnitude . . . . .	112
4.5	Seismic Noise Spectrum . . . . .	115
4.6	Mode 2 . . . . .	116
4.7	Mode 99 . . . . .	117

4.8	Typical sample of the time-series of channel H1:LSC-AS_1FSR. . .	119
4.9	FFT Spectrum (magnitude) for 2800 averages. BW resolution 0.0625 Hz. . . . .	120
4.10	High resolution, $BW = 0.78125 \times 10^{-3}$ Hz, spectrum in the region of a thermally excited resonance at $f = 37,812.5618$ Hz. The fit is also shown and gives $Q = 2.68 \times 10^7$ , or full-width at half-power $\Delta f = 1.41$ mHz. The presence of the two sidebands is not understood. . . . .	122
5.1	Overlap Reduction Function $\gamma(f)$ shown for the LHO-LLO detectors [21]. The value of $ \gamma $ is a little less than unity at 0 Hz because the interferometer arms are not exactly co-planar and co-aligned between the two sites. . . . .	138
5.2	Fitted spectrum and data for $37,200 < f < 37,800$ Hz. The comprehensive fit for all parameters is used. See text for details. .	143
5.3	As in Fig.5.2 but for a 40 Hz span in the fsr region. . . . .	144
5.4	$\chi^2$ vs the magnitude of the differential mode signal with no contribution from mechanical resonances. . . . .	146
5.5	$\chi^2$ vs the magnitude of the differential mode signal with mechanical resonances of fixed magnitude included. . . . .	147
5.6	$\chi^2$ vs the magnitude of the differential mode signal where the magnitude of the mechanical resonances is being simultaneously fit. .	148
5.7	$\chi^2$ vs the magnitude of the mechanical resonance amplitude when the magnitude of the differential mode is being simultaneously fit. .	149
5.8	$\chi^2$ contour plot with the magnitude of the differential mode vs the magnitude of the mechanical resonance contribution. The central point is the minimum fit, contours are $1 \sigma$ and $2 \sigma$ . Note the minimal correlation of the two parameters. . . . .	150
5.9	Predicted LIGO strain sensitivity with upper limit placed at FSR (37520 Hz) . . . . .	154
5.10	Stochastic characteristic strain spectra predicted in [11]. Also shown is the design sensitivity of Advanced LIGO . . . . .	155
A.1	Coordinate System . . . . .	168
A.2	$h$ sensitivity as function of angle for the “+” polarization, the “ $\times$ ” polarization and the averaged polarization. . . . .	170
A.3	Amplitude correction(left) and time delay of a gravitational wave with non-normal incident and frequencies of 200 Hz (solid curve), 1000 Hz (dashed) and 5000 Hz. . . . .	172

- A.4  $h$  sensitivity for arm length  $\lambda/2$  as function of angle for the “+” polarization, the “ $\times$ ” polarization and the averaged polarization. . 174

# Chapter 1

## Introduction

Many of the current gravitational metric theories predict gravitational radiation in the form of quadrupolar transverse waves. There is strong indirect evidence for these waves from radio astronomy: the gradual orbital decay of PSR 1913+16 has been observed since its discovery in 1974, and perfectly matches predictions based on energy loss due to gravitational radiation. However, gravitational radiation has not yet been directly detected. Gravitational radiation should appear to inertial observers as an oscillation of the distance between **free falling** objects at the frequency of the gravitational wave. In the LIGO gravitational detector (See fig: 1.4), the test masses (which are also the optics) are suspended by thin wires, in an attempt to approximate freely falling bodies, and thus make them sensitive to gravitational radiation. This is achieved using a series of vibration-isolation mechanisms, from which the optic is eventually suspended by a thin wire.

Following Einstein's theory of gravitation [25], gravity can be thought of as a deformation of space-time around objects with mass. Because it is not possible to shield a gravitational field, the field has infinite extent. When an object

moves, this field changes; however, the field at infinity cannot change at the same instant as the object moves without instantaneous action at a distance. Thus, any change in field propagates from the source in the form of gravitational waves traveling at the speed of light. As gravity determines the curvature of space-time, a gravitational wave is regarded as a ripple in the curvature of space-time. Since the distance between objects is measured along [47] geodesics that follow the curvature of space-time, a gravitational wave changes the distance between objects as it passes by them. If a gravitational wave is traveling along the  $z$  axis, and is polarized along the  $x, y$  axes, then the metric (the square of the distance between space-time events) has a simple form which shows that a gravitational wave of amplitude  $h$  causes a change  $\Delta x = 1 + \frac{1}{2}h$  along the  $x$  direction, and a change  $\Delta y = 1 - \frac{1}{2}h$  along  $y$  (see Sect. 1.1). With this in mind one could use a Michelson type of interferometer to measure the passage of a gravitational wave. This holds despite the fact that light is also affected by the curvature of space-time [61].

A quadrupole moment is the lowest-order moment in a mass distribution, which can have an oscillatory acceleration, and thus produce a gravitational wave. The monopole term cannot contribute because of conservation of energy, so the second derivative with respect to time (yielding acceleration and radiation) of the total mass of the system must vanish. Similarly, the dipole term cannot contribute because that would violate conservation of momentum. Given the 4 km long arms of LIGO, the anticipated mirror motion is  $10^{-18}$  meters  $\simeq 1/1000$  of the diameter of a proton, for an  $h = \delta l/L = 10^{-21}$ . Of the possible sources of gravity waves, the best understood is the orbital decay of a binary neutron star system. Modeling such systems suggests a typical wave amplitude ( $h$ ) of  $10^{-21}$ , which is distressingly small, and furthermore lasts for only a few seconds

(within the LIGO frequency band).

## 1.1 General Relativity

In the realm of general relativity, gravity is not an external force transmitted through space and time but a curvature of space-time.<sup>1</sup> Special Relativity postulates the invariance of the interval between space-time events given by  $ds^2$  which in Cartesian coordinates is

$$ds^2 = -c^2 dt^2 + dx^2 + dy^2 + dz^2 \quad (1.1)$$

Which can be written more compactly as

$$ds^2 = \eta_{\mu\nu} dx^\mu dx^\nu \quad (1.2)$$

with

$$\eta_{\mu\nu} = \begin{pmatrix} -1 & 0 & 0 & 0 \\ 0 & 1 & 0 & 0 \\ 0 & 0 & 1 & 0 \\ 0 & 0 & 0 & 1 \end{pmatrix} \quad (1.3)$$

In General Relativity the Minkowski metric  $\eta_{\mu\nu}$  is modified and is no longer “flat”, and Eq.(1.2) must now be written as

$$ds^2 = g_{\mu\nu} dx^\mu dx^\nu \quad (1.4)$$

where  $g_{\mu\nu}$  is the metric of the curved space. When the curvature is small, as is usually the case, one can treat the curvature as a perturbation to the flat metric

$$g_{\mu\nu} = \eta_{\mu\nu} + h_{\mu\nu} \quad (1.5)$$

---

<sup>1</sup>Quintessentially speaking: *Space-time grips mass, telling it how to move; and mass grips space-time, telling it how to curve.*

The metric perturbation notation is particularly useful when investigating gravitational waves. There is a great deal of gauge freedom in GW theory. A particularly useful gauge is known as the “Transverse Traceless Gauge”, where the coordinates are marked by freely falling hypothetical test masses. In this gauge and in the weak field limit, Einstein’s equations reduce to a wave equation

$$\left(\nabla^2 - \frac{1}{c^2} \frac{\partial^2}{\partial t^2}\right) h_{\mu\nu} = -\frac{16\pi G}{c^4} T_{\mu\nu} \quad (1.6)$$

In free space the stress energy tensor  $T_{\mu\nu} = 0$ . Consider a wave propagating in the  $z$  direction; it is represented in the Transverse Traceless gauge by

$$h_{\mu\nu} = \begin{pmatrix} 0 & 0 & 0 & 0 \\ 0 & a & b & 0 \\ 0 & b & -a & 0 \\ 0 & 0 & 0 & 0 \end{pmatrix} \quad (1.7)$$

which breaks down into two independent polarizations  $h = a\hat{h}_+ + b\hat{h}_\times$ . With the basis vectors

$$\hat{h}_+ = \begin{pmatrix} 0 & 0 & 0 & 0 \\ 0 & 1 & 0 & 0 \\ 0 & 0 & -1 & 0 \\ 0 & 0 & 0 & 0 \end{pmatrix} \quad \hat{h}_\times = \begin{pmatrix} 0 & 0 & 0 & 0 \\ 0 & 0 & 1 & 0 \\ 0 & 1 & 0 & 0 \\ 0 & 0 & 0 & 0 \end{pmatrix} \quad (1.8)$$

Thus, elements of  $h$  take the form  $h(\omega t - kx)$ . The two polarizations are  $45^\circ$  apart while a  $90^\circ$  rotation takes one of these tensors onto itself, up to a change in sign. This can be visualized as shown in Fig. 1.1.

If a gravitational wave of amplitude  $h$  is traveling along the  $z$  axis, and is



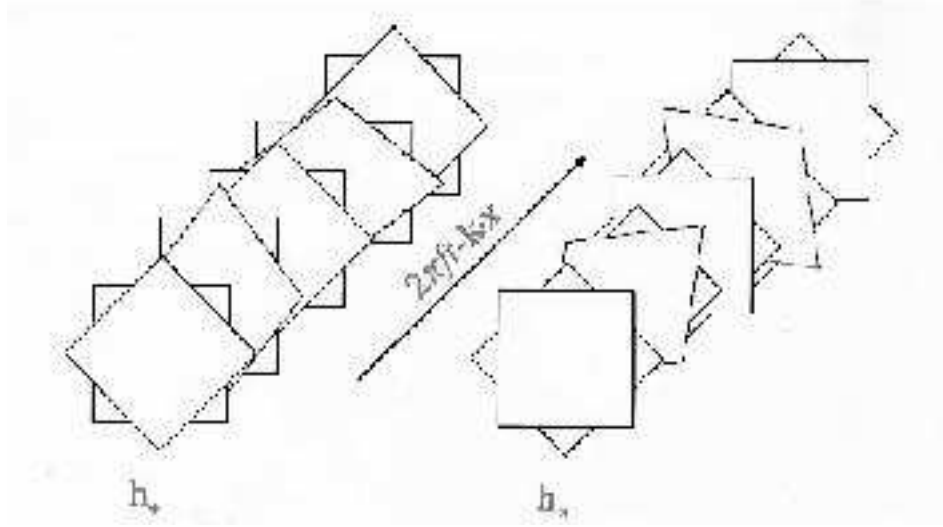


Figure 1.1: Graphical simulation of Gravitational Wave Polarizations

polarized along the  $x, y$  axes then  $h_{\mu\nu} = h\hat{h}_+$ . This leads to a metric tensor

$$g_{\mu\nu} = \begin{pmatrix} -1 & 0 & 0 & 0 \\ 0 & 1+h & 0 & 0 \\ 0 & 0 & 1-h & 0 \\ 0 & 0 & 0 & 1 \end{pmatrix} \quad (1.9)$$

To determine the effect of this metric tensor on lengths along  $x$  or  $y$ , Eq.(1.4) is used with either  $dx^\mu$  or  $dx^\nu$  set to the dimension of interest. Thus  $\Delta x = \sqrt{ds^2}$  with  $dx^\mu = dx^\nu = (0 \ 1 \ 0 \ 0)$ , so  $\Delta x = \sqrt{g_{11}dx^1dx^1}$  and using the metric in Eq.(1.9),  $\Delta x = \sqrt{1+h} \simeq 1 + \frac{1}{2}h$ ; similarly  $\Delta y = \sqrt{1-h} \simeq 1 - \frac{1}{2}h$ .

## 1.2 Binary Pulsar Evidence for GW

The primary evidence thus far for the existence of gravitational radiation is the Binary Pulsar PSR 1913+16, discovered by Hulse and Taylor in 1974 [34, 73], for which they were awarded the Nobel Prize in 1993. This is a binary neu-

tron star system, with an orbit slightly larger than our Sun's diameter. Observations over more than twenty years have confirmed that the orbital decay of this system matches predictions based on general relativity, as shown in Fig. 1.2. One measure of this decrease in orbital period is the steady shift of the time of the pulsar's closest approach (periastron) to its companion star. The cumulative value of this shift measured by J. Taylor and J. Weisberg at the Arecibo radio telescope in Puerto Rico over several decades is shown in Fig.1.2. The points are their measured data. The agreement with theory is **better than a third of a percent**, and there are no free parameters in the fit! This plot is taken from Ref. [53]. The system has been observed in great detail, and is documented in several sources, including Ref. [17]. The masses of the system are deduced to be  $M_1 = 1.4410 \pm 0.0005 M_\odot$  (the pulsar) and  $M_2 = 1.3874 \pm 0.0005 M_\odot$  (the companion). The period and eccentricity of the binary orbit were  $P_{\text{orb}} = 27906.9808968 \pm 0.0000016$  s and  $e = 0.6171308 \pm 0.0000004$  in 1990, respectively. As the system radiates energy, the system's orbit decreases and the periastron (where the two neutron stars are nearest each other) precesses. The measured value of  $4.22626^\circ$  per year is in good agreement with the theoretical value. This effect is cumulative, making it easier to measure the longer the system is observed. The rate at which the orbital period changes due to gravitational radiation is

$$\dot{P}_{\text{orb}} = \frac{dP_{\text{orb}}}{dt} = -\frac{96 G^3 M^2 \mu}{5 c^5} \left( \frac{4\pi^2}{GM} \right)^{4/3} \frac{f(e)}{P_{\text{orb}}^{5/3}}, \quad (1.10)$$

where

$$\begin{aligned} M &= M_1 + M_2 \\ \mu &= \frac{M_1 M_2}{M_1 + M_2} \end{aligned}$$

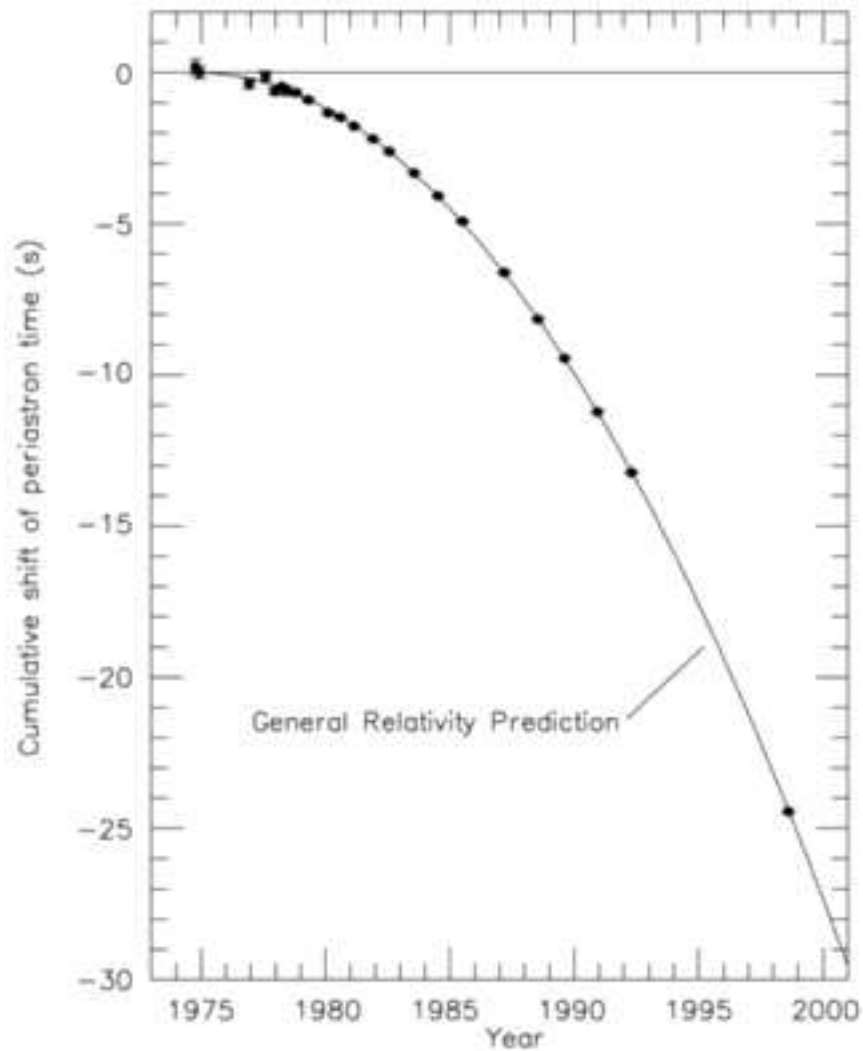


Figure 1.2: The orbital period of any body around another decreases because of the energy lost to gravitational radiation. That effect is strongest in highly relativistic systems such as the binary pulsar PSR1913+16.

and  $f(e)$  describes the effect of the eccentricity of the orbit,

$$f(e) = \left(1 + \frac{73}{24}e^2 + \frac{37}{96}e^4\right) (1 - e^2)^{-7/2}.$$

Higher order correlation terms are neglected in the above formula. This leads to an expected decrease in orbital period of  $\dot{P}_{\text{orb}} = -2.40259 \times 10^{-12}$ , which, as indicated above, agrees with the measured value to within 0.3%. When reporting their findings in 1984, Joel Weisberg and Joseph Taylor wrote: “It now seems an inescapable conclusion that gravitational radiation exists as predicted by the general relativistic quadrupole formula.”

## 1.3 Detectors

Initially predicted by Einstein [25], the field of Gravitational Wave (GW) detection was pioneered by J. Weber [71] in the early 1960s. Weber’s paper of 1969 [72] inspired a community of independent researchers to confirm his reported detection of a GW event. Although Weber’s initial report of an observation has never been confirmed, and was later determined to be in error, the search continues. There are two primary types of gravitational wave detectors, resonant bars and interferometers.

### 1.3.1 Resonant Bars

Figure 1.3 shows a bar detector currently on display at the LIGO Hanford IFO site. The bar was one of three used by Weber at the University of Maryland in his experiments to search for gravitational waves from astrophysical sources. Another of the bars is on exhibit at the Smithsonian Institution in Washington DC. The bar is a solid object, held together, as usual, through electrostatic forces



Figure 1.3: Resonant Bar Gravitational Wave Antenna

which are dependent upon the distance its constituent components. Thus, when a gravitational wave passes through the area of space-time occupied by a bar detector the distances between points within that space are changed as described by the GW metric. This change in distance between the molecules of the bar causes a change in the internal pressure of the bar at the frequency of the GW. If this frequency corresponds to the resonant frequency of the bar, then the bar will resonate and “ring”. The amount of vibrational energy in this ringing would correspond to the amount of energy transferred to the bar by the gravitational wave, which is to say very small. Modern bar detectors are cooled to cryogenic temperatures to reduce thermal noise, and thereby enhance the possibility of detecting the motion by transducers attached to the end faces. The bar antenna is essentially a simple device, but it has a narrow frequency response and for most bars it is centered at  $\simeq 700 - 900$  Hz.

### 1.3.2 LASER Interferometers (IFOs)

The other type of detector is a LASER Interferometer. Here a LASER beam is split by a beamsplitter and sent in orthogonal directions to semitransparent

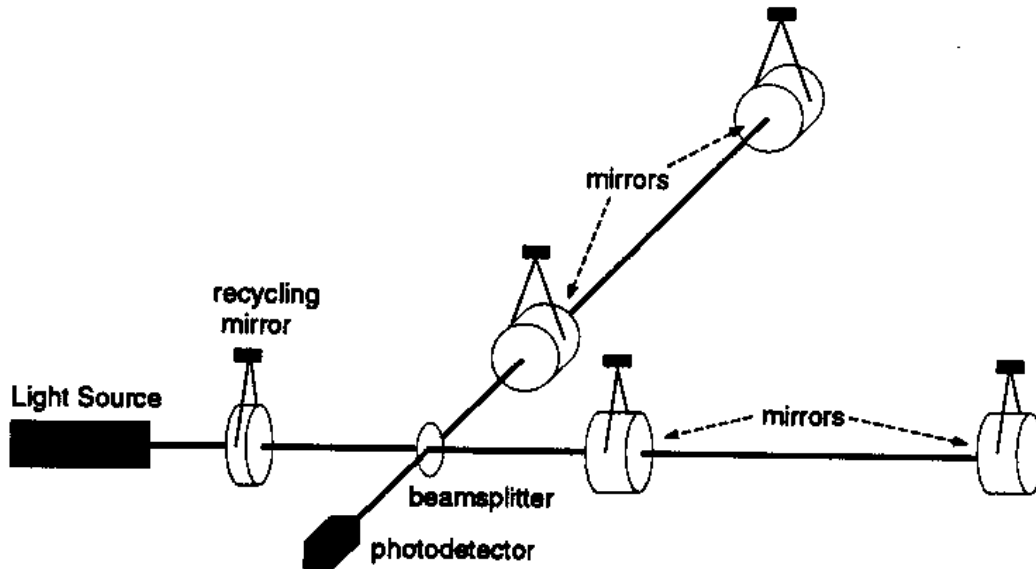


Figure 1.4: Schematic layout of the Interferometer showing mirror suspensions

mirrors which reflect the light back to the beamsplitter. When a gravitational wave is incident on the IFO, it moves the mirrors in each arm in a differential way which changes the interference pattern of the light returning to the beamsplitter. To obtain the desired sensitivity, further refinements are needed and these will be discussed in detail in the following chapters. The main benefit of an IFO over a bar is that the IFO is a broadband device, sensitive to GW events of much lower frequency and can therefore reach greater sensitivity. Figure 1.4 shows a simple diagram of an IFO with Fabry-Perot arm cavities and a power recycling mirror.

## 1.4 Expected Sources of Gravitational Waves

The primary interest in the direct observation of GWs lies in the expectation of carrying out GW-astronomy, opening up a new window on the universe. Because GW's interact so weakly with matter, it will be possible to observe sources for which electro-magnetic (EM) radiation is absorbed, such as sources within galactic interiors. It will also make possible the study of violent astrophysical phenomena, such as the coalescence of binary stars and supernovae explosions. Such events are rare, and must therefore be detectable over large distances in order to observe even a few events per year.

The intensity of a GW falls off as  $1/R^2$ , where  $R$  is the distance of the source to the observer on earth. Thus, the GW amplitude  $h(t)$ , falls off as  $1/R$ . The distance  $R$  at which a source can be detected is proportional to the inverse of the minimum strain sensitivity,  $h_d$ , of the detector. Lowering the sensitivity by a factor  $D$ , increases the observation volume and the number of observable sources by a factor of  $D^3$ .

Because of the weakness of the GW signal relative to the noise in the instruments, it is important to exploit coincident detection at several sites. Given the low frequency of the GW, these sites can be widely separated as indicated in Fig. 1.5. There are three LIGO interferometers (IFOs), two at the Hanford site in Washington State (a 4 km IFO and a 2 km IFO) and one at the site in Livingston, Louisiana (4 km IFO). Furthermore, a signal received at several sites can be used to establish the direction of arrival of the GW. Collaboration with the other IFO GW detector groups VIRGO, GEO and TAMA can improve the localization of the source, as is illustrated in Fig. 1.6.

GW sources are categorized in three main groups: (a) Quasi-periodic and truly periodic sources, (b) Burst events of short duration, and (c) An incoher-



Figure 1.5: LIGO Detectors in Richland, WA (LHO) and Livingston, LA (LLO)

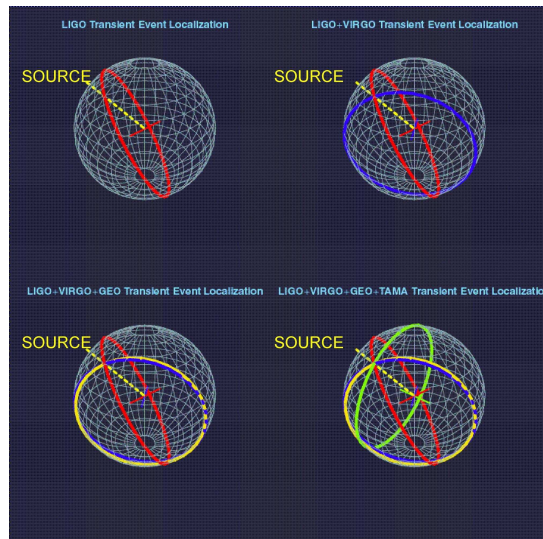


Figure 1.6: Measurement of GW source by inter-collaboration correlation measurements



ent stochastic background. In the first category, the coalescence of binary-star systems leads to a chirped frequency signal with a very distinct pattern. This pattern lasts only a few minutes in the LIGO frequency band, but this is sufficient to extract the signal from the noise. Truly periodic sources such as pulsars and non-coalescing binary systems (see Section 1.2) also emit GW, but the expected amplitude on earth is very weak or not within the LIGO frequency band. Long integration time can be used to extract the signal from the noise, provided Doppler corrections are properly applied. This implies knowledge of the position of the source in the sky, which is not available a priori when searching for new sources.

Burst events occur during the core-collapse of supernovae (SN) or in other similar phenomena. While SN are extensively studied, there is no information on the fraction of energy ( $\epsilon$ ) that is converted to GWs, as it depends on the asymmetry of the collapse. The theoretical prejudice is that  $\epsilon < 10^{-7}$  to  $10^{-8}$ . In contrast, LIGO at design sensitivity could detect a SN with  $\epsilon \gtrsim 10^{-4}$ , at a distance of 55 kpc [26]. The expected SN rate within this volume is only one event per  $\approx$  thirty years. The waveform of the emitted burst is unknown, and in general, it is difficult to distinguish a “burst” event from background noise, even with coincidence between multiple detectors. One can, however, take advantage of observational data, because the light curve of a SN fixes the time of collapse to within an hour. Similar considerations apply to  $\gamma$ -ray bursts, which are now routinely observed, and are assumed to occur during the formation of  $M_{\odot}$  black holes. These are referred to as “triggered” searches.

Estimates of the GW amplitude as a function of frequency for several periodic sources are shown in Fig. 1.7, and for burst sources in Fig. 1.8 [70]. These graphs also show the sensitivity of the LIGO detector and of Advanced LIGO (see

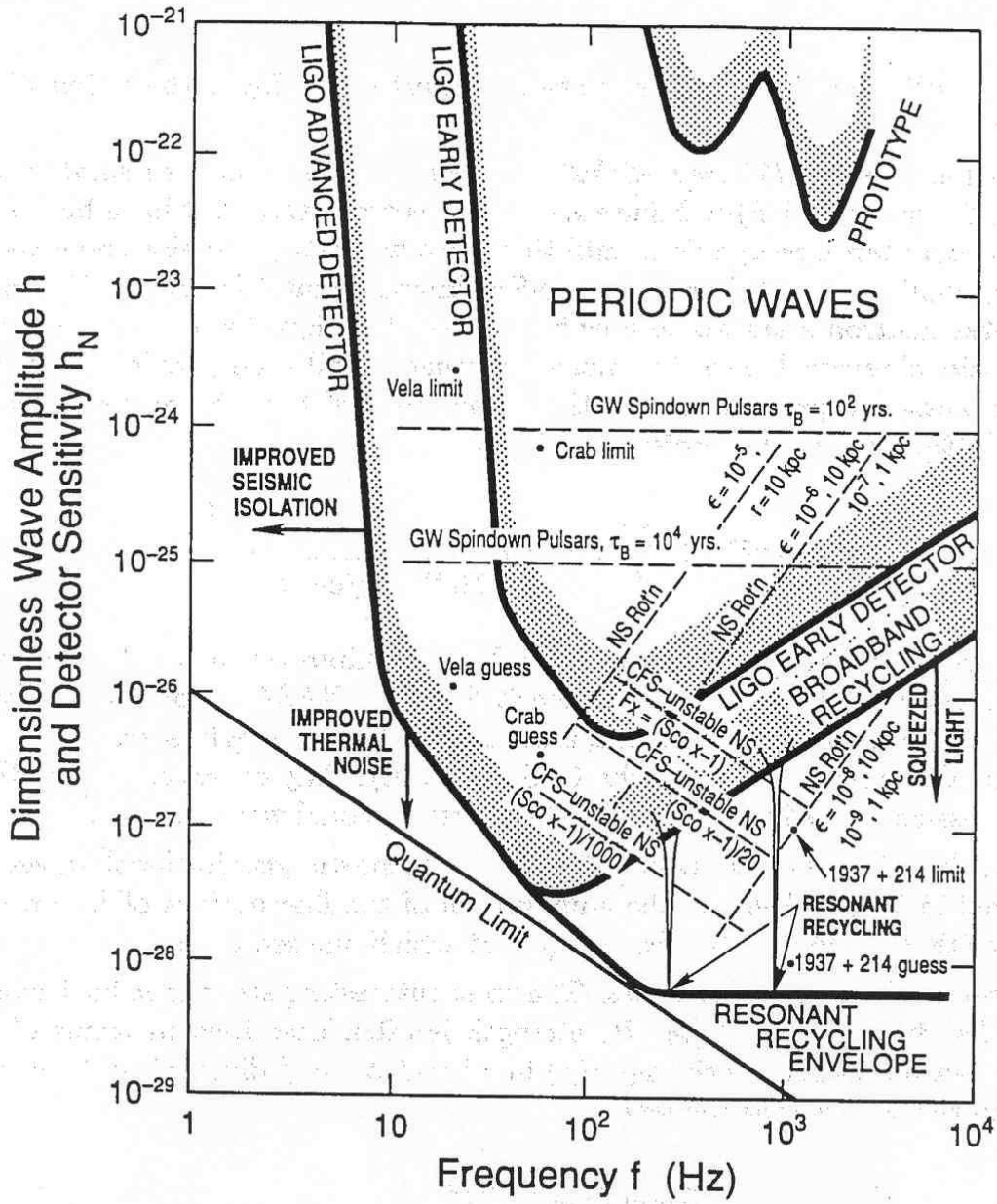


Figure 1.7: LIGO Sensitivity to Periodic Sources, estimated 1989 [70]

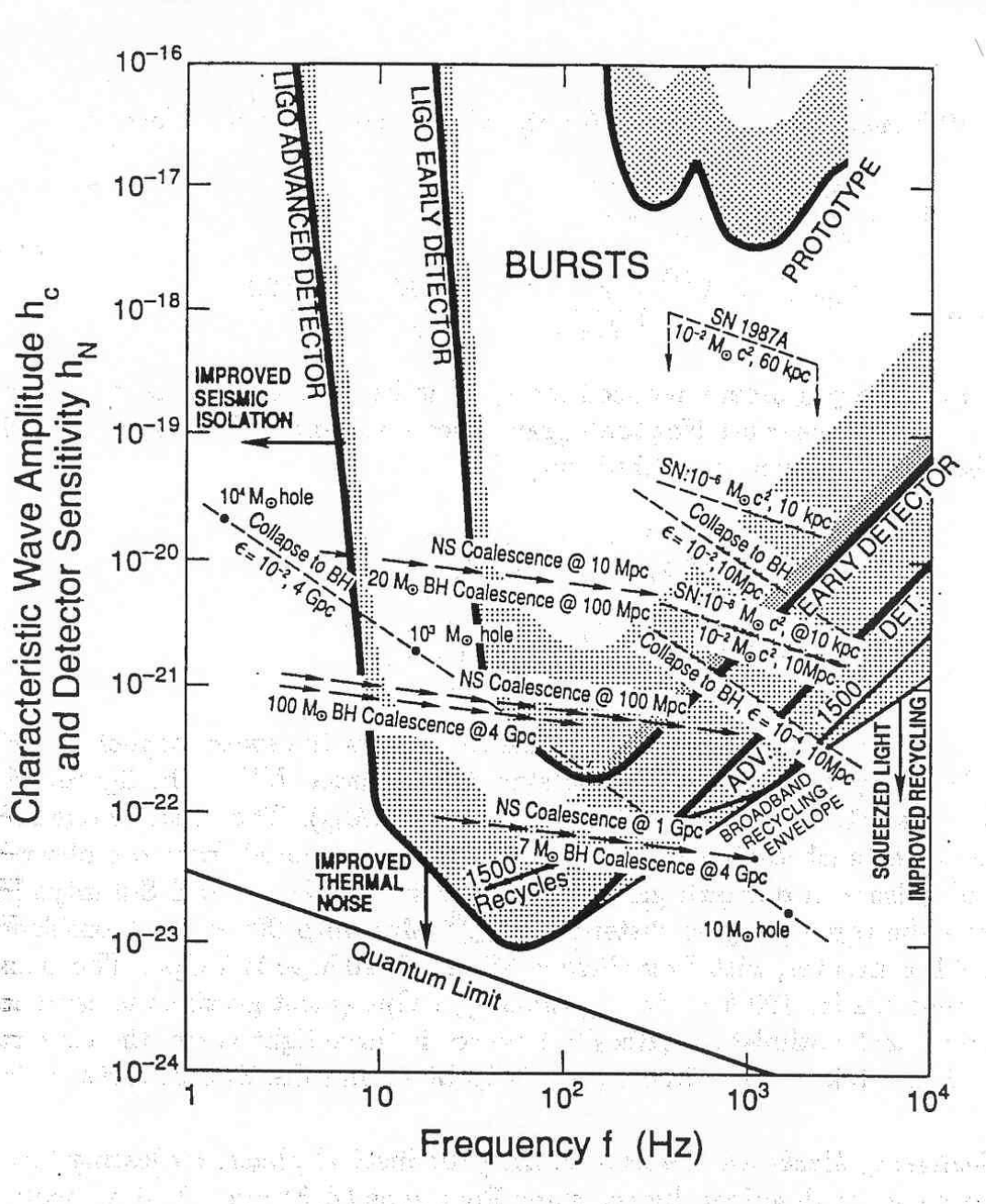


Figure 1.8: LIGO Sensitivity to Burst Sources, estimated 1989 [70]

following Section 1.5.1). The following abbreviations are used in the figures:  $f$  = frequency,  $\tilde{h}(f)$  = square root of the spectral density of the IFO's noise, SN = supernova, NS = neutron star, BH = black hole,  $M_{\odot}c^2$  = one solar rest mass (in units of energy carried by GWs) and  $\epsilon$  = fraction of mass emitted in GWs. One parsec (pc)  $1 \text{ pc} = 3.086 \times 10^{16} \text{ m} = 3.26 \text{ light years}$ . For the periodic sources in Fig. 1.7 the LIGO sensitivity curve represents a detected signal-to-noise ratio of unity, after integration of a source of known frequency for  $\hat{\tau} = 10^7$  seconds (4 months) with  $h_N$  related to the square root of the noise by  $h_N = \tilde{h}(f)/\sqrt{\hat{\tau}}$ . For burst sources in Fig. 1.8, the characteristic amplitude  $h_c \simeq h\sqrt{n}$ , where  $n$  is the number of cycles in the burst for which the amplitude is near  $h$  and the frequency is near  $f$  and the benchmark sensitivities are  $h_N \simeq \tilde{h}(f)\sqrt{f}$ .

LIGO has a fixed configuration unlike Advanced LIGO, described in Section 1.5.1. Design requirements call for a peak sensitivity for the LIGO instrument of  $\tilde{h}(f) = (3 - 6) \times 10^{-23} / \sqrt{\text{Hz}}$  in the 75-500 Hz frequency band. Of interest is the distance at which LIGO will be able to “see” a a given gravitational event, or the volume of space searched for such events. The distance is defined for a specific type of binary inspiral event, defined as a binary system with mass  $M = (1.4 + 1.4) M_{\odot}$  and radius  $r \approx M^{5/6}$ ; this gives the expected strain of  $h = 10^{-21}$  mentioned earlier. With a signal to noise ratio of  $\approx 8$  this gives LIGO a *Science Reach* of  $r = 14 \text{ Mpc}$ . For comparison, note that the Milky Way has a disk diameter of approximately 50 kilo-parsecs (kpc), a halo diameter of 100 kpc, and the Sun's distance from the center of the galaxy is approximately 8.5 kpc [74]. Our Milky Way Galaxy and the Andromeda Galaxy (M31) are part of a cluster of galaxies called the local group, which spans about 1 Mpc along its largest dimension. The Virgo cluster of galaxies is approximately 15.7 Mpc away.

Stochastic GW can be of cosmological origin (e.g. the Big Bang), or can originate from an incoherent addition of GWs emitted from several independent astrophysical sources. It is customary to define the strength of the stochastic background in terms of the fractional energy in a logarithmic interval (see Chapter 5)

$$\Omega_{\text{gw}}(f) \equiv \frac{f}{\rho_c} \frac{d\rho_{\text{gw}}}{df}$$

where  $\rho_c$  is the critical energy density required to close the universe and  $\rho_{\text{gw}}$  is the energy density of gravitational waves. In this model, the amplitude  $h(f)$ , in a bandwidth  $\Delta f = f$  falls off as  $1/f^2$ . This is shown in Fig. 1.9 for an integration time of  $10^7$  seconds. Theoretical prejudice and limits on  $\Omega_{\text{gw}}$  are discussed in Section 5.1.

Figure 1.10 shows the sensitivity achieved by the LIGO instruments (H1 = LHO 4k IFO, H2 = LHO 2k IFO, L1 = LLO 4k IFO) during the S1 science run (Sept. 2002). Significant improvements have been made since that time, resulting in an overall reduction of the noise floor of roughly a factor of 10. This compares favorably with the “Early Detector” design shown in the previous figures. New calculations on source characteristics and expected signal levels are constantly being done; see for instance [12, 33, 43].

## 1.5 Future Detectors

### 1.5.1 Advanced LIGO

Advanced LIGO is an upgrade proposed for the current LIGO configuration, and has an anticipated sensitivity more than ten times better than LIGO, and also extends the detection sensitivity to lower frequencies. As the volume of search space grows with the cube of the sensitivity it is estimated that 2.5 hours of run-

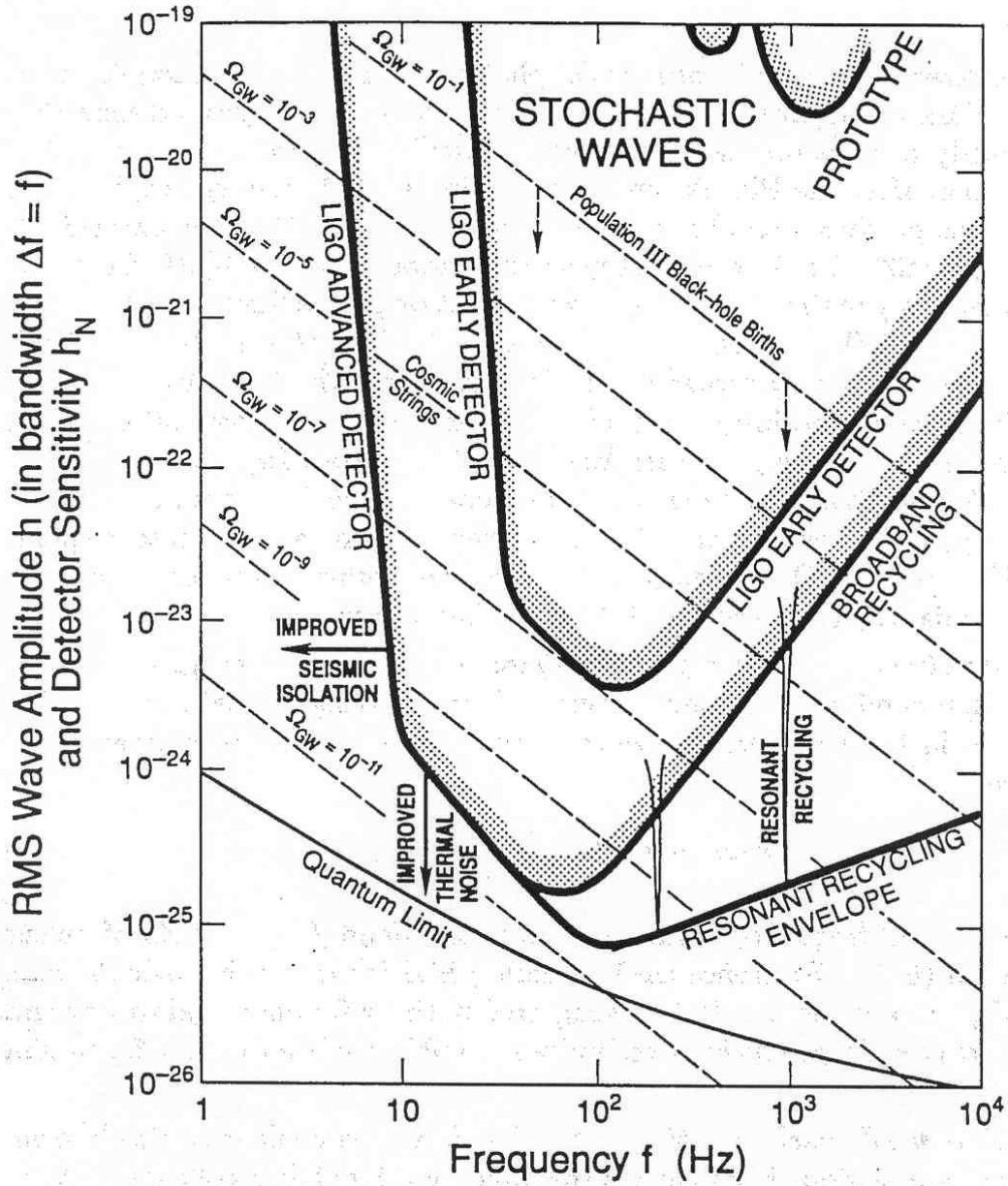


Figure 1.9: LIGO Sensitivity to Stochastic Sources, estimated 1989 [70]

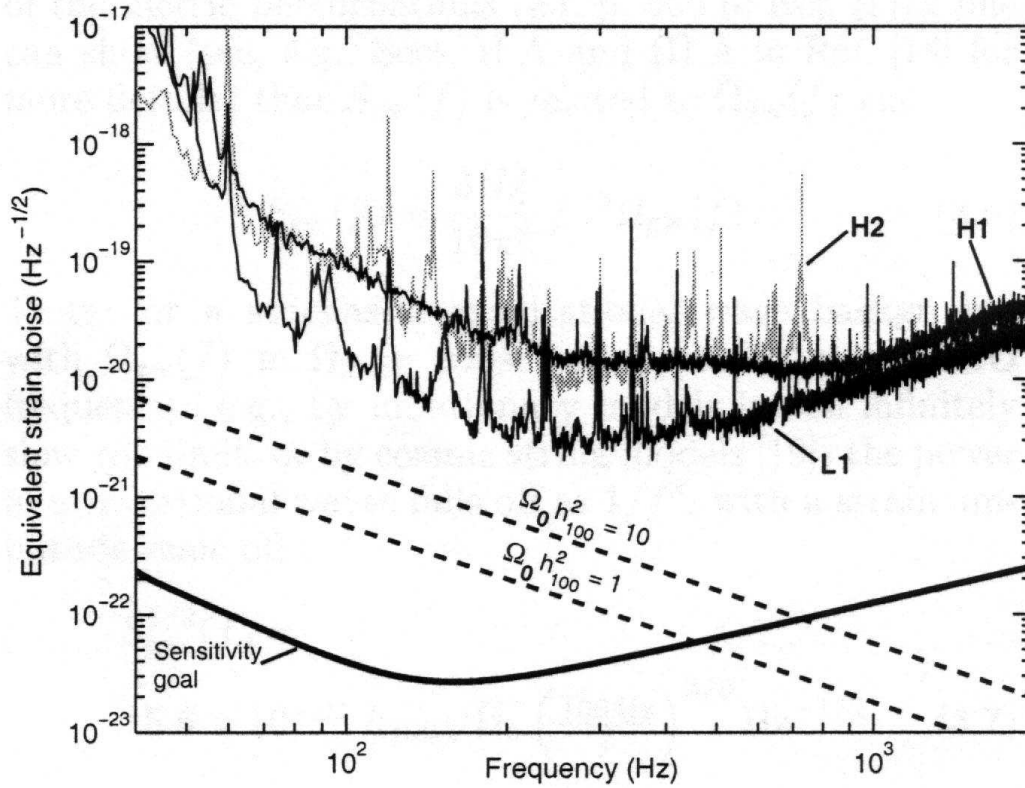


Figure 1.10: LIGO S1 calibrated strain measurements as of Sept. 2002, for the L1 = Livingston 4k IFO, H1 = Hanford 4k IFO and H2 = Hanford 2k IFO. Also shown is the design sensitivity, and two stochastic GW background levels for comparison

ning with Advanced LIGO should be equivalent to 1 year of running with LIGO. Primarily the upgrade calls for higher input LASER power, better optics, quieter suspension and a more sophisticated vibration isolation system[38]. Advanced LIGO is expected to have a much higher probability of detecting gravitational events as it is designed to have a search space more than 1,000 times larger than LIGO. Advanced LIGO should theoretically have a search space containing the nearest one or two million galaxies. It is expected that approximately one binary neutron-star merger per year should occur within this search space [36] of radius 200 Mpc. The exact timing of the upgrade from LIGO to Advanced LIGO is still unknown, but installation is slated to begin in 2007 [54].

The upgrade from LIGO to Advanced LIGO involves an improvement in sensitivity by a factor of more than ten over the entire initial LIGO band and increased bandwidth in the low-frequency regime (from  $\approx 40$  Hz to  $\approx 10$  Hz). The installation of a signal-recycling mirror (much like the power-recycling mirror on the input port but the signal-recycling mirror will be on the anti-symmetric port) will allow the instrument to be used as a tunable narrow band detector. This could also provide higher-frequency operation than for the initial LIGO.

Advanced LIGO was to use Sapphire optics instead of Fused Silica, as currently used in LIGO. Continuing research has shown that there *may* not be as much of an advantage to this technique as originally predicted, and a decision is expected soon. In addition, the optics are to be larger to reduce thermal noise ( $\approx 30$  cm up from 25 cm) and more massive to reduce radiation pressure noise ( $\approx 40$  kg up from 11 kg). It is also expected that compensation for thermal lensing (changing the curvature of the optics by LASER heating) will be incorporated into the optics design. Test mass suspensions will be switched from steel wire slings to fused silica fibers improving both the magnitude and shape of the



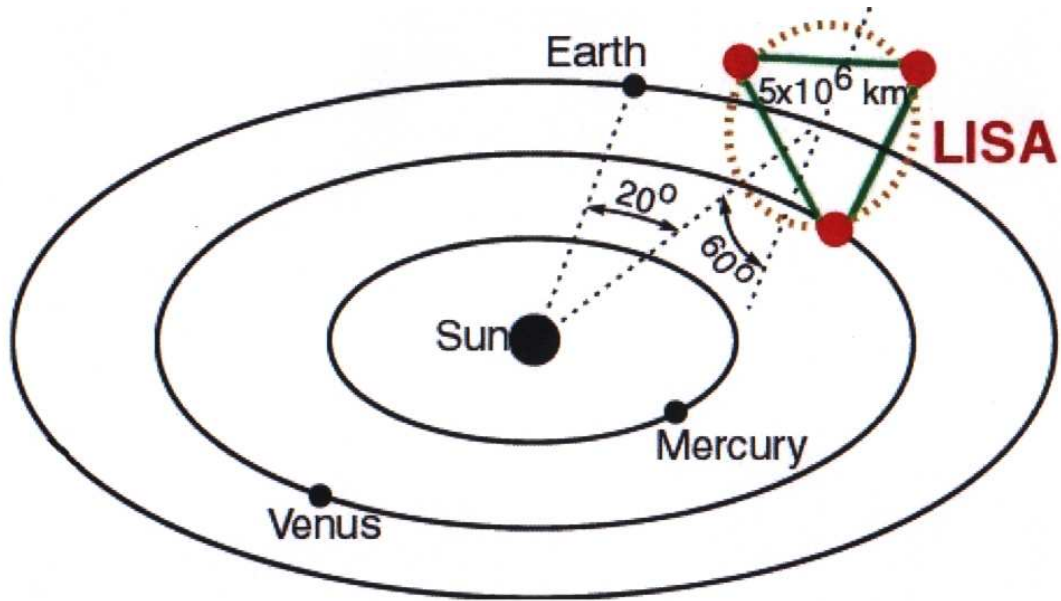


Figure 1.11: Orbital Schematic of LISA: LASER Interferometer Space Antenna

contribution from suspension thermal noise.

One of the most important changes will be the upgrade of the seismic isolation system required to move the “seismic wall” from 40 Hz to 10 Hz. The suspension system will become more complicated, and involve several layers of passive isolation as well as isolation based on active feedback.

### 1.5.2 LISA

Seismic noise, both natural and man-made, is the primary limiting factor to LIGO sensitivity at low frequency. As it is expected that a great number of sources are generating signals at frequencies below 1 Hz, one would like to have a gravitational wave detector that is *not* limited by seismic noise. One way to achieve this is to place the detector in outer space. This is the motivation for LISA: the LASER Interferometer Space Antenna (see Fig. 1.11).



Figure 1.12: Cutaway of LISA's instrument. The actual spacecraft will be protected with a cover. Image from LISA webpage [19].

LISA is expected to detect a completely different (lower) range of the spectrum than LIGO. LISA is comprised of three Y-shaped spacecrafts (Fig. 1.12), moving together in helio-centric orbit, following the orbit of the earth around the sun. Each of LISA's three arms would stretch five million kilometers. Small telescopes in each spacecraft would collect the LASER light sent sixteen seconds earlier from the other two crafts. The test masses used would be metal cubes, four centimeters across, free-floating in space within (but not touching) the spacecraft [35]. Each of LISA's spacecrafts houses two separate test masses, as shown in Fig. 1.13. Because of the vast distances involved, the relative positions of the test masses must be measured only to an accuracy of two-tenths of an angstrom ( $2 \times 10^{-11}$  m), which should be easier than LIGO's requirement of one thousandth the diameter of a proton ( $1 \times 10^{-18}$  m).

LISA is a joint European-U.S. mission, with a currently estimated launch date of 2011. The total costs range from a 2002 estimate of \$600 million to more than \$1 billion. Design and engineering projects are underway for satellite flight by the European Space Agency (ESA) planned for 2006 to check crucial LISA technology [37]. The ESA satellite SMART-2 will fly two test packages of proof masses and hardware, to validate the engineering to within a factor of ten of

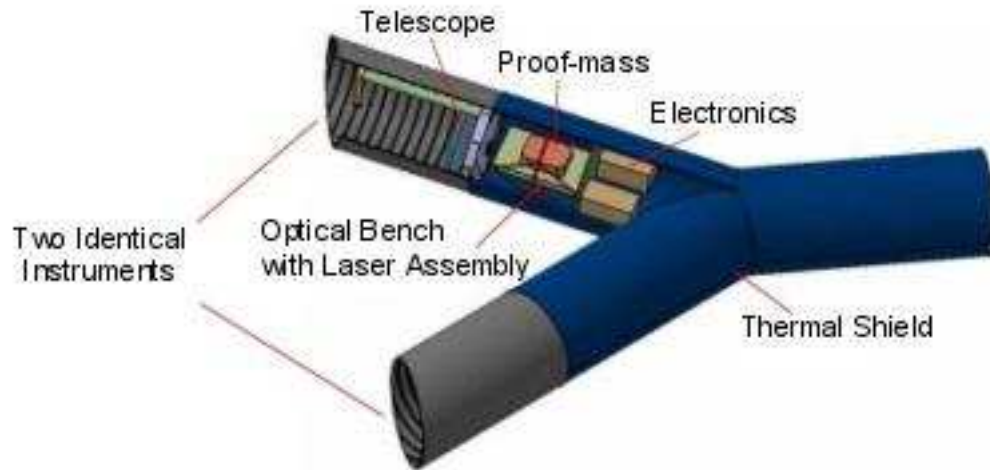


Figure 1.13: LISA Instrument

LISA's goals.

Gravitational radiation expected in LISA's low frequency band ( $10^{-4} - 10^{-1}$  Hz) provides cause for optimism. According to Neil Cornish of Montana State University, Bozeman: "We have a massive signal-to-noise, far better than for some optical instruments. We will see sources within the first hour of turning on." Not only is the signal strength expected to be much higher, but also LISA is sensitive to more sources than LIGO or Advanced LIGO. It is even possible that these sources will combine into a noise source for LISA. Some predictions show that LISA should be sensitive to GW emissions from close pairs of white dwarfs within our own galaxy, the Milky Way.



# Chapter 2

## The LIGO IFOs

### 2.1 LIGO Layout

Many of the terms and acronyms used at LIGO are difficult to recall without having worked at the site. Also I have found that simple lists of acronyms do little to alleviate the confusion. For this reason I have included Figure 2.1, as well as a walk through the system introducing the acronym's as they are encountered.

The LASER source for the system is a 10 Watt industry LASER from Light-Wave. This is frequency locked onto a Reference Cavity, which is a Fabry-Perot Cavity (cavity or FP) of fixed length suspended in vacuum inside an insulated chamber to minimize thermal variations. The LASER output is then passed through a Pre-Mode Cleaner (PMC). The PMC is a small ring cavity which changes its length to stay locked onto the LASER frequency, the primary purpose of which is to filter out the non TEM<sub>00</sub> LASER output. After the PMC the beam is sent through Electro-Optic Modulators (EOMs) to put the phase modulated sidebands on the carrier frequency. These are necessary for locking the interferometer with the Pound-Drever-Hall [24] locking method. The configura-

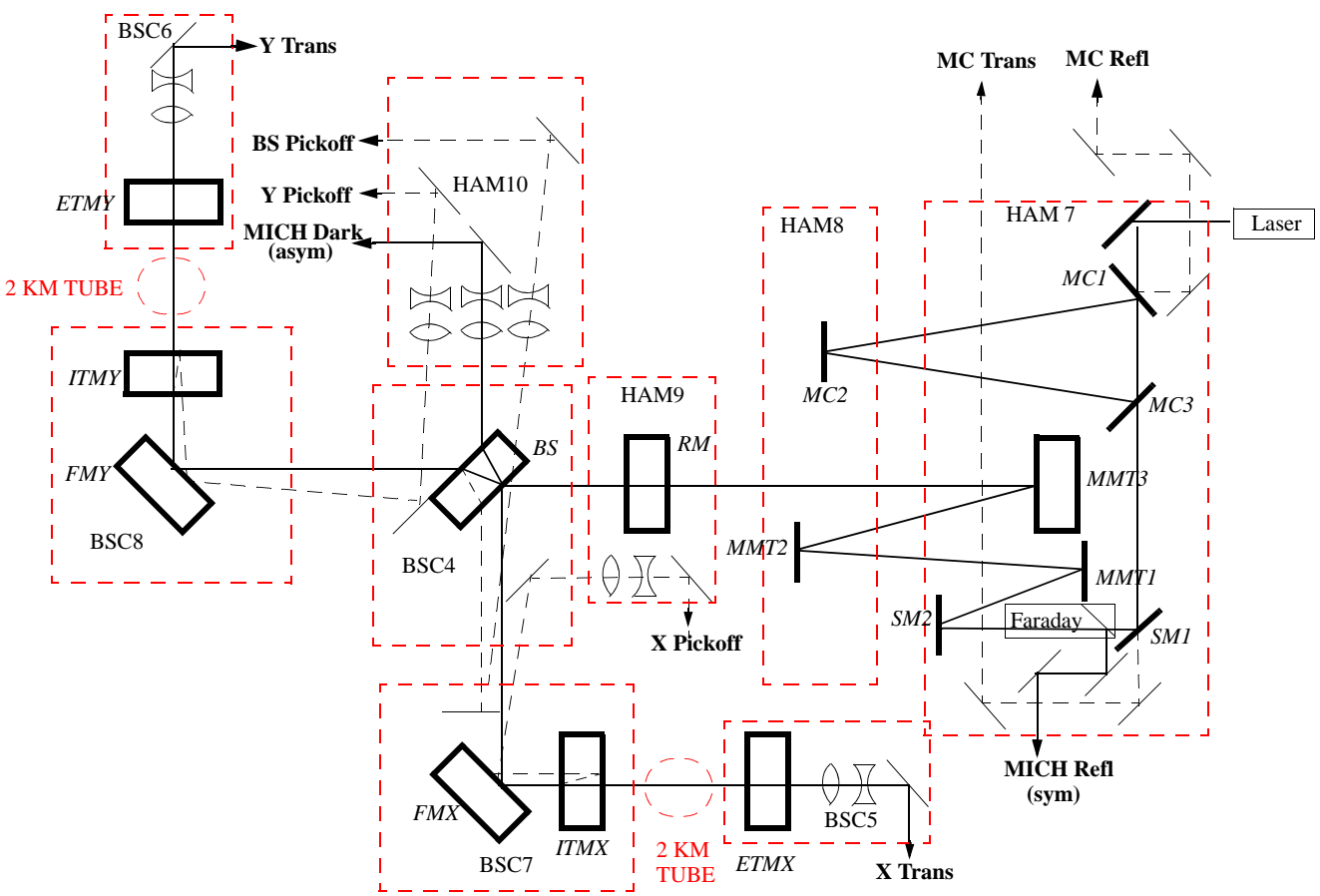


Figure 2.1: 2k Hanford LIGO Schematic

tion described so far is referred to as the Pre-Stabilized LASER (PSL). The PSL is contained entirely on one LASER table in the LASER Vacuum Equipment Area (LVEA) and is enclosed in an acoustic shielding cabinet.

The PSL output is directed into the vacuum system. The rest of the interferometer components are in vacuum with some LASER beams exiting through view-ports for diagnostic and detection purposes. All exiting beams are carefully contained and are routed onto optics tables with suitable diagnostic and detection equipment used to lock and characterize the interferometer. The PSL output enters HAM7 and is mode matched into the Mode Cleaner (MC). There are two types of vacuum chambers used to contain optics: HAMs and BSCs. A HAM is a Horizontal Access Module and a BSC is a Beam Splitter Chamber (or a Bi-Symmetric Chamber). Figure 2.2 is a computer generated image of a HAM chamber, Fig. 2.3 similarly shows a BSC chamber. The BSCs are larger and



Figure 2.2: HAM Chamber and its seismic isolation



Figure 2.3: BSC Chamber and its seismic isolation

the optics table is suspended from the top of the chamber while in the HAM the optics table is mounted from the bottom. Both types of chambers use similar passive vibration/seismic isolation systems consisting of stacked layers of masses and springs, referred to as stacks. Although initially designed for different purposes many of the reasons for the differences between HAMs and BSCs were later abandoned.<sup>1</sup> The chamber's numbers reference the order in which they were manufactured. Thus although it is useful to reference HAM7 and HAM8 as containing the Mode Cleaner, the numbers 7 and 8 do not necessarily have any relation to the chamber's location in the interferometer.

The suspended optics are labeled in Fig. 2.1, these consist of the small optics and the large optics. The small optics are 0.25 kg and are used in the Mode

---

<sup>1</sup>HAMs and BSCs are also occasionally referred to as WHAMs or LHAMs and WBSCs or LBSCs, the preceding W or L referencing the Washington or Louisiana site.



Cleaner (MC), the Mode Matching Telescope (MMT) and as Steering Mirrors (SM). The large optics are 11 kg and are used for the core interferometer optics: Recycling Mirror (RM), Beam Splitter (BS), Folding Mirrors (FM), Input Test Masses (ITM) and End Test Masses (ETM). The exception is the third Mode Matching Telescope mirror MMT3 which is a large optic. The MC is a three mirror ring cavity 15 meters in length. The mirrors are 0.25 kg and are suspended in much the same way as the primary interferometer optics. The MC stabilizes the LASER in frequency and intensity and selects the  $TEM_{00}$  mode. The PSL is locked onto the MC using a standard PDH (Pound Drever Hall) method. The feedback control signal for this is split and filtered for low frequency and high frequency. The idea is that at high frequency the MC is very stable and is used as a reference to change the frequency of the PSL. It does this by sending a feedback signal to an Acousto-Optic Modulator (AOM) which is placed before the PSL reference cavity. The LASER into the reference cavity passes through the AOM twice to remove the AOM induced angle in the beampath. Since the AOM changes the frequency of the light incident on the reference cavity, the frequency of the LASER light out of the LASER has to change in the opposite direction to stay locked to the reference cavity (the reference cavity locking signal is sent back to the LASER). The high frequency MC feedback signal is sent through a high pass filter and is labeled as MC\_F (Mode Cleaner Frequency).

Since the MC is suspended by wires it may drift at low frequency and therefore the feedback at low frequency is used to control the MC length. This feedback signal is sent through a low pass filter and is labeled as MC\_L (Mode Cleaner Length). The entire signal name is H2:IOO-MC\_L. H2 indicates the second interferometer at the Hanford site, H1 would be the 4k interferometer at Hanford and L1 would be the 4k interferometer at Louisiana. IOO references

the Input Output Optics subsystem of the interferometer.

After the Mode Cleaner the LASER is steered (with SM1 and SM2) into the Mode Matching Telescope (MMT1, MMT2 and MMT3) which “mode matches” the LASER into the interferometer. The LASER “mode” references the spatial characteristics of the LASER beam, minimum beam size, shape and location. The first core optic encountered is the Recycling Mirror (RM), the purpose of which is to reflect most of the interferometer output light back into the interferometer. The instrument is referred to by the components: Arm Cavities, which consist of an ITM and an ETM forming a FP cavity and Power Recycled Michelson (PRM) which consists of the RM, BS and both ITMs also forming a FP cavity. If one were to lock both arm cavities and lock the interferometer on a dark fringe at the antisymmetric port of the BS while having the RM completely misaligned (so that it simply acts as an input attenuator and doesn’t form a cavity) the system is referred to as being in recombined mode. This is to distinguish the recombined interferometer configuration used during the second engineering run (E2) from the power recycled interferometer (PRIFO) configuration as originally designed and currently in use.

## 2.2 The mirror equations

Here I derive the equations for the electric fields at various locations in the power recycled interferometer. Then I investigate how symmetry arguments can simplify those equations. This allows for an analytic investigation of the interferometer response to various stimuli.

When dealing with reflection and transmission from real mirrors there can be some confusion on how to deal with relative phases acquired during the light/mirror interaction. In some of the LIGO related documents (e.g. [29,

39, 57]) the convention used is to give reflection from one side of the mirror as a negative coefficient and reflection from the other as a positive coefficient. However, most optics documentation (e.g. [59, 65]) uses a convention where the reflection is the same from either side of the optic as is the transmission, but the transmission is given an additional factor of  $i$ . Siegman [65] has a nice discussion about the two conventions in Chapter 11, page 405-6 of his book.

For all future analysis of LASER cavities and interferometers in this book, however, I will arbitrarily choose the complex symmetric form  $\mathbf{S} = [r, it, it, r]$ , with  $r$  and  $t$  purely real, as the scattering matrix form to describe all mirrors and beam-splitters. This arbitrary choice will make no difference in any of the physical conclusions I reach about LASER devices. It seems easier, however, to remember that transmission coefficients always have a factor of  $i$  associated with them than to remember which side of each mirror in a LASER system is the +r and which is the -r side. [Siegman [65] page 406]

I will also use the Siegman convention as its use of symmetry does tend to make the math easier to follow. The physics is the same independent of convention. In fact the LIGO Length Sensing and Control design [68] is convention independent. I also use the convention that a propagation phase is given by  $e^{-i\phi}$  (and not  $e^{i\phi}$ ), this is arbitrary but consistency is necessary.

### 2.2.1 Simple Fabry-Perot

In the case of a generic two mirror Fabry-Perot Cavity as shown in Fig. 2.4 the circulating field can be represented as an infinite summation.

$$E_{cir} = it_1 E_0 + r_1 r_2 e^{-i\phi} it_1 E_0 + r_1^2 r_2^2 e^{-2i\phi} it_1 E_0 + r_1^3 r_2^3 e^{-3i\phi} it_1 E_0 + \dots \quad (2.1)$$

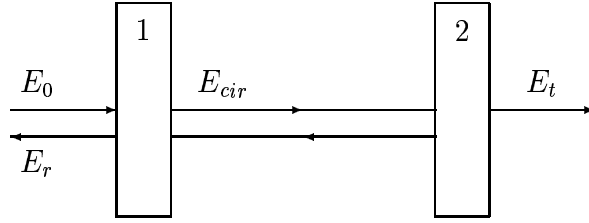


Figure 2.4: Simple Fabry-Perot Cavity

This equals:

$$E_{cir} = \frac{it_1 E_0}{1 - r_1 r_2 e^{-i\phi}} \quad (2.2)$$

where  $\phi$  is the phase collected in one round trip through the cavity (nominally  $\frac{\omega}{c}2L$  with  $L =$  length of the cavity),  $r$  is the electric field amplitude reflectivity of the optic,  $t$  is the amplitude transmission coefficient of the optic and  $A$  is the intensity absorption (or loss) of the optic. For any given optic the relation  $r^2 + t^2 + A = 1$  is true.

**NOTE:** The circulating field is given in terms of the  $E$  field traveling in the direction of the incident beam at mirror 1. There is a counter propagating field given by  $r_2 e^{-i\phi} E_{cir}$  at mirror 1. This field is not used in these calculations.

So the cavity field equations are:

$$\begin{aligned} E_r &= r_1 E_0 + it_1 r_2 e^{-i\phi} E_{cir} \\ E_{cir} &= it_1 E_0 + r_1 r_2 e^{-i\phi} E_{cir} \\ E_t &= it_2 e^{-i\frac{\phi}{2}} E_{cir} \end{aligned}$$

which combine to give the field equations for a Fabry-Perot cavity in terms of

the incident field  $E_0$ :

$$\frac{E_r}{E_0} = \frac{r_1 - r_2(r_1^2 + t_1^2)e^{-i\phi}}{1 - r_1r_2e^{-i\phi}} \quad (2.3)$$

$$\frac{E_{cir}}{E_0} = \frac{it_1}{1 - r_1r_2e^{-i\phi}} \quad (2.4)$$

$$\frac{E_t}{E_0} = \frac{-t_1t_2e^{-i\frac{\phi}{2}}}{1 - r_1r_2e^{-i\phi}} \quad (2.5)$$

and the power built up in the cavity can be obtained by taking the absolute magnitude squared of  $E_{cir}$ . Thus the “power build up factor” is:

$$\left| \frac{E_{cir}}{E_0} \right|^2 = \frac{t_1^2}{1 - 2r_1r_2 \cos(\phi) + r_1^2r_2^2} \quad (2.6)$$

A cavity is said to be “resonant” when the phase of the light obtained while traveling through the cavity interferes constructively with the phase of the light incident on the cavity. That is to say, a cavity is resonant when  $\phi$  is a value providing equation 2.6 with the lowest denominator and thus the highest build up factor. Thus a Fabry-Perot cavity is resonant when  $\cos(\phi) = 1$  and:

$$\left| \frac{E_{cir}}{E_0} \right|^2 = \frac{t_1^2}{(1 - r_1r_2)^2} \quad (2.7)$$

A cavity is said to be “anti-resonant” when the phase is such that the denominator is largest, giving the smallest build up factor.

$$\left| \frac{E_{cir}}{E_0} \right|^2 = \frac{t_1^2}{(1 + r_1r_2)^2} \quad (2.8)$$

### 2.2.2 Interferometer with Fabry-Perot Arms

A Michelson IFO utilizes a beamsplitter and two mirrors to reflect the split beams back toward the beamsplitter to measure small differences in the distances to those mirrors through observation of the interference of the reflected light at the beamsplitter. This is shown in Fig. 2.6. An interferometer with Fabry-Perot

arms is similar with the difference that instead of single mirrors, Fabry-Perot cavities are used, as shown in Fig. 2.5.

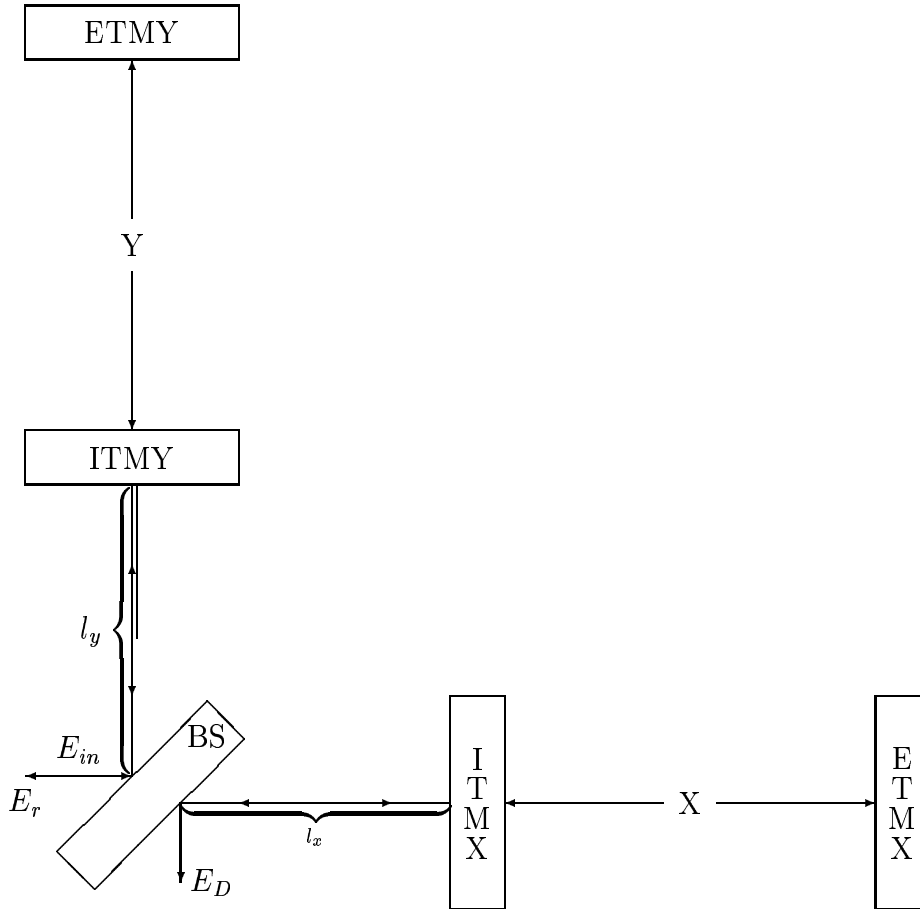


Figure 2.5: Michelson Interferometer with Fabry-Perot Arms

Figure 2.5 can be simplified to Fig. 2.6 by treating the arm cavities as mirrors with complex reflectance given by Eq.(2.3) and transmission given by Eq.(2.5) divided by  $i$  as per the adopted convention. Thus the Fabry-Perot arms X and Y are replaced with mirrors X and Y with complex reflectance  $r_x$  and  $r_y$ .

Here the input light is specified as  $E_{in}$  with the phase defined as 0 at the

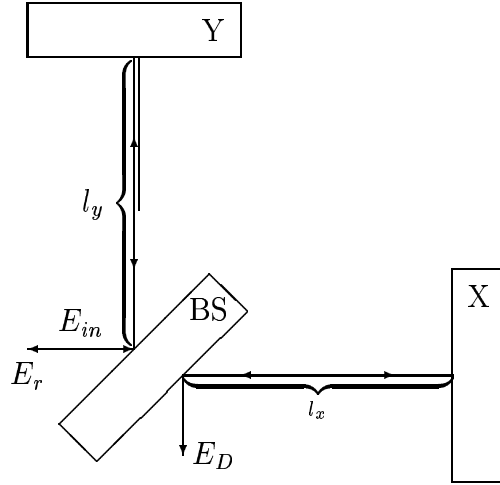


Figure 2.6: Michelson Interferometer

Beam-Splitter (BS). The light will be split at the beam-splitter and reflect off the mirrors X and Y, return and interfere at the beam-splitter. If I define the distance between the beam-splitter and the Y mirror as  $l_y$  and the distance from the beam-splitter and the X mirror as  $l_x$  then the phases picked up during one round trip are  $e^{-i\frac{\omega}{c}2l_x}$  or  $e^{-i\frac{\omega}{c}2l_y}$  respectively. Therefore the fields for the light returning to the BS from the X,Y mirrors are:

$$\text{from Y} \quad r_y r_{bs} e^{-i\frac{\omega}{c}2l_y} E_{in}$$

$$\text{from X} \quad r_x i t_{bs} e^{-i\frac{\omega}{c}2l_x} E_{in}$$

The fields will interfere, sending some light back toward the input beam in the symmetric direction (the “reflected beam”  $E_r$ ) and some in the anti-symmetric direction (the “dark port”  $E_D$ ).

$$\frac{E_D}{E_{in}} = i t_{bs} r_y r_{bs} e^{-i\frac{\omega}{c}2l_y} + i r_{bs} r_x t_{bs} e^{-i\frac{\omega}{c}2l_x} \quad (2.9)$$

$$\frac{E_r}{E_{in}} = r_{bs} r_y r_{bs} e^{-i\frac{\omega}{c}2l_y} - t_{bs} r_x t_{bs} e^{-i\frac{\omega}{c}2l_x} \quad (2.10)$$

Note: Special attention has and will be paid to keeping the reflection and

transmission coefficients in the proper order so that the general equations which result may be used with matrix coefficients (useful when mixing fields of different frequencies).

### 2.2.3 Power Recycled Interferometer

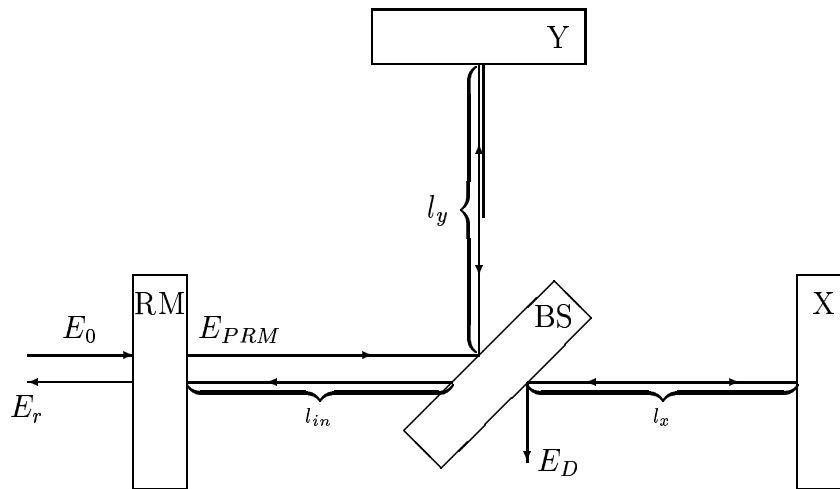


Figure 2.7: Power Recycled Michelson Interferometer

Now, for the Power Recycled Interferometer, a mirror is placed at the symmetric port to reflect most of the light being sent toward the LASER, Eq.(2.10), back into the interferometer. This can be thought of as a simple Fabry-Perot cavity with a complex back mirror formed from the interferometer with reflection coefficient given by Eq.(2.10) and transmission coefficient given by Eq.(2.9) divided by  $i$ . Fields of interest are the built up field incident upon the beam-splitter ( $E_{PRM}$ ) and the field exiting the “dark” port ( $E_D$ ). The field inside the cavity ( $E_{PRM}$ ) is given by using Eq.(2.4) with  $r_2$  specified by Eq.(2.10) and  $r_1$  given by the recycling mirror with the “cavity” length specified as the distance



between the recycling mirror and the beam-splitter<sup>2</sup> ( $l_{in}$ ). The “dark” port field ( $E_D$ ) is given by combining Eqs.(2.5, 2.9) in a similar fashion. Thus:

$$\begin{aligned}\frac{E_{PRM}}{E_0} &= \frac{it_{rm}}{1 - r_{rm}(r_{bs}r_yr_{bs}e^{-i\frac{\omega}{c}2l_y} - t_{bs}r_x t_{bs}e^{-i\frac{\omega}{c}2l_x})e^{-i\frac{\omega}{c}2l_{in}}} \\ \frac{E_D}{E_0} &= \frac{-t_{rm}(t_{bs}r_yr_{bs}e^{-i\frac{\omega}{c}2l_y} + r_{bs}r_x t_{bs}e^{-i\frac{\omega}{c}2l_x})e^{-i\frac{\omega}{c}l_{in}}}{1 - r_{rm}(r_{bs}r_yr_{bs}e^{-i\frac{\omega}{c}2l_y} - t_{bs}r_x t_{bs}e^{-i\frac{\omega}{c}2l_x})e^{-i\frac{\omega}{c}2l_{in}}}\end{aligned}$$

Now I do a simple variable redefinition. Since the  $l_{in}$  distance is common to both arms of the interferometer I add it to  $l_x$  and  $l_y$  and redefine the  $l_x$ ,  $l_y$  distances.

$$\begin{aligned}l_x + l_{in} &\rightarrow l_x \\ l_y + l_{in} &\rightarrow l_y\end{aligned}$$

The formulae now become:

$$\frac{E_{PRM}}{E_0} = \frac{it_{rm}}{1 - r_{rm}(r_{bs}r_yr_{bs}e^{-i\frac{\omega}{c}2l_y} - t_{bs}r_x t_{bs}e^{-i\frac{\omega}{c}2l_x})} \quad (2.11)$$

$$\frac{E_D}{E_0} = \frac{(-t_{rm})(t_{bs}r_yr_{bs}e^{-i\frac{\omega}{c}2l_y} + r_{bs}r_x t_{bs}e^{-i\frac{\omega}{c}2l_x})e^{i\frac{\omega}{c}l_{in}}}{1 - r_{rm}(r_{bs}r_yr_{bs}e^{-i\frac{\omega}{c}2l_y} - t_{bs}r_x t_{bs}e^{-i\frac{\omega}{c}2l_x})} \quad (2.12)$$

and for completeness I also give the field returning to the LASER:

$$\frac{E_r}{E_0} = \frac{r_{rm} - (r_{bs}r_yr_{bs}e^{-i\frac{\omega}{c}2l_y} - t_{bs}r_x t_{bs}e^{-i\frac{\omega}{c}2l_x})(r_{rm}^2 + t_{rm}^2)}{1 - r_{rm}(r_{bs}r_yr_{bs}e^{-i\frac{\omega}{c}2l_y} - t_{bs}r_x t_{bs}e^{-i\frac{\omega}{c}2l_x})} \quad (2.13)$$

At this point one can define a Power Recycled Michelson Interferometer with Fabry-Perot Arms by using Eq.(2.3) for  $r_x$  and  $r_y$ . I will not do this substitution in general form as it provides ample opportunity for error, makes the equations even less understandable and provides no further insight into the operation of the interferometer.

---

<sup>2</sup>The distance between the Recycling Mirror (RM) and the Beam-Splitter (BS) is actually the same for both  $E_{PRM}$  and the counter propagating beam.

## 2.2.4 A Perfect Interferometer

### Common and Differential cavity lengths of the PRM

In order to obtain a feel for how the interferometer is locked some simplifying assumptions are needed. This will allow me to check that the calculations performed in sections 2.2.1 through 2.2.3 are correct as well as help me to understand how certain feedback signals are obtained and how to best feed them back to the interferometer. In sections 2.2.1 through 2.2.3 I took special care to maintain the proper order of operations for reflection and transmission through the optics. In this section I will assume that the mode matching from cavity to cavity is perfect and therefore will not consider scattering into higher order modes. Thus the reflection and transmission coefficients are scalars and therefore commute. Also for simplification I will consider the beam-splitter to be a perfect optic (i.e.  $r_{bs} = t_{bs} = \frac{1}{\sqrt{2}}$ ) and that the arms are identical (i.e.  $r_x = r_y = r_a$ ). Thus Eqs.( 2.11, 2.12) become:

$$\begin{aligned}\frac{E_{PRM}}{E_0} &= \frac{it_{rm}}{1 - r_{rm}(\frac{1}{2}r_a e^{-i\frac{\omega}{c}2l_y} - \frac{1}{2}r_a e^{-i\frac{\omega}{c}2l_x})} \\ \frac{E_D}{E_0} &= \frac{-t_{rm}(\frac{1}{2}r_a e^{-i\frac{\omega}{c}2l_y} + \frac{1}{2}r_a e^{-i\frac{\omega}{c}2l_x})e^{i\frac{\omega}{c}l_{in}}}{1 - r_{rm}(\frac{1}{2}r_a e^{-i\frac{\omega}{c}2l_y} - \frac{1}{2}r_a e^{-i\frac{\omega}{c}2l_x})}\end{aligned}$$

which simplify to

$$\frac{E_{PRM}}{E_0} = \frac{it_{rm}}{1 - \frac{1}{2}r_{rm}r_a(e^{-i\frac{\omega}{c}2l_y} - e^{-i\frac{\omega}{c}2l_x})} \quad (2.14)$$

$$\frac{E_D}{E_0} = \frac{\frac{-1}{2}t_{rm}r_a(e^{-i\frac{\omega}{c}2l_y} + e^{-i\frac{\omega}{c}2l_x})e^{i\frac{\omega}{c}l_{in}}}{1 - \frac{1}{2}r_{rm}r_a(e^{-i\frac{\omega}{c}2l_y} - e^{-i\frac{\omega}{c}2l_x})} \quad (2.15)$$

where

$$r_a = \frac{r_{itm} - r_{etm}(r_{itm}^2 + t_{itm}^2)e^{-i\frac{\omega}{c}2L}}{1 - r_{itm}r_{etm}e^{-i\frac{\omega}{c}2L}} \quad (2.16)$$

At this point the almost sinusoidal form of these equations becomes obvious, the complication being that  $l_x \neq l_y$ . Defining the new variables  $l_p = l_x + l_y$  and

$l_m = l_x - l_y$  and performing the algebra gives:<sup>3</sup>:

$$\begin{aligned} e^{-i\frac{\omega}{c}2l_x} + e^{-i\frac{\omega}{c}2l_y} &= e^{-i\frac{\omega}{c}l_p}(e^{-i\frac{\omega}{c}l_m} + e^{-i\frac{\omega}{c}l_m}) \\ &= e^{-i\frac{\omega}{c}l_p}(2 \cos(\frac{\omega}{c}l_m)) \end{aligned} \quad (2.17)$$

$$\begin{aligned} e^{-i\frac{\omega}{c}2l_x} - e^{-i\frac{\omega}{c}2l_y} &= e^{-i\frac{\omega}{c}l_p}(e^{-i\frac{\omega}{c}l_m} - e^{-i\frac{\omega}{c}l_m}) \\ &= e^{-i\frac{\omega}{c}l_p}(-2i \sin(\frac{\omega}{c}l_m)) \end{aligned} \quad (2.18)$$

This allows for the description of the fields in terms of the Common ( $l_p$ ) and Differential<sup>4</sup> ( $l_m$ ) cavity lengths. Combining Eq.(2.14) with Eq.(2.18) as well as combining Eq.(2.15) with Eqs.(2.17, 2.18) gives:

$$\frac{E_{PRM}}{E_0} = \frac{it_{rm}}{1 + ir_{rm}r_a e^{-i\frac{\omega}{c}l_p} \sin(\frac{\omega}{c}l_m)} \quad (2.19)$$

$$\frac{E_D}{E_0} = \frac{-t_{rm}r_a e^{-i\frac{\omega}{c}(l_p - l_m)} \cos(\frac{\omega}{c}l_m)}{1 + ir_{rm}r_a e^{-i\frac{\omega}{c}l_p} \sin(\frac{\omega}{c}l_m)} \quad (2.20)$$

Which can be multiplied by their corresponding complex conjugate to give the power at the recycling mirror or the dark port as a fraction of the incident power on the cavity.

$$\left| \frac{E_{PRM}}{E_0} \right|^2 = \frac{t_{rm}^2}{1 + r_{rm}^2 r_a^2 \sin^2(\frac{\omega}{c}l_m) + 2r_{rm}r_a \sin(\frac{\omega}{c}l_m) \sin(\frac{\omega}{c}l_p)} \quad (2.21)$$

$$\left| \frac{E_D}{E_0} \right|^2 = \frac{t_{rm}^2 r_a^2 \cos^2(\frac{\omega}{c}l_m)}{1 + r_{rm}^2 r_a^2 \sin^2(\frac{\omega}{c}l_m) + 2r_{rm}r_a \sin(\frac{\omega}{c}l_m) \sin(\frac{\omega}{c}l_p)} \quad (2.22)$$

## Resonance Conditions

In this section I look at the resonance conditions for the whole interferometer for both the carrier and the first order r.f. sidebands. These are used to mix with

---

<sup>3</sup>For calculation purposes it is necessary to note that within LIGO these parameters are generally defined as 1/2 these values (eg.  $l_p = (l_x + l_y)/2$ ).

<sup>4</sup>A small  $l$  is used to denote PRM lengths as a large  $L$  is reserved for the arm cavity lengths, see page 41.

the carrier to give the feedback to keep the arms locked by the Pound-Drever-Hall locking technique. The carrier should be resonant in the cavity but not the r.f. sidebands; this is the desired operating condition for the arm cavities. Referencing section 2.2.1 these conditions are specified in Eqs.(2.4 - 2.8). Thus for resonance I let  $e^{-i\phi} \rightarrow 1$  or  $\cos(\phi) \rightarrow 1$ . However I want the r.f. sidebands to be almost anti-resonant<sup>5</sup> which means that  $e^{-i\phi} \rightarrow -1$ . This means that  $r_a$  from Eq.(2.3) can be approximated as  $-1$  for a resonant carrier and  $1$  for the sidebands when numerical values from Table 2.1 are used.

$$\begin{aligned} \text{Carrier : } r_a &\approx -1 \\ \text{Sideband : } r_a &\approx 1 \end{aligned} \tag{2.23}$$

In order for the sidebands to be incident upon the arm cavities at all, they must be resonant in the power recycled Michelson. However, in order to provide maximum signal for the feedback to the arms I want the maximum amount of sideband light to leak out of the dark port. Thus taking a look at section 2.2.2 along with the assumptions for this section I can see that:

$$\frac{E_D}{E_{in}} = \frac{1}{2} r_a (e^{-i\frac{\omega}{c} l_y} + e^{-i\frac{\omega}{c} l_x})$$

so as  $r_a \rightarrow 1$  for the sidebands

$$\left| \frac{E_D}{E_{in}} \right|^2 \rightarrow \cos^2\left(\frac{\omega}{c} l_m\right)$$

For maximum transmission of sideband light we want  $\left| \frac{E_D}{E_{in}} \right| \rightarrow t_{rm}$ . This gives a restriction on the static differential PRM length  $l_m$ , which is commonly referred

---

<sup>5</sup>If the first order r.f. sidebands are exactly anti-resonant then all the even order r.f. sidebands are resonant.

to as the PRM “asymmetry”. Giving the dark port resonance condition of

$$\begin{aligned} \text{Carrier : } \quad \sin\left(\frac{\omega}{c}l_m\right) &\approx 1 & \cos\left(\frac{\omega}{c}l_m\right) &\approx 0 \\ \text{Sideband : } \quad \sin\left(\frac{\omega}{c}l_m\right) &\approx r_{rm} & \cos\left(\frac{\omega}{c}l_m\right) &\approx t_{rm} \end{aligned} \quad (2.24)$$

This leaves to be specified the resonance condition for the power recycled Michelson itself which are found by combining Eqs.(2.19 or 2.21) with Eqs.(2.23 and 2.24)

$$\begin{aligned} \text{Carrier : } \sin\left(\frac{\omega}{c}l_p\right) &\approx 1 & \text{With Arms Resonant} \\ \text{Sideband : } \sin\left(\frac{\omega}{c}l_p\right) &\approx -1 \\ \text{Carrier : } \sin\left(\frac{\omega}{c}l_p\right) &\approx -1 & \text{With Arms NOT Resonant} \\ \text{Sideband : } \sin\left(\frac{\omega}{c}l_p\right) &\approx -1 \end{aligned} \quad (2.25)$$

Note the 180° phase change in Power Recycled Michelson resonance condition when the arms are unlocked vs. when they are locked. As locking the Full IFO requires first locking the PRM without the arms (so that light is then incident upon the arms) and *then* locking the arms; the  $l_p$  feedback signal must be inverted the moment the arms resonate. This creates a need for some good electronics and some excellent programming in the control system and by the operators.

### Common and Differential Arm Lengths

While investigating the PRM it was assumed that the arm cavity lengths were exactly the same, and it was observed that the lengths between the BeamSplitter and each Input Test Mass could be combined into common and differential length variables. I use the resonant conditions to show a similar redefinition of variables for the Arm cavity lengths. I continue to assume that the reflection and transmission coefficients are commuting scalars and that the beamsplitter

is perfect. Combining equations 2.24 and 2.25 for the carrier<sup>6</sup>, one can see that:

$$l_x - l_y = \frac{1}{k} \frac{\pi}{2} \qquad l_x + l_y = \frac{1}{k} \frac{\pi}{2}$$

so that

$$2l_x = \frac{2}{k} \frac{\pi}{2} \qquad 2l_y = 0$$

where  $k$  is the wave vector of the carrier  $k = \omega/c$ .

Now when I put these resonant conditions along with my stated assumptions into equations 2.11 through 2.13 I get:

$$\frac{E_{PRM}}{E_0} = \frac{it_{rm}}{1 - r_{rm}(\frac{1}{2}r_y + \frac{1}{2}r_x)} \qquad (2.26)$$

$$\frac{E_D}{E_0} = \frac{-it_{rm}(\frac{1}{2}r_y - \frac{1}{2}r_x)}{1 - r_{rm}(\frac{1}{2}r_y + \frac{1}{2}r_x)} \qquad (2.27)$$

$$\frac{E_R}{E_0} = \frac{r_{rm} - \frac{1}{2}(r_y + r_x)(r_{rm}^2 + t_{rm}^2)}{1 - r_{rm}(\frac{1}{2}r_y + \frac{1}{2}r_x)} \qquad (2.28)$$

where  $r_x$  and  $r_y$  are the arm cavity reflectivities from equation 2.3 with  $\phi$  being given by  $2kL_x$  and  $2kL_y$ . With the desired resonance conditions I can use  $L_x$  and  $L_y$  as the small perturbations off resonance instead of the complete length of the cavities (at least where it regards phase conditions), as the nominal resonance condition shows the resonant phase terms to be integer multiples of  $2\pi$ . One can begin to see a similarity with the common and differential length parameters from the PRM. Since the item of interest is in signal variations due to length differences I will assume that that is the only difference between the two arms. A GW signal changes the effective differential length of the IFO arms, allowing me to initially set the other parameters in the equation to be the same in both arms. Experimental observation shows that some non-negligible effects are caused by

---

<sup>6</sup>Since the r.f. sidebands are not resonant in the arms it is unnecessary to see how arm length changes affect them.

differences in effective losses and possibly other parameters between the arms; this is better handled by a computational method described in section 3.2.2. Combining equation 2.16 to form  $r_y + r_x$  and  $r_y - r_x$  with an analogous variable re-definition  $L_p = L_x + L_y$  and  $L_m = L_x - L_y$  as used in equations 2.17 and 2.18 leads to

$$r_y + r_x = \frac{2 \left[ \begin{array}{l} r_{itm} - r_{etm} \cos(\frac{\omega}{c} L_m) (2r_{itm}^2 + t_{itm}^2) \\ + r_{itm} r_{etm}^2 (r_{itm}^2 + t_{itm}^2) e^{-i\frac{\omega}{c} L_p} \end{array} \right] e^{-i\frac{\omega}{c} L_p}}{1 - 2r_{itm} r_{etm} \cos(\frac{\omega}{c} L_m) e^{-i\frac{\omega}{c} L_p} + r_{itm}^2 r_{etm}^2 e^{-i\frac{\omega}{c} L_p}} \quad (2.29)$$

$$r_y - r_x = \frac{-2i r_{etm} t_{itm}^2 \sin(\frac{\omega}{c} L_m) e^{-i\frac{\omega}{c} L_p}}{1 - 2r_{itm} r_{etm} \cos(\frac{\omega}{c} L_m) e^{-i\frac{\omega}{c} L_p} + r_{itm}^2 r_{etm}^2 e^{-i\frac{\omega}{c} L_p}} \quad (2.30)$$

The above equations could then be used in conjunction with Eqs. (2.26, 2.27 and 2.28) to get the effect of common or differential arm motion on the key fields of the IFO. These are, however, still rather cumbersome equations so I will not perform the combination algebraically.

### Buildup Factors

The nominal parameters for the LIGO Washington 2k interferometer are specified in Table 2.1. Using Eqs.(2.6, 2.21 and 2.22) along with the resonance conditions specified in section 2.2.4 and the values in Table 2.1, I get the buildup factors shown in Table 2.2. MATLAB simulations used to fit data in chapter 3 showed that mirror losses and approximations made here had a non-negligible effect on the calculated build-up factors leading to much better agreement with experimental measurements. Those measurements and simulations however, were done for the 4k IFO and not the 2k IFO. Table 2.3 shows a comparison of the build-up values with lossless mirrors and perfectly reflective ETMs to build-up values using nominal mirror values.

Table 2.1: Nominal Parameters for WA 2k Interferometer

Parameter	Value
LASER Power in TE00 Mode	6 (W)
Resonant SB frequency*	29505880 (Hz)
Resonant SB modulation depth	0.45
Distance RM to BS*	3.022 (m)
Distance BS to in-line ITM*	9.528 (m)
Distance BS to off-line ITM*	9.828 (m)
BS Reflectance <sup>†</sup>	0.5
BS Transmittance <sup>†</sup>	0.5
RM Reflectance <sup>†</sup>	0.969
RM Transmittance <sup>†</sup>	0.028
RM Loss <sup>†</sup>	1e-3
ITM Reflectance <sup>†</sup>	0.971825
ITM Transmittance <sup>†</sup>	0.0281
ITM Loss <sup>†</sup>	75e-6
ETM Reflectance <sup>†</sup>	0.999925
ETM Transmittance <sup>†</sup>	5e-6
ETM Loss <sup>†</sup>	70e-6

\*The dark port resonance conditions were used instead of these distances and frequencies due to the extreme length sensitivity involved.

<sup>†</sup>Values are Power coefficients, for amplitude coefficients take the square root.



Table 2.2: Build-up Factors for Carrier and Resonant Sidebands for the 2k Recycled Interferometer as calculated by the Algebraic method.

Field Frequency		Field	Build-up
Arms*:	carrier	$\left  \frac{E_{cir}}{E_{in}} \right ^2$	138.9
	sideband	$\left  \frac{E_{cir}}{E_{in}} \right ^2$	0.007
PRM:	carrier	$\left  \frac{E_{PRM}}{E_0} \right ^2$	114.7
	sideband	$\left  \frac{E_{PRM}}{E_0} \right ^2$	29.1
Dark Port:	carrier	$\left  \frac{E_D}{E_0} \right ^2$	0.000
	sideband	$\left  \frac{E_D}{E_0} \right ^2$	0.816

---

\*Remembering that the buildup factor for the arm cavities is with respect to the field incident upon the arm cavity  $|E_{in}| = \frac{1}{\sqrt{2}} |E_{PRM}|$

Table 2.3: Build-up Factors for Carrier and Resonant Sidebands in the 4k Recycled Interferometer as calculated by the Numerical method of Sec. 3.2.2

Field Frequency		Field	Build-up (lossless)	Build-up (nominal)
Arms*:	carrier	$\left  \frac{E_{cir}}{E_{in}} \right ^2$	140.3	138.9
	sideband	$\left  \frac{E_{cir}}{E_{in}} \right ^2$	0.008	0.008
PRM:	carrier	$\left  \frac{E_{PRM}}{E_0} \right ^2$	140.9	46.5
	sideband	$\left  \frac{E_{PRM}}{E_0} \right ^2$	40.3	40.0
Dark Port:	carrier	$\left  \frac{E_D}{E_0} \right ^2$	0.000	0.000
	sideband	$\left  \frac{E_D}{E_0} \right ^2$	0.945	0.937

---

\*Remembering that the buildup factor for the arm cavities is with respect to the field incident upon the arm cavity  $|E_{in}| = \frac{1}{\sqrt{2}} |E_{PRM}|$



# Chapter 3

## Characterization of the Instrument

### 3.1 Sideband Injection

In the Fall of 2002 measurements were taken that contribute to the characterization of the LIGO Hanford 4k Interferometer (LHO 4k IFO)[5] examining high frequency signals around the *free spectral range* (FSR)

$$f_{\text{fsr}} = \frac{c}{2L} = 37.52 \text{ kHz}$$

This work was aimed at establishing the sensitivity and noise level of the IFO to a stochastic background of gravitational radiation at this frequency. Similar measurements were carried out by M. Rakhmanov and R. Savage[63] and a calculation of the sensitivity at the FSR was recently carried out by D. Sigg[66]

The LIGO IFO (conceptually in Fig 1.4, schematically in Fig 2.1) can be operated in various configurations including single arm mode and power recycled IFO. The measurements reported in sections 3.1.2 and 3.1.3 were obtained by injecting frequency sidebands upon, (frequency modulation of) the incident light

and sweeping around the free spectral range frequency (FSR). This was done in the single arm mode for both the X and Y arms. Sweeping the frequency around the  $1/2$  and  $3/2$  free spectral range frequencies provides additional information on cavity arm lengths, and the results are particularly sensitive to the demodulation phase and to the non-resonant sideband frequency. Pertinent references on cavities, FSR, sidebands and Electro-Optic or Acousto-Optic modulation of light can be found in [59, 65, 55].

The readout of the signal is done via the appropriate RF phase of the demodulated IFO dark port output[57]. For single arm measurements this is the in-phase component, and for Full-IFO measurements this is the quadrature-phase component. Details about signal readout are given in greater detail in [57, 68]. Appropriate mixing between the I and Q channels is determined as discussed in section 3.1.1 and is used for fitting the plots presented in section 3.1.2 and 3.1.3. For single arm measurements I simply misalign the recycling mirror (RM) and the arm that is not of interest. Then the signal which returns to the dark port (AS) is the reflection off the FP cavity. For full IFO locking, all mirrors are aligned and the primary signal of interest (differential arm motion) comes out the AS port. The r.f. output of the diode is taken via coaxial cable to a demodulator board, the output of which is processed and digitized for filtering and feedback as well as data analysis. On the demodulator board there are also monitor points where I connected the spectrum analyzer to obtain an analog version of the demodulated output prior to its input into the DAQ (Data Acquisition) system.

The spectrum analyzer that I use (Stanford Research Systems SRS785) can operate in several modes. The primary functions which I use are the FFT and Frequency Response. When I take an FFT I simply look at the output signal

in the frequency domain. When I sweep the frequency range of interest then I use the Frequency Response mode. This function takes a series of measurements at different frequencies in which the transfer function from drive to output is measured. In this mode both magnitude and phase response are recorded.

In section 3.2 I examine parametric conversion due to the motion of one of the test masses near the FSR frequencies. As a result (audio) sidebands are imposed on the carrier. Obviously there are similarities, but also differences, between sideband injection directly on the carrier and through test mass motion. In the latter case the data are fitted using some MATLAB routines which are inspired by the matrix method from the program TWIDDLE [58] and described in detail in section 3.2.2.

The presence of dips (cancellation) for sidebands injected at  $f_{\text{fsr}}$  has been known for a long time [48, 58, 67, 56], however I believe this to be the first systematic experimental study of these effects [28]. The measurements confirm the theory to a great accuracy and this reflects the advanced status of alignment and control of the IFO.

Perhaps the most interesting conclusion is that the LASER phase noise has a minimum at  $f_{\text{fsr}}$ . This is to be expected from my analysis, since the sidebands imposed by phase noise are symmetric and thus the level of the noise is greatly attenuated at  $f_{\text{fsr}}$ . In Fig 3.16 I show the noise floor around  $f_{\text{fsr}}$  and a narrow 6 db drop is clearly observed at the fsr.

### 3.1.1 Calculation of Fields

To model the response of the IFO to frequency sidebands on the incident light a first order expansion of the fields is sufficient. However one must avoid the assumption that the upper and lower sidebands are equivalent. The signal read

out by the diode is the absolute square of the complex field expansion of the light out of the AS port (or reflected off the cavity). This will be of the form<sup>1</sup>  $|E\{J_0(\Gamma_m) + J_1(\Gamma_m)e^{i\omega_m t} - J_1(\Gamma_m)e^{-i\omega_m t}\}\{J_0(\Gamma_s) + J_1(\Gamma_s)e^{i\omega_{rf} t} - J_1(\Gamma_s)e^{-i\omega_{rf} t}\}|^2$  where  $E$  is the unmodulated field. Adopting the notation that a subscript of 0 indicates the carrier field (the corresponding  $e^{i\omega_c t}$  is left off as it conveniently cancels when evaluating the power as it is common to all terms, r.f. and audio modulation frequencies are indicated relative to the carrier frequency), a subscript of ‘ $m$ ’ indicates the applied modulation frequency (audio), a subscript of ‘ $s$ ’ indicates the non-resonant r.f. sidebands on the light necessary for locking the cavity by an optical heterodyning technique[68] such as the Pound-Drever-Hall (PDH) method. A subscript of ‘ $a$ ’ indicates the sideband at the sum of the r.f. and modulation frequencies, and ‘ $b$ ’ indicates the sideband at the difference of the r.f. and modulation frequencies. It is also necessary to distinguish between the upper and lower sidebands as they obtain different phases upon reflection from the cavity (indicated by a ‘+’ for the upper sideband and a ‘-’ for the lower). Thus the signal is proportional to:

$$\text{AS}_{\text{rf}} = \left| \begin{array}{l} E_0 + E_{m+}e^{i\omega_m t} - E_{m-}e^{-i\omega_m t} + E_{s+}e^{i\omega_s t} - E_{s-}e^{-i\omega_s t} \\ + E_{a+}e^{i(\omega_s+\omega_m)t} + E_{a-}e^{-i(\omega_s+\omega_m)t} - E_{b+}e^{i(\omega_s-\omega_m)t} - E_{b-}e^{-i(\omega_s-\omega_m)t} \end{array} \right|^2 \quad (3.1)$$

Where all E-fields specified are the fields reflected off the cavity. Reflection off a simple Fabry Perot cavity is given by

$$\frac{E_r}{E_0} = \frac{r_1 - r_2(r_1^2 + t_1^2)e^{-i\phi}}{1 - r_1 r_2 e^{-i\phi}} \quad (3.2)$$

This is derived in [14] and section 2.2.1 which also includes expressions for the other fields. The parameter  $\phi$  is nominally  $2L\omega/c$  where  $L$  = length of the cavity.

---

<sup>1</sup>For pure phase modulation I adopt the convention of the sidebands being real, the upper one positive and the lower one negative.

This was simulated in software by  $\phi = 2\pi x/f_{\text{fsr}}$  where  $f_{\text{fsr}} = c/2L$ .

The output of the photo-diode is sent through a bandpass filter to limit the signal to the range of interest around the r.f. sideband frequency. Thus after demodulation the signal of interest is once again at the applied modulation frequency. So I take equation 3.1 and expand it while keeping only the terms at  $\pm(\omega_s \pm \omega_m)$  then separate it out so that it can be written in terms of  $\cos(\omega_s t)$  and  $\sin(\omega_s t)$ . The result is (where \* indicates the complex conjugate field):

$$\begin{aligned} \text{AS}_{\text{rf}} = \cos(\omega_s t) & \left[ \begin{array}{l} e^{i\omega_m t} \left( \begin{array}{l} E_0^* E_{a+} + E_0 E_{a-} - E_{m+} E_{s-} - E_{m-}^* E_{s+} \\ -E_0^* E_{b-} - E_0 E_{b+} + E_{m+} E_{s+} + E_{m-}^* E_{s-} \end{array} \right) \\ + e^{-i\omega_m t} \left( \begin{array}{l} E_0^* E_{a-} + E_0 E_{a+} - E_{m-} E_{s+} - E_{m+}^* E_{s-} \\ -E_0^* E_{b+} - E_0 E_{b-} + E_{m-} E_{s-} + E_{m+}^* E_{s+} \end{array} \right) \end{array} \right] \\ + i \sin(\omega_s t) & \left[ \begin{array}{l} e^{i\omega_m t} \left( \begin{array}{l} E_0^* E_{a+} + E_0 E_{a-} - E_{m+} E_{s-} - E_{m-}^* E_{s+} \\ + E_0^* E_{b-} + E_0 E_{b+} - E_{m+} E_{s+} - E_{m-}^* E_{s-} \end{array} \right) \\ + e^{-i\omega_m t} \left( \begin{array}{l} -E_0^* E_{a-} - E_0 E_{a+} + E_{m-} E_{s+} + E_{m+}^* E_{s-} \\ -E_0^* E_{b+} - E_0 E_{b-} + E_{m-} E_{s-} + E_{m+}^* E_{s+} \end{array} \right) \end{array} \right] \end{aligned} \quad (3.3)$$

Eq.(3.3) may be written compactly as

$$\text{AS}_{\text{rf}} = \cos(\omega_s t)[e^{i\omega_m t}(\alpha) + e^{-i\omega_m t}(\beta)] + i \sin(\omega_s t)[e^{i\omega_m t}(\gamma) + e^{-i\omega_m t}(\delta)] \quad (3.4)$$

where I substitute  $\alpha$ ,  $\beta$ ,  $\gamma$  and  $\delta$  for the corresponding sets of field terms. Upon closer inspection of Eq.(3.3) it is apparent that  $\beta = \alpha^*$  and  $\delta = -\gamma^*$ , so that Eq.(3.4) can be further simplified to

$$\begin{aligned} \text{AS}_{\text{rf}} &= \cos(\omega_s t)[\alpha e^{i\omega_m t} + \alpha^* e^{-i\omega_m t}] + \sin(\omega_s t)[i\gamma e^{i\omega_m t} - i\gamma^* e^{-i\omega_m t}] \\ &= 2 \cos(\omega_s t) \Re\{\alpha e^{i\omega_m t}\} + 2 \sin(\omega_s t) \Re\{i\gamma e^{i\omega_m t}\} \end{aligned} \quad (3.5)$$

In-line demodulation selects the term oscillating as  $\sin(\omega_s t)$  while quadrature demodulation selects the term oscillating as  $\cos(\omega_s t)$ . Thus the demodulated signals are

$$\begin{aligned} \text{AS-I} &= \Re\{i\gamma e^{i\omega_m t}\} \\ \text{AS-Q} &= \Re\{\alpha e^{i\omega_m t}\} \end{aligned} \quad (3.6)$$

Spectral analysis of these signals at the frequency  $\omega_m$  yields the magnitude and phase of the complex amplitudes  $i\gamma$  and  $\alpha$  respectively. These amplitudes are defined in Eq.(3.3) and are frequency dependent because the fields in Eq.(3.3) are *reflected* fields.

So far I have assumed that the phase of the demodulating r.f. coincided exactly with the phase of the r.f. component of the detected signal. This is not always the case and a possible phase difference  $\phi$  may exist. Thus

$$\begin{aligned} \text{AS-I}(\phi) &= \frac{1}{T} \int_0^T \text{AS}_{\text{rf}} \sin(\omega_s t + \phi) \\ \text{AS-Q}(\phi) &= \frac{1}{T} \int_0^T \text{AS}_{\text{rf}} \cos(\omega_s t + \phi) \end{aligned} \quad (3.7)$$

where  $T = 2\pi/\omega_s$  and I assume integration over multiples of the r.f. period. Expanding the sine and cosine I immediately find that

$$\begin{aligned} \text{AS-I}(\phi) &= \Re\{(i\gamma \cos \phi + \alpha \sin \phi)e^{i\omega_m t}\} \\ \text{AS-Q}(\phi) &= \Re\{(\alpha \cos \phi - i\gamma \sin \phi)e^{i\omega_m t}\} \end{aligned} \quad (3.8)$$

I have fitted the data to the complex amplitude indicated in Eq.(3.8) where  $\alpha$  and  $i\gamma$  are given by Eq.(3.3). As a simple example I can consider the case when the injected sideband frequency is far from  $f_{\text{fsr}}$  (resonance). Then the reflected fields are approximately the same as the incident fields (except for the carrier which is reversed). Thus I can take the fields as real and write

$$E_0 \simeq -1 \quad E_{s+} \simeq E_{s-} \simeq \Gamma_s \quad E_{m+} \simeq E_{m-} \simeq \Gamma_m$$



$$E_{a+} \simeq E_{a-} \simeq E_{b+} \simeq E_{b-} \simeq \Gamma_m \Gamma_s$$

It then follows that

$$\alpha \simeq 0 \quad \gamma \simeq -8\Gamma_m \Gamma_s \quad \text{far off resonance} \quad (3.9)$$

When the injected sideband equals  $f_{\text{fsr}}$  then also  $E_{m+}$  and  $E_{m-}$  change sign, and it follows that

$$\alpha \simeq 0 \quad \gamma \simeq 0 \quad \text{on resonance} \quad (3.10)$$

### 3.1.2 Response to sideband injection at $f_{\text{fsr}}$ and $2f_{\text{fsr}}$

The primary method of injecting the sidebands is through the use of the Mode Cleaner feedback circuit which at this frequency feeds back almost directly to the VCO controlling the LASER frequency. This has the disadvantage of suffering from a non-linear transfer function from drive to output. However it has the advantage of providing an injection point that does not disturb the control system. A different injection point was considered which in principle had a flat drive with respect to frequency, however the DC shift caused by connecting the readout instruments typically resulted in the IFO losing lock. The modulation frequency was swept (“swept sine” mode) between two limits and the magnitude and phase of the transfer function was recorded by the spectrum analyzer.

Data for the X-arm are shown in Figs (3.1, 3.2) and for the Y-arm in Figs (3.4, 3.5, 3.6). The fitting was done in MATLAB to the form<sup>2</sup>

$$\text{fit} = x1 \times (\text{fpi}(f, x2) + x3) \quad (3.11)$$

where fpi is the calculated signal for pure I-phase [Eqs.(3.3,3.6)] and

---

<sup>2</sup>It is necessary to include  $x3$  in the high resolution fit (Fig. 3.1) to account for very slight effects near resonance.

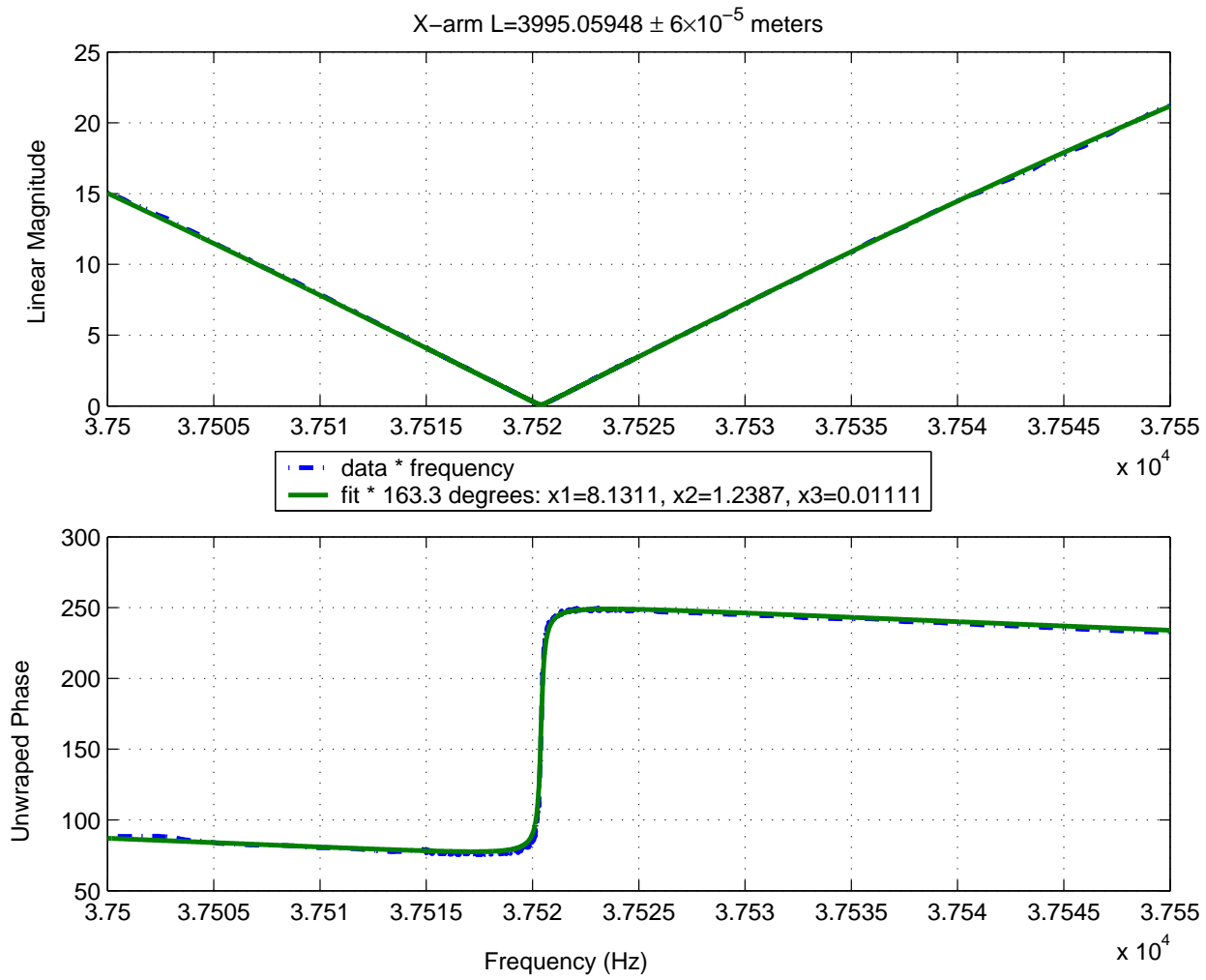


Figure 3.1: X-arm 1 FSR

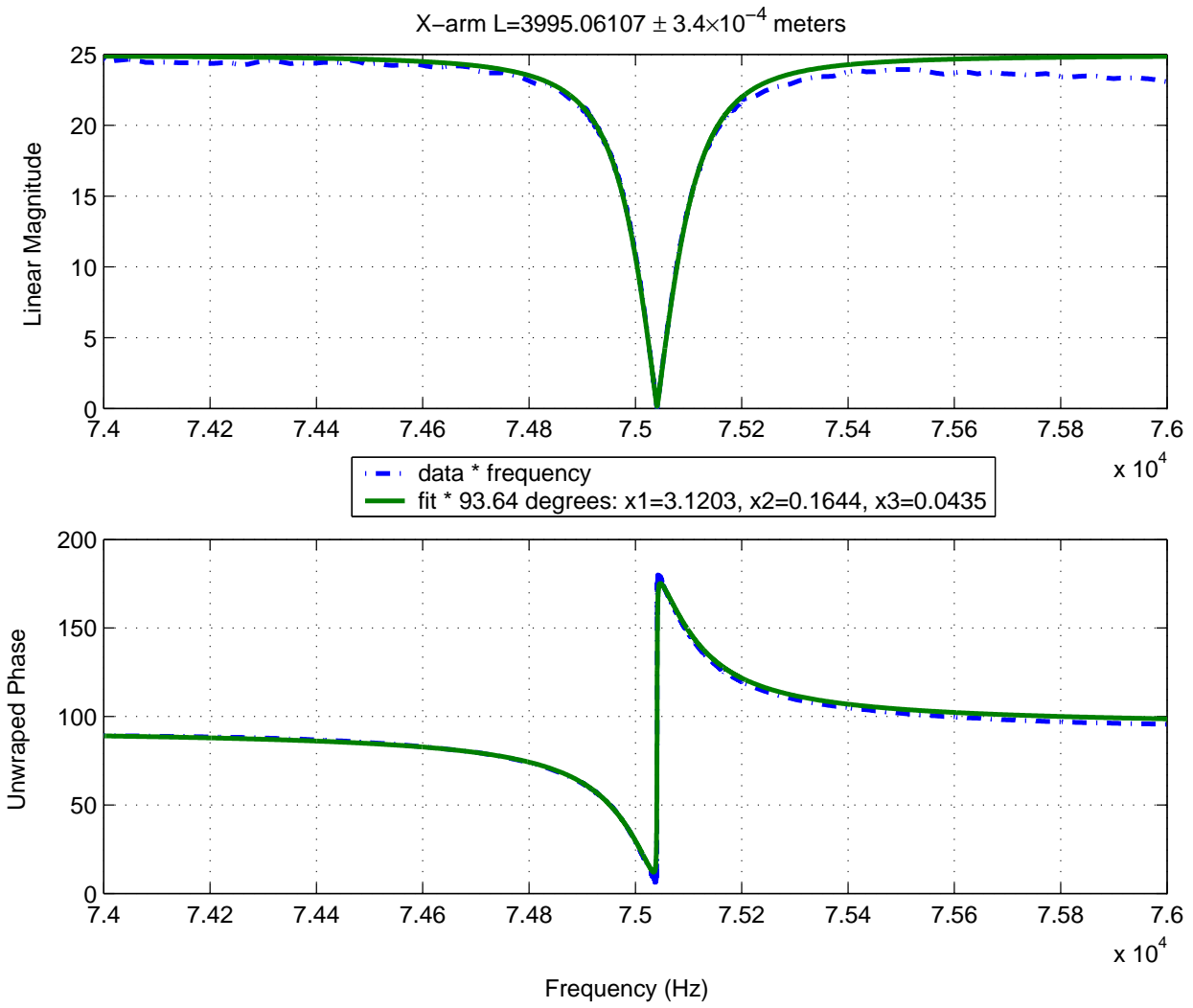


Figure 3.2: X-arm 2 FSR

- $x1$  = overall normalization to account for different gains
- $x2$  = the demodulation phase  $\phi$  in degrees
- $x3$  = a background (noise) level

For some fits  $x1$  and  $x3$  were allowed to be complex in order to fit both the magnitude and the phase of the data as well as allow an overall relative phase difference between the noise (parameter  $x3$ ) and the model results. This was found to be unnecessary, so all parameters  $x1$ ,  $x2$  and  $x3$  are real. In Figs 3.1 and 3.2 the magnitude was fit and the “initial phase” angle was determined by comparing the data and initial fit at some specific frequency point (usually the FSR). Thus the final fit is the initial fit multiplied by a complex number with unity magnitude and phase set at the “initial phase” (in degrees). It was found necessary to include a  $1/f$  dependence to account for the response of the servo loop. This was achieved in practice by multiplying the data points by  $f$ . In addition to optimizing  $x1$  through  $x3$  with the fit routine, I sought the best value of arm length and of the initial phase. The results returned by the fit are indicated in the figures. The arm length is a parameter hard coded into the `fpi` function and varied manually while fitting the other parameters.

In the X-arm measurements the demodulation phase  $\phi$  is sufficiently small so that there is essentially no signal in the Q-phase channel, as suggested by introducing the result of Eq.(3.9) into Eq.(3.6). The I-phase signal shows a sharp dip at the  $f_{\text{fsr}}$  as suggested by Eq.(3.10), and provides a very accurate measure of the arm length.

Fig. 3.1 is a combination of several runs and contains a total of 2,000 data points. The data can not be distinguished from the fit except in the wings of the plot. To estimate the error on the fitted parameters I form the  $\chi^2$  of the fit by assigning equal errors to each data point such that  $\chi^2/\text{DF} \simeq 1$ . DF are

the degrees of freedom, the number of data points being fitted minus the fit parameters and  $\chi^2 = \sum_i (x_i - \bar{x}_i)^2 / \sigma_i^2$  where  $\sigma_i$  is the error of the data point  $i$  which is *defined* such that  $\sigma_i = \sigma$  and  $\chi^2/\text{DF} \simeq 1$ . A plot of  $\chi^2$  as a function of X-arm length is shown in Fig. 3.3, and I take the one standard deviation error to be given by the values that increase  $\chi^2$  by one unit. I find for the two arms

$$L_x = 3995.05948 \pm 0.00006 \text{ m}$$

$$L_y = 3995.01332 \pm 0.00041 \text{ m}$$

The above values are, of course, directly dependent on the accuracy of the frequency of the injected sidebands. This frequency is read off the spectrum analyzer and at this point can not be trusted to better than  $1/10^6$ .

For the Y-arm measurements (Figures 3.4, 3.5 and 3.6) the demodulation phase is sufficiently different from zero so that both the I-phase and Q-phase show a signal. The resulting phase error as extracted from the data is  $\phi \simeq 6$  degrees. During the measurements of the Y-arm, instead of the phase of the transfer function, the absolute phase of the response was recorded. This manifests itself in that the measured phase has a large monotonic increase corresponding to the phase of the drive signal. Thus the parameters  $x_1$ ,  $x_2$ ,  $x_3$  and the arm length are fit in the same manner as for the X-arm, but no initial phase is calculated.

Finally Figs. 3.7 and 3.8 show sideband injection with the complete PRIFO. These fits were obtained using parameters given in section 3.2.3 and the modeling techniques described in section 3.2.2. This is because the full PRIFO configuration results (unlike the single arm results) are highly sensitive to a number of additional parameters, not all of which were directly measurable. To account for some of these effects I introduced the parameter  $\xi$ , defined in section 3.2.2, which controls the dark port resonance conditions of the simulation. The fit to

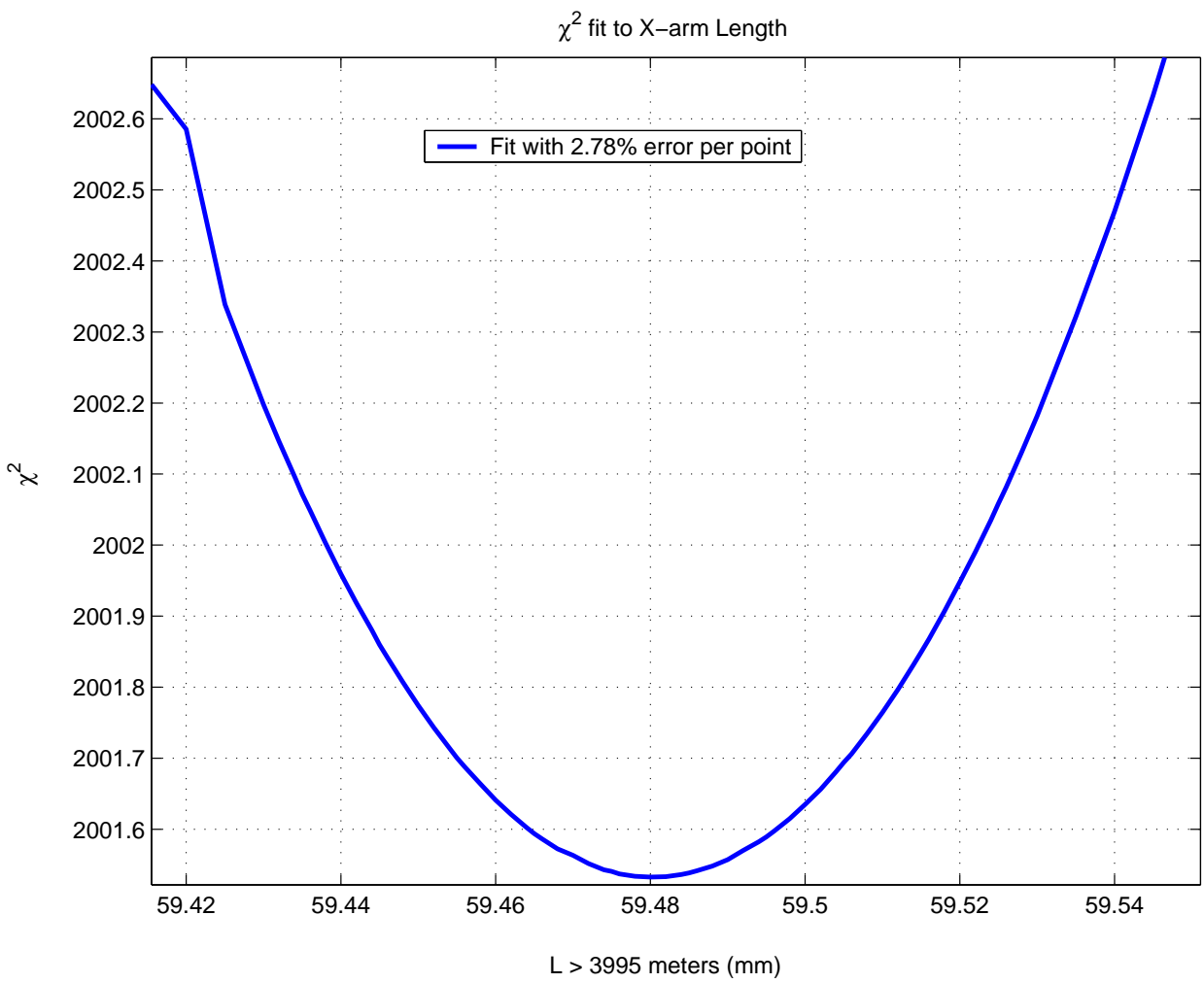


Figure 3.3: Typical chi squared fit for IFO arm length

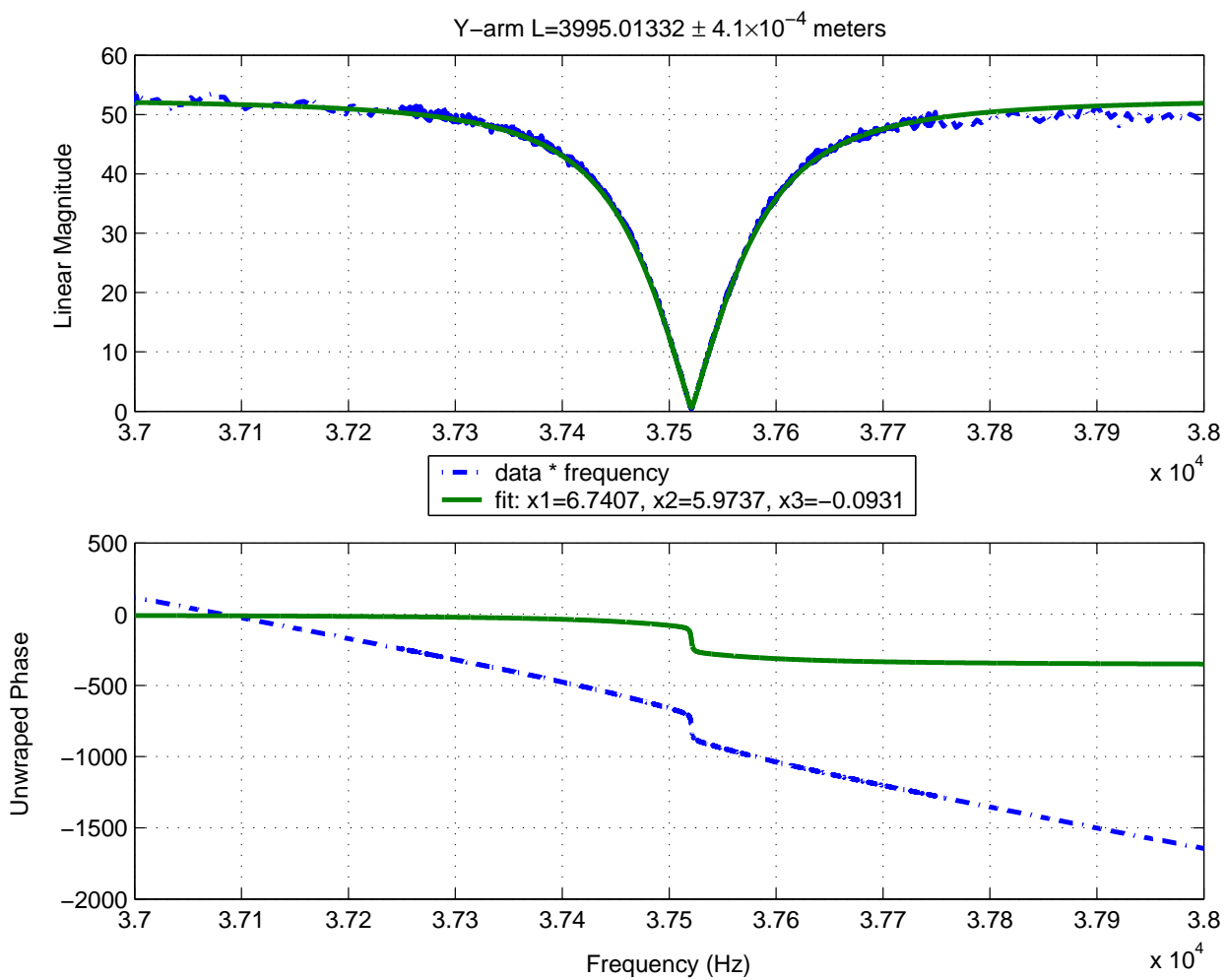


Figure 3.4: Y-arm FSR, I-phase

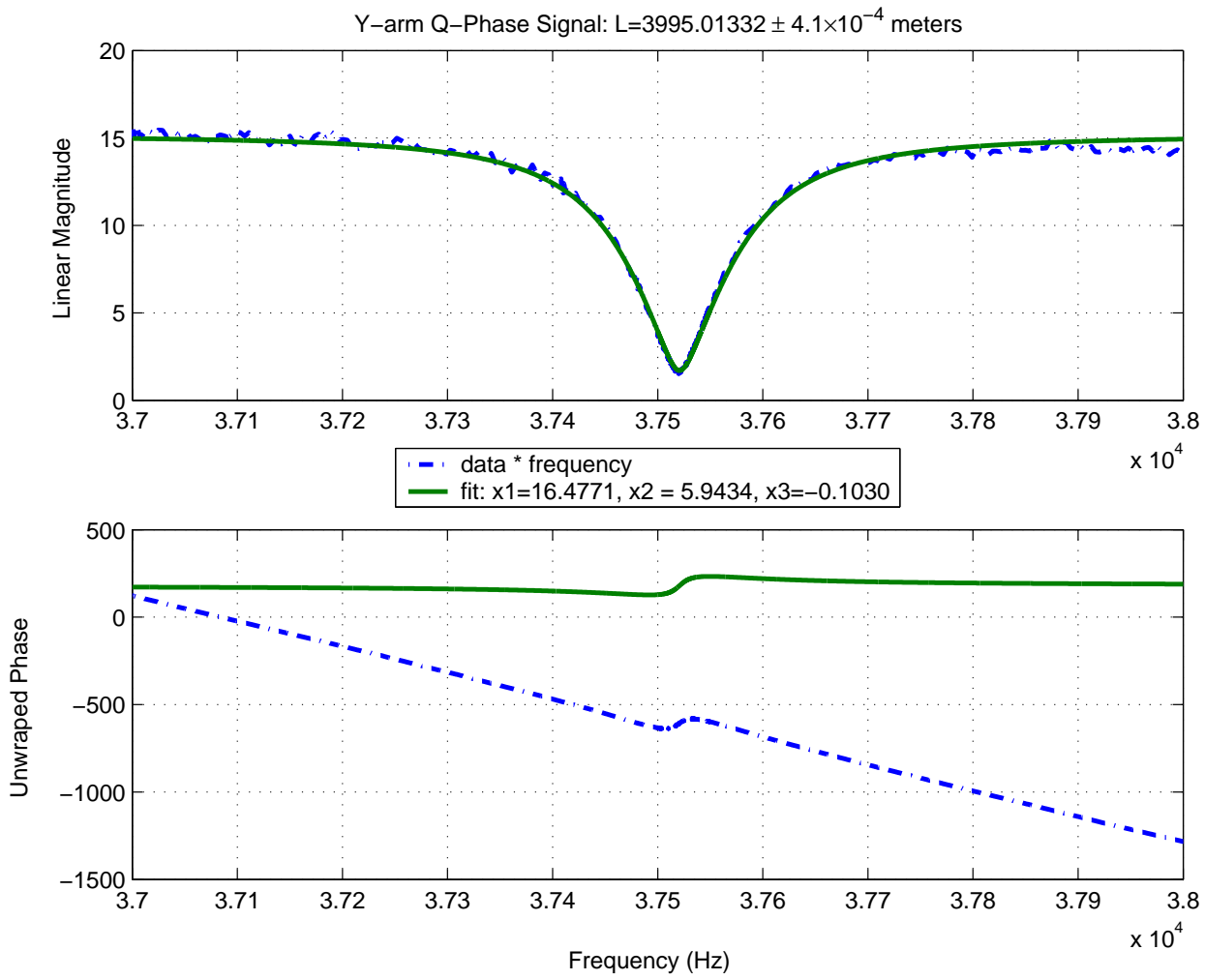


Figure 3.5: Y-arm FSR, Q-phase



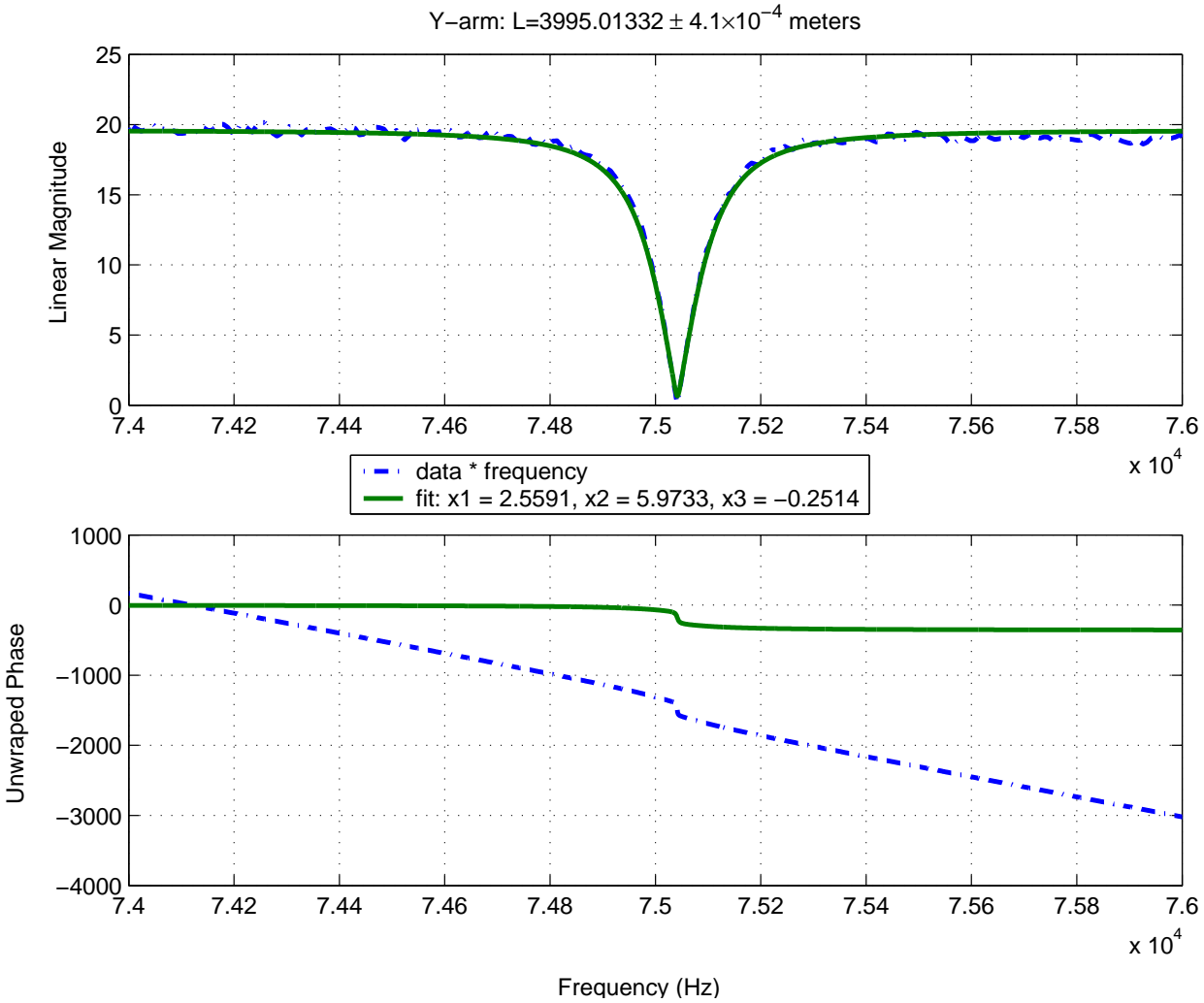


Figure 3.6: Y-arm 2 FSR, I-phase

the Q-phase (Fig 3.7) is satisfactory and returned the following values:

$$\begin{aligned} N &= 7.08 \times 10^{-3} \\ A_{\text{noise}} &= 0.12 \\ \xi &= 4.16^\circ \end{aligned}$$

Note that the resonant peak has a FWHM of  $\simeq 2\text{Hz}$  as expected for the double cavity pole. This corresponds to a Q-value  $\nu/\Delta\nu = 1.5 \times 10^{14}$ ! One may also note that the normalization is significantly larger than that for the single arm measurement. This is due to the fact that for the single arm measurement the light must be transmitted through both the recycling mirror and the beam-splitter (without resonating) before encountering the arm cavity, while the simulation starts at the arm cavity with no input attenuation. For the PRIFO, both the experiment and the simulation start at effectively the same input level.

The fit for the I-phase returns different parameters. Both the  $\xi$  term and the normalization are different.

$$\begin{aligned} N &= 15.13 \times 10^{-3} \\ A_{\text{noise}} &= 0.01 \\ \xi &= 2.50^\circ \end{aligned}$$

This can be understood because the signal is very noisy. However, the mirror excitation measurement (Fig. 3.19) taken shortly after the sideband injection measurements was reasonably fit with similar parameters. Thus I conclude that sideband injection with the full PRIFO is much more sensitive to the fit parameters than for the single arm. This was verified by my modeling.

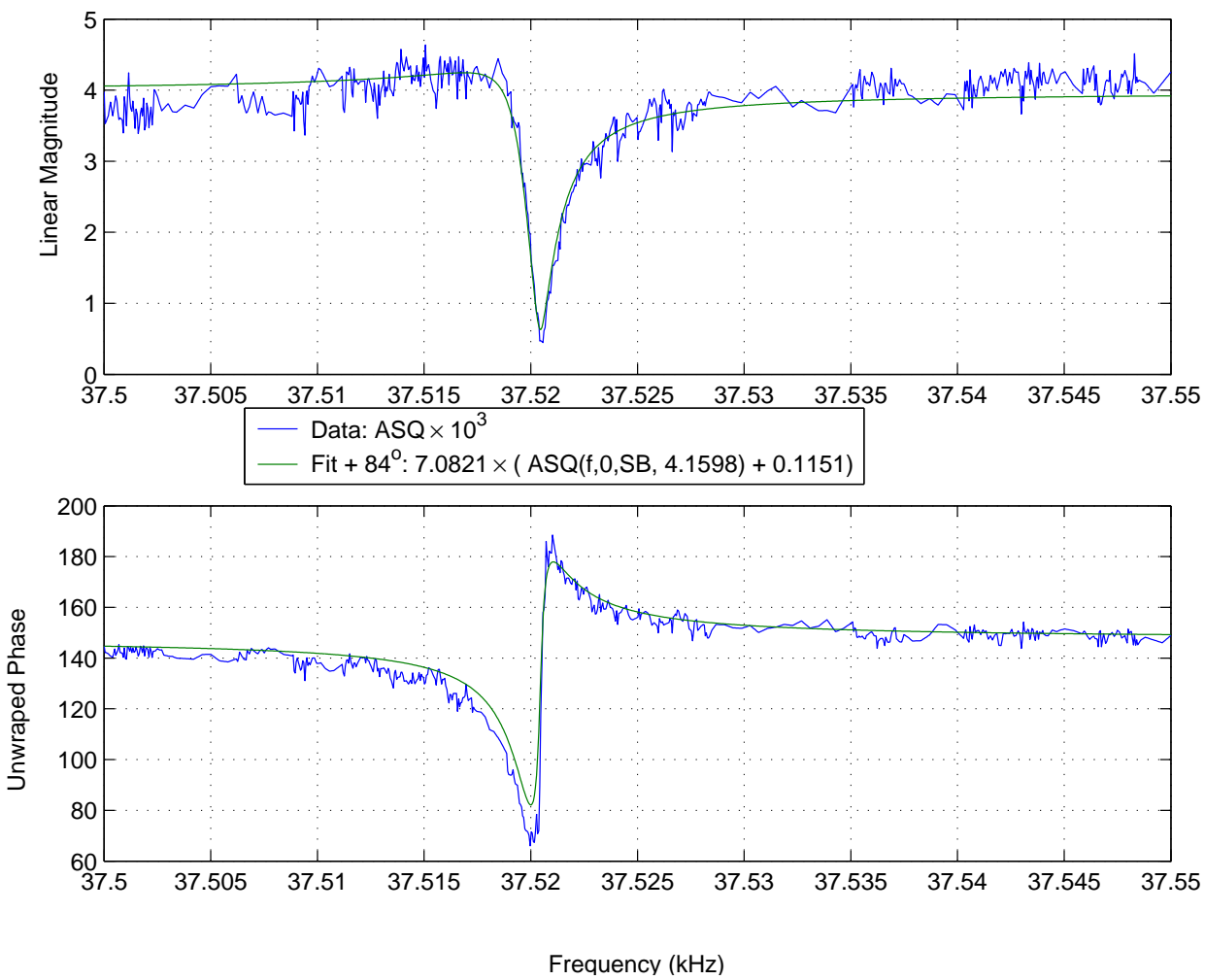


Figure 3.7: Full-IFO Sideband Injection Response,  $Q$ -phase

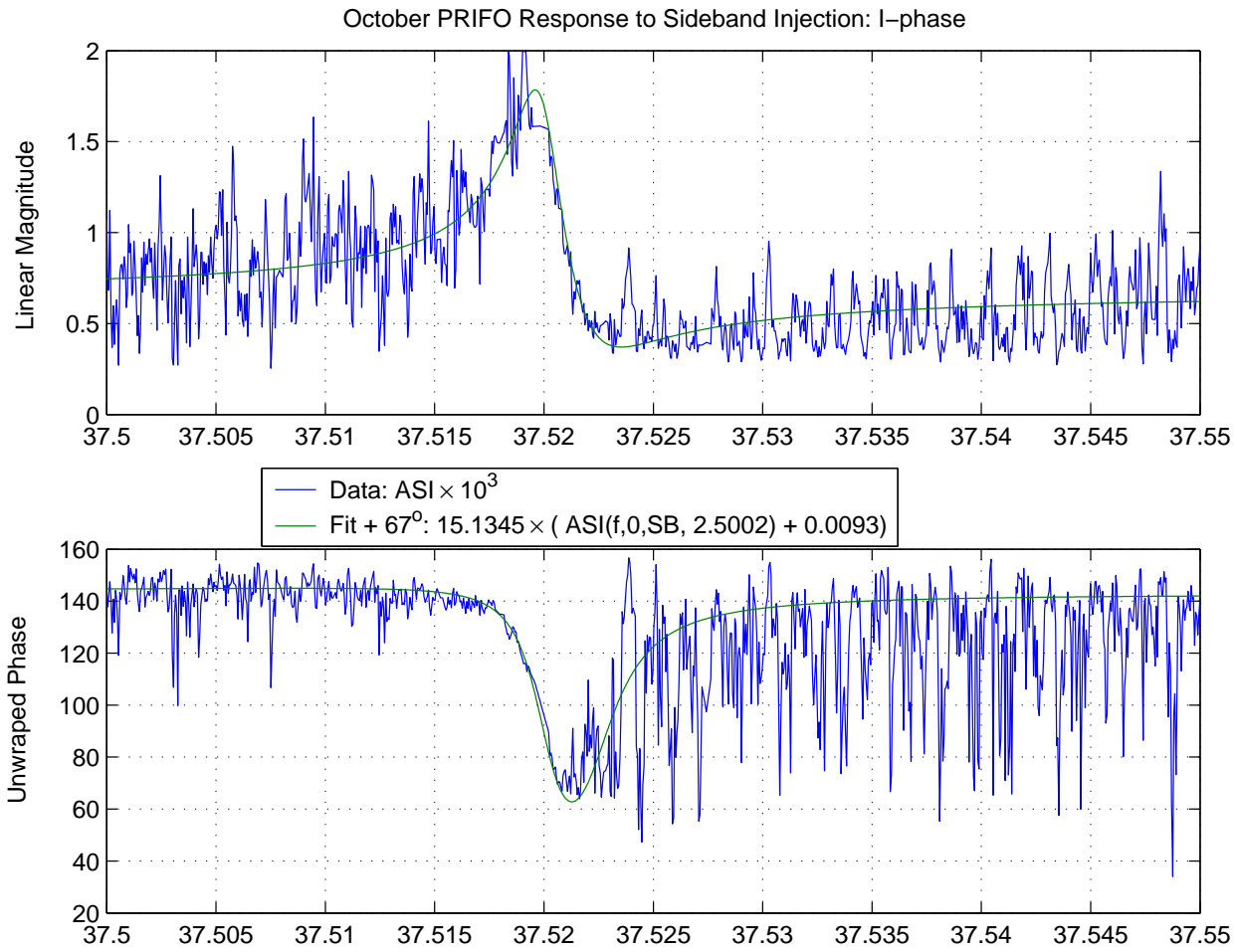


Figure 3.8: Full-IFO Sideband Injection Response, I-phase

### 3.1.3 Response to sideband injection at $\frac{1}{2}f_{\text{fsr}}$ and $\frac{3}{2}f_{\text{fsr}}$

If the r.f. sidebands were exactly anti-resonant, then the injected sidebands would resonate at half-integer values of  $f_{\text{fsr}}$ . This is not the case and therefore the sidebands resonate at two nearby frequencies as can be understood intuitively.

If I designate by  $\lambda_s, f_s$  the wavelength and frequency of the r.f. sidebands, exact anti-resonance would imply

$$\lambda_s \left( N + \frac{1}{2} \right) = 2L$$

or

$$f_s = \left( N + \frac{1}{2} \right) f_{\text{fsr}}$$

with  $N$  an integer, and as usual  $f_{\text{fsr}} = c/2L$ . In practice the r.f. frequency is chosen to deviate from the above condition by a frequency decrement<sup>3</sup>  $\Delta$

$$f_s = \left( N + \frac{1}{2} \right) f_{\text{fsr}} - \Delta \quad (3.12)$$

Resonance will occur when the injected sideband frequency,  $f_m$ , satisfies

$$f_s \pm f_m = \left( N + \frac{1}{2} \right) f_{\text{fsr}} \pm f_m - \Delta = \begin{cases} (N+1)f_{\text{fsr}} \\ Nf_{\text{fsr}} \end{cases}$$

or equivalently

$$\begin{aligned} f_m^+ - \Delta &= \frac{1}{2}f_{\text{fsr}}, \frac{3}{2}f_{\text{fsr}}, \text{ etc...} \\ f_m^- + \Delta &= \frac{1}{2}f_{\text{fsr}}, \frac{3}{2}f_{\text{fsr}}, \text{ etc...} \end{aligned} \quad (3.13)$$

It follows that the two resonant peaks are separated by

$$f_m^+ - f_m^- = 2\Delta$$

---

<sup>3</sup>To avoid feedback problems caused by the fact that the second order sidebands would be resonant.

which is measured experimentally to be of the order  $\Delta = 456$  Hz. From Eq.(3.12) which defines  $\Delta$  I see that it depends on both  $f_s$  and  $f_{\text{fsr}}$ . Indeed the error on  $\Delta$  is given by

$$\delta\Delta \simeq f_s \left[ \frac{\delta f_{\text{fsr}}}{f_{\text{fsr}}} - \frac{\delta f_s}{f_s} \right] \quad (3.14)$$

The data are shown in Figs 3.9 and 3.10 for  $f_m \simeq \frac{1}{2}f_{\text{fsr}}$  and in Figs 3.11 and 3.12 for  $f_m \simeq \frac{3}{2}f_{\text{fsr}}$ . They were obtained with only the X-arm locked. Note that there is signal in both the I-phase and in the Q-phase. Furthermore the “shape” of the response is extremely sensitive to the demodulation phase.

The fits to the data are done in the same way as discussed in section 3.1.2 using the expression for the signals derived in section 3.1.1 Eqs.(3.3 - 3.8). However now the fit must also optimize the r.f. frequency because the reflected fields  $E_a$  and  $E_b$  in Eqs.(3.1 - 3.3) become *strongly* frequency dependent. As before the fits are excellent and return an average demodulation phase  $\phi \simeq -10$  degrees and an r.f. frequency

$$f_s = 24,481,843 \pm 1 \text{ Hz} \quad (\text{derived})$$

The derived value of  $f_s$  differs significantly from the directly measured<sup>4</sup> value of  $f_s$

$$f_s = 24,481,698 \text{ Hz} \quad (\text{measured})$$

I assign the observed difference to an error in the  $f_{\text{fsr}}$  reading obtained from the spectrum analyzer. According to Eq.(3.14), this error amounts to  $\delta f_{\text{fsr}}/f_{\text{fsr}} \simeq 6 \times 10^{-6}$ ; large, but not excluded for an uncalibrated instrument.

---

<sup>4</sup>Which was later checked against a Rubidium standard (Stanford FS725) and found to have an error  $\simeq 1/10^6$ .

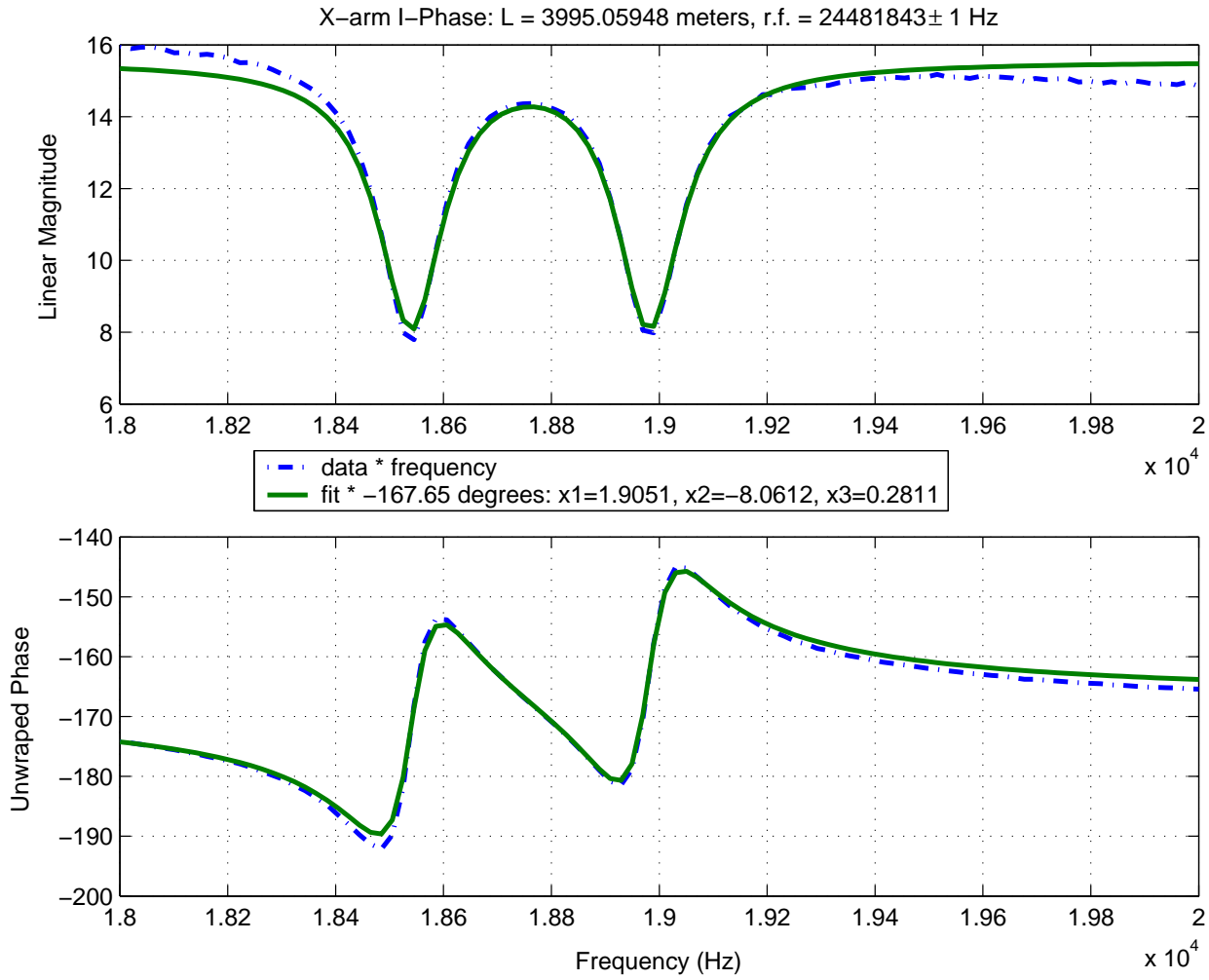
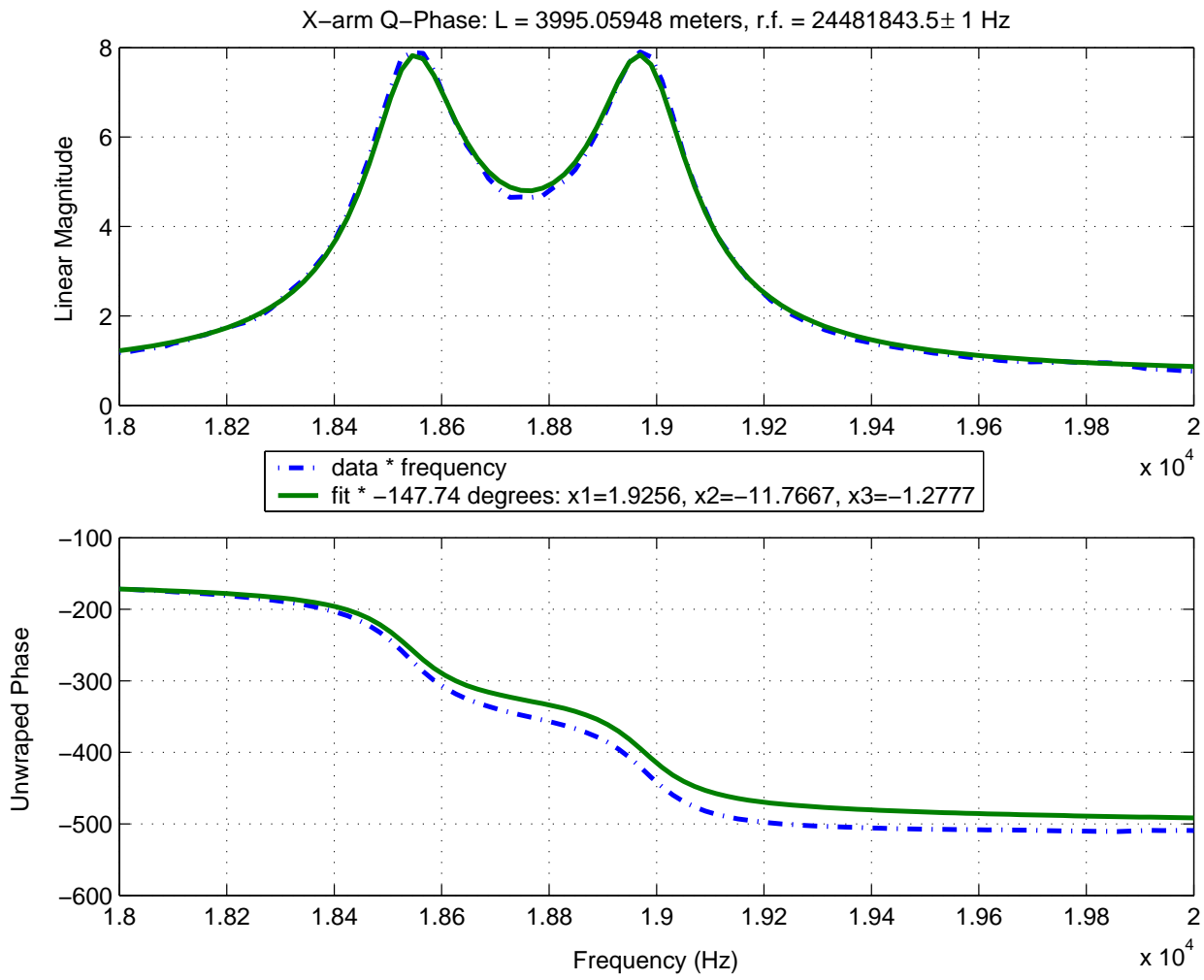


Figure 3.9:  $\frac{1}{2}$ FSR, I-phase

Figure 3.10:  $\frac{1}{2}$ FSR, Q-phase



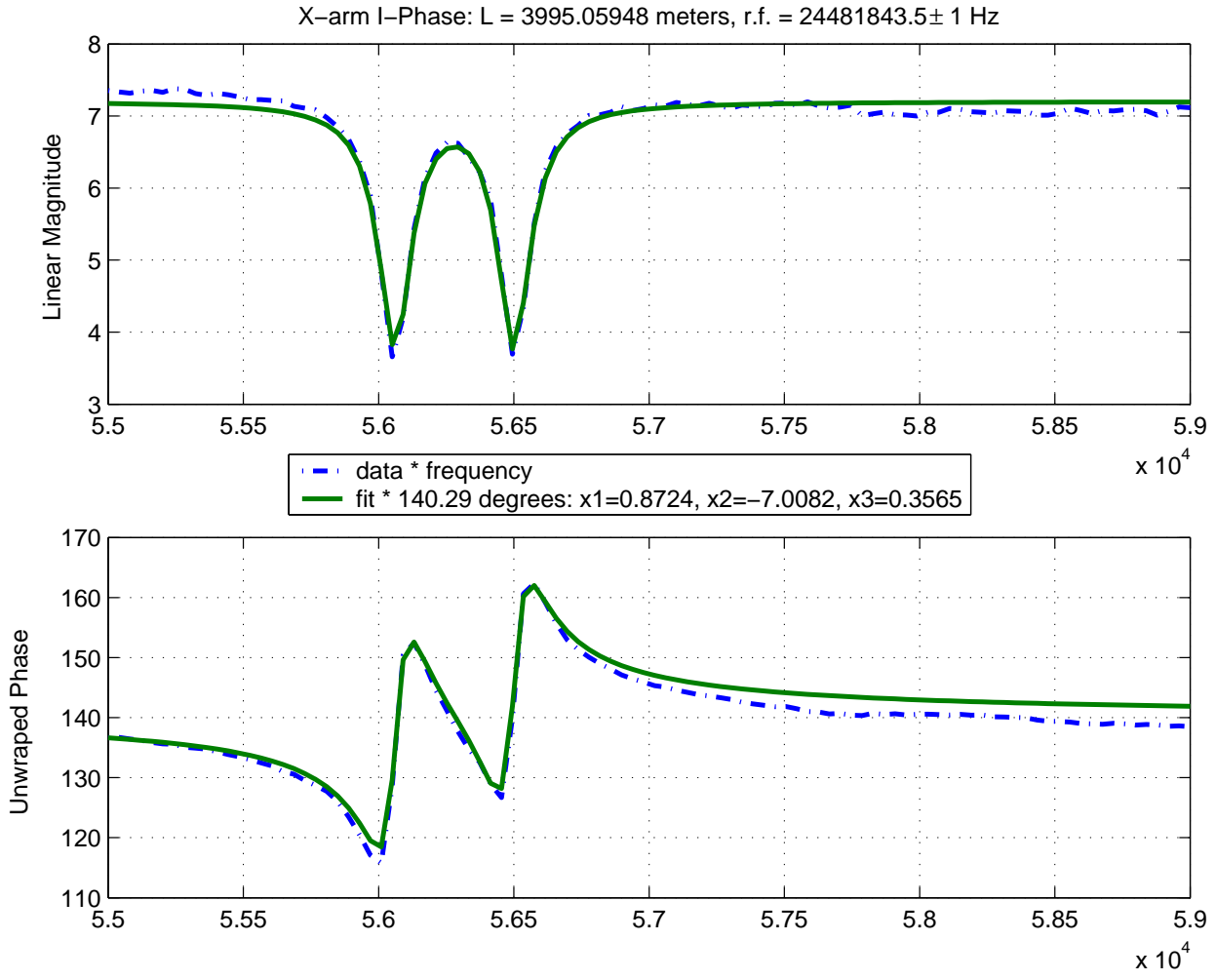
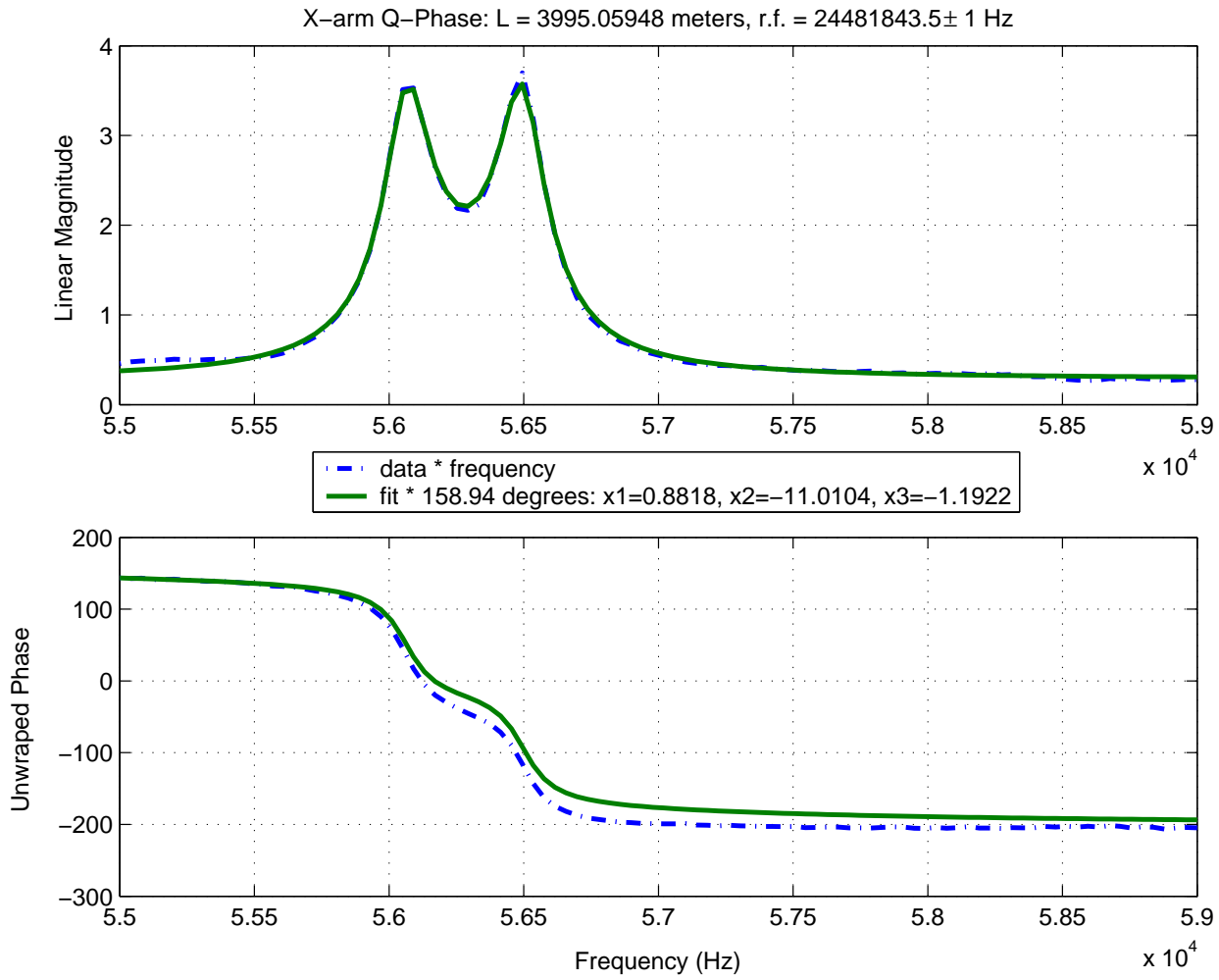


Figure 3.11:  $\frac{3}{2}$ FSR, I-phase

Figure 3.12:  $\frac{3}{2}$ FSR, Q-phase

### 3.1.4 Transverse Modes

It is well known that optical cavities will support Hermite-Gaussian modes of the fields [55, 65]. Such modes are distinguished by the axial index  $n \simeq L/2\lambda$  ( $L$  is the length of the cavity and  $\lambda$  the wavelength) and labeled by the small integers  $m, \ell$  which specify the field distribution in the two directions transverse to the cavity axis. For a cavity with spherical mirrors of radii  $R_1$  and  $R_2$  the frequency of the  $n, m, \ell$  mode is

$$\nu_{nml} = \frac{c}{2L} \left[ n + (1 + m + \ell) \frac{\cos^{-1} \sqrt{g_1 g_2}}{\pi} \right] \quad (3.15)$$

and

$$g_i = 1 - L/R_i \quad i = 1, 2 \quad (3.16)$$

I decided to search for the lowest transverse mode [13] by injecting a sideband onto the carrier. When the sideband frequency is exactly at the difference between the populated  $TEM_{00}$  mode and a transverse mode, a dip should be observed in the demodulated signal similar to that seen in Figs. 3.1 and 3.2 and described in section 3.1.2.

The IFO is injected with a LASER beam precisely aligned to the axis of the optical cavity and matched to the  $TEM_{00}$  mode. Thus the transverse modes are not excited in the arm. To observe the transverse mode I locked a single arm and intentionally misaligned the cavity. Using the digital suspension controls, the input test mass was rotated either around a vertical axis (yaw) or a horizontal axis (pitch). This coupled the input LASER beam to the  $\ell = 1, m = 0$  (horizontal) mode in the first case or to the  $\ell = 0, m = 1$  (vertical) mode in the second. Fig. 3.13 shows a typical response curve obtained when the suspension control “slider” was set at 2.241 units; the observed frequency was 11.48 kHz.

Misalignment of the ITM not only increases the coupling to the transverse

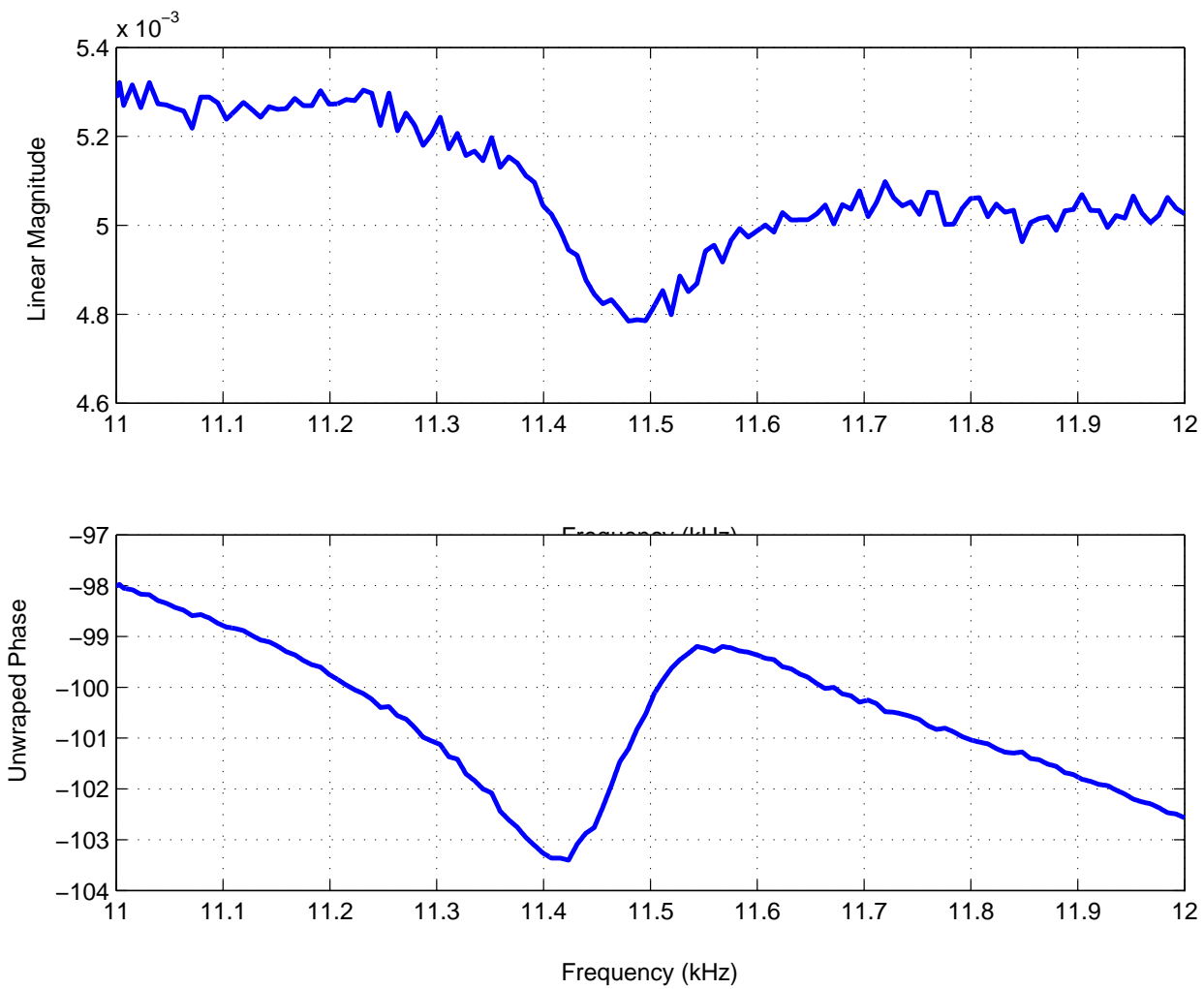


Figure 3.13: Sideband Injection Sweep for Transverse Mode Characterization

mode but also shifts the frequency of the mode. This was immediately evident from the data shown in Fig. 3.14 for the horizontal mode and in Fig. 3.15 for the vertical mode. In these figures the mode frequency is shown as a function of pitch or yaw of the ITM, the angle being labeled in slider units. Since the frequency shift must be symmetric with respect to the pitch or yaw angle the lowest contribution is proportional to the angle squared. Therefore a quadratic fit was made to the data as shown in Figs. 3.14 and 3.15. The peak of the curve corresponds to the properly aligned cavity for which the measured frequency shifts as obtained from the fit are

$$\Delta\nu_{\text{horizontal}} = 11,530 \pm 5 \text{ Hz} \quad (3.17)$$

$$\Delta\nu_{\text{vertical}} = 11,560 \pm 5 \text{ Hz}$$

From Eq.(3.16) I see that the frequency shift is related to the mirror curvatures by

$$\Delta\nu = \frac{\nu_{\text{fsr}}}{\pi} \cos^{-1}(\sqrt{g_1 g_2}) \quad (3.18)$$

and find

$$\begin{aligned} g_1 g_2 &= 0.3239 \pm 0.0004 && \text{horizontal mode} \\ &= 0.3215 \pm 0.0004 && \text{vertical mode} \end{aligned}$$

The values deduced from the measurement of the two modes differ by  $\sim 4\sigma$  and this may be due to a deformation of the mirror surface.

The design values for the curvature are given in [8] and the “as built” values [9] are

$$\begin{aligned} R_1 &= 14,240 \text{ m} && \text{(ITM)} \\ R_2 &= 7,260 \text{ m} && \text{(ETM)} \end{aligned}$$

This leads to

$$g_1 = 0.719 \quad g_2 = 0.450 \quad \text{and} \quad g_1 g_2 = 0.324$$

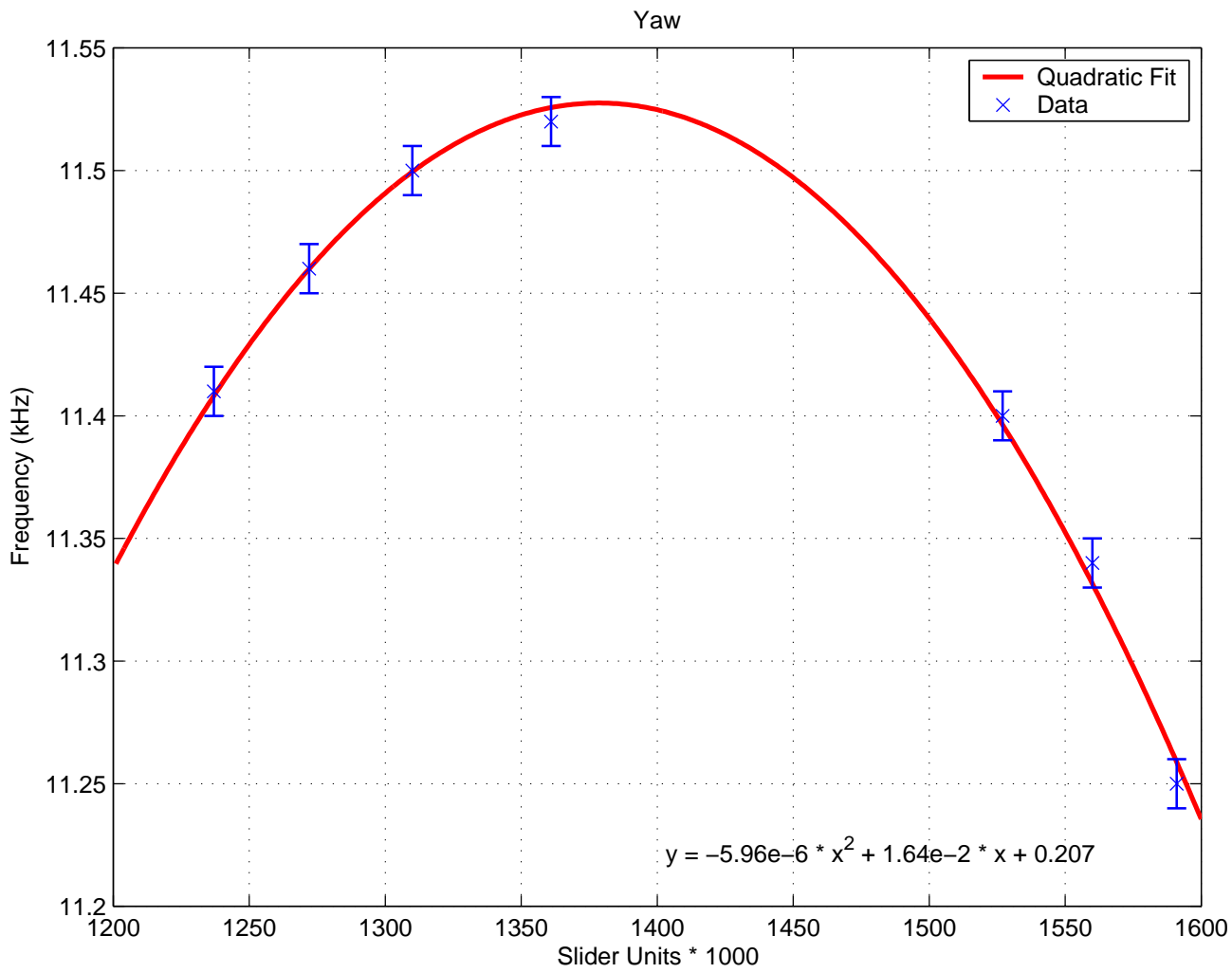


Figure 3.14: Transverse Mode Frequency variance with Yaw

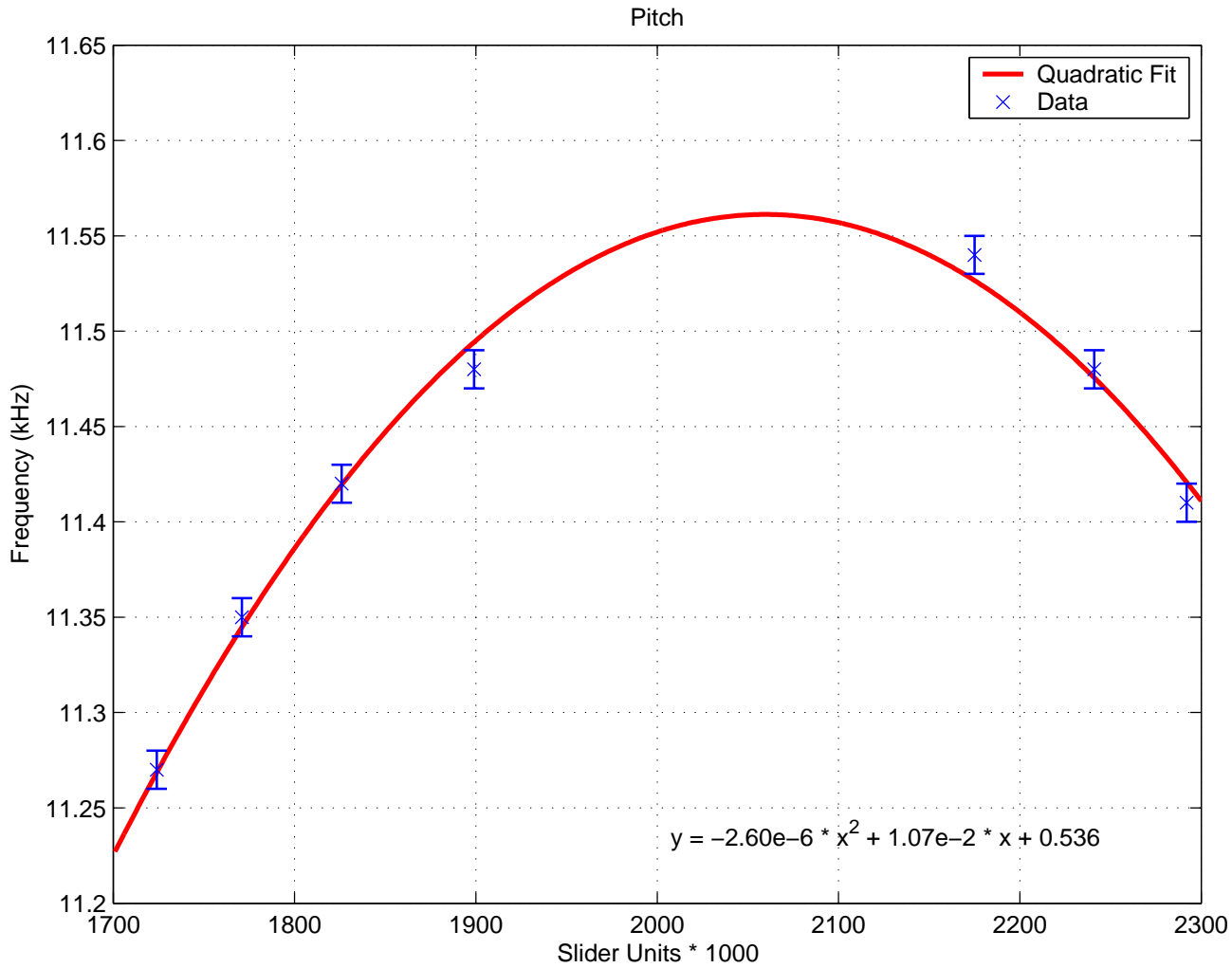


Figure 3.15: Transverse Mode Frequency variance with Pitch

in close agreement with the  $g_1 g_2$  product obtained from the frequency of the horizontal mode.

## 3.2 Parametric Conversion

In section 3.1 and [15] I examined the response of a single arm cavity to frequency sideband injection at multiples of 1/2 the free spectral range (FSR). Here I continue the IFO characterization by investigating the response of a single arm cavity as well as the response of the complete power recycled interferometer (PRIFO) to mirror motion. I use the term “parametric conversion” in the sense that harmonic variation ( $\Omega$ ) of one parameter of the system (in this case the arm length) results in the conversion of a fraction of the carrier ( $\omega_c$ ) to the sum and difference frequency ( $\omega_c \pm \Omega$ ). For an optical cavity the effect can also be interpreted as arising from the Doppler shift of the carrier when reflected from a moving mirror. The conversion is most pronounced when the sidebands coincide with one of the resonant modes of the system. Since the modes of the IFO are equally spaced by the  $f_{\text{fsr}} = c/2L$ , with  $L$  the arm length, the parametric conversion response is peaked when  $\Omega = 2\pi f_{\text{fsr}}$ . The width of the line is given by the  $Q$  of the arm cavity (or the PRIFO). For a simple cavity

$$Q = \frac{2L}{\lambda} F \simeq \frac{L}{\lambda} \frac{2\pi}{1 - r_A} = kL \frac{1}{1 - r_A}, \quad (3.19)$$

where  $r_A$  is the (amplitude) reflectivity of the entrance mirror, I have ignored any losses, and set  $r_B = 1$  and  $k = 2\pi/\lambda$ . It follows that

$$\Delta f = \frac{f_c}{Q} \simeq f_{\text{fsr}} \frac{1 - r_A}{\pi}, \quad (3.20)$$

where  $\Delta f$  is the FWHM power, or the FWHM at  $1/\sqrt{2}$  of the fields.



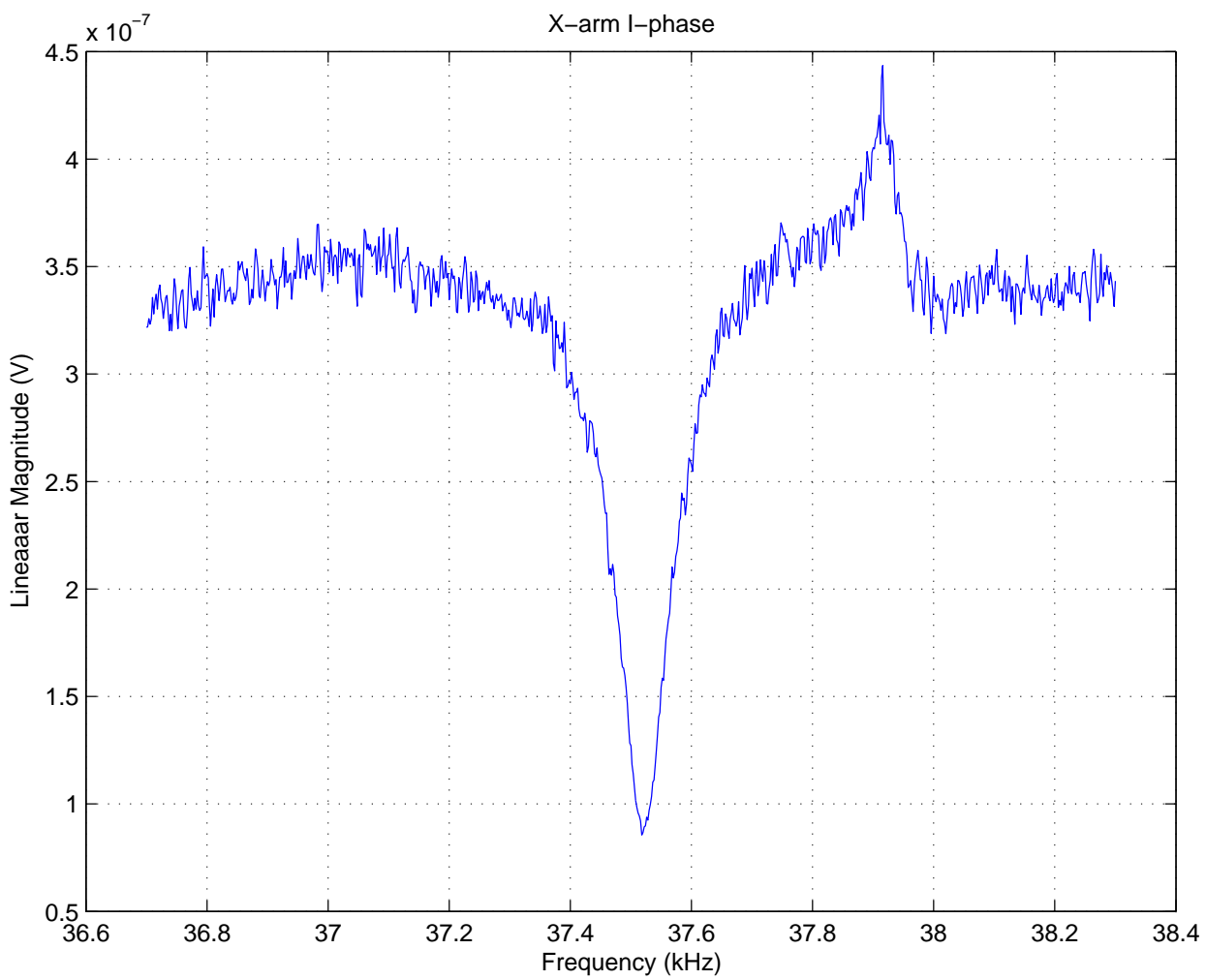


Figure 3.16: FFT of X-arm signal with no excitation

The amplitude  $E'$  of the parametrically converted signal is given on resonance by

$$E' = 2 \times \frac{1}{2} h Q E_c, \quad (3.21)$$

where  $E_c$  is the carrier amplitude and  $h$  the fractional parametric perturbation. The additional factor of two is introduced because both the upper and lower sidebands are populated. Eq(3.21) is valid for  $hQ \ll 1$ .

If the mirror position is given by

$$x(t) = x_0 \cos(\Omega t),$$

then  $h = x_0/L$ . Introducing this expression for  $h$  and the definition of  $Q$  in Eq(3.21) I find (on resonance)

$$E' = E_c k x_0 \frac{2}{1 - r_A}. \quad (3.22)$$

Note that both fields,  $E_c$  and  $E'$  are measured inside the cavity (at the mirror) but have different frequencies. To relate Eq(3.22) to the observed fields I must propagate the incident carrier into the cavity as well as propagate the sideband  $E'$  out of the cavity to the detection port. This is done using the matrix method described in section 3.2.2.

The results that I obtain agree with Regehr [57] and Lyons [44] who start from Eq(3.22) and propagate the fields analytically using the *low frequency* approximation. Since all response functions are valid modulo  $f_{\text{fsr}}$ , the expressions given by Regehr and Lyons are equally applicable to the present case where  $\Omega/2\pi \simeq f_{\text{fsr}}$ .

### 3.2.1 Modulation and Demodulation

As in section 3.1.1 a first order expansion in the fields is sufficient and I must still treat the upper and lower sidebands separately. However, the modulation

and resulting demodulation is slightly different in the case of mirror motion. This is because the r.f. sidebands are anti-resonant and do not enter the cavity. Thus they are not parametrically converted. With sideband injection there were 8 demodulation terms of interest: 4 terms with  $f_{\pm rf}$  beating against  $f_{\pm m}$  and 4 terms with  $f_{\pm(rf\pm m)}$  beating against the carrier (where  $f_{rf}$  indicates the non-resonant sideband required for heterodyne locking and  $f_m$  indicates the sideband injected at the frequency of interest.) In the case of mirror motion only the 4 terms with  $f_{\pm rf}$  beating against  $f_{\pm m}$  are present where in this case  $f_m$  is the mirror motion frequency; compare Eqs.(3.3) and (3.24).

One may be justly concerned about the signal when the front mirror, on which the r.f. is incident, is excited. This case can be analyzed by a thought experiment. Consider a simple two mirror cavity. Now consider that both mirrors are moving in a common motion, that is to say they are both oscillating sinusoidally at the same frequency and with the same phase so that they both move in the same direction at the same time. The frequency response to this situation would be null, as the length of the cavity never changes leaving the resonance conditions static. Thus  $E_m = 0$  and the sum of the terms  $E_{\pm(rf\pm m)}$  is also 0 (as essentially  $f_m = 0$  and the sum of  $E_{\pm rf}$  is the locking signal which is null on resonance). Next consider moving only the back mirror. As the  $f_{rf}$  is non-resonant there are no  $E_{rf}$  sidebands incident on the moving mirror. Thus there can be no fields at frequency  $f_{rf\pm m}$  so all fields  $E_{\pm(rf\pm m)} = 0$ . Finally consider moving only the front mirror. By superposition and comparison with the common mode motion of both mirrors I know that the sum of the fields at  $f_{\pm(rf\pm m)}$  of the back mirror motion is equal in magnitude and negative in sign to the sum of the fields at  $f_{\pm(rf\pm m)}$  of the front mirror motion. But these fields of the back mirror motion are zero so I can set all  $E_{\pm(rf\pm m)} = 0$  in front mirror motion as well. It may be

of interest to recall that resonance of the  $E_{\pm(rf \pm m)}$  sidebands within the cavity gave rise to the  $(1/2)f_{\text{ISR}}$  features from sideband injection as demonstrated in section 3.1.3. As such fields are not present when mirrors move, I do not expect (nor do I see) any such features with mirror excitation.

For pure phase modulation I repeat the initial steps of section 3.1.1 using real sidebands. However, as I have just shown that the  $f_{rf}$  and  $f_m$  terms do not mix in the case of mirror excitation, Eq.(3.1) can be simplified to

$$\text{AS}_{\text{rf}} = \left| E_0 + E_{m+}e^{i\omega_m t} - E_{m-}e^{-i\omega_m t} + E_{s+}e^{i\omega_s t} - E_{s-}e^{-i\omega_s t} \right|^2 \quad (3.23)$$

For the demodulation signal I need only terms of the form  $e^{\pm i(\omega_s \pm \omega_m)t}$ . Thus I obtain

$$\begin{aligned} \text{AS}_{\text{rf}} = & \cos(\omega_s t) \left[ \begin{array}{l} e^{i\omega_m t} \left( E_{s-}E_{m-}^* + E_{m+}E_{s+}^* - E_{m+}E_{s-}^* - E_{s+}E_{m-}^* \right) \\ + e^{-i\omega_m t} \left( E_{s+}E_{m+}^* + E_{m-}E_{s-}^* - E_{m-}E_{s+}^* - E_{s-}E_{m+}^* \right) \end{array} \right] \\ & - i \sin(\omega_s t) \left[ \begin{array}{l} e^{i\omega_m t} \left( E_{s-}E_{m-}^* + E_{m+}E_{s+}^* + E_{m+}E_{s-}^* + E_{s+}E_{m-}^* \right) \\ - e^{-i\omega_m t} \left( E_{s+}E_{m+}^* + E_{m-}E_{s-}^* + E_{m-}E_{s+}^* + E_{s-}E_{m+}^* \right) \end{array} \right] \end{aligned} \quad (3.24)$$

I write Eq.(3.24) compactly as

$$\text{AS}_{\text{rf}} = \cos(\omega_s t)[e^{i\omega_m t}\alpha' + e^{-i\omega_m t}\beta'] - i \sin(\omega_s t)[e^{i\omega_m t}\gamma' + e^{-i\omega_m t}\delta'] \quad (3.25)$$

where I substitute  $\alpha'$ ,  $\beta'$ ,  $\gamma'$  and  $\delta'$  for the corresponding sets of field terms. Upon closer inspection of Eq.(3.24) it is apparent that  $\beta' = \alpha'^*$  and  $\delta' = \gamma'^*$ , so that Eq.(3.25) can be further simplified to

$$\begin{aligned} \text{AS}_{\text{rf}} &= \cos(\omega_s t)[\alpha'e^{i\omega_m t} + (\alpha'e^{i\omega_m t})^*] - i \sin(\omega_s t)[\gamma'e^{i\omega_m t} - (\gamma'e^{i\omega_m t})^*] \\ &= 2 \cos(\omega_s t)\text{Re}\{\alpha'e^{i\omega_m t}\} - 2 \sin(\omega_s t)\text{Re}\{i\gamma'e^{i\omega_m t}\} \end{aligned} \quad (3.26)$$

Since I have adopted the convention of the sidebands being real, we imply that the r.f. sidebands were imposed by a *sine* modulation. If I had adopted

the convention of imaginary sidebands it would imply *cosine* modulation. Thus in my convention in-line demodulation selects the term oscillating as  $\sin(\omega_s t)$  while quadrature demodulation selects the term oscillating as  $\cos(\omega_s t)$ . Cosine modulation would reverse which term is selected by in-line vs. quadrature demodulation, however it would also change  $\alpha'$  and  $\gamma'$  such that regardless of the convention, in-line (or quadrature) signals are convention independent. If I assume a phase difference  $\phi$  between the demodulating r.f and the r.f. component of the detected signal I find

$$\begin{aligned} \text{AS-I}(\phi) &= \Re\{(-i\gamma' \cos \phi + \alpha' \sin \phi)e^{i\omega_m t}\} \\ \text{AS-Q}(\phi) &= \Re\{(\alpha' \cos \phi + i\gamma' \sin \phi)e^{i\omega_m t}\} \end{aligned} \quad (3.27)$$

The LIGO convention for modulation and resulting demodulation is to use cosine modulation [57, 68]. Nominally the fact that I am using a different convention should not cause any problems with readout of the signals from the IFO as the in-line signal is the same regardless of convention as is the quadrature signal. It did cause a certain amount of confusion as the readouts being used (*I<sub>mon</sub>* and *Q<sub>mon</sub>*) were analog monitoring points located on the demod board and once they were digitized their phase was adjusted by 90 degrees, thus making *I<sub>mon</sub>* = *Q*, and *Q<sub>mon</sub>* = *I*. However, it also appears that in the formulation of the LIGO demodulation convention the distance from the recycling mirror (RM) to the beam-splitter (BS) was not taken into account. As that distance is approximately 1/4 of the wavelength of the r.f. sidebands it has the effect of switching the r.f. modulation convention. All this has no effect upon the operation of the IFO as in practice the signal is routed to the demod board and the phase is tuned until one of the channels provides a maximum for the signal. This channel is then *defined* as the channel of interest. The effect upon fitting routines can be summarized as follows: In single-arm mode, *I<sub>mon</sub>* = *Q*

and  $Q_{mon} = I$ , in PRIFO mode,  $I_{mon} = I$  and  $Q_{mon} = Q$ .

### 3.2.2 Field Calculation Methods

Two separate methods are used to model the IFO output. The first method is through algebraic calculation and the use of the formulae given in [14]. This was used to fit the sideband injection into the IFO as the computational requirements of this method are significantly smaller. This also allows a point of comparison with results obtained from the second method. The second method was through a matrix inversion process similar to that done in TWIDDLE [58]. The primary reason for using the matrix method of calculation is that some of the symmetry arguments used to obtain the formulae for the first method do not hold when shaking a single mirror. Although a single mirror excitation could theoretically be modeled by the superposition of a common and a differential shake (both of which have sufficient symmetry to be adapted to the formulae in [14]) the matrix method is well adapted to computer calculation.

Both simulation methods required an additional parameter to properly simulate a locked PRIFO using the conventions adopted earlier. As previously described the fields returning from the arms (Eqs. 2.9 and 2.10) are given by

$$\frac{E_D}{E_{in}} = it_{bs}r_y r_{bs}e^{-i\frac{\omega}{c}2l_y} + ir_{bs}r_x t_{bs}e^{-i\frac{\omega}{c}2l_x} \quad (3.28)$$

$$\frac{E_r}{E_{in}} = r_{bs}r_y r_{bs}e^{-i\frac{\omega}{c}2l_y} - t_{bs}r_x t_{bs}e^{-i\frac{\omega}{c}2l_x} \quad (3.29)$$

which eventually lead to (Eq. 2.12) the dark port output

$$\frac{E_D}{E_0} = \frac{(-t_{rm})(t_{bs}r_y r_{bs}e^{-i\frac{\omega}{c}2l_y} + r_{bs}r_x t_{bs}e^{-i\frac{\omega}{c}2l_x})e^{i\frac{\omega}{c}l_{in}}}{1 - r_{rm}(r_{bs}r_y r_{bs}e^{-i\frac{\omega}{c}2l_y} - t_{bs}r_x t_{bs}e^{-i\frac{\omega}{c}2l_x})} \quad (3.30)$$

The calculational procedure that I have adopted involves setting the carrier frequency to zero and using modulation frequencies relative to the carrier. Although

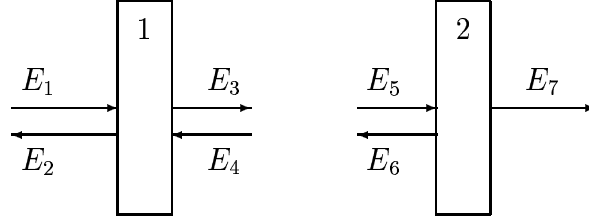


Figure 3.17: Simple Fabry-Perot Cavity

this method worked fine with no adjustments for the simple cavity calculations it can be seen from Eqs.(3.28 & 3.29) that under these conditions the “dark” port has a field magnitude  $\simeq 2$  while the “refl” port has a field magnitude  $\simeq 0$ . When the full carrier frequency is used then the length values of  $l_x$  and  $l_y$  can be set such that the “dark” port is arbitrarily dark. As this leads to an over-sensitivity of the simulation to some of the input lengths, the equations were modified to establish proper resonance conditions with relative frequencies. A parameter  $\xi$  was introduced to control the resonance condition. The modified equations are:

$$\frac{E_D}{E_{in}} = -it_{bs}r_yr_{bs}e^{-i\frac{\omega}{c}2l_y}e^{i\xi} + ir_{bs}r_x t_{bs}e^{-i\frac{\omega}{c}2l_x}e^{-i\xi} \quad (3.31)$$

$$\frac{E_r}{E_{in}} = -r_{bs}r_yr_{bs}e^{-i\frac{\omega}{c}2l_y}e^{i\xi} - t_{bs}r_x t_{bs}e^{-i\frac{\omega}{c}2l_x}e^{-i\xi} \quad (3.32)$$

$$\frac{E_D}{E_0} = \frac{(-t_{rm})(-t_{bs}r_yr_{bs}e^{-i\frac{\omega}{c}2l_y}e^{i\xi} + r_{bs}r_x t_{bs}e^{-i\frac{\omega}{c}2l_x}e^{-i\xi})e^{i\frac{\omega}{c}l_{in}}}{1 - r_{rm}(-r_{bs}r_yr_{bs}e^{-i\frac{\omega}{c}2l_y}e^{i\xi} - t_{bs}r_x t_{bs}e^{-i\frac{\omega}{c}2l_x}e^{-i\xi})} \quad (3.33)$$

The nominal value is  $\xi = 0$  for which resonance conditions are established at zero frequency. To fit the data  $\xi$  is varied off nominal, and this is a measure of how well the IFO is tuned.

The second method used to model the data is a matrix inversion calculation. Each location at an optic within the system is given a number to denote the electric field at that location. This includes the fields incident on the optic and those fields leaving the optic in all directions of interest. Then the field equations (with the carrier frequency set to zero) are set out in a matrix form. For example

for an optic with fields incident from both sides (like the input mass for a simple cavity) I can label the field incident from the left as 1, the field leaving to the left as 2, the field leaving to the right as 3 and the field incident from the right as 4, as illustrated in Fig.(3.17). I set field 1 equal to itself and leave it at that. Field 2 is itself plus field 1 times the optic's reflectivity plus field 4 times the optic's transmissivity. Field 3 is itself plus field 4 times the reflectivity and field 1 times the transmissivity. Field 4 is itself plus likely another field with a spatial propagation term. I write this set of linear equations so that they are all equal to zero, except in the case of field 1, which is equal to 1. Written in matrix form, the element  $(j,k)$  refers to the contribution of field  $k$  to the field  $j$ . In the simple example used above  $(1,1) = 1$ ,  $(2,2) = 1$ ,  $(2,1) = -r_1$ ,  $(2,4) = -it_1$ . The matrix, when multiplying a column vector of the actual field values, should equal the input column vector, in this case  $[1,0,0,0,\dots]$ . Thus when the matrix (M) is inverted and multiplied into the input vector  $[1,0,0,\dots]$  the resulting vector contains the fields at all locations in the system. It is a simple matter to modify the input vector to simulate injection of sidebands at a different location, for example by shaking a mirror instead of sideband injection on the incident field.

The example discussed above is shown in Fig.(3.17) and the accompanying Eqs.(3.34 and 3.35) show the equations in matrix form. The  $\phi_l$  in the equations is the length propagator to appropriately adjust the phase and is given by  $\phi_l = \omega l/c$  where  $l$  is the length of the cavity. Given that the matrix is frequency dependent, when implemented in MATLAB, a 3-dimensional matrix is used so that a 2-dimensional matrix is available for each frequency of interest. For the full PRIFO a 22x22 matrix is needed.



$$\begin{bmatrix}
1 & 0 & 0 & 0 & 0 & 0 & 0 \\
-r_1 & 1 & 0 & -it_1 & 0 & 0 & 0 \\
-it_1 & 0 & 1 & -r_1 & 0 & 0 & 0 \\
0 & 0 & 0 & 1 & 0 & -e^{-i\phi_l} & 0 \\
0 & 0 & -e^{-i\phi_l} & 0 & 1 & 0 & 0 \\
0 & 0 & 0 & 0 & -r_2 & 1 & 0 \\
0 & 0 & 0 & 0 & -it_2 & 0 & 1
\end{bmatrix}
\times
\begin{bmatrix}
E_1 \\
E_2 \\
E_3 \\
E_4 \\
E_5 \\
E_6 \\
E_7
\end{bmatrix}
=
\begin{bmatrix}
1 \\
0 \\
0 \\
0 \\
0 \\
0 \\
0
\end{bmatrix}
\quad (3.34)$$

$$\begin{bmatrix}
E_1 \\
E_2 \\
E_3 \\
E_4 \\
E_5 \\
E_6 \\
E_7
\end{bmatrix}
=
\begin{bmatrix}
1 & 0 & 0 & 0 & 0 & 0 & 0 \\
-r_1 & 1 & 0 & -it_1 & 0 & 0 & 0 \\
-it_1 & 0 & 1 & -r_1 & 0 & 0 & 0 \\
0 & 0 & 0 & 1 & 0 & -e^{-i\phi_l} & 0 \\
0 & 0 & -e^{-i\phi_l} & 0 & 1 & 0 & 0 \\
0 & 0 & 0 & 0 & -r_2 & 1 & 0 \\
0 & 0 & 0 & 0 & -it_2 & 0 & 1
\end{bmatrix}^{-1}
\times
\begin{bmatrix}
1 \\
0 \\
0 \\
0 \\
0 \\
0 \\
0
\end{bmatrix}
\quad (3.35)$$

### 3.2.3 Data Fits

I have fit the following data sets:

- (a) Single arm excitation of ITMX (Data obtained in October 2002; Fig. 3.18)
- (b) PRIFO excitation of ITMX (Data obtained in October 2002; Fig. 3.19)
- (c) PRIFO excitation of ITMX (Data obtained in December 2002; Fig. 3.20);  
Both Q-phase and I-phase are shown.
- (d) Figure 3.21 is an enlarged view of the I-phase data and fit of Figure 3.20
- (e) Figure 3.22 is an enlarged view of the Q-phase data and fit of Figure 3.20.

Case (a) is simple to fit either algebraically or with the matrix method. The parameters varied were the normalization, demodulation phase and a frequency independent noise level (which is also multiplied by the normalization factor). The fit is shown in Fig.3.18 and it returned the following values:

$$\begin{aligned} N &= 3.42 \times 10^{-9} \\ \phi &= 0^\circ \\ A_{\text{noise}} &= 2.06 \times 10^{-8} \end{aligned}$$

Note that the noise level is essentially zero. The noise parameter was a remnant from the fits to sideband injection [15] where it was very important in order to obtain a good fit. The arm length was kept fixed at 3995.05948 m as determined previously in section 3.1.2. The data is cut off at 37.75 kHz due to the presence of a strong internal resonance of the test mass at 37.8 kHz. This may also be the reason that the data does not agree better with the fitted curve.

Data on the full Power Recycled Interferometer (PRIFO) was taken primarily in two distinct periods (case b and c). As extensive commissioning work was constantly in progress on the IFO at this time, there are substantial differences in the instrument response. Primarily this can be explained as a decrease in the amount that  $\xi$  (as defined in Sec. 3.2.2) varied off the “perfect” dark port condition. It is believed that all other parameters that would affect the fit stayed essentially constant during this period. The  $\xi$  parameter can vary from measurement to measurement as it is dependent on the quality of the lock. Thus if the control loop is already near its limit, then a small increase in the ambient noise, although not necessarily enough to cause a loss of lock, would result in a decrease of the lock quality (an increase in  $\xi$ ) and not an increase in the feedback signal.

With the complete PRIFO many more parameters have to be specified. These are given in Table 3.1 and were obtained from a combination of design specifications, measured values and best fits as indicated. With the complete PRIFO the data exhibits the same broad resonance observed when a single arm is excited (Fig 3.18) which is referred to as the “cavity pole”, and an additional much narrower peak referred to as the “double cavity pole”. This arises because the recycling mirror significantly improves the finesse of the common mode signal. However, the common mode signal can not appear at the AS port except for a small leakage that arises because of the “asymmetry” between the two arms. This asymmetry is introduced in order to provide maximal r.f. sideband power at the AS port. When the PRIFO is not perfectly locked ( $\xi \neq 0$ ) the common mode signal becomes more pronounced at the AS port. This is the case in Fig. 3.19.

Moving a mirror in one arm is equivalent to the presence of both a differential mode and a common mode signal as the excitation of a single ITM is equivalent to a linear combination of common and differential motion of both ITMs. That is, by changing the length of a single arm one changes both the average length of the two arm cavities as well as the difference between the lengths of the two arm cavities. The PRIFO is designed to have the anti-symmetric (AS) port on a common motion “dark fringe” and a differential motion “bright fringe”. Thus common motion of the arm cavities will not result in a signal (this is because a properly polarized gravitational wave excites the differential motion of the test masses).

As far as the differential signal is concerned there is no recycling mirror, the light simply leaves the arm cavity and exits to the AS port diode. A differential motion signal from the PRIFO is the same as that from a single arm. A common

Table 3.1: Nominal Parameters for WA 4k Interferometer

Parameter	Value
LASER Power in TE00 Mode	1 (W)
Resonant SB frequency*	24481323 (Hz)
Resonant SB modulation depth	0.45
Distance RM to BS <sup>†</sup>	3 (m)
Distance BS to in-line ITM <sup>‡</sup>	6.191 - asym (m)
Distance BS to off-line ITM <sup>‡</sup>	6.191 + asym (m)
Michelson Asymmetry (asym) <sup>‡</sup>	0.151 (m)
Michelson Asymmetry (asym) <sup>§</sup>	0.110 (m)
Distance in-line Arm*	3995.05948 (m)
Distance off-line Arm*	3995.01332 (m)
BS Reflectance <sup>¶</sup>	0.49997999
BS Transmittance <sup>¶</sup>	0.49997999
BS Loss <sup>¶</sup>	40e-6
RM Reflectance <sup>¶</sup>	0.971825
RM Transmittance <sup>¶</sup>	0.0281
RM Loss <sup>¶</sup>	75e-6
ITM Reflectance <sup>¶</sup>	0.971825
ITM Transmittance <sup>¶</sup>	0.0281
ITM Loss <sup>¶</sup>	75e-6
ETM Reflectance <sup>¶</sup>	0.999925
ETM Transmittance <sup>¶</sup>	5e-6
ETM Loss <sup>¶</sup>	70e-6
ITM / ETM pendulum frequency <sup>  </sup>	0.74 (Hz)

\* Obtained from fits in [15].

<sup>†</sup> Estimate based on experience on-site.

<sup>‡</sup> Obtained from [23].

<sup>§</sup> Obtained from fits presented in this paper.

<sup>¶</sup> Values are Power coefficients, for amplitude coefficients take the square root. Values obtained from specifications [8] and previously designed simulations for the E2E program [7, 6].

<sup>||</sup> Obtained from [41].

motion signal however, is sent back to the recycling mirror and is reflected back to the arm cavities. This has the effect of increasing the reflectivity of the respective arm cavity's input mirror; thus giving it a higher finesse and a more narrow frequency response. The common mode appears as a narrow peak or "glitch" superimposed on the differential mode broad signal. Fig. 3.19 shows the data obtained in October 2002 with the complete PRIFO and the corresponding fit. The parameters are

fit :

$$N = 0.46 \times 10^{-6}$$

$$A_{\text{noise}} = -0.32$$

$$\xi = 4.00^\circ$$

specified, not fit :

$$\phi = 0^\circ$$

$$\text{Mich Asymmetry} = 0.110 \text{ meters}$$

$$\text{Length of Y Arm} = 3995.0134 \text{ meters}$$

Fig. 3.20 shows the data obtained in December 2002 with the complete PRIFO and the corresponding fit to the I phase. I had both quadratures of data for the December data and was therefore able to extract more information from the fitting of the data. To fit this data I varied two additional parameters while eliminating another. I varied the Michelson asymmetry and the Y arm length (to vary the arm asymmetry); I was able to eliminate the noise parameter from the fit as its contribution was inconsequential. I was then able to obtain a fit to the I phase data where the same parameters produced a Q phase

prediction with good agreement to the data.

fit :

$$N = 2.82 \times 10^{-6}$$

$$\xi = 6.82^\circ$$

$$\text{Mich Asymmetry} = 0.21 \text{ meters}$$

$$\text{Length of Y Arm} = 3995.01112 \text{ meters}$$

specified, not fit :

$$\phi = 0^\circ$$

The agreement in this case is quite encouraging. Expanded views of these curves are shown in Figs 3.21, 3.22. Fig 3.21 shows the I-phase data and the corresponding fit, while Fig 3.22 shows the Q-phase data and the Q-phase prediction using the parameters obtained in the I-phase fit. As a significant amount of work had taken place on the instrument between the measurements leading to the values listed in Table 3.1 and given the time these measurements were taken, some of the parameters in the Table may have been modified. Nevertheless the quality of the fits demonstrates the validity and predictive power of the model used.

### 3.2.4 Calibration and Normalization

In the measurements discussed in the previous section ITMX was driven at frequencies around  $f_{\text{sr}} = 37.52$  kHz. This was rather unusual (since in normal IFO operations only frequencies up to a few kHz are used to calibrate the instrument response) and was achieved by introducing a modified controller which could drive the test mass coils at high current. To relate the drive signal to mirror motion I use the D.C. calibration values:

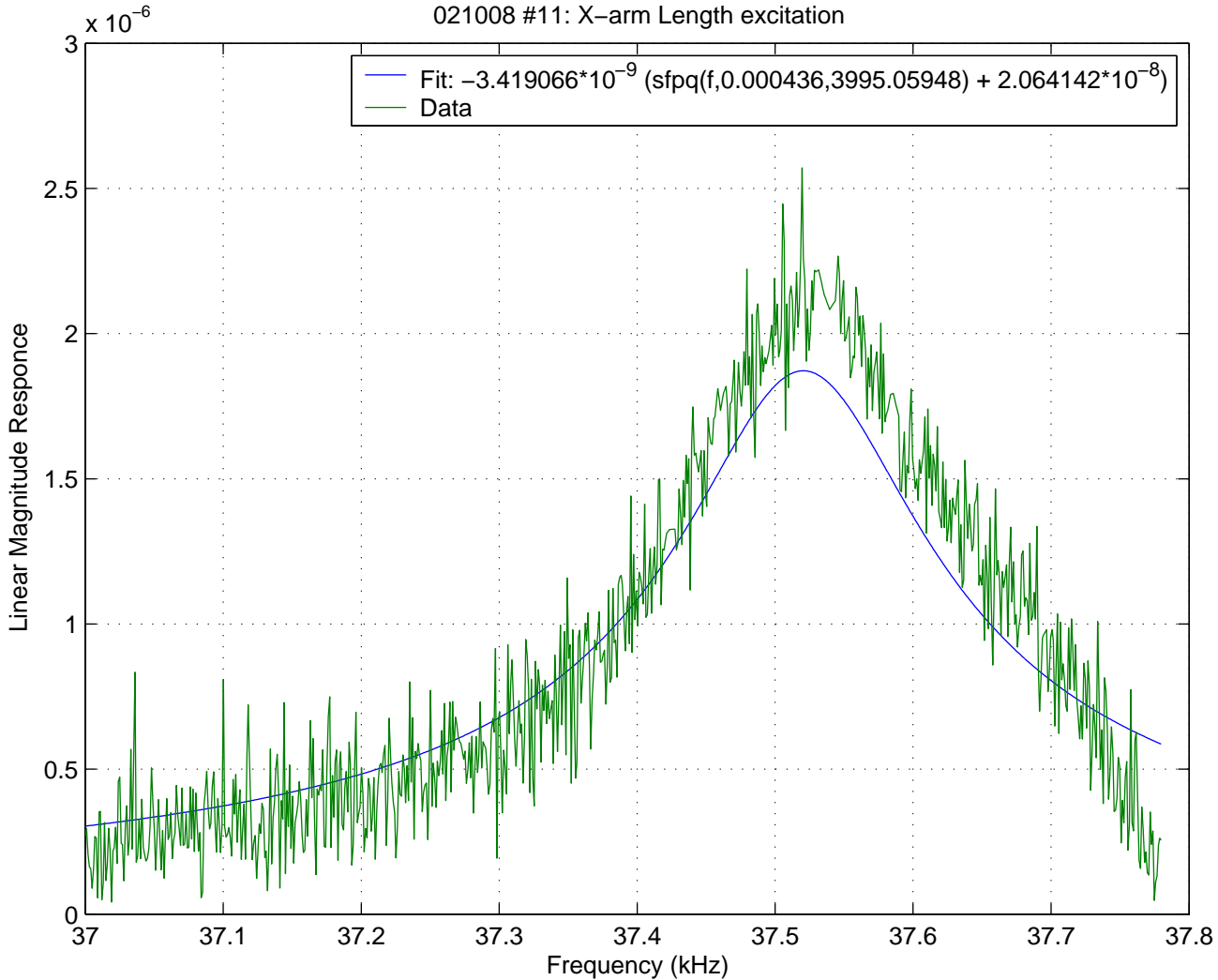


Figure 3.18: X-arm Shake Response

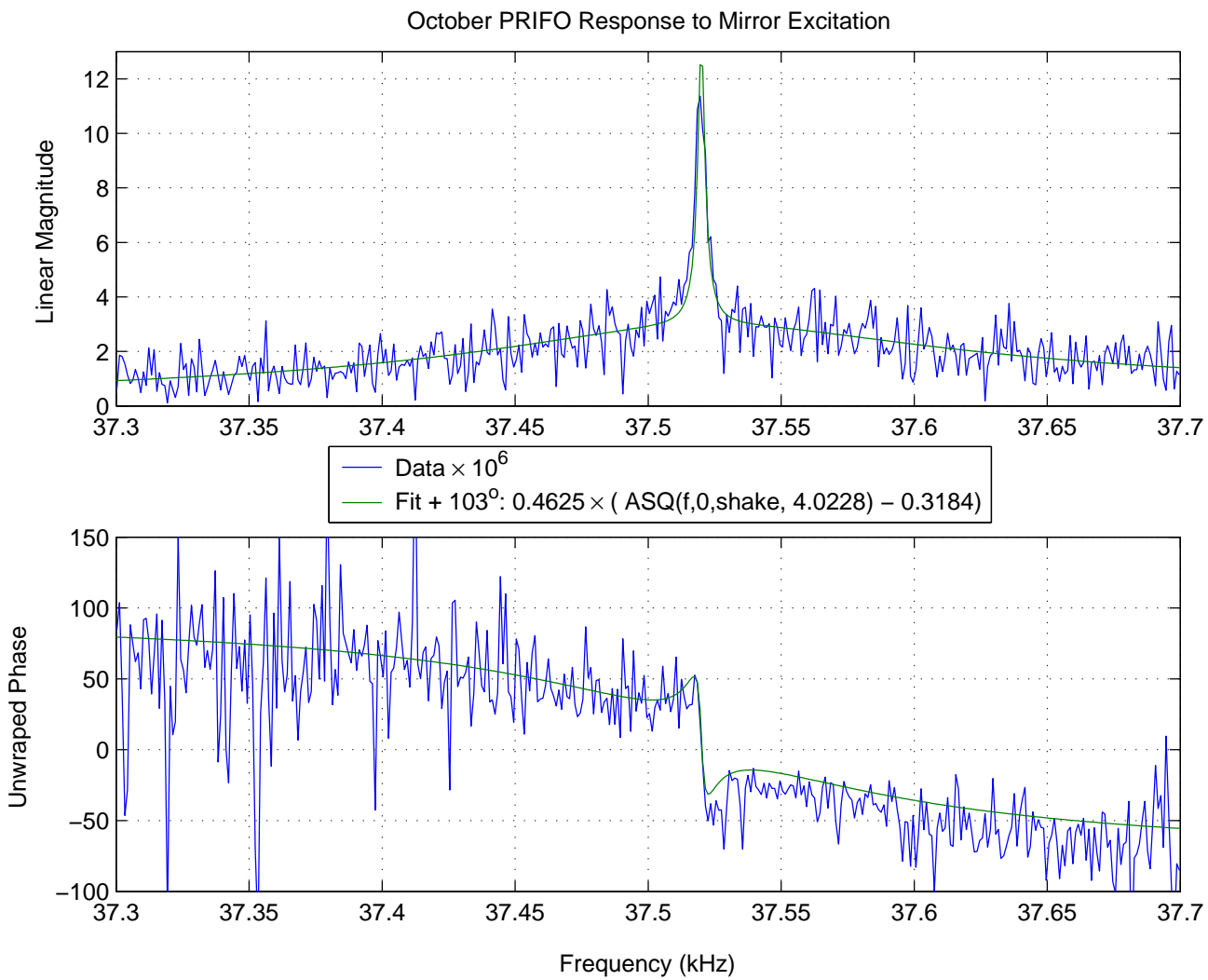


Figure 3.19: Full-IFO Mirror Excitation Response, Q-phase October



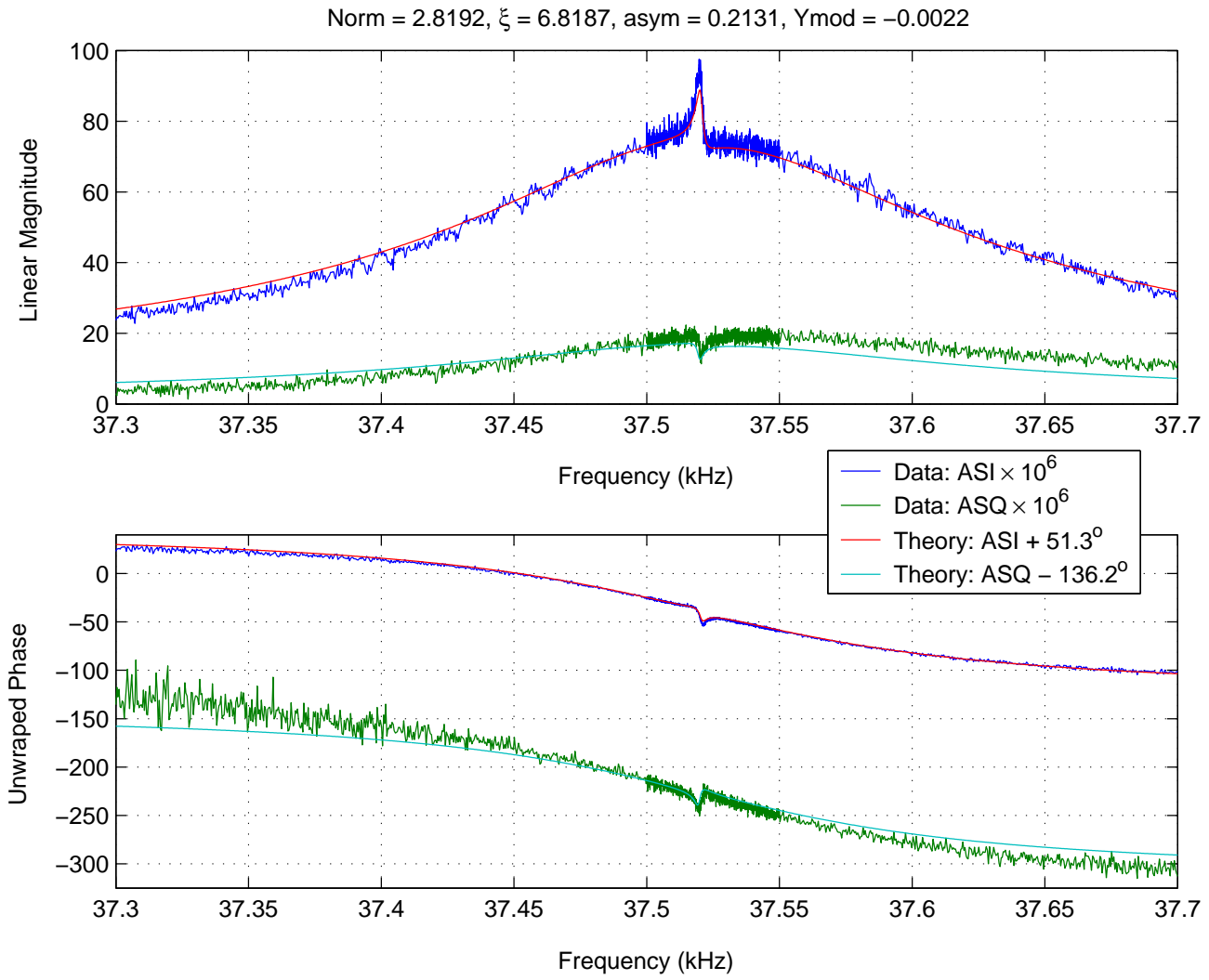


Figure 3.20: Full-IFO Mirror Excitation Response, I and Q phase

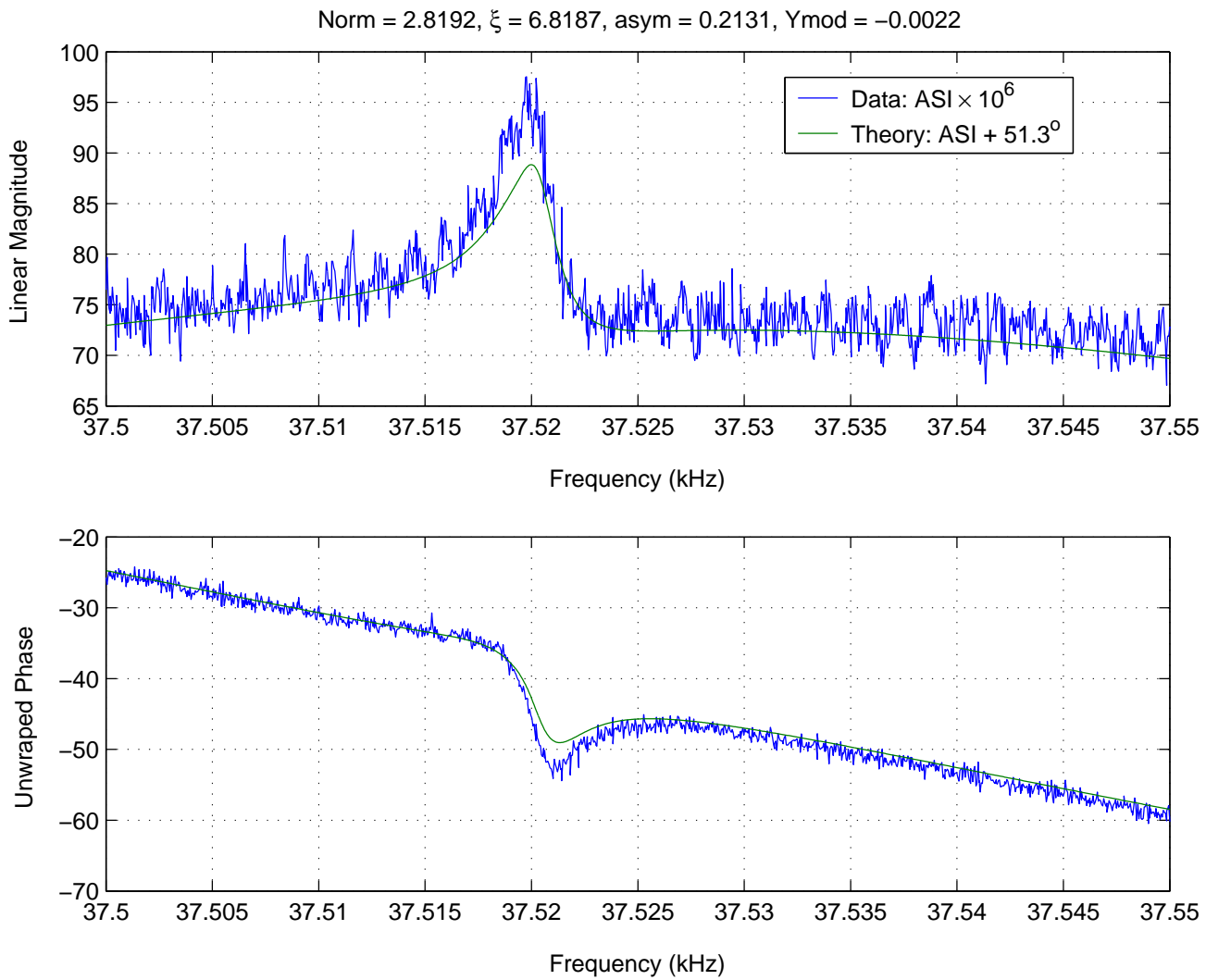


Figure 3.21: Full-IFO Mirror Excitation Response, I-phase

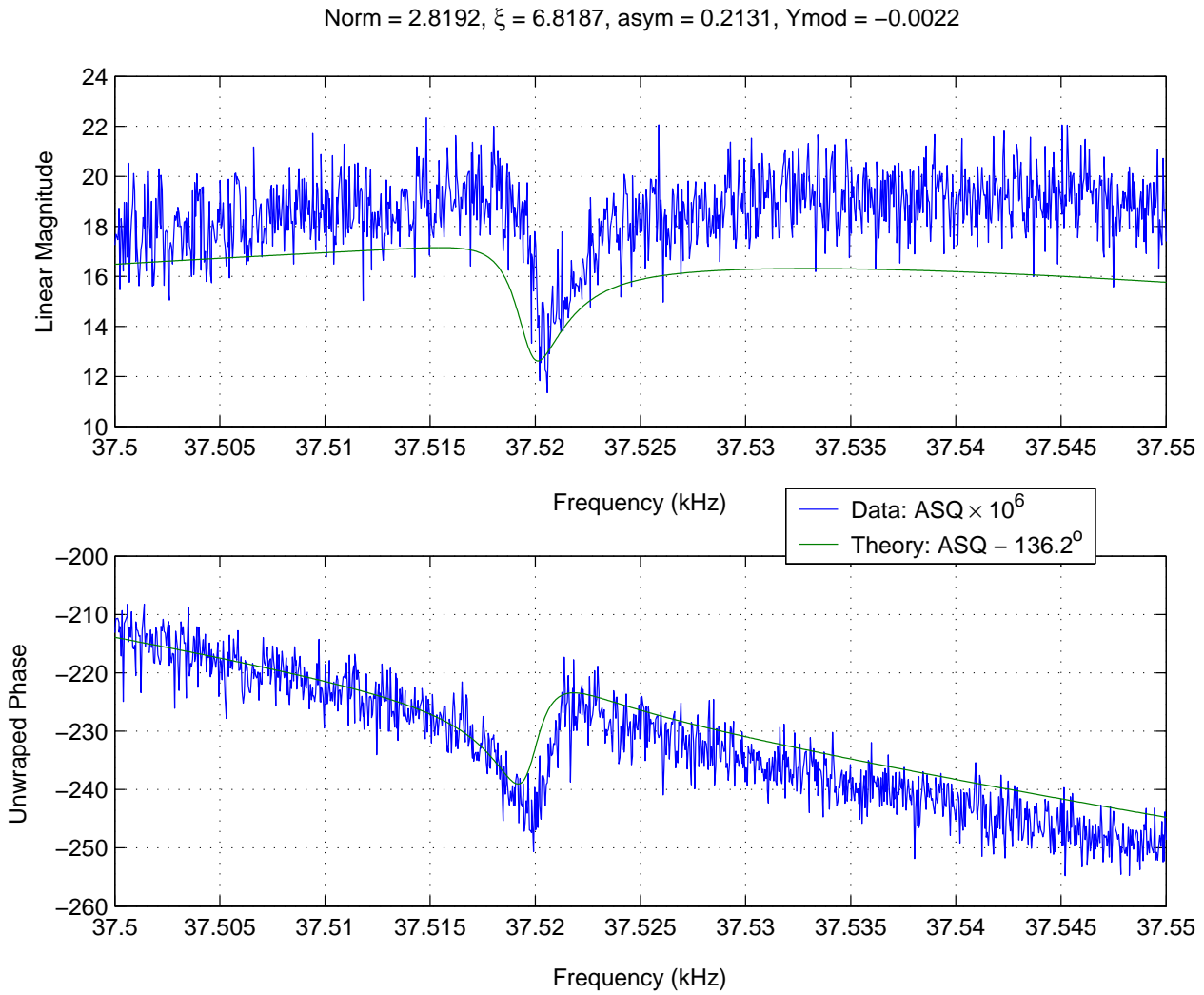


Figure 3.22: Full-IFO Mirror Excitation Response,  $Q$ -phase

0.163	nm / count drive <sup>5</sup>
20,000 / 175	counts drive / mV <sub>pp</sub> on coils
22 / .2	mV <sub>pp</sub> on coils / V <sub>pp</sub> drive <sup>6</sup>

Thus at DC (0.1 Hz) the calibration is:

$$x_{\text{DC}} = 2.049 \mu\text{m} / V_{\text{pp}} \text{ drive} \quad (3.36)$$

To obtain the calibration at  $f = f_{\text{fsr}} = 37.52$  kHz we treat the optic as a simple pendulum driven far off resonance [49]

$$x(f) = \frac{x_{\text{DC}}}{\sqrt{[1 - (\frac{f}{f_0})^2]^2 + (\frac{1}{Q} \frac{f}{f_0})^2}}. \quad (3.37)$$

Here  $f_0$  is the resonant frequency of the pendulum mode  $f_0 = 0.743$  Hz [41] and  $Q$  the Q-value. For  $f/f_0 \gg 1$ , Eq(3.37) reduces to

$$x(f) \simeq x_{\text{DC}} \left( \frac{f_0}{f} \right)^2. \quad (3.38)$$

Therefore I take the calibration at  $f_{\text{fsr}} = 37.52$  kHz as

$$x(37.52 \text{ kHz}) = 8.04 \times 10^{-16} \text{ m} / V_{\text{pp}} \text{ drive}. \quad (3.39)$$

Next I must establish the relation between the optical power (at the frequency that is demodulated) and the signal recorded on the SRS spectrum analyzer. These factors are shown in Table 3.2 below and consist of: (a) Signal attenuation by an E/O shutter, (b) A series of pick-offs (as the LIGO design calls for an eventual set of four photodiodes at the AS port), (c) The photodiode conversion efficiency, (d) The photodiode r.f. impedance and (e) The signal transmission efficiency from r.f. output to the demodulated output. Thus 1 W of optical

---

<sup>5</sup>At D.C., obtained from the calibration group at LHO [40].

<sup>6</sup>Measured ratio of the drive seen by the optic divided by the drive signal sent to the optic.

Table 3.2: Output Attenuation

Parameter	Value
E/O Shutter	7 %
Beam-path	0.245
Diode Eff.	0.64 A / W
Diode Imped.	4000 $\Omega$
Signal Transfer	0.269 $V_{pk}$ (SRS) / $V_{pk}$ signal
Total	11.76 $V_{pk}$ (SRS) / W

power yields 11.76 V on the SRS spectrum analyzer or

$$11.76 \text{ V} / \text{W}. \quad (3.40)$$

Finally to compare my model to the data I must relate the field  $E_0$  in the arm to the input LASER power (including the recycling effects). I must also know the r.f. sideband field at the AS port. I initially will assume an input power  $I_{\text{in}} = 1 \text{ W}$ .

The PRM (power) build-up factor is determined as follows: with the recycling mirror misaligned the intensity through a single locked arm is measured. The measurement is repeated with the PRIFO locked and the ratio of the transmitted intensities is designated as NPTR (the Normalized Power TRansmitted through the arm cavity).

$$NPTR = \frac{I_{\text{in}} \frac{1}{2} B_{\text{PRM}} B_X T_X}{I_{\text{in}} \frac{1}{2} T_{\text{RM}} B_X T_X} = \frac{B_{\text{PRM}}}{T_{\text{RM}}} \quad (3.41)$$

where  $B_X$  and  $B_{\text{PRM}}$  are the build up factors in the arm and the recycling cavity,  $T_X$  and  $T_{\text{RM}}$  the (power) transmission coefficients of the arm end mirror and of the recycling mirror.

The field in the arm is given by

$$E_X = E_{\text{incident}} \sqrt{B_X} = \sqrt{I_{\text{in}} \frac{1}{2} B_{\text{PRM}} B_X} \quad (3.42)$$

The measured value of NPTR was 1400 and  $T_{\text{RM}} = 0.03$  and therefore  $B_{\text{PRM}} = 42$ . For  $B_X$  I can use

$$\frac{t_{\text{ITM}}^2}{(1 - r_{\text{ITM}}r_{\text{ETM}})^2} = 139. \quad (3.43)$$

Thus for  $I_{\text{in}} = 1$  W

$$E_X = 54 \text{ (W}^{\frac{1}{2}}\text{)} \quad (3.44)$$

The modulation index during this period was  $\Gamma = 0.45$ , so that

$$J_0(\Gamma) = 0.95 \quad J_1(\Gamma) = 0.22$$

Therefore the carrier field of Eq(3.44) must be multiplied by 0.95 and the sideband field at the AS port is

$$E_S = 0.22 \text{ (W}^{\frac{1}{2}}\text{)} \quad (3.45)$$

In my numerical program, the term driving the audio sideband

$$xkE_0 \quad (3.46)$$

was set to unity, as was the r.f. sideband field. Here  $k$  is the carrier wave vector

$$k = \frac{2\pi}{\lambda_{\text{light}}} = 5.91 \times 10^6 \quad (3.47)$$

Using the results of Eqs(3.39, 3.47, 3.44 and 3.45) the output of the program must be multiplied by

$$(8.04 \times 10^{-16})(5.91 \times 10^6)(54 \times 0.95)(0.22) = 5.36 \times 10^{-8} \quad (3.48)$$

to give the optical power at the demodulation frequency. Finally multiplying by the factor of Eq(3.40) I obtain the normalization that leads to signal voltage

$$N = 6.30 \times 10^{-7}. \quad (3.49)$$

Eq(3.49) is valid for 1 V drive and 1 W input.

I compare this normalization with the data of Fig. 3.20. Since the data gives the transfer function, it already assumes 1 V drive. The input power was estimated at 0.9 W<sup>7</sup> so that the calculated normalization factor should be

$$N = 5.68 \times 10^{-7} \quad (3.50)$$

The observed normalization instead is:

$$N = 2.82 \times 10^{-6} \quad (3.51)$$

In view of the uncertainty in the mirror motion given in Eq(3.39) due to nearby test mass resonances and the long extrapolation in Eq(3.38) the factor of four between the calculated and observed values is acceptable. I also stress that the same normalization is used for both the ASQ and ASI quadratures.

### 3.3 Sensitivity @ 37.52 kHz

So far I have shown “transfer functions” obtained by sweeping the frequency at which the ITM was excited, or of the sidebands injected around  $f_{\text{fsr}}$ . To establish the sensitivity of the PRIFO to a G.W. (i.e. a parametric perturbation) I drive the ITM at a fixed frequency and record the FFT at the AS port. This is shown in Figure 3.23 where the ITM was driven at  $f_{\text{fsr}}$ , and the AS\_I quadrature was monitored.

I note that the signal and noise levels are

$$V_S = 87 \mu\text{V} \quad V_N = 40 \text{ nV}$$

---

<sup>7</sup>As per elog entry 11/25/2002 by Nergis and PeterF

This signal level is in agreement with that displayed in Fig 3.20. The bandwidth of the data acquisition was  $50 \text{ Hz} / (800 \text{ channels}) = 0.0625 \text{ Hz}$  so that the noise spectral density is

$$S_N = 0.16 \mu\text{V}/\sqrt{\text{Hz}}$$

This noise level is in agreement with other measurements and corroborated by [62]. When the E/O shutter was closed from 7% to 3% the noise density decreased further to  $S_N = 0.11 \mu\text{V}/\sqrt{\text{Hz}}$ , an indication that not all the noise was from the electronics.

The signal responds linearly to the ITM drive as shown in Fig. 3.24 for both quadratures. One can therefore extrapolate to very small drive values, being limited only by the noise floor. Since 1 V drive corresponds to  $x_0 = 8 \times 10^{-16} \text{ m}$  drive, the strain in the arm is  $h = x_0/L = 2 \times 10^{-19}$  for 1 V drive. Assuming optimal orientation of the G.W., both arms will contribute. Thus signal to noise unity ( $S/N = 1$ ) is reached when

$$h = 4.5 \times 10^{-23} / \sqrt{\text{Hz}} \quad (3.52)$$

This level of strain can therefore be achieved in a single measurement with  $\text{BW} = 1 \text{ Hz}$ . Excluding DAQ overhead, 86,400 such measurements can be averaged in a day, reducing the noise fluctuations so that  $S/N = 1$  is reached for

$$h = 1.5 \times 10^{-25} / \sqrt{\text{Hz}} \quad (3.53)$$

This low value for the strain is valid only at  $f_{\text{fsr}}$  and falls off as the frequency is shifted from the resonant value.

If the G.W. signal is continuous in frequency, as is the case for the stochastic background, the response will have the typical shape of Fig. 3.20. Averaging over the direction of incidence and polarization for the stochastic background reduces the sensitivity by a factor of 5.3 as calculated by D.Sigg [66].



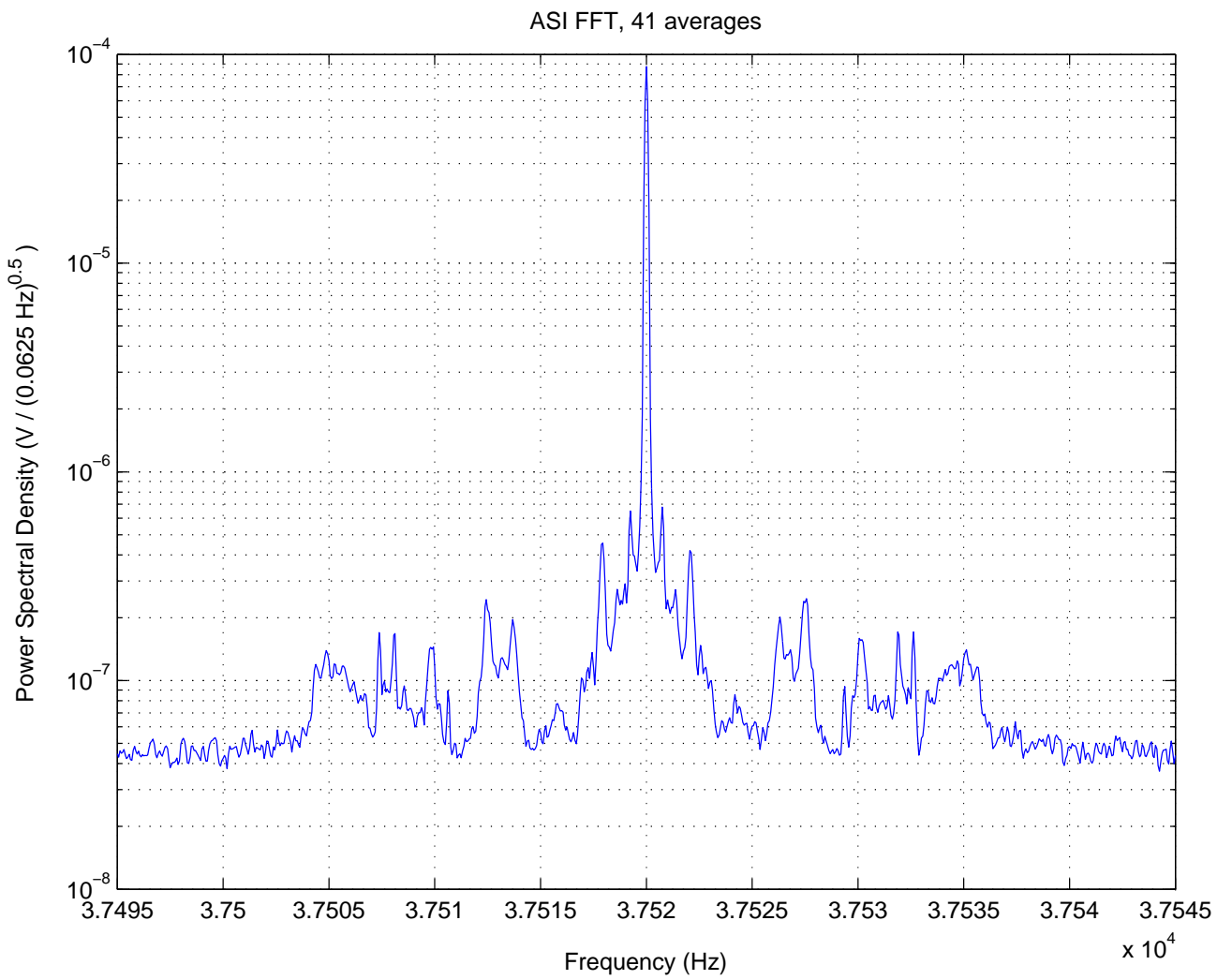


Figure 3.23: FFT of ASI with mass excitation of 1V<sub>pk</sub> @ 37.52 KHz

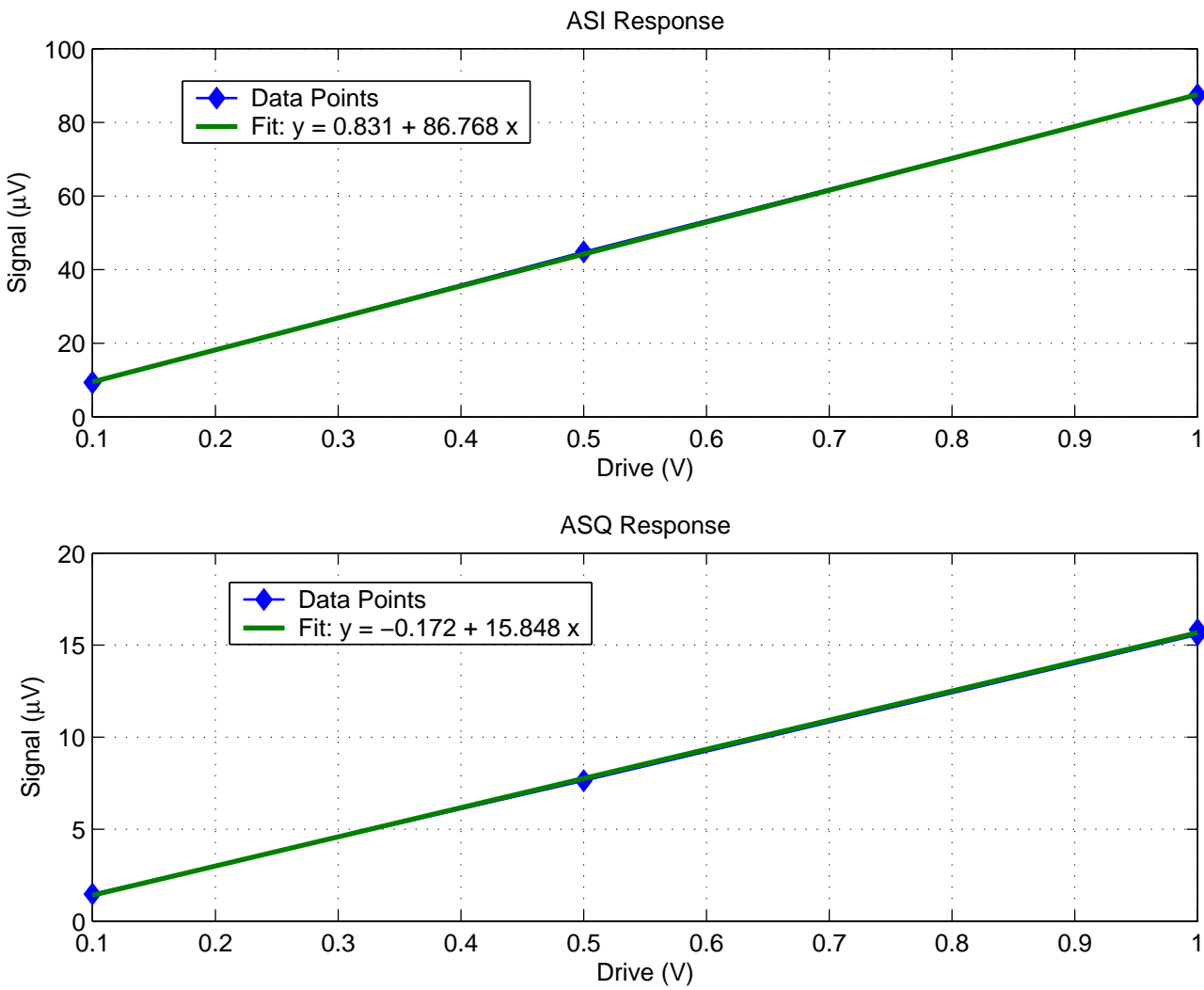


Figure 3.24: Response of the IFO to TTM excitation at varying magnitudes in both I and Q quadratures.

# Chapter 4

## Mechanical Noise

### 4.1 Active Measurements

There are several sources of noise within the IFO; as I am primarily interested in frequencies at or near the free spectral range I will confine my interest of mechanical noise sources to those observed in that range, such as internal test mass resonances. Other noise sources which are observable near the FSR frequency, such as phase noise and electronics noise, and their effect on the detection of a stochastic signal are discussed in Chap. 5.

The optimum method for characterizing internal test mass resonances is through a process known as “ring down” measurements. This involves exciting the resonance by driving the mass at a specified frequency (as close to the resonance frequency as possible) for a short time and observing the response as the resonance damps naturally. For a LIGO test mass the driving excitation is done through one or more of the positioning magnets and the response is measured through the feedback signal to keep the cavity on resonance. This allows one to accurately measure both the  $Q$  (quality factor) of the resonance

and its frequency to a high degree of accuracy in a reasonable amount of time. I assisted Gregg Harry with several measurements of this type in 2002. The modes measured at that time are too low in frequency to be of interest here, however, the measurements were helpful for calculations of non-homogeneous loss contributions to thermal noise [32].

A different method for characterizing the internal test mass resonances is by a “swept sine transfer function” measurement. The problem with this measurement method is that the width of the resonance is quite narrow, often smaller than the frequency step of a swept sine measurement. I did observe two resonances near the FSR frequency while doing swept sine measurements. This was possible because at the time I was investigating the narrow common mode response and was consequently sweeping very slowly through a small frequency range. The results of these measurements are presented here.

### 4.1.1 Test Mass Internal Resonances

The test masses are subject to elastic oscillations due to the finite temperature of the environment, what is referred to as Brownian motion. Such oscillations induce a phase shift on the incident (and stored) LASER beam and thus contribute a “random” noise at the read-out channel, in particular at low frequencies. The motion of the mirror surfaces can be expanded in the normal modes (resonances) of the test mass, as detailed by Gillespie and Raab [30, 60]. The individual mode  $n$  contributes to the displacement power density at the frequency  $f = \omega/(2\pi)$ .

$$S_{xn}(f) = \frac{4k_B T}{\alpha_n m \omega} \left[ \frac{\omega_n^2 \phi_n(\omega)}{(\omega^2 - \omega_n^2)^2 + \omega_n^4 \phi_n^2(\omega)} \right] \quad (4.1)$$

where  $k_B, T$  are the Boltzmann constant and temperature;  $\omega_n$  is the resonant angular frequency of the mode,  $m$  the mass of the optic and  $\omega = 2\pi f$ ;  $\alpha_n$  is an

effective mass coefficient which accounts for the coupling of that particular mode to the LASER beam. The coefficient  $\alpha_n$  can vary between  $10^{-2} - 10^1$ .  $\phi_n(\omega)$  is the loss function, and on resonance,  $\phi_n(\omega_n) = 1/Q_n$  where  $Q_n$  is the quality factor of the mode.

At frequencies much lower than  $\omega_n$ , one can sum all the modes to find the total displacement power density [30, 60].

$$S_x(f) \simeq \sum_n \frac{4k_B T}{\alpha_n m \omega_n^2} \frac{\phi_n(\omega)}{\omega} \quad \left( \frac{\text{m}^2}{\text{Hz}} \right) \quad (4.2)$$

Simulations by Gillespie and Raab find that at  $f = 100$  Hz the LIGO 4km IFO has

$$S_x(100 \text{ Hz}) \simeq 8 \times 10^{-40} \text{ m}^2/\text{Hz}$$

Similar results were obtained by Y. Levin [42] using a more general technique.

Fig.4.1 shows the response of the full IFO to a frequency sweep of ITMX. The same data were presented in Fig. 3.19 of Sec. 3.2.3 where parametric conversion was discussed [16]. In that case however the data was cropped at 37.7 kHz to exclude the two peaks appearing at 37.804 and 37.971 kHz. I attribute these peaks to internal resonances (modes) of the optic driven by the exciting force applied to the back plane.

To fit the data I model the test mass as a simple harmonic oscillator [30, 60] in which case the force to displacement transfer function is [49]

$$H(f) = \frac{1}{[1 - (\omega/\omega_n)^2 + i(\omega/\omega_n)\phi_n(\omega)]} \quad (4.3)$$

Replacing  $\phi_n(\omega)$  by  $1/Q$  and introducing a normalization factor  $N/Q$ , I write for the measured transfer function (Volts drive to Volts signal)

$$H(f) = \frac{N/Q}{1 - (\omega/\omega_n)^2 + (i/Q)(\omega/\omega_n)} \quad (4.4)$$

On resonance  $|H(f_n)| = N$  independently of the  $Q$ -value.

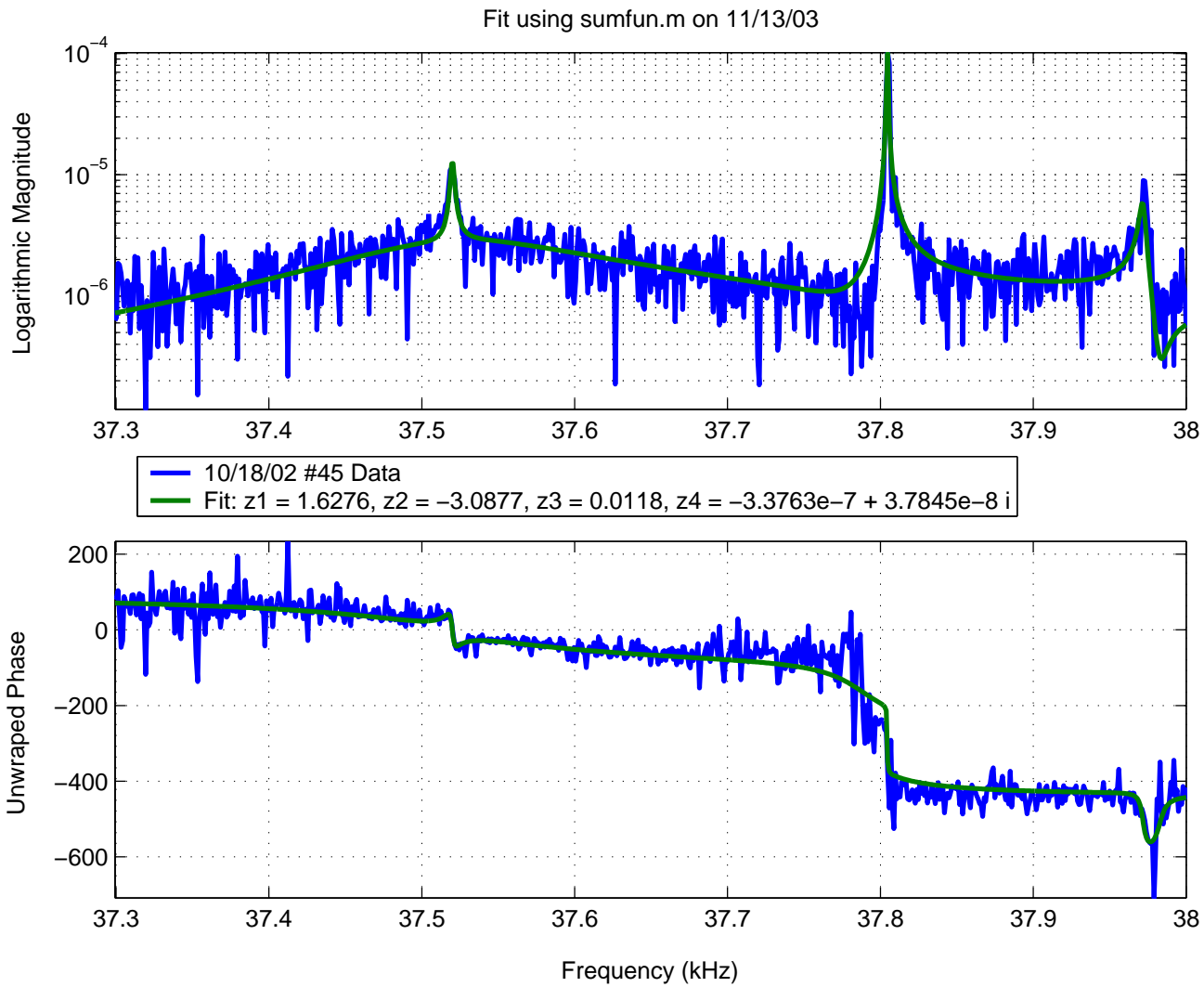


Figure 4.1: Swept Sine Response to FTM excitation in full PRIFO configuration.

While Eq.(4.4) is suitable for fitting the data, the real  $Q$ -value cannot be extracted because of the relatively low frequency resolution with which the data was acquired. Typically I expect  $Q \sim 10^6$  to  $10^7$  which implies a full width of .04 to .004 Hz as compared to the resolution of the data  $\Delta f = 1$  Hz. Thus the values of  $Q$  returned by the fit are lower limits of the real  $Q_n$ .

The two resonance peaks were first fit independently to Eq.(4.4) in order to determine the corresponding values of  $N$  and  $Q_{\min}$ . Then the two resonances were combined with the parametric conversion response of the IFO [16] to produce an overall fit in the range 37.3 to 38.0 kHz. In this case each of the internal resonances was given an adjustable phase, and an overall noise floor was added as well. The results of the fits are shown in Tables 4.1 and 4.2.

Table 4.1: Test Mass Internal Resonances

Central Frequency $f$ (Hz)	$Q_{\min}$	Normalization $N$
$37804.5 \pm 0.5$	$1.03 \times 10^5$	$1.87 \times 10^{-4}$
$37971.7 \pm 0.5$	$1.00 \times 10^4$	$5.65 \times 10^{-6}$

Table 4.2: Overall Fit Parameters

Resonance #1	Phase	$-171^\circ$
Resonance #2	Phase	$1^\circ$
Noise Floor	Phase	$174^\circ$
Noise Floor	Magnitude	$3.4 \times 10^{-7}$
Overall Additive	Phase	$93^\circ$

As can be seen in Fig. 4.1 these parameters produce an excellent fit not only to the magnitude of the response but also to the measured phase over the entire frequency band.

## 4.2 Passive Measurements

When using the instrument of a large collaboration for a non-standard investigation it is often not possible to perform active measurements on the instrument. However, it is often possible to obtain a great deal of information from passive measurements. Measurements of this type take longer and this leads to the problem of validating the consistency of various parameters throughout the period of the measurement. For this reason the LIGO operating procedures specify time periods to be set aside as “Science Runs” during which extensive effort is made to maintain consistent running of the instrument with a minimal change to the operating parameters. When attempting to measure the parameters of a mechanical resonance, the stability of the resonance being measured is a possible problem. When I mentioned the frequency domain method of measuring these resonances to Gregg Harry he replied “I have always found this to be problematic as drifting temperature changes the normal mode frequency, and can widen the peak.”

Section 4.2.1 is an investigation into noise observed through an only partially passive measurement. In this case an active excitation was used, but not an active excitation of the resonances observed. Section 4.2.2 is a discussion of several internal test mass resonances observed by a passive measurement during a “Science Run” referred to as S3.

### 4.2.1 Up-converted Seismic and Suspension Noise

FFT’s obtained with high resolution when the test mass was driven at the fixed frequency of 37.52 kHz are presented in Figs. 4.2, 4.3 and 4.4. As expected they show a strong response at the driving frequency since it corresponds to the fsr (free spectral range) of the IFO. However the FFT’s also exhibit sidebands



around the main peak. The symmetric appearance of the sidebands indicates that they are due to low frequency oscillations up-converted to near the driving frequency.

If the amplitude of the low frequency oscillation (at  $f_\beta$ ) is  $x_\beta$  then the sidebands will appear at frequencies ( $f_0 \pm f_\beta$ ) and with a relative amplitude  $A_\beta/A_0 = 2kx_\beta$ . Here  $f_0$  is the driving frequency and  $A_0$  the amplitude of the response at  $f_0$ ;  $k$  is the wavenumber of the carrier light  $k = 2\pi/\lambda$ . I have assumed that the low frequency oscillations are independent of the high frequency excitation and that the mixing occurs at the detection point; recall that the diode signal is proportional to  $|E_{\text{total}}|^2$ .

While all three FFT's exhibit low frequency sidebands the details of the spectrum differ. The data in Figs. 4.2 and 4.3 were taken in December 2002; Fig. 4.2 with a 0.5 V drive, 0.125 Hz bandwidth and 483 averages. Fig. 4.3 with a 1 V drive, 0.0625 Hz bandwidth and 41 averages. The data in Fig. 4.4 were obtained in October 2002 and correspond to different operating conditions of the IFO; the drive was 2 V, the bandwidth 0.0625 Hz and only 11 averages were taken. The discrete lines at a fraction of a Hz and at a few Hz are identified as oscillation modes of the suspension, while the broader features, especially apparent in Fig. 4.3, are attributed to seismic noise.

To provide some quantitative measure of these data I have fitted the spectra as follows: A Gaussian was used for the central peak since its width is instrumental, and each sideband was fit by a Lorentzian [Eq.(4.4)]. In addition a noise floor was included. In Fig. 4.3 the central peak was fitted by a double Gaussian in order to account for some of the low frequency seismic noise. The quality of the fits can be judged better by the log-log plots shown in Figs. 4.2B, 4.3B and 4.4B. The results of the fits are summarized in Table 4.3 where I give the

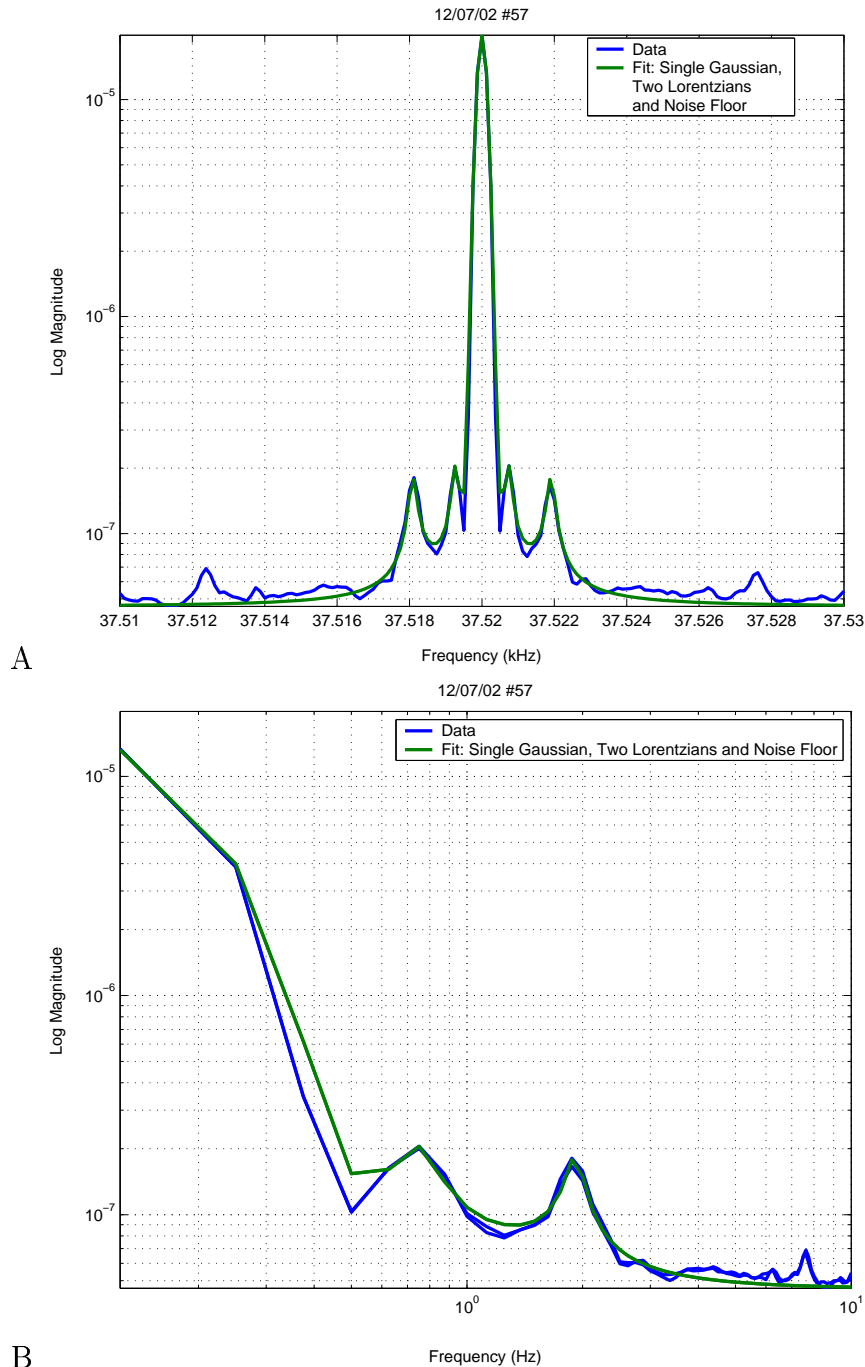


Figure 4.2: FFT of ASI with mass excitation of  $0.5V_{pk}$  @ 37.52 kHz taken in December of 2002. A) Linear frequency; B) Log frequency away from 37.52 kHz plotted vs. magnitude

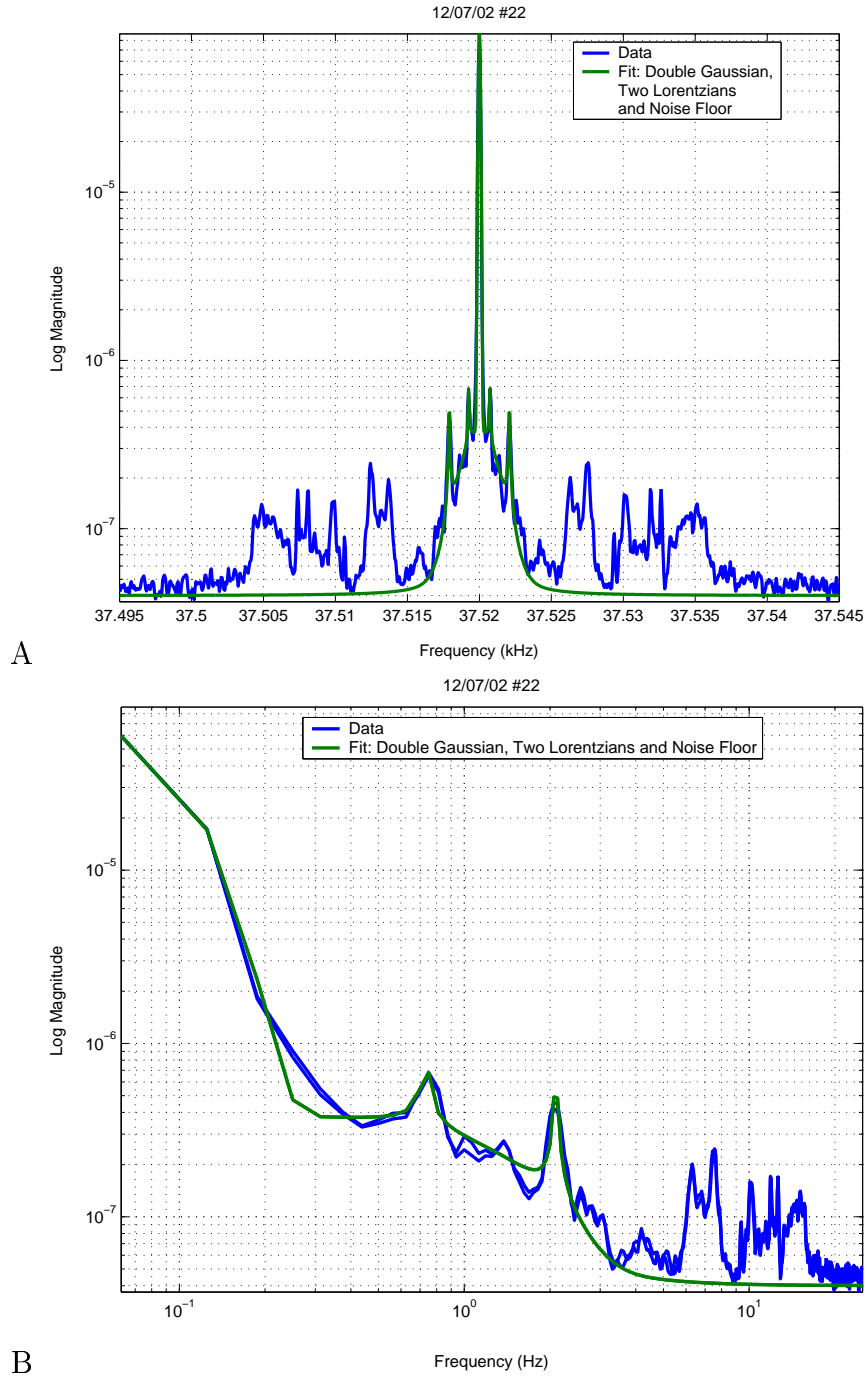


Figure 4.3: FFT of ASI with mass excitation of  $1.0V_{pk}$  @ 37.52 kHz taken in December of 2002. A) Linear frequency; B) Log frequency away from 37.52 kHz plotted vs. magnitude

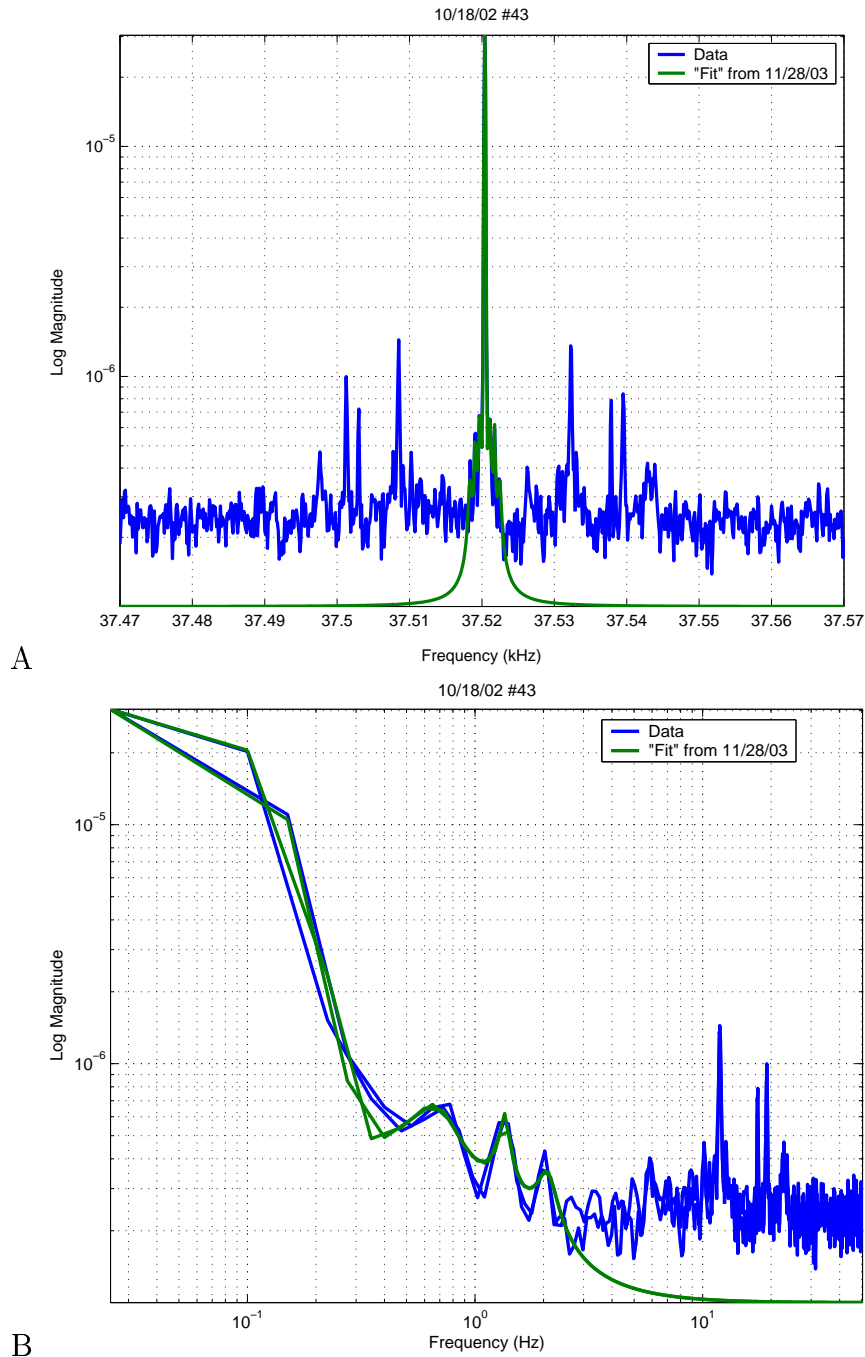


Figure 4.4: FFT of ASI with a 2V excitation @ 37.52 kHz taken in October of 2002 (at this time the drive was not calibrated). A) Linear frequency; B) Log frequency away from 37.52 kHz plotted vs. magnitude

sideband offset frequency and relative amplitude separately for each of the three spectra.

The peak at  $\sim 0.75$  Hz is clearly the pendulum mode of the suspension which is known to be at 0.71 Hz [41]. The peak around 2 Hz may be the third harmonic of the above resonance; possibly the peak at 1.3 Hz seen in Fig. 4.4 is the second harmonic. The prominent peaks in Fig. 4.4 at  $\sim 11$  Hz and  $\sim 19$  Hz can be identified with the bounce mode of the suspension which is located at 11.9 Hz and the roll mode, expected to be at 17.5 Hz [41]. If I use an average value of the relative amplitude as  $A/A_0 \simeq 10^{-2}$  I conclude that  $x_\beta \simeq 8 \times 10^{-10}$  m which is of the order of the thermal excitation of such low frequency modes [using Eq.(4.1) and  $Q \simeq 10^4$ ].

Finally I consider the quasi-continuous noise level extending out to  $\sim 15$  Hz that is most pronounced in Fig. 4.3. I believe that it is due to seismic noise exciting the mirror suspension as well as tables and chambers on which the optics are mounted. Support for this interpretation is provided by Fig. 4.5 which shows low frequency measurements made with a seismometer (top) in the LVEA and of the motion of the Beam Splitter, ITMX and ITMY (bottom). The similarity of this spectrum with the sidebands in Fig. 4.3 is notable, including the cut-off at  $\sim 15$  Hz which is probably due to vibration suppression or active feedback.

### 4.2.2 Test Mass Internal Resonances

When analyzing the contribution to thermal noise of the IFO from internal test mass resonances one would hope for a combination of measurements both active and passive. As all of the resonances are excited by thermal contact (primarily radiative with a small conductive contribution) to the heat bath of the outside environment at a relatively constant temperature, the amount of energy

Table 4.3: Up-converted Noise

	<u>From fig.4.2</u>	<u>From fig.4.3</u>	<u>From fig.4.4</u>
$f_1(\text{Hz})$	0.75	0.73	0.61
$A_1/A_0$	$7 \times 10^{-3}$	$7.9 \times 10^{-3}$	$1.6 \times 10^{-2}$
$f_2(\text{Hz})$	--	--	1.35
$A_2/A_0$	--	--	$1.3 \times 10^{-2}$
$f_3(\text{Hz})$	1.91	2.09	2.01
$A_3/A_0$	$7 \times 10^{-3}$	$8.3 \times 10^{-3}$	$7 \times 10^{-3}$
$f_4(\text{Hz})$	7.60	--	--
$A_4/A_0$	$10^{-3}$	--	--
$f_5(\text{Hz})$	--	--	11.90
$A_5/A_0$	--	--	$3.8 \times 10^{-2}$
$f_6(\text{Hz})$	--	--	17.44
$A_6/A_0$	--	--	$2 \times 10^{-2}$
$f_7(\text{Hz})$	--	--	19.13
$A_7/A_0$	--	--	$2.3 \times 10^{-2}$

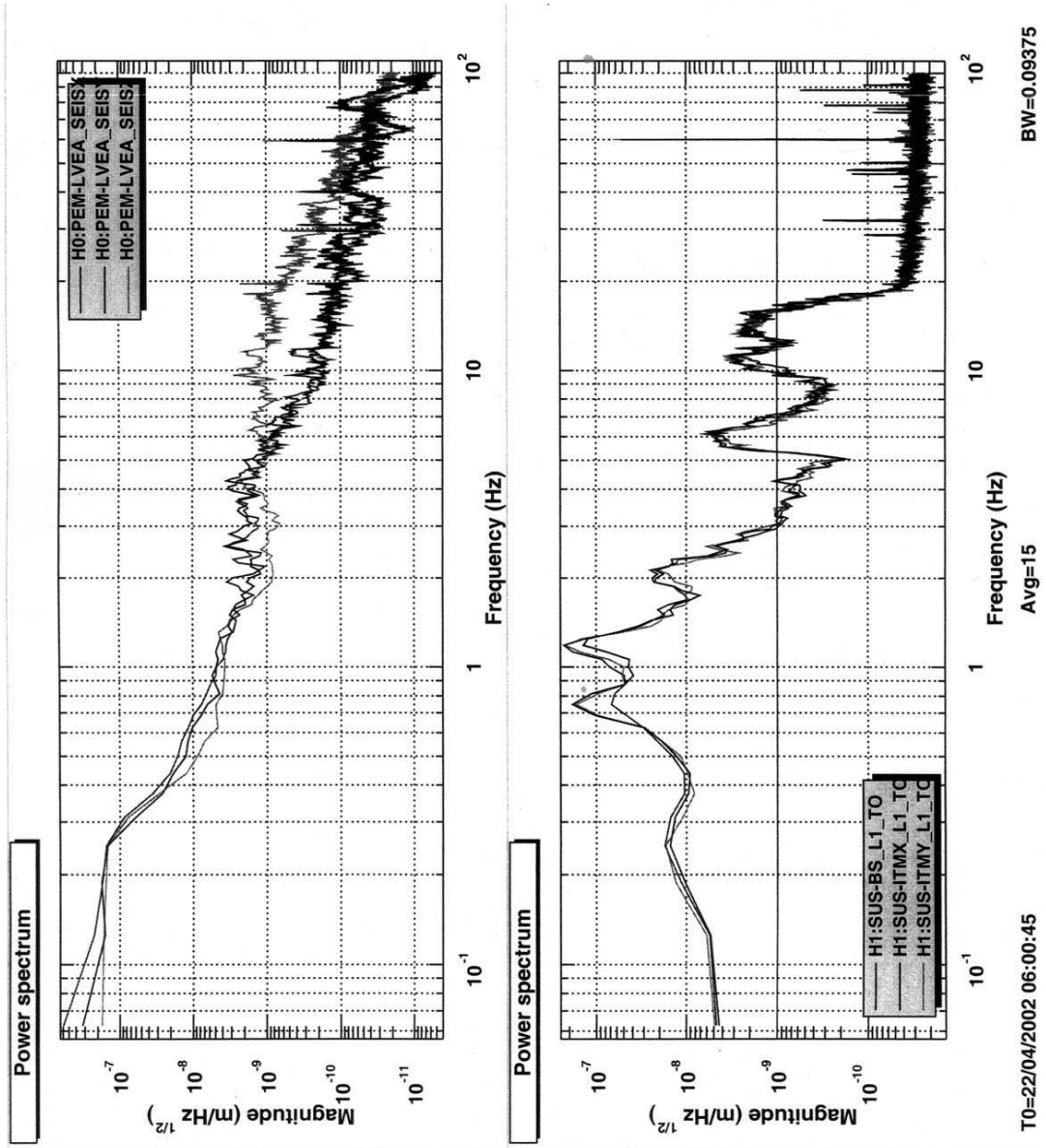


Figure 4.5: Seismic Noise Spectrum

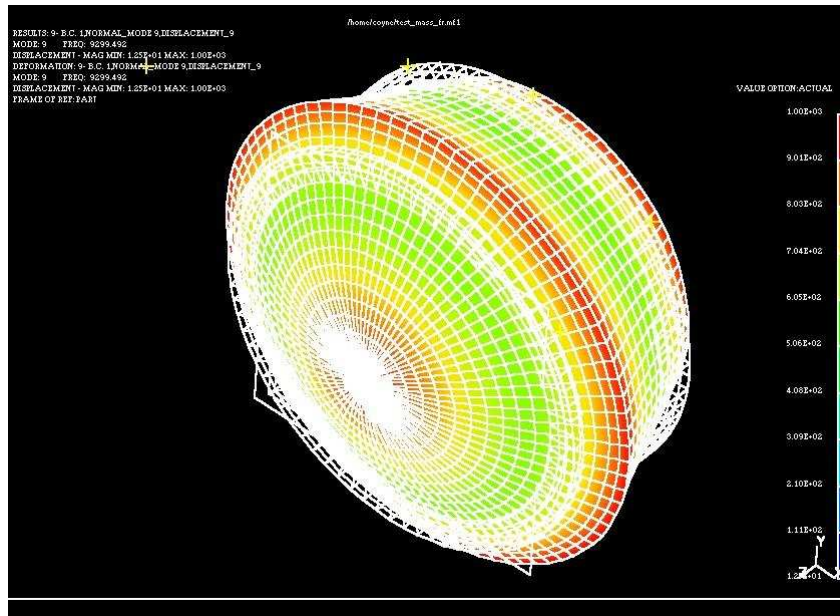


Figure 4.6: Mode 2

contained in each resonant mode is known. Knowing both this, as well as the frequency and the Q of the resonance, it is possible to calculate the amplitude of the mechanical mode. Initially one might believe that this is sufficient information to calculate the mode's contribution to noise detected by the IFO. Further thought will reveal that the noise contribution is strongly dependent on the mode shape and the overlap function with the LASER light. If the mass resonance mode is one in which the center of the optic does not move, and the LASER light is centered on the optic, then there will be very little coupling between the noise in the mode and the noise detected by the IFO system. This is discussed in the literature, for example by Gillespie and Raab [30] as well as by Bondu and Vinet [10]. The noise dependence on the overlap function is also somewhat obvious when visualizing the mode shapes. For example compare Figs. 4.6 and 4.7 as calculated by Dennis Coyne using finite element analysis [22].

During the S3 run at the end of 2003 and beginning of 2004 a significant



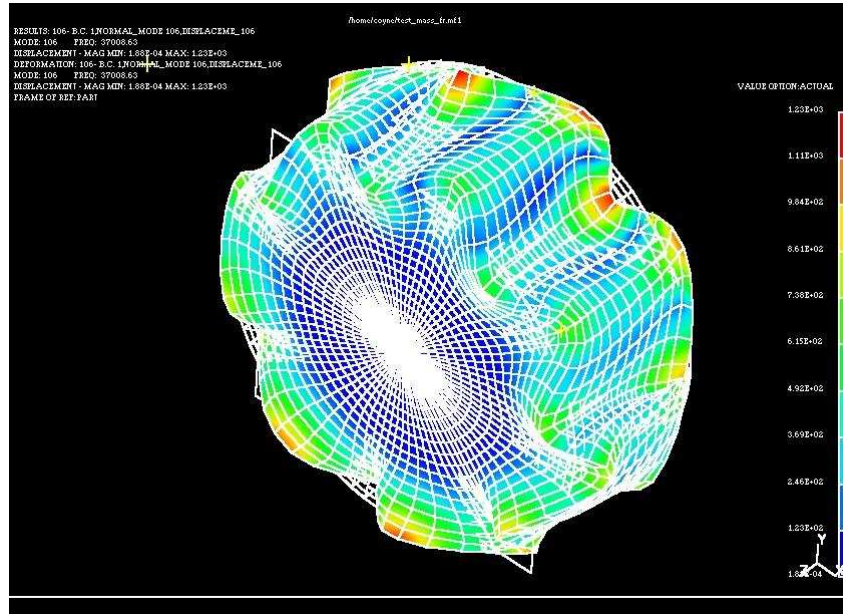


Figure 4.7: Mode 99

amount of quiet running data was taken and stored for future analysis which allowed for passive measurements of the mechanical resonances near 37.5 kHz. To record the frequency spectrum in the vicinity of the FSR a lock-in detector was used to heterodyne the AS\_Q signal (AS2\_Q monitor port). The local oscillator was set at 37.0 kHz and the output was filtered and digitized at 2048 samples per second to be written in the DAQ (Data Acquisition) stream [46]. Each frame contains 16 seconds of data. The results presented here are based on 12.4 hours of a continuous lock of the Hanford 4k IFO on December 12th, 2003 [51]. No image rejection was used so the data represent not only the frequency range of interest, from 37.0 to 38.024 kHz, but also from 37.0 to 35.976 kHz.

The data stream includes significant “glitches” as can be seen from a typical segment of the time series displayed in Fig.4.8. To remove these anomalous entries I replaced data points with amplitude less than  $-900$  counts by the mean value of the time series (a more accurate method was not used due to

limitations on computation time). This resulted in loss of 1.1% of the data points. The corrected data in each frame was Fourier analyzed without and with a (Hanning) window. The resulting FFT spectra were similar and I chose to use the Hanning window with 0% overlap. The magnitude of the Fourier amplitudes was *averaged* over the  $\sim 2,800$  frames to produce the spectrum shown in Fig. 4.9.

The spectrum extends from 37.0 kHz to 38.024 kHz and one recognizes the effects of the filter used by the lock-in detector at the upper limit of the range. Note also the pronounced sequence of odd harmonics (as well as some even harmonics at lower amplitude) of the line frequency. These lines are most probably introduced by the digitizer and can be removed in software. The other distinctive features of the spectrum are narrow lines which can be clearly identified with test mass resonances. In fact, the lines at 37.804 kHz and 37.972 kHz correspond exactly to the measured resonances of ITMX (see Table 4.1). That the test mass resonances come in nearly degenerate groups of four is to be expected. This, because there are four different test masses that predominately contribute to the differential signal, each at a slightly different frequency. Finally, the spectrum shows a small but distinct dispersive feature at the exact fsr frequency. This, I believe, is due to laser frequency (phase) noise which is discussed later. Here I will concentrate on analyzing the data to characterize the peaks which are most likely due to internal test mass resonances.

One of the difficult aspects of passively measuring resonances is in selecting the proper bandwidth for the Fourier transform (or FFT) of the time series. If the bandwidth is too large (relative to the resonance width), then one cannot resolve the resonance accurately. If the bandwidth is too small, then the resonance does not remain coherent over the extent of the time series and the peak does not show up in the FFT. As the overall sample was fixed, increasing the resolution of the

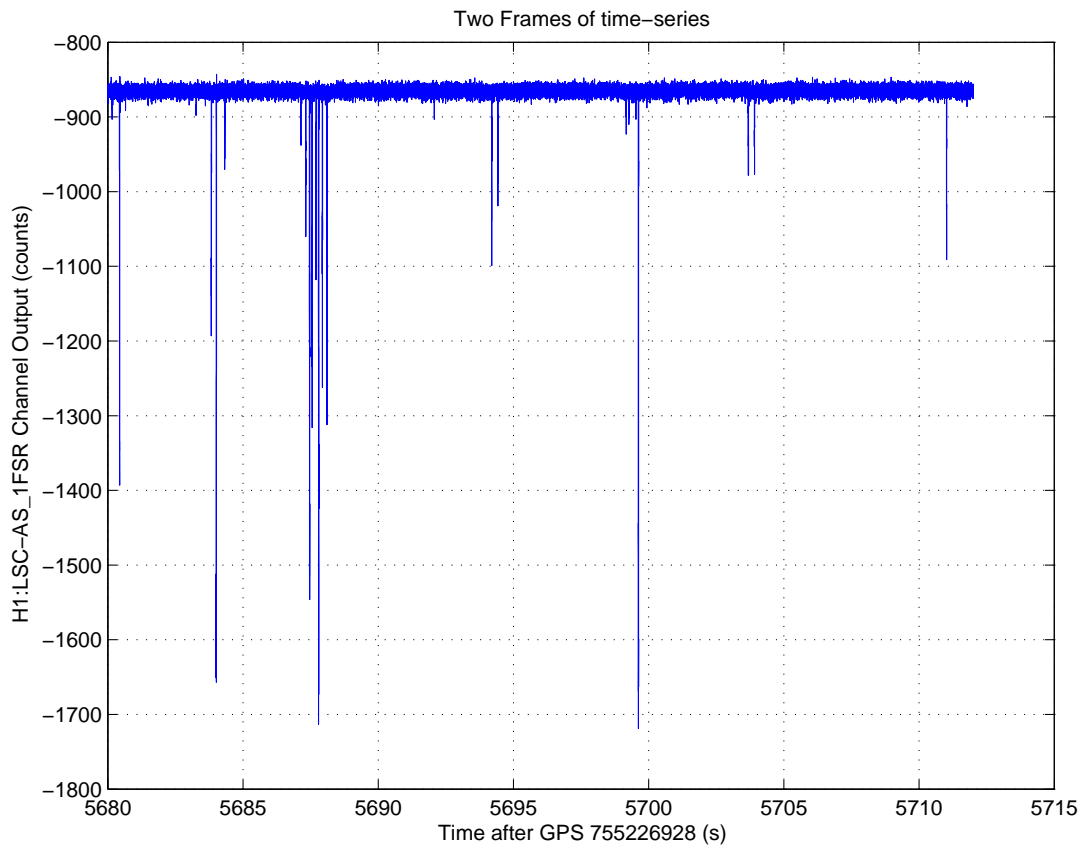


Figure 4.8: Typical sample of the time-series of channel H1:LSC-AS\_1FSR.

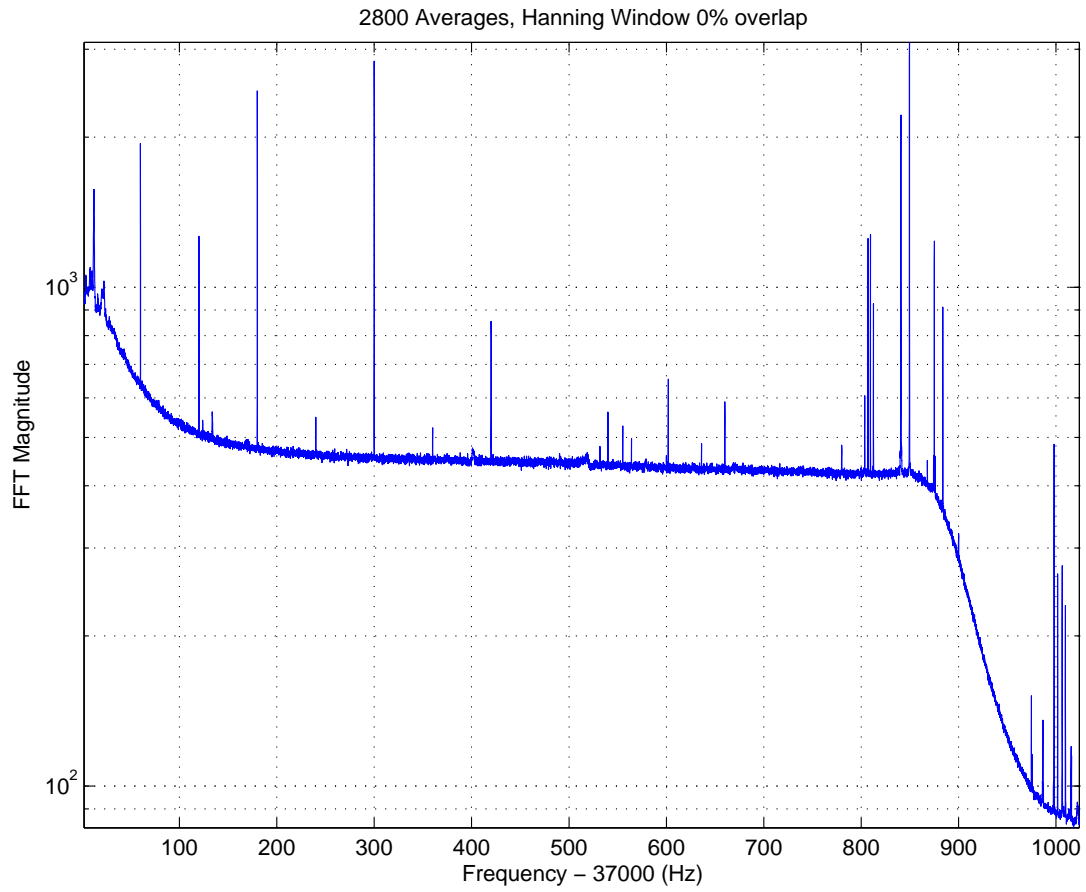


Figure 4.9: FFT Spectrum (magnitude) for 2800 averages. BW resolution 0.0625 Hz.

FFT implies a reduction in the number of averages. As a result, I took five sets of averages with different bandwidths: 2800 averages at 1 frame per FFT (BW = 0.0625 Hz, shown in Fig. 4.9), 280 averages at 10 frames per FFT (BW = 0.00625 Hz), 140 averages at 20 frames per FFT (BW = 0.003125 Hz), 70 averages at 40 frames per FFT (BW = 0.0015625 Hz) and 35 averages at 80 frames per FFT (BW = 0.00078125 Hz). This allowed for a reasonably accurate measurement of the resonance characteristics as well as a consistency check. Figure 4.10 is an example of a high resolution FFT and a fit to the measured mechanical resonance. I have no explanation for the sidebands that appear in Fig.4.10 and which are separated by 0.0685 Hz. Most probably this is an instrumental effect introduced by the lock-in detector used for the down-conversion. Measured values are shown in Table 4.5 and are obtained by the method discussed in section 4.1.1 using Eq. 4.4. The first group of four resonances (37803 - 37812 Hz) are sufficiently close to the previously observed resonance (37805 Hz in sec. 4.1.1) that I conclude that they are the same resonance mode with slight frequency differences caused by differences in test masses. In particular some differences between test masses are the way suspension offsets and drive magnets are mounted as well as wedge angle differences between ITMs and ETMs. The indicated higher frequencies are assumed (at this time) to be internal test mass resonances as no evidence exists to the contrary. Table 4.4 shows the modes calculated by Dennis Coyne [22] in the region of 37.5-39 kHz.

As this channel (H1:LSC-AS\_1FSR) is uncalibrated, the primary calibration of interest is the level of contribution from the mechanical resonances at the FSR frequency. The first step is to determine a common bandwidth at which to specify the parameters. For this, I use the single frame per FFT shown in Fig. 4.9 as it is the bandwidth at which I will perform stochastic background

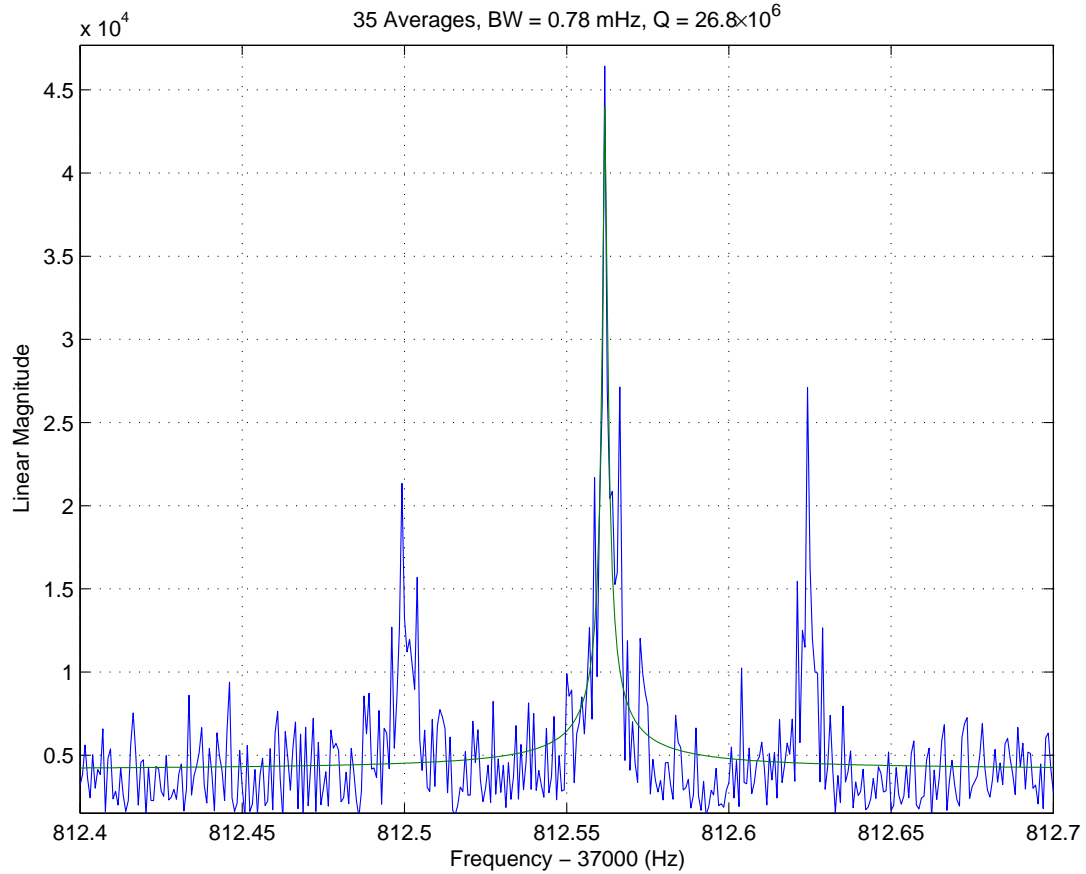


Figure 4.10: High resolution,  $BW = 0.78125 \times 10^{-3}$  Hz, spectrum in the region of a thermally excited resonance at  $f = 37,812.5618$  Hz. The fit is also shown and gives  $Q = 2.68 \times 10^7$ , or full-width at half-power  $\Delta f = 1.41$  mHz. The presence of the two sidebands is not understood.

Table 4.4: Test Mass Modes prediction [22]

Mode Number	Frequency (Hz)
105	37009
106	37009
107	37296
108	37296
109	37570
110	37570
111	37749
112	37749
113	37806
114	37806
115	38497
116	38567
117	38569

analysis in Chap. 5.

Complete comparison using a common bandwidth could pose a problem as quantities which are invariant in the regime with a bandwidth smaller than the resonance width are not invariant when the bandwidth is larger than the resonance width. Thus different conversion calculations would be needed near the resonance frequencies than would be needed far away from the resonance (over frequency ranges more than a few resonance widths away from the resonance frequency). If, however, I limit my comparisons to areas of the spectrum which are several resonance widths off the resonance, this is no longer a problem.

The FFT routine within MATLAB returns quantities which I shall label  $A_j^\alpha$  where  $j$  indicates the bin number of the FFT. Each bin of the FFT can be associated with a specific frequency when given the bandwidth  $BW^\alpha$  associated with the FFT. A superscript  $\alpha$  refers to the parameters associated with each FFT, allowing me to indicate differing FFTs. Before I can get at the spectral density (which is scale invariant) I need to normalize the values output by the

Table 4.5: Parameters for Passively Measured Mechanical Resonances.

Frequency (Hz)	Q ( $\times 10^6$ )	Peak Value ( $\times 10^3$ /sqrtHz)
80 Frames per FFT		
—	—	—
37806.9548	16.0	35.7
37809.4857	13.1	41.3
37812.5618	26.9	40.1
37840.9297	0.8	26.9
37849.6636	5.0	75.0
37875.0699	9.1	36.2
37883.7849	11.9	25.5
40 Frames per FFT		
—	—	—
37806.9549	15.3	23.8
37809.4827	16.6	28.3
37812.5616	18.7	22.6
37840.9300	0.7	18.3
37849.6637	5.3	53.2
37875.0697	10.6	28.9
37883.7848	9.0	16.2
20 Frames per FFT		
37803.5942	0.4	1.3
37806.9568	6.2	8.5
37809.4836	6.1	13.5
37812.5645	8.0	9.4
37840.9255	0.6	12.4
37849.6612	3.7	30.7
37875.0689	6.8	15.1
37883.7837	8.9	10.3
10 Frames per FFT		
37803.5958	0.4	0.9
37806.9670	2.6	4.4
37809.4898	3.4	6.5
37812.5706	3.8	3.9
37840.9172	0.5	7.8
37849.6529	1.0	13.9
37875.0670	7.3	11.3
37883.7811	4.8	5.3



MATLAB FFT routine using

$$B_j^\alpha = \frac{A_j^\alpha}{N/2} = \frac{A_j^\alpha}{R_s} BW^\alpha \quad (4.5)$$

where  $N$  is the total number of points, which is equal to the sample rate times the total time. The sample rate  $R_s$  is a constant as all of the FFTs are from the same time series (previously stated as 2048 samples per second) and the total time is simply the inverse of the bandwidth  $BW^\alpha$ . Note that the power can be written as either the square of the normalized FFT coefficient or as a simple function of the power spectral density

$$S(f) df_\alpha = \text{Power} = |B_j^\alpha|^2 \quad (4.6)$$

and therefore  $\sqrt{S(f)}$  the square root of the spectral density is given by

$$\sqrt{S(f)} = \frac{B_j^\alpha}{\sqrt{df_\alpha}} = \frac{B_j^\alpha}{\sqrt{BW^\alpha}} = \frac{A_j^\alpha}{R_s} \sqrt{BW^\alpha} \quad (4.7)$$

In the limit where the bandwidth is less than the feature width, the square root of the spectral density (given by Eq. 4.7) is independent of the chosen bandwidth. Therefore I can convert the resonance peak value from one bandwidth FFT to another by the formula

$$A_j^\beta = \frac{\sqrt{S(f)} R_s}{\sqrt{BW^\beta}} = A_j^\alpha \sqrt{\frac{BW^\alpha}{BW^\beta}} \quad (4.8)$$

For example if I designate the resonance peak value as  $A$  and specify that  $\alpha = 80$  frames and  $\beta = 1$  frame then

$$A^{1 \text{ frame}} = A^{80\text{frames}} \sqrt{\frac{1}{80}}$$

As resolution limits do not allow me to determine the resonance  $Q$  and error, I shall use the fit parameters which result in the highest  $Q$  for each resonance. As this fitting method will tend toward an underestimation of the resonance  $Q$

Table 4.6: Measured Parameters used for Mechanical Resonance Characterization

$\nu_0$ (Hz)	Q ( $\times 10^6$ )	Peak Value ( $\times 10^3$ )	Frames / FFT
37803.5942	0.38	1.32	20
37806.9548	16.00	35.66	80
37809.4827	16.58	28.33	40
37812.5618	26.87	40.12	80
37840.9297	0.76	26.89	80
37849.6637	5.26	53.25	40
37875.0697	10.62	28.88	40
37883.7849	11.90	25.45	80

rather than an overestimation, this seems an appropriate course of action. The parameters used are specified in Table 4.6 and their renormalized peak values are shown in Table 4.7.

The final step of this analysis is to establish the contribution to the spectrum at the FSR frequency (37.52 kHz) due to the various mechanical resonances. For this I assume that each resonance produces a frequency dependent motion equivalent to that of a single test mass excitation transfer function with a drive equal to the magnitude of the mechanical resonance spectral function. Thus I multiply (frequency point by frequency point) the single test mass transfer function (as obtained in sec. 3.2.2) by the magnitude of the mechanical resonance spectral function. As the magnitude of the resonance spectral function was determined through a measurement of the ambient excitation of the test mass, I re-normalize by dividing by the test mass transfer function magnitude at the mechanical resonance frequency. This results in the same peak value as measured, with an accurate measure of the contribution due to differential arm motion at the FSR frequency. The resulting transfer functions can be added (coherently or incoherently as desired) to determine the overall contribution of test mass resonances at any frequency of the measured spectrum (Fig. 4.9). This procedure is used in the

Table 4.7: Parameters used for Mechanical Resonance Characterization, Normalized to 1 Frame per FFT

$\nu_0$ (Hz)	Q ( $\times 10^6$ )	Peak Value ( $\times 10^3$ )
37803.5942	0.38	147.88
37806.9548	16.00	3986.59
37809.4827	16.58	4479.45
37812.5618	26.87	4485.07
37840.9297	0.76	3005.89
37849.6637	5.26	8418.82
37875.0697	10.62	4566.98
37883.7849	11.90	2845.54

analysis presented in section 5.4 after their combined contribution is calculated as specified in section 4.3.1.

## 4.3 Test Mass Resonance Comparison with Theory

### 4.3.1 Contributions to FSR Signal

I am interested in the contribution of the test mass resonances to the noise measured at the IFO FSR frequency (37.52 kHz). I have only characterized resonances above this frequency as resonances below this frequency will have a negligible contribution. As each resonance has been measured and its peak value re-normalized for comparison at this bandwidth (see table 4.7) the remaining task was to combine them in a plausible way to find the total contribution off resonance. First it was recognized that a vibrating test mass will have some contribution similar to a differential mass motion, as it involves motion of the surface of the optic. Therefore, a calculation was made for the IFO response to a single ETM motion in the same way that the phase noise and differential motion transfer functions were calculated. This transfer function shows the IFO response

assuming a constant magnitude motion of the test mass at different frequencies. The test mass does not move with the same magnitude at all frequencies however, the magnitude of motion can be described as a function of frequency by the magnitude of the resonance spectral function. Therefore I multiply the single test mass transfer function by the magnitude of the resonance spectral function (I do this separately for all of the measured resonances). Then, as the peak values were measured through the IFO response, I re-normalize the product to the peak value of the resonance (thus the predicted peak value is the value specified in table 4.7). As there is no physical reason for the resonances to maintain a constant phase relative to the other resonances I add the contributions from the eight resonances incoherently by multiplying each resonance spectral function by a random phase (and unity magnitude) and then summing. Finally to simulate a randomly changing phase of the total mechanical contribution relative to the LASER phase noise I take the magnitude of the sum and hold its relative phase at zero (the same as several other terms used for the fits described in Chap. 5).

### 4.3.2 Calibration and Coupling

Although the down-converted channel containing the FSR frequency information is not calibrated or validated at this time, some information (including a rough calibration) can be recovered with a minimal number of assumptions. If I assume that the noise floor of this channel is the same as the noise floor measured previously (in Chap. 3 and by others [46]) then I can translate the fit value of the differential mode into an equivalent strain due to a gravitational signal. If I further assume that the mechanical resonances measured in Chap. 4 are thermally excited and not driven in any other way, then I can ascertain the effective mass coefficients of their modes which relate the overlap of the optic's

motion with the laser spot.

First I will look at the mechanical resonances. To compare the observed resonance amplitudes with a physical model I need to express the PSD (Power Spectral Density) in absolute units<sup>1</sup>. In the region  $f_{\text{fsr}} = 37.520$  kHz the FFT coefficients have an average value

$$C_k = 430 \quad (4.9)$$

This corresponds to a PSD, at that frequency

$$\text{PSD}(f_{\text{fsr}}) = \frac{1}{\text{BW}} \frac{2|C_k|^2}{N^2} \quad (4.10)$$

Here,  $N$  is the total number of points in the record, namely the sampling frequency  $R = 2,048$  Hz multiplied by the length of the record  $T = 16$  s. The bandwidth  $\text{BW} = 1/T = 0.0625$  Hz.

Numerically

$$\text{PSD}(f_{\text{fsr}}) = 5.51 \times 10^{-3} (X_c)^2 \text{ m}^2/\text{Hz} \quad (4.11)$$

or

$$\sqrt{\text{PSD}(f_{\text{fsr}})} = 7.42 \times 10^{-2} (X_c) \text{ m}/\sqrt{\text{Hz}} \quad (4.12)$$

Where  $X_c$  is a calibration factor with dimensions of length. For this analysis I adopt (from Chap. 3 and reference [46])

$$X_c = 2 \times 10^{-17} \text{ m} \quad (4.13)$$

The eight resonances in the range 37.8 - 37.9 kHz were fitted to a Lorentzian spectral density

$$y(f) = Y \left\{ [1 - (f/f_0)^2]^2 + \frac{1}{Q^2} (f/f_0)^2 \right\}^{-1/2} \quad (4.14)$$

---

<sup>1</sup>Such an absolute calibration is not necessary to calculate the contribution of the resonances to the spectrum as was done in section 4.3.1

The fitted values of  $f_0, Q$  and  $YQ$  (the value of  $y$  at the resonance peak) are given in columns 1-3 of Table 4.8. The observed value of  $y(f)$  is related to an effective displacement of the mirror surface,  $x_{\text{eff}}(f)$ , through the transfer function for ITMX motion

$$y(f) = H_{\text{ITMX}}(f)x_{\text{eff}}(f) \quad (4.15)$$

Finally,  $x_{\text{eff}}(f)$  is related to the amplitude,  $x_{\text{sho}}(f)$ , of a s.h.o mode of the test mass through a coefficient  $\beta$  which accounts for the coupling of the particular mechanical mode to the Gaussian ( $\text{TEM}_{00}$ ) laser beam profile, or

$$x_{\text{eff}}(f) = \frac{y(f)}{H_{\text{ITMX}}(f)} = \beta x_{\text{sho}}(f) \quad (4.16)$$

The s.h.o. amplitude  $x_{\text{sho}}(f)$  can be obtained from a simple model, and on the resonance peak<sup>2</sup>

$$x_{\text{sho}}(f_0) = \sqrt{\frac{4k_B T Q}{m(2\pi f_0)^3}} \quad (4.17)$$

with  $m = 11$  kg,  $f_0 = 37.8$  kHz and  $T = 300^\circ$  K. It follows that

$$\beta = x_{\text{eff}}(f_0)/x_{\text{sho}}(f_0) \quad (4.18)$$

The values of  $x_{\text{eff}}(f_0)$  as calculated from the data using Eq.(4.16) are given in column 4 of Table 4.8 while  $x_{\text{sho}}$  is given in column 5, and  $\beta$  in column 6. The deduced values of  $\beta$  are reasonable and fall in two groups. For the first four resonances the  $\beta$ 's are similar suggesting that all four lines correspond to the same mode. The next two lines have significantly larger values indicating a different mode. The last two lines are more problematic but I note that they are on the edge of the frequency range passed by the filter in the lock-in detector. Overall, the  $\beta$ 's are of the correct order of magnitude, validating the calibration adopted in Eq.(4.13).

---

<sup>2</sup> $H_{\text{ITMX}}(f_0 = 37.8 \text{ kHz}) = 0.131$

Table 4.8: Measured Resonance Parameters

$f_0$ (kHz)	$Q$ ( $10^6$ )	$YQ/\sqrt{\text{Hz}}$ (uncalibrated)	$x_{\text{eff}}(f_0)$ ( $10^{-17}\text{m}/\sqrt{\text{Hz}}$ )	$x_{\text{sho}}(f_0)$ ( $10^{-17}\text{m}/\sqrt{\text{Hz}}$ )	$\beta$
37.8036	0.38	0.052	0.79	21	0.04
37.8066	16.0	0.69	10.5	134	0.08
37.8095	15.0	0.79	12.1	130	0.09
37.8126	27.0	0.77	11.9	174	0.07
37.8409	0.74	0.52	7.9	29	0.27
37.8497	5.1	1.45	22.1	76	0.29
37.8751	9.8	0.74	11.3	105	0.11
37.8838	10.5	0.50	7.6	109	0.07

To improve modeling of the internal test mass resonances and their contribution to the signal I would propose two things. Mirror excitation transfer function measurements (as in Chap. 3) on all of the core optics should identify which resonances are contributed by which optics. Once this is done it would be possible to perform resonance ring-down measurements (described in sec. 4.1.1) on each resonance to obtain a more accurate measure of the resonance frequency and  $Q$ . This measurement would be particularly useful as many of the measured  $Q$ 's in table 4.7 are higher than anticipated, especially given temperature broadening. Harry [31] states that “the 27 million is, by far, the highest  $Q$  reported for an in situ LIGO test mass. And the 15 and 16 million ones are about the same as the highest measured by ringdowns.” It might also be worthwhile to repeat the finite element analysis models of the optics to determine the mode shape of the pertinent resonances and perform a more detailed comparison between

measurement and prediction.



## Chapter 5

# Stochastic Gravitational Wave Signal

Stochastic gravitational background radiation is analogous to the cosmic microwave background radiation. In the several kilohertz frequency region the primary source of stochastic background should be from the Big Bang. Other sources of astrophysical origin can also contribute but should be more prevalent at lower frequencies. Examples of cosmological sources are zero-point fluctuations of the space-time metric amplified during inflation, and first-order phase transitions and decaying networks of cosmic strings in the early universe. An interesting feature of the model based on string cosmology is the prediction that the relic GW spectral density increases with the third power of frequency in certain ranges of frequency.[11] An example of an astrophysical source is the random superposition of many weak signals from binary-system inspirals, coalescent ring-downs, and supernovae. At lower frequencies, such as that of the primary region of sensitivity for the LIGO instruments, a likely astrophysical source would be the random superposition of many weak signals from binary-star systems.

## 5.1 Present Limits

The spectrum of a stochastic background is usually described by the dimensionless quantity  $\Omega_{\text{gw}}(f)$  which is the gravitational-wave energy density per unit logarithmic frequency interval [1, 2, 45], divided by the critical energy density  $\rho_c$  required to close the universe:

$$\Omega_{\text{gw}}(f) \equiv \frac{f}{\rho_c} \frac{d\rho_{\text{gw}}}{df} \quad (5.1)$$

where  $\rho_{\text{gw}}$  is the gravitational-wave energy density. The critical density  $\rho_c \equiv 3c^2 H_0^2 / 8\pi G$  depends on the present day rate of Hubble expansion  $H_0$ . A dimensionless factor  $h_{100}$  is introduced to remove the dependence on changes in the measured value of the Hubble constant

$$h_{100} \equiv H_0 / H_{100}, \quad (5.2)$$

where

$$H_{100} \equiv 100 \frac{\text{km}}{\text{sec} \cdot \text{Mpc}} \simeq 3.24 \times 10^{-18} \frac{1}{\text{sec}}. \quad (5.3)$$

Thus  $\Omega_{\text{gw}}(f)h_{100}^2$  is independent of the Hubble expansion rate. Of particular interest is the relation between  $\Omega_{\text{gw}}$  and the one-sided power spectrum of the gravitational-wave strain  $S_{\text{gw}}(f)$  in a single detector arising from the gravitational-wave signal  $h(t)$ ,

$$\lim_{T \rightarrow \infty} \frac{1}{T} \int_{-T/2}^{T/2} dt |h(t)|^2 = \int_0^\infty df S_{\text{gw}}(f) \quad (5.4)$$

Since

$$\rho_{\text{gw}} = \frac{c^2}{32\pi G} \left\langle \dot{h}_{\alpha\beta}(t) \dot{h}^{\alpha\beta}(t) \right\rangle \quad (5.5)$$

and  $h(t)$  has the space-time dependence  $h(x, t) = h_0 \cos(\omega t - \vec{k} \cdot \vec{x})$ , it follows that [2]

$$S_{\text{gw}}(f) = \frac{3H_0^2}{10\pi^2} f^{-3} \Omega_{\text{gw}}(f) = 2 \left| \tilde{h}_{\text{ST}} \right|^2 \quad (5.6)$$

where  $\tilde{h}_{\text{ST}}(f)$  is the stochastic amplitude density per square root Hz.

While predictions from cosmological models vary over many orders of magnitude, there are several observational results that place upper limits on  $\Omega_{\text{gw}}(f)$  in various frequency bands. These are given in Table 5.1 which is taken from Ref. [21].

The high degree of isotropy observed in the cosmic microwave background radiation (CMBR) places a strong constraint on  $\Omega_{\text{gw}}(f)$  at very low frequencies. This limit applies only over several decades of frequency that are far below the reach of current, and currently planned, Earth-based or space-based detectors. Time-of-arrival jitter of radio pulses from several millisecond pulsars also places an observational constraint on  $\Omega_{\text{gw}}(f)$ . These constraints are valid at frequencies on the order of the inverse of the observation time of the pulsars,  $1/T \sim 10^{-8}$  Hz, which corresponds to a much lower frequency band than that probed by either Earth or space-based detectors.

The only limit on  $\Omega_{\text{gw}}(f)$  that could apply at frequencies high enough to be probed by Earth-based detectors comes from the observed abundances of the light elements in the universe, coupled with the standard model of big-bang nucleosynthesis. One of the constrained parameters is the expansion rate of the universe at the time of nucleosynthesis, thus setting a limit on the energy density of the universe at that epoch, and consequently also on the energy density in a cosmological background of gravitational radiation. Contributions to a stochastic gravitational background from non-cosmological sources such as a superposition of supernovae signals would not be affected by these arguments.

Table 5.1: Summary of upper limits on  $\Omega_0 h_{100}^2$  over a large range of frequency bands (from [21]).

Observational Technique	Observed Limit	Frequency Domain
Cosmic Microwave Background*	$\Omega_{\text{gw}}(f)h_{100}^2 \leq 10^{-13} \left(\frac{10^{-16} \text{ Hz}}{f}\right)^2$	$3 \times 10^{-18} \text{ Hz} < f$ $1 \times 10^{-16} \text{ Hz} > f$
Radio Pulsar Timing*	$\Omega_{\text{gw}}(f)h_{100}^2 \leq 9.3 \times 10^{-8}$	$4 \times 10^{-9} \text{ Hz} < f$ $4 \times 10^{-8} \text{ Hz} > f$
Big-Bang Nucleosynthesis*	$\int_{f>10^{-8}} d \ln f \Omega_{\text{gw}}(f)h_{100}^2 \leq 10^{-5}$	$1 \times 10^{-8} \text{ Hz} \lesssim f$
Interferometers†	$\Omega_{\text{gw}}(f)h_{100}^2 \leq 3 \times 10^5$	$100 \text{ Hz} \lesssim f$ $1000 \text{ Hz} \gtrsim f$
Room Temp. Resonant Bar (correlation)†	$\Omega_{\text{gw}}(f)h_{100}^2 \leq 3000$	$f_0 = 985 \pm 80 \text{ Hz}$
Cryogenic Resonant Bar (single)†	$\Omega_{\text{gw}}(f)h_{100}^2 \leq 300$	$f_0 = 907 \text{ Hz}$
Cryogenic Resonant Bar (single)†	$\Omega_{\text{gw}}(f)h_{100}^2 \leq 5000$	$f_0 = 1875 \text{ Hz}$
Cryogenic Resonant Bar (correlation)†	$\Omega_{\text{gw}}(f)h_{100}^2 \leq 60$	$f_0 = 907 \text{ Hz}$

\*Indirect limit derived from Astrophysical Observations

†Direct Gravitational Wave Measurement

## 5.2 Correlation Technique

Within the primary frequency band of interest to LIGO, a signal generated by stochastic background radiation has the same spectral shape as the noise generated within or picked up by the system. If only a single IFO were used for signal detection within this frequency band then only an upper limit on the signal could be placed at the detector's strain-noise level. There would be no way to distinguish signal from noise. This is noted in a paper using the cross-correlation between resonant bar detectors Explorer and Nautilus [3].

If, however, more than one detector is used, the equivalent strain output of each detector can be written as:

$$s_i(t) \equiv h_i(t) + n_i(t), \quad (5.7)$$

where  $h_i(t)$  is the strain signal in the  $i$ -th detector due to a gravitational signal, and  $n_i(t)$  is the detector's equivalent strain noise. When the outputs of two detectors are *cross-correlated*, then it is possible to take advantage of the fact that the sources of noise  $n_i$  in each detector will be, in general, independent [1, 2, 45, 18, 27] while the strain signal  $h_i$  will not. Detailed calculations are given in Refs.[1, 21] to show that the upper limit placed on  $\Omega_0 h_{100}^2$  through cross-correlation is smaller (i.e. more constraining) than that obtainable from one detector by a factor of  $\gamma_{\text{rms}} \sqrt{T \Delta_{\text{BW}}}$ , where  $\Delta_{\text{BW}}$  is the bandwidth over which the relevant integrand is significant and  $\gamma_{\text{rms}}$  is the rms value of  $\gamma(f)$  over that bandwidth. The *overlap reduction function*  $\gamma(f)$  is a real function that characterizes the reduction in sensitivity to a stochastic background arising from the separation time delay and relative orientation of the two detectors. This function is shown in Fig. 5.1 for the Hanford and Livingston LIGO detectors. It depends only on the relative detector geometry (for coincident and co-aligned

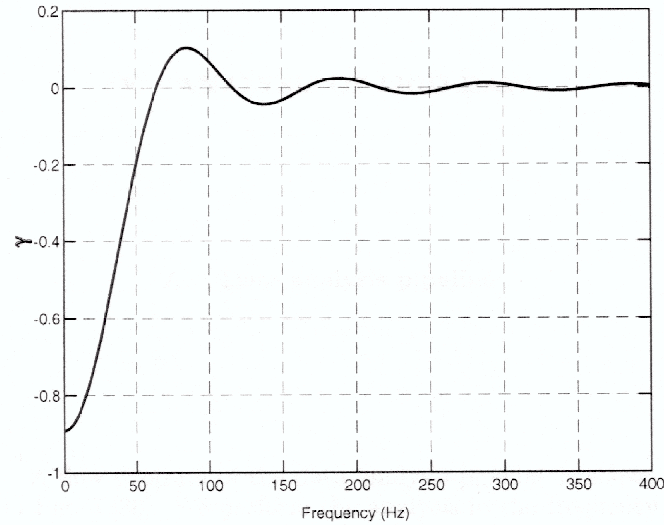


Figure 5.1: Overlap Reduction Function  $\gamma(f)$  shown for the LHO-LLO detectors [21]. The value of  $|\gamma|$  is a little less than unity at 0 Hz because the interferometer arms are not exactly co-planar and co-aligned between the two sites.

detectors  $\gamma(f) = 1$  for all frequencies). For the LHO-LLO correlations in the S1 analysis [21],  $T \simeq 2 \times 10^5$  sec,  $\Delta_{\text{BW}} \simeq 100$  Hz, and  $\gamma_{\text{rms}} \simeq 0.1$ . Hence, using cross-correlation techniques, a limit can be set on the signal that is a factor of several hundred below the individual detectors' strain noise.

The most recent result from the LIGO Collaboration [21] (accepted for publication in Phys. Rev. D) sets a limit of  $\Omega_0 h_{100}^2 \leq 23$ . Design sensitivities are expected to probe  $\Omega_0 h_{100}^2 \leq 10^{-6}$ .

### 5.3 Free Spectral Range (FSR) Technique

As already mentioned, using a single detector one can place an *upper limit* on a stochastic signal, but not measure its value. For instance an upper limit of  $\tilde{h} < 2 \times 10^{-21} / \sqrt{\text{Hz}}$  on GW stochastic background at 1.8 kHz was established

in 1999 by using the ALTAIR resonant bar detector [4] (see Table 5.1). Using the noise floor from the S3 run as given by Eq.(5.15) I place a similar limit on  $\tilde{h}$  at a frequency of 37.5 kHz.

However one can do better if the signal can be distinguished from the noise, for instance due to a different spectral response of the detector to the signal and noise. Not only can a much more sensitive upper limit be resolved, but detection becomes possible.

It has been pointed out by several authors [64, 69, 56, 50, 66] that the response of the IFO's to a differential mode signal is substantially enhanced at the free spectral range (fsr) frequency. For the 4 km IFO's,  $f_{\text{fsr}} = 37.52$  kHz. Most importantly the differential signal has a definite *spectral shape* (frequency response) centered at  $f_{\text{fsr}}$  with a width characterized by the so called ‘‘cavity pole’’  $\omega_c \simeq [(1 - r_{\text{ITM}}r_{\text{ETM}})/\sqrt{r_{\text{ITM}}r_{\text{ETM}}}]f_{\text{fsr}} = 560$  r/s. On the other hand, the noise is *relatively flat* over this frequency range.

Recently, it was proposed [50, 66] to exploit these two features to distinguish the contribution of a stationary (in time) differential mode signal from the noise in the power spectrum of the AS port. The method depends, of course, on the assumption that the noise does not follow the cavity pole spectrum. This seems to be the case because at 37.52 kHz the primary noise sources are (a) shot noise (b) laser frequency (phase) noise and (c) test mass thermal noise. In addition instrumental (electronics) noise may be present. Seismic and environmental noise are highly suppressed. Shot and phase noise are flat in the frequency interval of interest, which for the present analysis was restricted to the range 37.2 to 37.8 kHz. Comprehensive knowledge of all noise sources contributing to the spectrum is necessary when using this detection method.

## 5.4 FSR Search Method

I have performed a proof of concept search for a stochastic gravitational wave signal at the FSR frequency (37.52 kHz) of the LIGO Hanford 4k IFO using data from the S3 run in December of 2003.

The same data was used for this analysis as is presented in sec. 4.2.2, see Fig. 4.9. Here, however, I am concerned with fitting the data using a more comprehensive method to determine the differential mode contribution to the data, if any. As all features of interest were visible when using only a single frame of data per FFT this is the resolution used for this analysis. The length of the time series allowed for 2800 magnitude averages using a single frame of data (16 seconds) per average; this results in a bandwidth  $BW = 0.0625$  Hz. A 60 Hz line mask was applied to the averaged data to remove multiples of the 60 Hz line noise and replace it with the average value. The code for this is given in Appendix B. Although some remnant of line noise can still be observed at 300 Hz after the mask application, the method was found to be quite effective. The data is left as the magnitude of the units returned by MATLAB's FFT function which is proportional to the square root of the power spectrum. This is also discussed in section 4.2.2 on page 125.

To fit the FFT magnitude to the expected response from a d.m. signal I restricted the data in the range 37.2 to 37.8 kHz. The fit included the following terms:

- (a) Constant term
- (b) Linear term
- (c) Phase noise
- (d) Differential mode signal
- (e) Internal Test Mass Resonance Contribution



The constant term and the linear term are each held to the same relative phase (zero) and have no frequency dependent phase. The phase noise contribution maintains its frequency dependent phase and has a relative (or starting) phase which is fit. Both the Differential Mode signal and the Internal Test Mass Resonance contribution terms are held at a zero relative phase and only the magnitude calculation is used (no frequency dependent phase for either term). This leads to significantly less correlation between their fit parameters as well as being more physically plausible due to the stochastic nature of both signals.

I have not modeled specific processes in the IFO which correspond to the first two terms of the fit (the constant and the linear proportionality to frequency), they arise from the contribution of: electronics noise (analog to digital conversion, demodulation phase jitter etc.), shot noise, radiation pressure noise and lower frequency fold-over contributions from fit noise sources (phase noise, test mass motion).

To estimate the expected level of shot noise I give a simple calculation (following the method presented in [57]). Note that this is not actually a parameter to be fit from the data. I express the shot noise contribution as an equivalent strain as follows

$$\sqrt{\bar{S}}_{\text{motion}} = \frac{\sqrt{S_{\text{light}}}}{H(f)} = \frac{(3E_+^2 + E_{\text{dc}}^2)^{1/2} (1 - r_{\text{itm}}r_{\text{etm}})^2}{2k|E_2|E_+ T_{\text{itm}}r_{\text{etm}}} \left[ 1 + \left( \frac{2\pi f}{\omega_c} \right)^2 \right]^{1/2} \frac{\text{m}}{\sqrt{\text{Hz}}} \quad (5.8)$$

Where  $H(f)$  is the IFO transfer function to convert optical signal into a length measurement,  $E_+$  is the r.f. sideband field at the AS port,  $E_{\text{dc}}$  is the d.c. leakage of carrier field at the AS port,  $E_2$  is the carrier light incident upon the beamsplitter from inside the PRM,  $r$  is the amplitude reflectivity of the indicated optic and  $T$  is the power transmission of the indicated optic. For this calculation I will make some simplifying assumptions:  $f = 0$  (FSR sensitivity is theoretically

equivalent to DC sensitivity),  $r_{\text{etm}} = 1$ ,  $1 - r_{\text{itm}} = 1.419 \times 10^{-2}$ ,  $T_{\text{itm}} = 0.0281$  (the optics are ideal), and  $E_{\text{dc}} = 0$  (the IFO is perfectly aligned). Now Eq.(5.8) simplifies to

$$\sqrt{\tilde{S}_{\text{motion}}} = \frac{\sqrt{3}}{4\pi} \frac{\lambda}{|E_2|} (7.2 \times 10^{-3}). \quad (5.9)$$

I express  $|E_2|^2$  in units of photoelectrons per second, then for 1 Watt of input light and a PRM build-up value of 42,  $|E_2| = \sqrt{2.6 \times 10^{20}} \text{ s}^{-1/2}$ , leading to

$$\sqrt{\tilde{S}_{\text{motion}}} = 6.13 \times 10^{-20} \quad \frac{\text{m}}{\sqrt{\text{Hz}}} \quad (5.10)$$

which translates into a strain density of

$$\tilde{h} = 1.5 \times 10^{-23} \quad / \sqrt{\text{Hz}} \quad (5.11)$$

This result is at least a factor of ten below the estimated noise floor of the data given in Eq.(5.15) indicating that at this point the instrument was not shot-noise limited.

The phase noise and differential motion models used in the fit are generated by the matrix calculation method described in section 3.2.2. Using IFO parameters obtained in Chap. 3 by fitting injected signals in the model, I calculate the transfer function in the frequency range of interest (37.2 -37.8 kHz). Then I normalize this transfer function by its peak magnitude value. For the phase noise contribution, the full complex simulation results are used to maintain the frequency dependent phase information. For the differential motion only the magnitude of the model result is used in the fit since a stochastic source is incoherent. Contributions from internal test masses are calculated as specified in section 4.3.1.

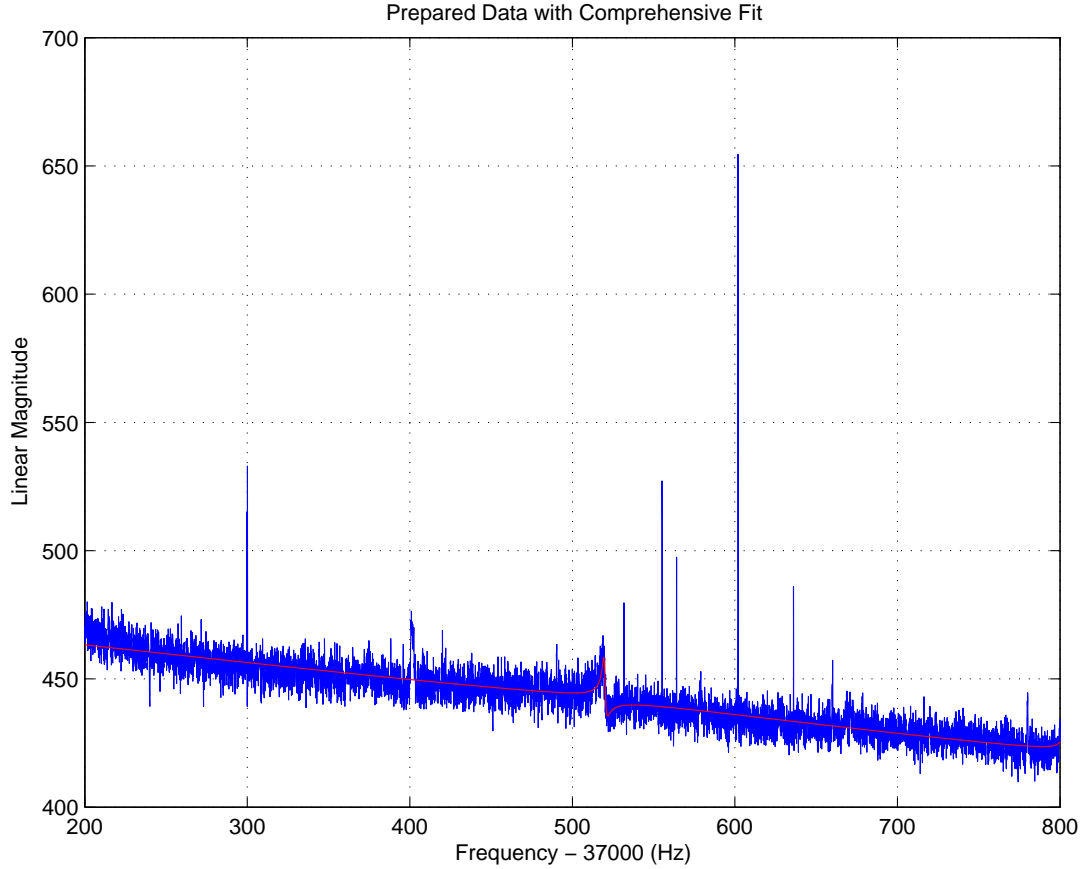


Figure 5.2: Fitted spectrum and data for  $37,200 < f < 37,800$  Hz. The comprehensive fit for all parameters is used. See text for details.

## 5.5 FSR Search Results

The best fit to the data is shown in Fig. 5.2 and on an expanded scale in Fig. 5.3.

The results are summarized in Table 5.2. The  $\chi^2$  was calculated by assuming a constant error for each point and choosing  $\sigma = 5.9433$  so that for a fit to the constant, linear and phase noise terms the  $\chi^2$  value was exactly equal to the number of data points (9600). Thus

$$\chi^2 = \sum_i \frac{(x_i - \bar{x}_i)^2}{\sigma^2} \quad (5.12)$$

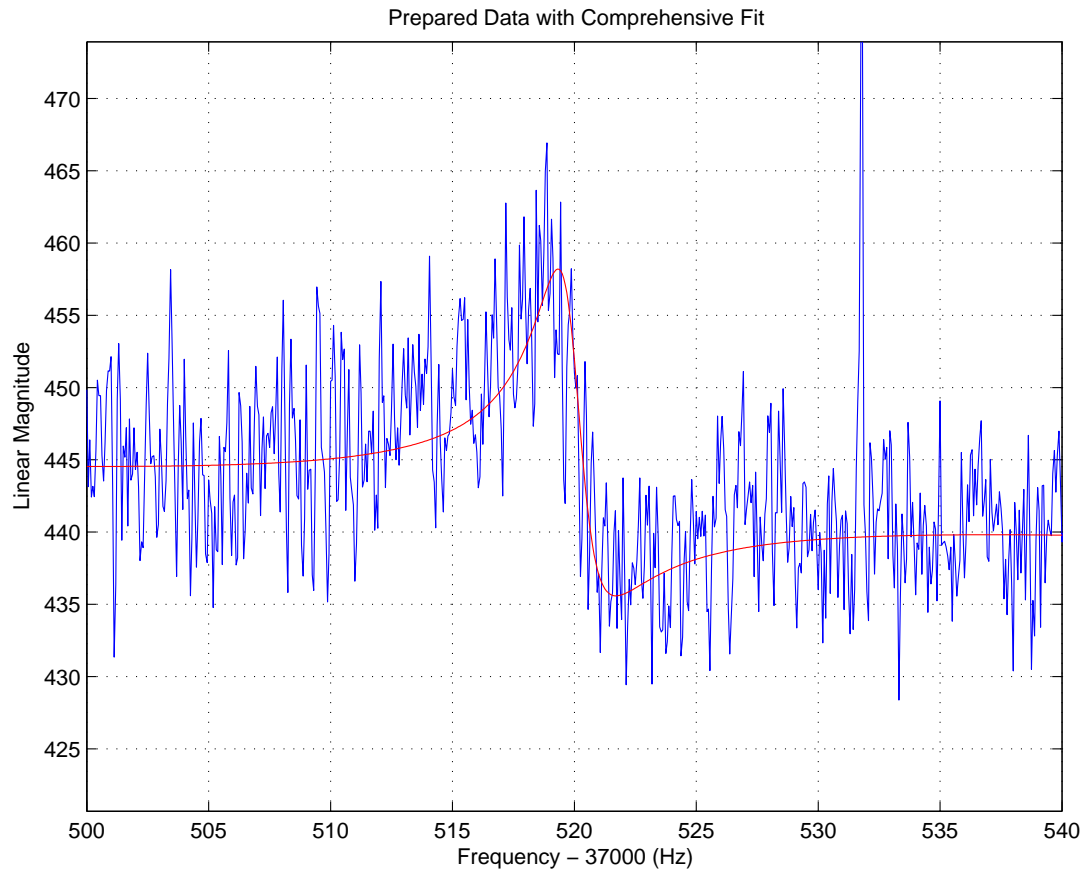


Figure 5.3: As in Fig.5.2 but for a 40 Hz span in the fsr region.

Table 5.2: Fit Coefficients

$ A $	477	476	478	477	478	477	Constant term*
$\phi_A$	(0°)	(0°)	(0°)	(0°)	(0°)	(0°)	
$ B $	-0.07	-0.07	-0.07	-0.07	-0.07	-0.07	Linear term*
$\phi_B$	(0°)	(0°)	(0°)	(0°)	(0°)	(0°)	
$ C $	22.6	22.3	22.3	21.9	22.3	22.0	Phase noise
$\phi_C$	117°	115°	116°	114°	116°	114°	
$ D $	-	1.23	-	1.17	-	1.17	Differential Motion*
$\phi_D$	-	(0°)	-	(0°)	-	(0°)	
$ E $	-	-	(1)	(1)	0.89	0.85	Mechanical term*
$\phi_E$	-	-	(0°)	(0°)	(0°)	(0°)	
$\chi^2$	9,599.9	9,578.5	9,578.7	9,559.7	9,578.3	9,559.1	
D.O.F.	9,597	9,596	9,597	9,596	9,596	9,595	

---

\*Parameters in parenthesis imply fixed value.

where  $x_i$  is the value of the data point in array index  $i$  and  $\bar{x}_i$  is the value of the fit prediction for array index  $i$ . When the properly normalized  $\chi^2$  increases by one unit, the corresponding parameters constitute the  $1\sigma$  values, 4 units constitute the  $2\sigma$  limits etc.

The first two columns in Table 5.2 show fits with and without a Differential mode (DM) signal, with no contributions from mechanical resonances. In this case inclusion of a DM signal lowers the  $\chi^2$  by 22 units. A quadratic fit to the  $\chi^2$  distribution is shown in Fig. 5.4. The next two columns show fits with and without DM signal, with a contribution from incoherently added mechanical res-

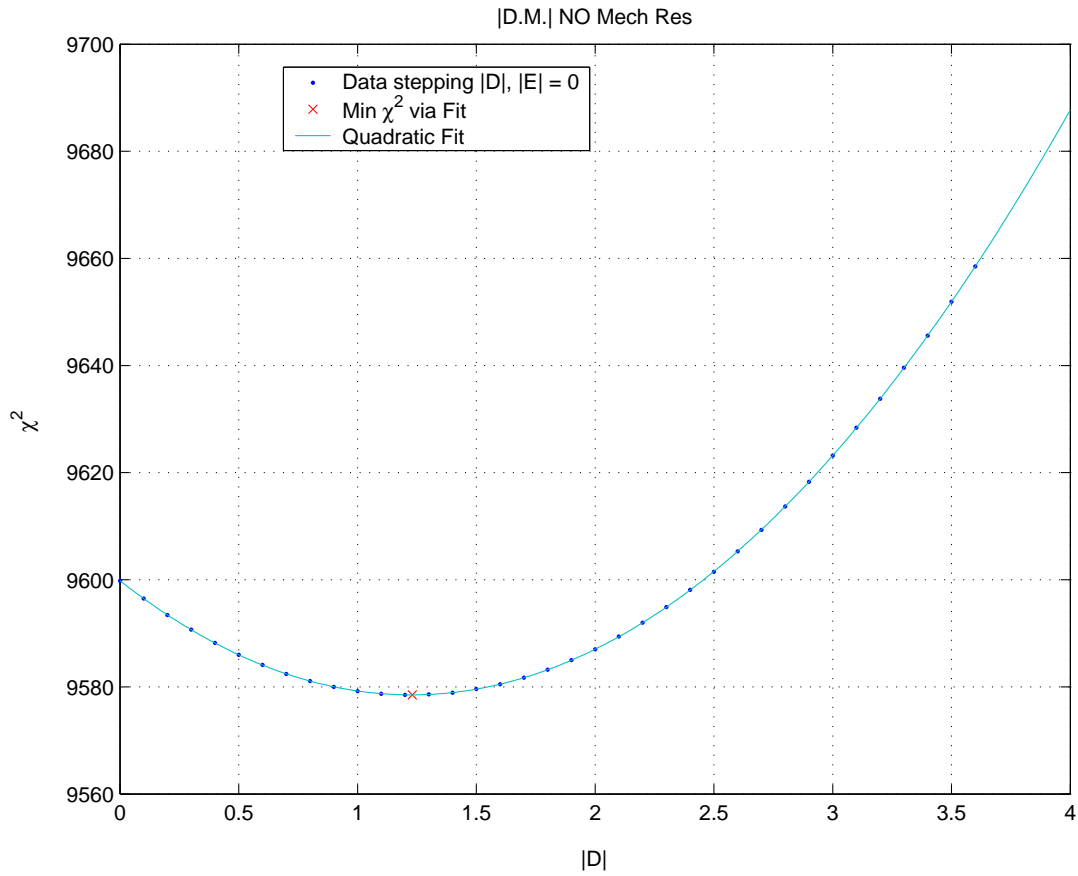


Figure 5.4:  $\chi^2$  vs the magnitude of the differential mode signal with no contribution from mechanical resonances.

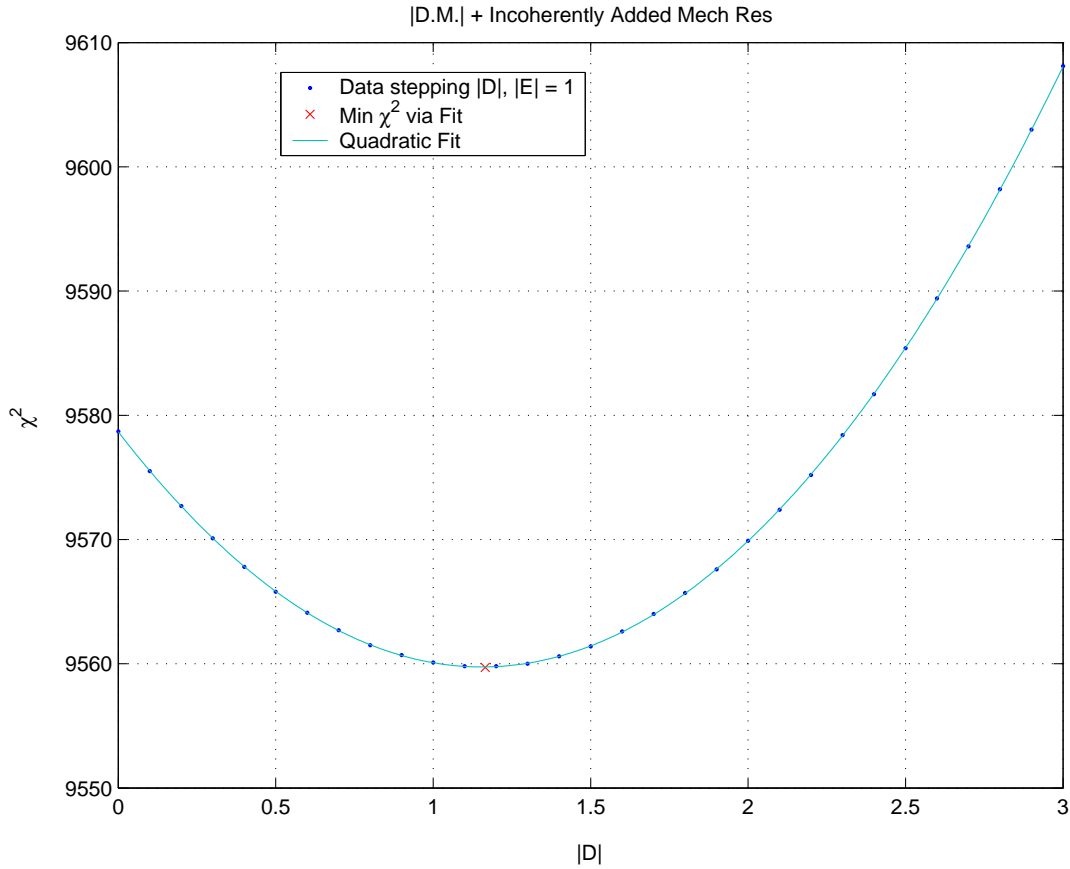


Figure 5.5:  $\chi^2$  vs the magnitude of the differential mode signal with mechanical resonances of fixed magnitude included.

onances with a magnitude set at the value predicted in Chap. 4. The inclusion of the DM signal results in a  $\Delta\chi^2 = 19$  units. A quadratic fit to the  $\chi^2$  distribution is shown in Fig. 5.5. Finally the last two columns show fits with and without DM signal while also fitting the magnitude of the included mechanical resonance contributions. The same mechanical resonance contribution calculation is used for all fits shown in Table 5.2, here I simply fit an overall multiplicative factor. In this case the DM signal inclusion again results in  $\Delta\chi^2 = 19$  units. Fig. 5.6 shows a quadratic fit to the  $\chi^2$  distribution.

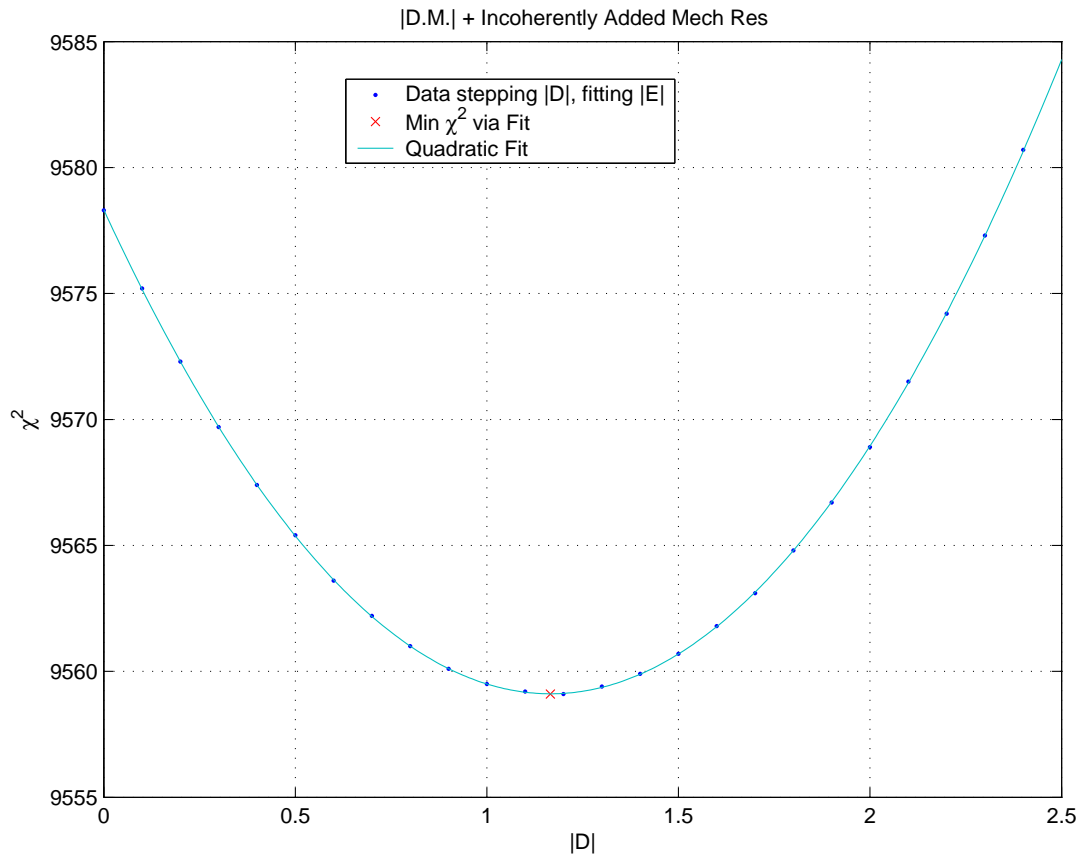


Figure 5.6:  $\chi^2$  vs the magnitude of the differential mode signal where the magnitude of the mechanical resonances is being simultaneously fit.



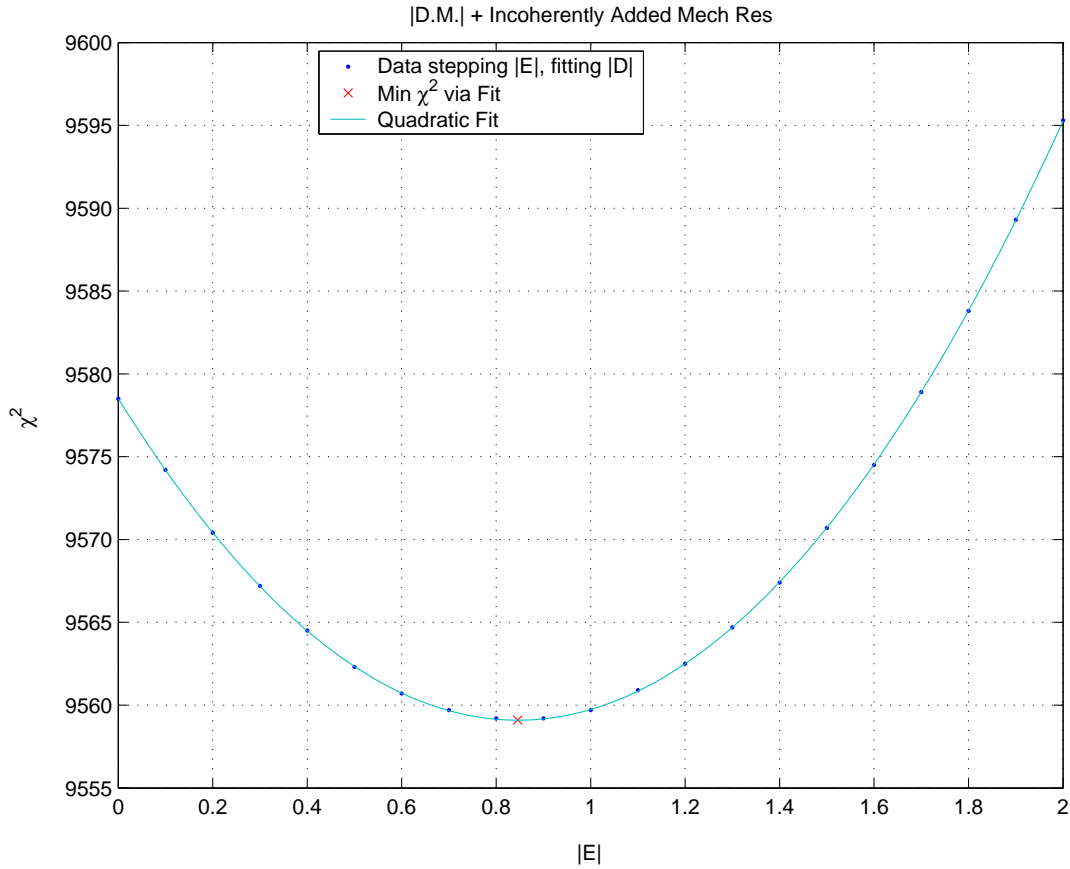


Figure 5.7:  $\chi^2$  vs the magnitude of the mechanical resonance amplitude when the magnitude of the differential mode is being simultaneously fit.

Figure 5.7 shows a quadratic fit to the  $\chi^2$  distribution while holding the DM contribution constant and varying the multiplicative magnitude of the mechanical resonance contribution. A contour plot showing the correlation (and relative independence) of the differential mode parameter to the mechanical resonance parameter is shown in Fig. 5.8.

Following the calibration method discussed in section 4.3.1, theoretically the mechanical resonance fit amplitude should be unity. As resonances are added incoherently with random phase, the over all contribution magnitude can vary

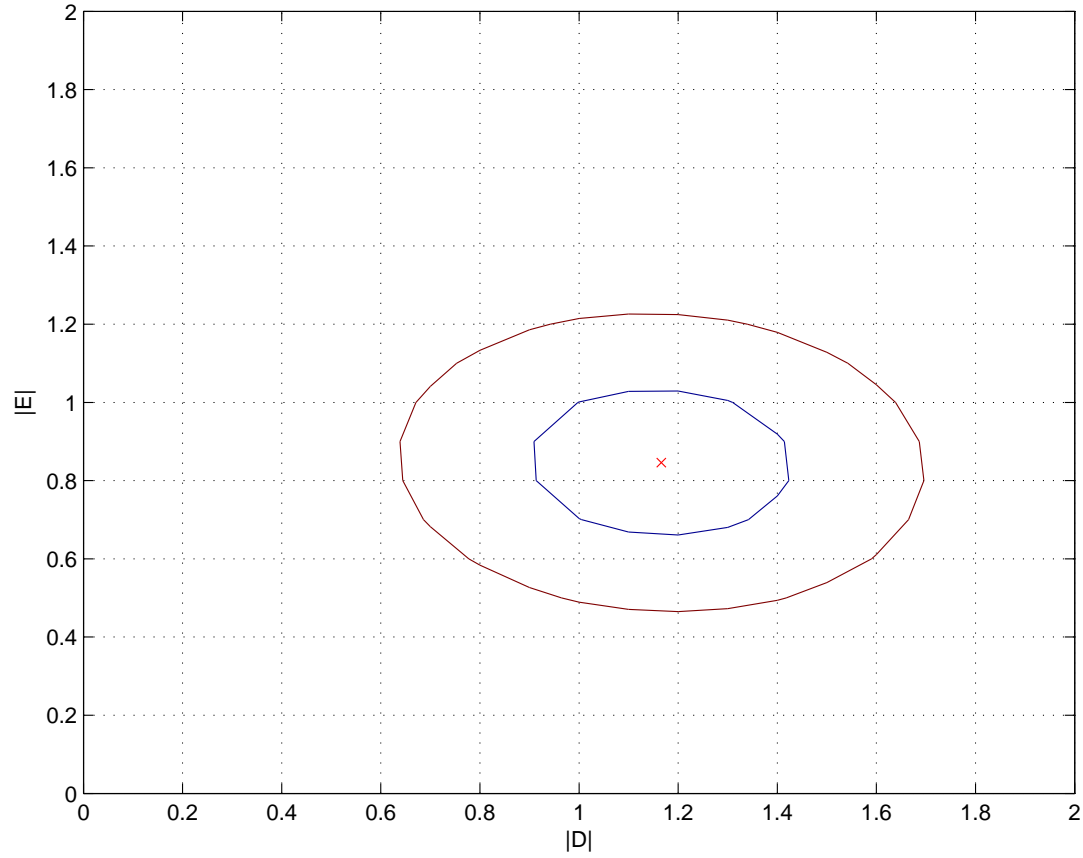


Figure 5.8:  $\chi^2$  contour plot with the magnitude of the differential mode vs the magnitude of the mechanical resonance contribution. The central point is the minimum fit, contours are  $1\sigma$  and  $2\sigma$ . Note the minimal correlation of the two parameters.

depending on what phases are used. For this reason I did fits where the mechanical resonance amplitude was varied as well (last two columns in Table 5.2). It is quite encouraging that the fit amplitude is very close to unity (Fig. 5.7) as well as the fact that the fit parameter is practically independent of the differential motion fit amplitude (Fig. 5.8).

The conclusion from this analysis is that a differential mode signal is present in the data with a confidence level of  $4\sigma$  to  $5\sigma$ . However the amplitude of this signal is only

$$1.17 \pm 0.25 \quad \text{FFT units} \quad (5.13)$$

as compared to the constant background (noise floor) of

$$430 \quad \text{FFT units} \quad (5.14)$$

Namely the spectral shape of the signal coupled with the large number of measured data points allows for a significant effective reduction in the noise level.

To check the validity of the fit I conducted a software injection of a differential mode signal into the data to measure the corresponding fit values and compare them with the injected value. A linear frequency spectrum was generated with random fluctuations corresponding to the experimental  $\sigma$  and a mean value of 400. This spectrum was then convolved with the Differential Mode (DM) transfer function. The magnitude of the spectrum was added to the data in the region 37.2-37.8 kHz. The resulting spectrum was fit as described in section 5.4 with a constant term, linear term, phase noise term, differential mode term and a term from incoherently added mechanical resonances.

Table 5.3 shows the results for the injected and recovered DM in columns 1,2; Column 3 shows the confidence level in terms of the standard deviation of the fit. Note that the recovered signal reflects **both** the *injected signal* and the *signal intrinsic to the data*. One concludes that an intrinsic signal at the

Table 5.3: Results of Differential Motion Signal Injection through software.

<u>Injected Signal</u>	<u>Recovered Signal</u>	<u>Confidence Level</u>
400	404	$1.52 \times 10^3 \sigma$
40	41.5	$156 \sigma$
4	5.20	$20 \sigma$
2	3.18	$12 \sigma$
1	2.17	$8 \sigma$
0.5	1.67	$6 \sigma$
--	1.17	$4 \sigma$

level of 1 to 1.5 units is present and detectable. The units refer to the scale of the FFT of the data time series, for  $BW = 0.0625$  and sampling frequency  $R = 2,048$  Hz, as also used in Eqs.(5.13, 5.14). Recall that the average value of the FFT coefficient at  $f = 37.52$  kHz is  $C_k = 430$ .

## 5.6 Calibration of FSR Data

While no direct calibration of the data stream used here is available I can estimate the calibration as indicated in section 4.3.1. Using the calibration introduced in Eqs.(4.13 and 4.12) and dividing by the arm length (4000 m) I get

$$\sqrt{\text{PSD}(f_{\text{fsr}})} = 3.71 \times 10^{-22} / \sqrt{\text{Hz}} \quad (5.15)$$

which corresponds to the total signal at the FSR frequency. For the proportion of that which is due to differential motion, and therefore possibly due to gravitational radiation, I multiply by the ratio of the DM fit parameter to the linear

term (as the DM theory used in the fit was normalized to a max value of unity). As this is best expressed as an upper limit, I use the  $3\sigma$  value of the DM fit parameter farthest from zero instead of the best fit value.

$$\tilde{h}_{\text{DM}} < \frac{1.95}{477} 3.71 \times 10^{-22} / \sqrt{\text{Hz}} \quad (5.16)$$

or

$$\tilde{h}_{\text{DM}} < 1.5 \times 10^{-24} / \sqrt{\text{Hz}} \quad (5.17)$$

with  $3\sigma$  confidence.

To relate the limit on a differential mode signal to a limit on the stochastic background I must average over the angle of incidence and polarizations. This average was calculated by D. Sigg [66] and is also presented for reference in Appendix A. The result is that

$$\langle h \rangle = h/5.3 \quad (5.18)$$

which leads to a  $3\sigma$  limit of

$$\tilde{h}_{\text{stochastic}}(37.52\text{kHz}) < 8.0 \times 10^{-24} / \sqrt{\text{Hz}} \quad (5.19)$$

To compare this result with the values of  $\Omega_{\text{gw}}$  discussed in section 5.1 I use Eq.(5.6) with  $H_0 = 100 \text{ Km/s} \cdot \text{Mpc}$

$$\tilde{h}_{\text{stoch}} = 5.6 \times 10^{-19} \left( \frac{1 \text{ Hz}}{f} \right)^{\frac{3}{2}} \sqrt{\Omega_{\text{gw}}(f)} \quad (5.20)$$

so that  $\Omega_{\text{gw}}(f = 37.5 \text{ kHz}) < 10,000$  at the  $3\sigma$  level (99% confidence for a gaussian distribution). Fig. 5.9 shows the strain sensitivity of LIGO for a stochastic background out to high frequencies and the upper limit from this measurement. This is not a very significant limit, even though it is of the same order as the limits from resonant bars included in Table 5.1. Of more interest is the fact that

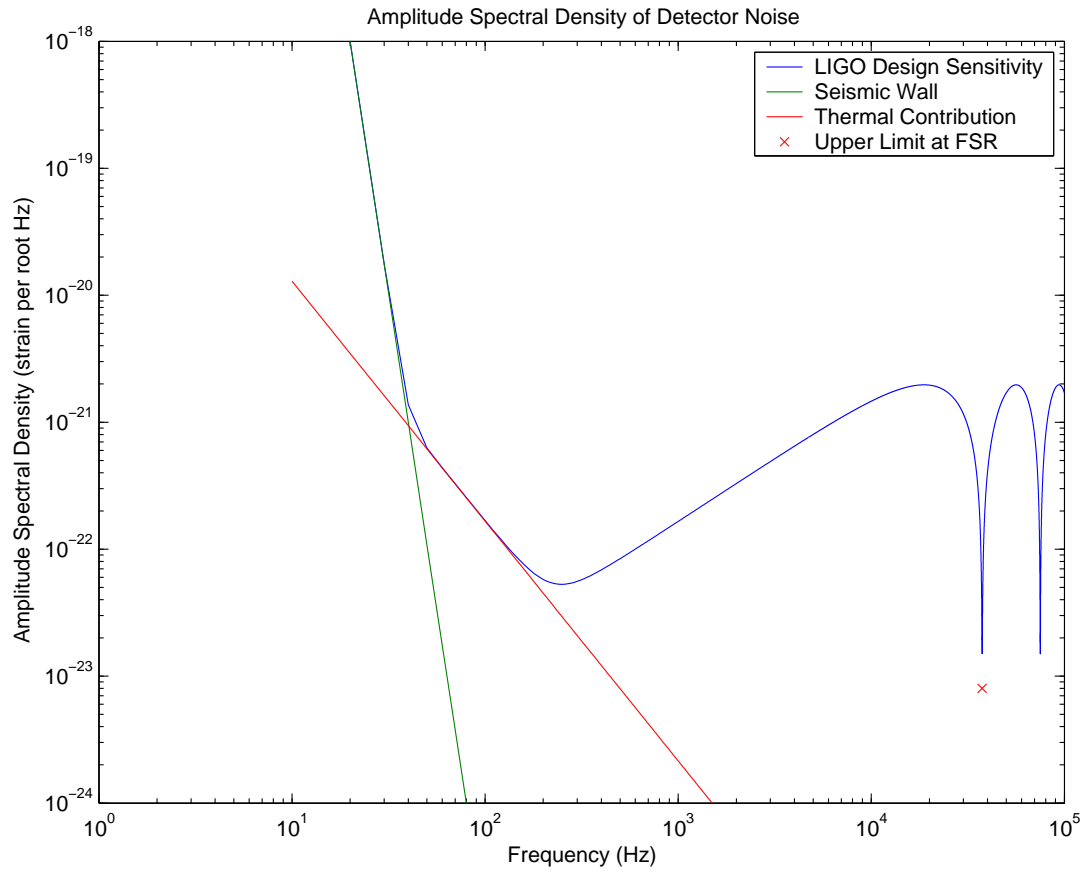


Figure 5.9: Predicted LIGO strain sensitivity with upper limit placed at FSR (37520 Hz)

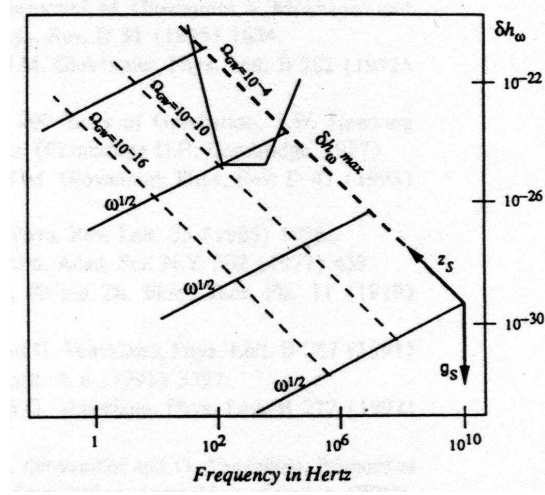


Figure 5.10: Stochastic characteristic strain spectra predicted in [11]. Also shown is the design sensitivity of Advanced LIGO

one can bound the stochastic gravitational amplitude to  $h \lesssim 10^{-23} / \sqrt{\text{Hz}}$  at a relatively high frequency. In the string model of ref [11] this value of  $h$  corresponds to  $\Omega_{\text{gw}} \sim 10^{-4}$  as shown in Fig. 5.10. This indicates the advantage of making measurements at high frequency if one wishes to test the string model.

## 5.7 Sensitivity of Future Measurements

It is clear that the result of Eq.(5.19) is preliminary, and based on an estimated calibration. Furthermore, it is based on only one out of  $\approx 40$  days of data from the S3 run. These shortcomings should be remedied in the next run of LIGO in late 2004.

Repeating the analysis, but using  $\approx 50$  days of data, should reduce the fluctuations in the noise by another factor of 7, and similarly improve the confidence limit on the differential mode signal. In addition, exact calibration of the high frequency channel, and other improvements planned in data taking, should con-

tribute a factor of 10 or more to signal sensitivity so that  $h_{\text{DM}} \lesssim 10^{-25} / \sqrt{\text{Hz}}$ . This would test the string model at the level of  $\Omega_{\text{gw}} = 10^{-8}$  (see Fig. 5.10). Using a single detector will never convince the community at large that a stochastic GW signal has been observed. To achieve this, it is necessary to carry out a correlation experiment. Fortunately, the LHO 4k and the LHO 2k IFOs are co-aligned and located in the same vacuum tunnel. Thus, they can be used to measure a correlation even at this high frequency. The difficulty is that the fsr for the H2 IFO is at 75 kHz so that in correlating the signal at 37.52 kHz the sensitivity of the H2 IFO will be reduced by a factor of 130 from its peak (DC) value. If common disturbances in the two instruments can be excluded from the correlation product, the correlation experiment should then be successful. This should be possible at these high frequencies. Also the eventual upgrade to Advanced LIGO calls for the H2 IFO to be extended to 4 km in length, thus both LHO IFOs would have the same fsr frequency.



# Bibliography

- [1] B. Allen, *The stochastic gravity-wave background: sources and detection*, Proceedings of the Les Houches School on Astrophysical Sources of Gravitational Waves (1998), 373, gr-qc/9604033.
- [2] B. Allen and J. Romano, *Detecting a stochastic background of gravitational radiation: Signal processing strategies and sensitivities*, Phys. Rev. **D59** (1999), 102001.
- [3] P. Astone and et al., *Cross-correlation measurement of stochastic gravitational waves with two resonant gravitational wave detectors*, Astronomy and Astrophysics **351** (1999), 881–814.
- [4] ———, *Upper limit at 1.8 khz for a gravitational-wave stochastic background with the ALTAIR resonant-mass detector*, Astronomy and Astrophysics **343** (1999), 19–22.
- [5] B. Barish and R. Weiss, *LIGO and the detection of gravitational waves*, Physics Today **52** (1999), 44, <http://www.ligo.caltech.edu/>.
- [6] Biplab Bhawal, Matt Evans, Edward Maros, Malik Rahman, and Hiro Yamamoto, *Overview of end-to-end model*, Tech. report, LIGO Internal #: T970193, November 1997.

- [7] ———, *Physics of end-to-end model*, Tech. report, LIGO Technical Report #: T970196, November 1997.
- [8] G. Billingsley, B. Kells, H. Yamamoto, J. Camp, D. Li, H. Armandula, S. Bell, and S. Elieson, *Core optics components final design*, Tech. report, Caltech, April 1998, LIGO Internal #: E980061.
- [9] GariLynn Billingsley, *COC as built*, LIGO Internal Web page <http://www.ligo.caltech.edu/~gari/COCAsBuilt.htm>.
- [10] François Bondu and Jean Yves Vinet, *Mirror thermal noise in interferometric gravitational-wave detectors*, Physics Letters **A 198** (1995), 74–78.
- [11] R. Brustein, M. Gasperini, M. Giovannini, and G. Veneziano, *Relic gravitational waves from string cosmology*, Physics Letters **B 361** (1995), 45–51.
- [12] T. Bulik, K. Belczyński, and B. Rudak, *Astrophysical significance of the detection of coalescing binaries with gravitational waves*, Astronomy and Astrophysics **415** (2004), 407–414.
- [13] W. Butler, A. Melissinos, and F. Raab, *Experimental determination of the mode spectrum of the locked arms of the Hanford 4k Interferometer*, Internal note July 3, 2002. The same suggestion was made independently by F. Bondu and R. Savage: private communication.
- [14] William E. Butler, *Field calculations for a power recycled michelson interferometer with fabry-perot arms, a first principles approach*, Tech. report, University of Rochester, Dept. of Physics & Astronomy, May 2001, LIGO Internal #: T030162.

- [15] William E. Butler and Adrian C. Melissinos, *Experimental Characterization of the High Frequency Response of the LHO 4k IFO, A: Sideband Injection*, Tech. report, University of Rochester, Dept. of Physics & Astronomy, 2003, LIGO Internal #: T030163.
- [16] ———, *Experimental Characterization of the High Frequency Response of the LHO 4k IFO, B: Parametric Conversion*, Tech. report, University of Rochester, Dept. of Physics & Astronomy, 2003, LIGO Internal #: T030263.
- [17] Bradley W. Carrol and Dale A. Ostlie, *An introduction to modern astrophysics*, Addison Wesley Longman, 1996.
- [18] N. Christensen, *Measuring the stochastic gravitational-radiation background with laser-interferometric antennas*, Physical Review **D46** (1992), no. 12, 5250–5266.
- [19] LISA collaboration, *LASER Interferometer Space Antenna*, <http://lisa.jpl.nasa.gov/>.
- [20] The LIGO Scientific Collaboration, *LSC web page*, <http://www.ligo.org/>.
- [21] ———, *Analysis of first LIGO science data for stochastic gravitational waves*, (2003), gr-qc/0312088.
- [22] Dennis Coyne, *Test mass modes*, LIGO Internal Web page [http://www.ligo.caltech.edu/~coyne/IL/COC/TM\\_modes/TM\\_modes.html](http://www.ligo.caltech.edu/~coyne/IL/COC/TM_modes/TM_modes.html).
- [23] ———, *Recycling cavity layout*, Tech. report, Caltech, 1997, LIGO Internal #: D970003.

- [24] R.W.P. Drever, J.L. Hall, F.V. Kowalski, J. Hough, G.M. Ford, A.J. Munley, and H. Ward, *Laser phase and frequency stabilization using an optical resonator*, Applied Physics **B31** (1983), 97 – 105.
- [25] A. Einstein, Preuss, Akad. Wiss. Berlin, Sitzungsberichte der Physikalisch-mathematischen Klasse (1916), 688.
- [26] Lee Samuel Finn, *LIGO science reach*, Feb 2001, LIGO Presentation: # G010175-00-R.
- [27] E. E. Flanagan, *Sensitivity of the laser interferometer gravitational wave observatory to a stochastic background, and its dependence on the detector orientations*, Physical Review **D48** (1993), no. 6, 2389–2407.
- [28] Peter Fritschel and Rana Adhikari, *LHO detector e-log entries*, Reference arm length measurement on 21st, July 2002.
- [29] Peter Kurt Fritschel, *Techniques for laser interferometer gravitational wave detectors*, Ph.D. thesis, Massachusetts Institute of Technology, 1992.
- [30] A. Gillespie and F. Raab, *Thermally excited vibrations of the mirrors of LASER interferometer gravitational-wave detectors*, Phys. Rev. **D52** (1995), no. 2, 577–585.
- [31] G. Harry, *Private communication*.
- [32] Gregory M Harry, Andri M Gretarsson, Peter R Saulson, Scott E Kittelberger, Steven D Penn, William J Startin, Sheila Rowan, Martin M Fejer, D R M Crooks, Gianpietro Cagnoli, Jim Hough, and Norio Nakagawa, *Thermal noise in interferometric gravitational wave detectors due to dielectric optical coatings*, Classical and Quantum Gravity **19** (2002), 897–917.

- [33] E. Howell, D. Coward, R. Burman, D. Blair, and J. Gilmore, *The gravitational wave background from neutron star birth throughout the cosmos*, Monthly Notices of the Royal Astronomical Society (2004), 16–+.
- [34] R.A. Hulse and J.H. Taylor, *Discovery of a pulsar in a binary system*, The Astrophysical Journal **195** (1975), L51–L53.
- [35] Robert Irion, *ASTROPHYSICS:LIGO's Laser-Packing Big Sister LISA May Hunt Black Holes From Space*, Science **288** (2000), no. 5465, 422.
- [36] ———, *ASTROPHYSICS:LIGO's Mission of Gravity*, Science **288** (2000), no. 5465, 420–423.
- [37] ———, *ASTROPHYSICS: Gravitational Wave Hunters Take Aim at the Sky*, Science **297** (2002), no. 5584, 1113–1115.
- [38] ———, *ASTROPHYSICS: LIGO: The Shakedown Continues*, Science **297** (2002), no. 5584, 1115.
- [39] Joseph Michael Kovalik, *A study of thermal noise*, Ph.D. thesis, Massachusetts Institute of Technology, 1994.
- [40] Michael Landry, Luca Matone, Benoit Mours, and Peter Shawhan, *E2 calibration study of the Hanford 2km IFO*, Tech. report, LIGO Internal #: T000115, October 2000.
- [41] Michael Landry and David Ottaway, *Summary of mechanical resonances in the LIGO Hanford interferometers*, Tech. report, LIGO Internal #: T000020, March 2000.
- [42] Yu. Levin, *Internal thermal noise in the LIGO test masses: A direct approach*, Phys. Rev. **D57** (1998), no. 2, 659–663.

- [43] L. C. Lovelace, *Gravitational waves from a pulsar kick caused by neutrino conversions*, Physics Review **D 69** (2004), 024008—+.
- [44] Torrey T. Lyons, *An optically recombined laser interferometer for gravitational wave detection*, Ph.D. thesis, California Institute of Technology, 1997.
- [45] M. Maggiore, *Gravitational wave experiments and early universe cosmology*, Phys. Reports **331** (2000), 283.
- [46] Jared Markowitz, Rick Savage, and Paul Schwinberg, *Development of a readout scheme for high-frequency gravitational waves*, Tech. report, LIGO Internal #: T030186, 2003.
- [47] G.C. McVittie, *General relativity and cosmology, the international astrophysics series volume four*, Chapman & Hall LTD.
- [48] Brian J. Meers, *Some aspects of the development of an optically sensed gravitational-wave detector*, Ph.D. thesis, Glasgow University, 1983.
- [49] Leonard Meirovitch, *Elements of vibration analysis*, McGraw-Hill Book Company, 1975.
- [50] A.C. Melissinos and W. Butler, *Search for high frequency signals at H4K*, Internal note 12/2002. See also LIGO-G030067-00-Z.
- [51] G. Mendell, We thank G. Mendell for assistance in obtaining the present data sample.
- [52] C.W. Misner, K.S. Thorne, and J.A. Wheeler, *Gravitation*, W.H. Freeman & Co., San Francisco, 1973.

- [53] Committee on Gravitational Physics, *Gravitational physics: Exploring the structure of space and time*, Board of Physics & Astronomy, Commission on Physical Sciences, Mathematics & Applications, 1999, <http://books.nap.edu/books/0309066352/html/index.html> page 35.
- [54] Operations and Research Sub panel for the National Science Foundation, *Advanced ligo webpage*, <http://www.ligo.caltech.edu/advLIGO/>.
- [55] Frank L. Pedrotti and Leno S. Pedrotti, *Introduction to optics*, Prentice Hall, Upper Saddle River, New Jersey 07458, 1993.
- [56] M. Rakhmanov, R.L. Savage Jr., D.H. Reitze, and D.B. Tanner, *Dynamic resonance of light in fabry-perot cavities*, Phys. Lett. **A305** (2002), 239–244.
- [57] Martin W. Regehr, *Signal extraction and control for an interferometric gravitational wave detector*, Ph.D. thesis, California Institute of Technology, 1995.
- [58] Martin W. Regehr, James E. Mason, and Hiro Yamamoto, *Twiddle (ver. 3.0) a program for analyzing interferometer frequency response (mathematica 3.0)*, Tech. report, Caltech, February 1999, LIGO Internal #: T990022.
- [59] Baha E.A. Saleh and M.C. Teich, *Fundamentals of photonics*, Wiley-Interscience, John Wiley & Sons, INC., 1991.
- [60] Peter R. Saulson, *Thermal noise in mechanical experiments*, Phys. Rev. **D42** (1990), no. 8, 2437–45.
- [61] ———, *If light waves are stretched by gravitational waves, how can we use light as a ruler to detect gravitational waves?*, American Journal of Physics **65** (1997), no. 6.

- [62] R. Savage and M. Rakhmanov, *Study of cavity field dynamics at high frequencies with the H1 interferometer*, LSC Meeting, Livingston, LA, March 2003, LIGO Internal #:G030058.
- [63] Rick Savage, *LHO detector e-log entries*, Reference arm length measurement on 4th, October 2002.
- [64] R. Schilling, *Angular and frequency response of LISA*, Classical and Quantum Gravity **14** (1997), 1513–1519.
- [65] Anthony E. Siegman, *Lasers*, University Science Books, 55D Gate Five Road Sausalito, California 94965, 1986.
- [66] Daniel Sigg, *Strain calibrations in LIGO*, Tech. report, LHO Hanford, March 1993, LIGO Internal #: T970101-B.
- [67] Daniel Sigg and ISC Group, *Frequency response of the LIGO interferometer*, Tech. report, LHO Hanford, February 2003, LIGO Internal #: T970084-B.
- [68] ISC team, *Length sensing & control subsystem final design*, Tech. report, Caltech, July 1998, LIGO Internal #: T980068.
- [69] M. Tinto, *Spacecraft to spacecraft coherent LASER tracking as a xylophone interferometer detector of gravitational radiation*, Phys. Rev. **D58** (1998), 102001.
- [70] Robbie Vogt, *A LASER interferometer gravitational-wave observatory (LIGO)*, Tech. report, Caltech and M.I.T., December 1989, LIGO Internal #: M890001.
- [71] J. Weber, Physical Review **117** (1960), 306.



- [72] ———, *Physical Review Letters* **22** (1969), 1302.
- [73] J. M. Weisberg and J. H. Taylor, *Observations of post-newtonian timing effects in the binary pulsar psr 1913+16*, *Physical Review Letters* **52** (1984), 1348–1350.
- [74] Michael Zeilik and Stephen A. Gregory, *Introductory astronomy and astrophysics*, Saunders College Publishing, Harcourt Brace & Company, 6277 Sea Harbor Drive Orlando, Florida 32887-6777, 1998.



# Appendix A

## “Strain Calibration in LIGO”

This appendix is a subsection of the LIGO Technical document T970101-B-D by D. Sigg [66]. The plots have been re-generated in matlab with the only difference appearing in Fig. A.3 in the time delay. As the difference between this plot and the one in the original paper only emphasize the point within the text (i.e. the effect is negligible) no further note shall be made of the difference.

### A.1 GW Interaction with an IFO Detector

#### A.1.1 The Coordinate System

We choose the coordinate system to be aligned with the two arms of the interferometer, where the origin is positioned at the beamsplitter and the z-axis points vertically upwards (see Fig. A.1). Spherical coordinates are defined by

$$r = \begin{bmatrix} r \sin \theta \cos \phi \\ r \sin \theta \sin \phi \\ r \cos \theta \end{bmatrix} \quad \text{with} \quad \begin{cases} 0 \leq \phi < 2\pi \\ 0 \leq \theta < \pi \end{cases} \quad (\text{A.1})$$

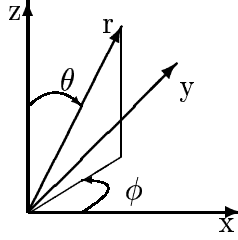


Figure A.1: Coordinate System

We then define the rotation operator  $O(\theta, \phi)$  which rotates the  $z$ -axis in the direction of  $r$ :

$$O(\theta, \phi) = O(\phi)O(\theta) \quad (\text{A.2})$$

$$\text{where } O(\phi) = \begin{bmatrix} \cos \phi & -\sin \phi & 0 \\ \sin \phi & \cos \phi & 0 \\ 0 & 0 & 1 \end{bmatrix} \quad \text{and} \quad O(\theta) = \begin{bmatrix} \cos \theta & 0 & \sin \theta \\ 0 & 1 & 0 \\ -\sin \theta & 0 & \cos \theta \end{bmatrix} \quad (\text{A.3})$$

### A.1.2 Round-Trip Phase Change

We write the phase of the light, which it acquires in one round-trip in one of the interferometer arms, as

$$\Phi_{rt}(t_0) = \int_{t_0}^{t_0+t(2L)} \omega dt \quad (\text{A.4})$$

where  $L$  is the length of the arm,  $\omega$  is the angular frequency of the light and  $t_0$  the time the photon leaves the origin. We now change the integration over time into one over length by using

$$d\tau^2 = dx_\mu g_{\mu\nu} dx^\nu = 0 \quad \text{with } g_{\mu\nu} = \eta_{\mu\nu} + h_{\mu\nu} \quad (\text{A.5})$$

where  $\eta_{\mu\nu}$  is the Minkovski metric and  $h_{\mu\nu}$  is the space-time ripple due to the gravitational wave [52]. For a gravitational wave traveling along the  $z$ -axis  $h_{\mu\nu}$

in the transverse-traceless gauge becomes

$$h_{\mu\nu} = \cos(\Omega t - kz) \left[ \begin{array}{c|ccc} 0 & 0 & 0 & 0 \\ \hline 0 & & & \\ 0 & & \hat{H}_{ik} & \\ 0 & & & \end{array} \right] \quad \text{with } \hat{H}_{ik} = \begin{bmatrix} h_+ & h_\times & 0 \\ h_\times & -h_+ & 0 \\ 0 & 0 & 0 \end{bmatrix} \quad (\text{A.6})$$

where  $\Omega$  is the angular frequency of the gravitational wave,  $k$  is its wave vector,  $h_+$  and  $h_\times$  are the wave amplitudes for the “+” and the “ $\times$ ” polarization, respectively.

For arbitrary directions one has to rotate both  $z$  and  $H_{ik}$  in the direction of the wave vector  $k$ .

$$kz \rightarrow k(k_x x + k_y y + k_z z) \quad \text{with} \quad \begin{cases} k_x = \sin \theta \cos \phi \\ k_y = \sin \theta \sin \phi \\ k_z = \cos \theta \end{cases} \quad (\text{A.7})$$

$$\hat{H}_{ik} \rightarrow H_{ik} = O(\theta, \phi) \hat{H}_{ik} O(\theta, \phi)^{-1} \equiv \begin{bmatrix} h_{xx} & h_{xy} & h_{xz} \\ h_{yx} & h_{yy} & h_{yz} \\ h_{zx} & h_{yz} & h_{zz} \end{bmatrix} \quad (\text{A.8})$$

For an integration along the x-axis or the y-axis  $h_{xx}$  and  $h_{yy}$  are the only relevant matrix elements, respectively.

$$h_{xx} = -\cos \theta \sin 2\phi h_\times + (\cos^2 \theta \cos^2 \phi - \sin^2 \phi) h_+ \quad (\text{A.9})$$

$$h_{yy} = \cos \theta \sin 2\phi h_\times + (\cos^2 \theta \sin^2 \phi - \cos^2 \phi) h_+ \quad (\text{A.10})$$

Fig. A.2 shows the angular dependence of  $|h_{xx} - h_{yy}|$  for both polarizations and their square-sum average. Using eqn.(A.5) we rewrite eqn.(A.4) as

$$\Phi_{rt}^x(t_0) = \frac{\omega}{c} \int_0^L \left\{ \sqrt{1 + h_{xx} \cos(\Omega t_0 + k(1 - k_x)x)} + \sqrt{1 + h_{xx} \cos(\Omega t_0 + k(2L - (1 + k_x)x))} \right\} dx \quad (\text{A.11})$$

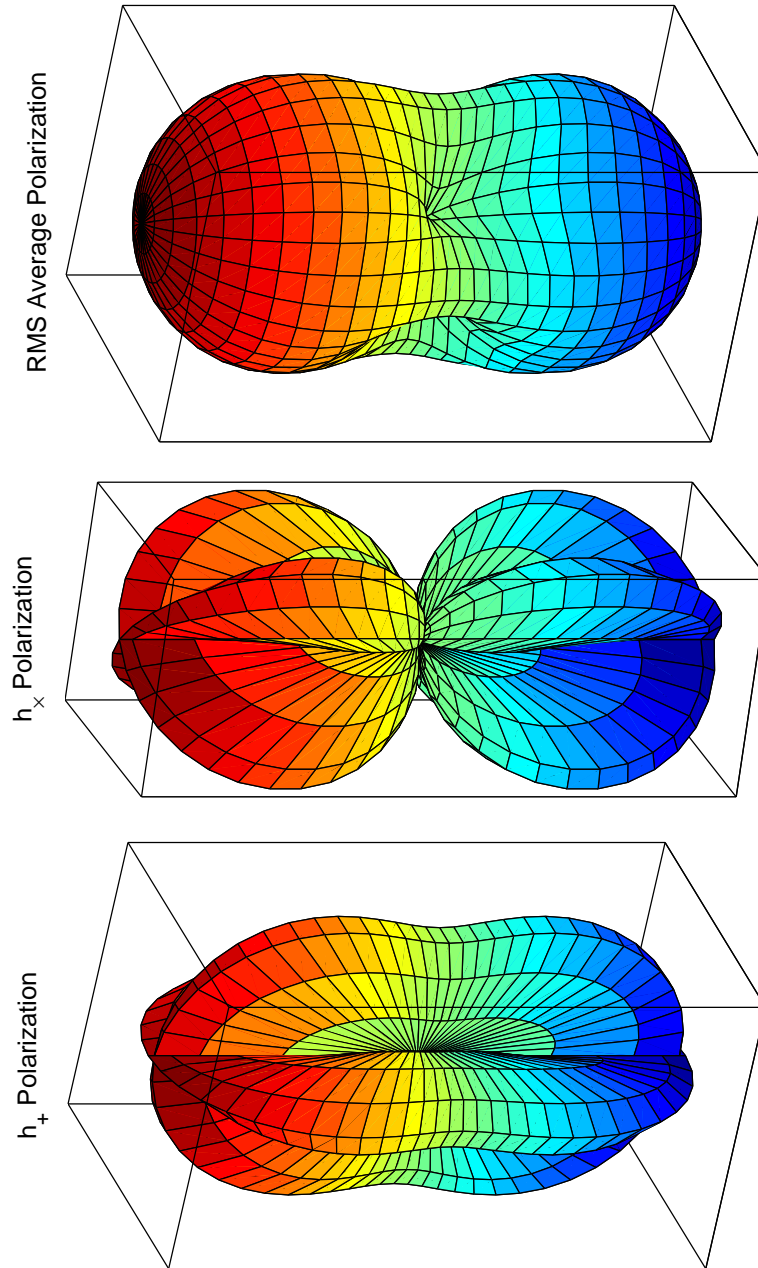


Figure A.2:  $h$  sensitivity as function of angle for the “+” polarization, the “ $\times$ ” polarization and the averaged polarization.

Similarly,  $\Phi_{rt}^y(t_0)$  can be obtained by integrating along the y-axis. Since  $h_{xx} \ll 1$  we can Taylor expand the square root of eqn.(A.11). Performing the integration, keeping only time-dependent terms, time-shift from departure to arrival, and changing to a complex notation where the absolute value denotes the amplitude and the argument denotes the phase shift, one gets:

$$\begin{aligned} \Delta\Phi_{rt}^x &= \frac{h_{xx}L\omega}{c} e^{-i\Phi_\Omega} \frac{\sin\Phi_\Omega + ik_x \cos\Phi_\Omega - ik_x e^{-ik_x\Phi_\Omega}}{\Phi_\Omega(1-k_x^2)} \\ &\approx \frac{h_{xx}L\omega}{c} \text{sinc}\Phi_\Omega \cos\left(\frac{k_x\Phi_\Omega}{\sqrt{12}}\right) e^{-i(1+k_x/2)\Phi_\Omega} \end{aligned} \quad (\text{A.12})$$

where  $\Phi_\Omega = L\Omega/c$ . The approximation yields the exact solution for a gravitational wave traveling along the z-axis. For all directions we assume  $\Phi_\Omega \ll 1$ . From eqn.(A.12) one sees that the signal delay for photons arriving at the origin is  $1 + k_x/2$  times half the round-trip time. The finite time a photon spends in a Michelson arm also leads to a small correction of the signal amplitude which would otherwise be determined by  $h_{xx}L$  only. Fig.A.3 shows the amplitude correction and time delay of the round trip phase of a gravitational wave as a function of  $k_x$  relative to one of normal incident and strength  $h_{xx}$ . These effects are generally small and in most cases negligible.

### A.1.3 Higher Frequency Response

It is useful to calculate the antenna pattern at higher frequencies. Since the arm cavities have a displacement response that is periodic in frequency and repeats itself every free-spectral-range, one might assume that response to gravitational waves follows this pattern. In particular, the displacement sensitivity of a Fabry-Perot cavity is as good at multiples of the free-spectral-range as it is at dc. However, at the free-spectral-range frequency the antenna length is also a multiple of a half-wave length of the gravitational wave. Using the variables

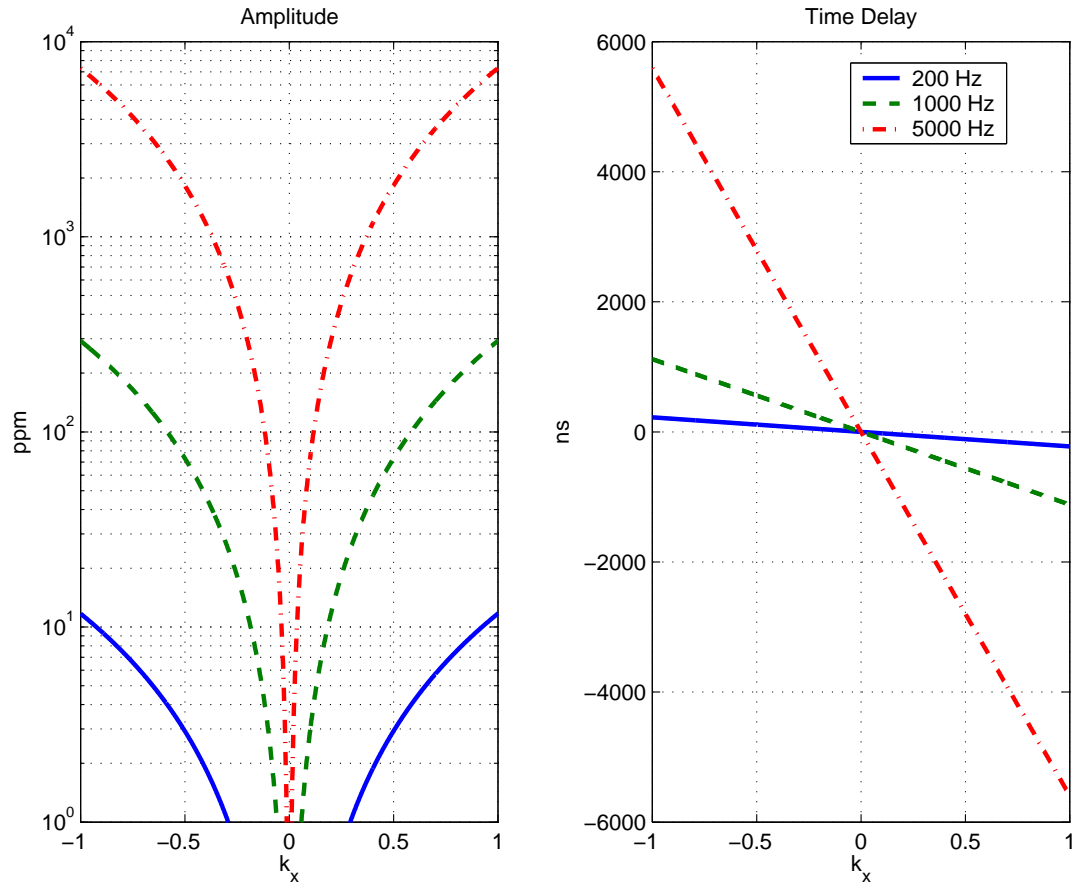


Figure A.3: Amplitude correction(left) and time delay of a gravitational wave with non-normal incident and frequencies of 200 Hz (solid curve), 1000 Hz (dashed) and 5000 Hz.



of eqn.(A.12) we can write:

$$\Omega = 2\pi m f_{\text{FSR}} = 2\pi m \frac{c}{2L} \Rightarrow \Phi_{\Omega} = \pi m \quad (\text{A.13})$$

This in turn will result in a zero of the term proportional to  $\text{sinc}\Phi_{\Omega}$  in the second line of eqn.(A.12), and may look like the response of a Fabry-Perot cavity to gravitational wave at the free-spectral-range frequency is identical zero. But, it was first recognized in ref.[64] that this is not true for all directions. Going back to the first line of eqn.(A.12) we see that for non-zero  $k_x$  the second and third term in the numerator will not vanish at the free-spectral-range. In Fig.A.4 we show the angular dependency of the sensitivity  $|H_{\text{FSR}}|$  for both polarizations and their square-sum average when the antenna length is  $\lambda/2$ . The boxes shown in this figure are roughly an order of magnitude smaller than the ones in Fig.A.2. The sensitivity at the first free-spectral-range can be simplified to:

$$H_{\text{FSR}} = \frac{h_{xx}(1 + e^{-i\pi k_x})ik_x}{\pi(1 - k_x^2)} - \frac{h_{yy}(1 + e^{-i\pi k_y})ik_y}{\pi(1 - k_y^2)} \quad (\text{A.14})$$

The polarization patterns are obtained as follows:

$$H_+ = H_{\text{FSR}}|_{h_{\times}=0, h_+=1}, H_{\times} = H_{\text{FSR}}|_{h_{\times}=1, h_+=0} \text{ and } \bar{H} = \sqrt{|H_+|^2 + |H_{\times}|^2} \quad (\text{A.15})$$

To estimate the overall loss of sensitivity at the free-spectral-range frequency we can compute the volume of the corresponding antenna pattern and compare it with the volume of the ‘‘peanut’’. The volume integral can be written as

$$V = \int_0^{2\pi} d\phi \int_0^{\pi} d\theta \int_0^{|H(\phi, \theta)|} dr r^2 \sin \theta. \quad (\text{A.16})$$

For the ratio of volumes  $V(\Phi_{\Omega} = \pi)/V(\Phi_{\Omega} = 0)$  we obtain a factor of about 1/150. Or, in other words the average range that a source can be seen is about a factor of 5.3 smaller at the first free-spectral-range frequency than at dc (assuming all other factors being equal).

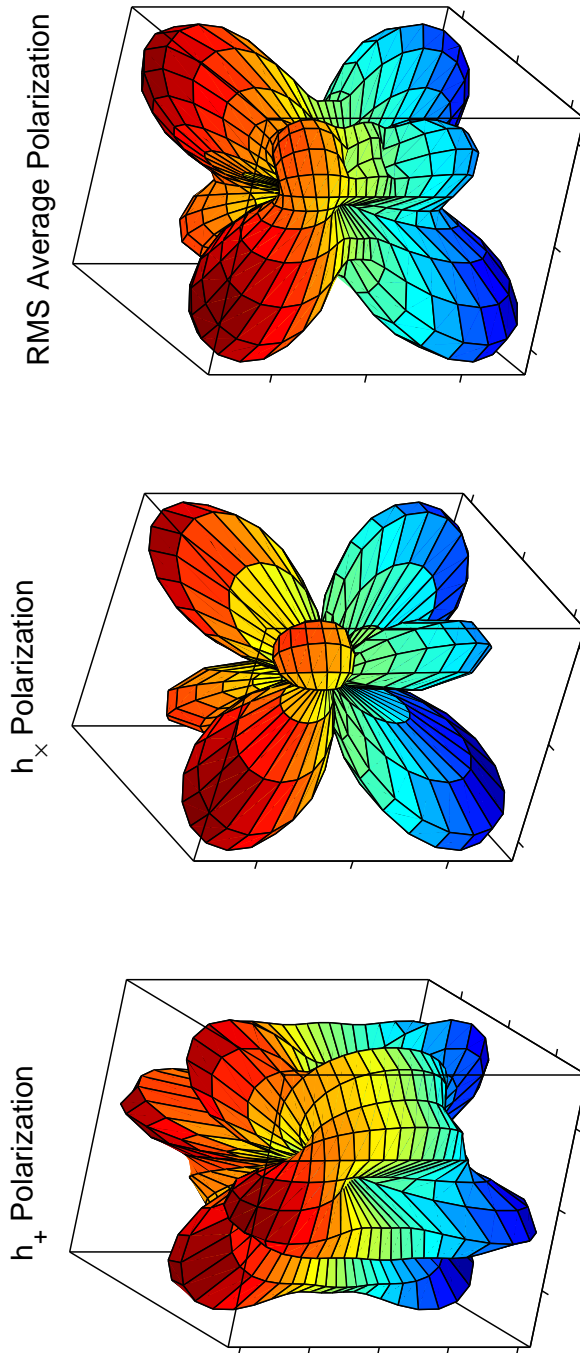


Figure A.4:  $h$  sensitivity for arm length  $\lambda/2$  as function of angle for the “+” polarization, the “ $\times$ ” polarization and the averaged polarization.

# Appendix B

## MATLAB functions and scripts

Throughout the course of data analysis I wrote and used several MATLAB scripts and functions. I will include some of the more relevant or referenced code here organized by directory structure. Please note that some of the command lines would extend well beyond the margins of the page if unedited. In these cases I have sometimes cut a single command into multiple lines. With this exception I have attempted to copy the code here verbatim.

This appendix is not included in this hardcopy version. The electronic version is available at <http://www.ligo.caltech.edu/> document number P040026-00-R.

## B.1 General Functions

Routines here are more general routines which were often called from within subdirectories for a variety of analysis.

### B.1.1 Bode Plot

Here is a simple function to input complex data and output a single figure with both a magnitude and phase plots. A variant form was used to plot the magnitude on a log scale which used the MATLAB function “semilogy” instead of “plot”. I will not include that variant.

```
function bplot(f,g)
%bode plot of g
figure;
subplot(2,1,1);
plot(f./1e3,abs(g));
grid on;xlabel('Frequency (kHz)');ylabel('Linear Magnitude');
phase = unwrap(angle(g),0.99*pi,2).*(180/pi);
subplot(2,1,2);
plot(f./1e3,phase);
grid on;xlabel('Frequency (kHz)');ylabel('Unwrapped Phase');
subplot(2,1,1);
return;
```

### B.1.2 Gaussian Curve Generation

Here is a routine to take needed input parameters and output a Gaussian curve. This was used in some instances to fit to data and is especially useful for masking

out 60 Hz line resonances.

```
function theory = gauss(f,f0,varargin)
% Series of Gaussian Curves
% gauss(f,f0,varargin)
% f = frequency for which the response is desired (can be array)
% f0 = resonant frequency (can be array)
% sigma = resonance sigma
%         (single number or array of same length as f0)
%         Default = 0.1
% A = resonance Amplitude (must be same length as sigma)
%         Default = 1
% N = Noise floor          (single number only)
%         Default = 0
% If complex parameters (f0,Q) are input then only the real part
% will be used.
% Complex A values are allowed to account for initial phase
% Complex N values are allowed to account for relative phase

sigma = 0.1;          % Default Q
A = 1;                % Default Normalization factor
N = 0;                % Default Noise Floor

if nargin > 2
    sigma = varargin{1}; % if supplied
    if nargin > 3
        A = varargin{2}; % Normalization factor if supplied;
```

```
if length(A) ~= length(sigma)
    disp('Error number of Amplitudes MUST = number of sigmas');
    theory = [];
    return;
end;
if nargin > 4
    N = varargin{3}; % Noise floor if supplied
    if length(N) > 1
        disp('Error Noise floor must be single value');
        theory = [];
        return;
    end;
end;
end;
end;
f0 = real(f0); % Just in Case Imaginary Arguments sent
sigma = real(sigma);
if length(f0) > 1
    if length(A) == length(sigma)
        if length(A) > 1
            % length(sigma) resonances each with their own sigma and A
            theory = 0;
            for k = 1:length(f0)
                tmp = (f-f0(k)).*(f-f0(k));
                term = A(k) .* exp(-tmp/(2*sigma(k)*sigma(k)));
                theory = theory + term;
            end;
        end;
    end;
end;
```

```
        end;
        theory = theory + N;
    else
        % length(f0) resonances each with SAME sigma and A
        theory = 0;
        for k = 1:length(f0)
            tmp = (f-f0(k)).*(f-f0(k));
            term = A .* exp(-tmp/(2*sigma^2));
            theory = theory + term;
        end;
        theory = theory + N;
    end;
end;

else
    if length(A) == length(sigma) == 1
        % single resonance single Q and N
        tmp = (f-f0).*(f-f0);
        theory = A .* exp(-tmp/(2*sigma^2)) + N;
    else
        disp('ERROR: Number of Resonances and attributes differ');
        mech = [];
        return;
    end;
end;

return;
```

### B.1.3 Mechanical Resonance Curve Generation

This routine is similar to the Gaussian curve generation in use, however it generates a Lorentzian curve as specified in Meirovitch [49] as a prediction for the resonance response of a mechanical system.

```
function mech = mech(f,f0,varargin)
% Mechanical Resonance Response as specified in Meirovitch
% "Elements of Vibration Analysis" Chapter 2
% mech(f,f0,varargin)
% f = frequency for which the response is desired (can be array)
% f0 = resonant frequency (only one per call)
% Q = resonance Q
% N = resonance Normalization
% If complex parameters (f0,Q) are input then only the real part
%   will be used.
% Complex N values are allowed to account for initial phase

Q = 1e6;          % Default Q
N = 1;           % Default Normalization factor

if nargin > 2
    Q = varargin{1};    % if supplied
    if nargin > 3
        N = varargin{2}; % Normalization factor if supplied;
    end;
end;

f0 = real(f0);      % Just in Case Imaginary Arguments sent
```



```

Q = real(Q);
if length(f0) > 1
    if length(N) == length(Q)
        if length(N) > 1
            % length(Q) resonances each with their own Q and N
            mech = 0;
            for k = 1:length(f0)
                den = 1 - (f./f0(k)).*(f./f0(k)) + i.*f ./ (Q(k)*f0(k));
                term = N(k)./(den.*Q(k));
                mech = mech + term;
            end;
        else
            % length(f0) resonances each with SAME Q and N
            % disp(length(f0));
            mech = 0;
            for k = 1:length(f0)
                den = 1 - (f./f0(k)).*(f./f0(k)) + i.*f ./ (Q*f0(k));
                term = N ./ (den .* Q);
                mech = mech + term;
            end;
        end;
    else
        disp('ERROR: Number of Normalizations and Qs differ');
        mech = [];
        return;
    end;
end;

```

```

else
    if length(N) == length(Q) == 1
        % single resonance single Q and N
        den = 1 - (f./f0).*(f./f0) + i.*f ./ (Q*f0);
        mech = N ./ (den.*Q);
    else
        disp('ERROR: Number of Resonances and attributes differ');
        mech = [];
        return;
    end;
end;

return;

```

### B.1.4 Step Function

On occasion it was useful to convolute some of the data with a step function to cut off data above (or below) a certain point.

```

function out = theta(in)
% theta (aka step) function
% out = 0 for all values of in < 0
% out = 1 for all values of in >= 0
% can take array of in values, returns array of out of same size
for k = 1:length(in)
    if in(k) < 0
        out(k) = 0;
    else

```

```
        out(k) = 1;
    end;
end;
return;
```

### B.1.5 Index Locator

Use of the theta function in combination with the MATLAB max function just to find the index of a specific frequency point was inefficient. Therefore this routine was written to more directly provide the index value. For example; if the current frequency (and data) arrays are for frequency values [0-1024] but I am only interested in frequencies from [200-800] Hz I can use the function in this way (where f is the full frequency array and d is the corresponding full data array):

```
i1 = index(f,200);
i2 = index(f,800);
f = f(i1:i2);
d = d(i1:i2);
```

This is most useful when interested in looking at the same frequency range through a series of data sets of variable frequency resolution.

```
function out = index(f,f0)
% index(array,value)
% input:  1) array of values
%         2) value of interest
% output:  index of the input array giving the location of the
%         value of interest.
```

```
% note: index returned is simply the first instance if multiple
%       instances if value is not in the array then 0 is returned

out = 0;
for ii = 1:length(f)
    if f(ii) == f0
        out = ii;
        break;
    end;
end;
return;
```

## B.2 Simple Fabry-Perot Cavity Calculations

Here are several functions which combine to give the response of a simple Fabry-Perot cavity.

### B.2.1 Reflectivity

The frequency dependent reflectivity of the cavity which is dependent also upon length.

```
function r = R(x,L)
%R = FP cavity reflectivityr1=(r1 + (r1^2 + t1^2)*r1)/(1+r1^2);
r1=sqrt(1-0.0281-0.000075);
r2=sqrt(1-0.000005-0.000070);
t1=sqrt(0.0281);
fsr=299792458/(2*L);
```

```

num = r1 - r2.*(r1^2 + t1^2).*exp(-i*2*pi*x/fsr);
den = 1 - r1.*r2.*exp(-i*2*pi*x/fsr);
r = num./den;
%lin = 9.041;
lin = 0;
r = exp(-i*2*pi*lin*x/299792458).*r;
return;

```

## B.2.2 Demodulation Parameter Calculation

Here is the  $\alpha$  parameter discussed in section 3.1.1.

```

function A = a(f,rf,L)
% alpha output
% f = frequency range of interest (in form of an array)
% rf = rf frequency
% nominally rf = 24481674.998;
% L = arm cavity length
% nominally L = 3995.056
A = conj(r(0,L)).*r(rf+f,L) + r(0,L).*conj(r(-rf-f,L))...
    -r(f,L).*conj(r(-rf,L)) - conj(r(-f,L)).*r(rf,L)...
    -conj(r(0,L)).*r(-rf+f,L) - r(0,L).*conj(r(rf-f,L))...
    +r(f,L).*conj(r(rf,L)) + conj(r(-f,L)).*r(-rf,L);
return;

```

Here is the  $\gamma$  parameter discussed in section 3.1.1.

```

function G = g(f,rf,L)
% gamma output

```

```

% f = frequency range of interest (in form of an array)
% rf = rf frequency
% nominally rf = 24481674.998;
% L = cavity arm length
% nominally L = 3995.056
G = conj(r(0,L)).*r(rf+f,L) + r(0,L).*conj(r(-rf-f,L))...
    -r(f,L).*conj(r(-rf,L)) - conj(r(-f,L)).*r(rf,L)...
    +conj(r(0,L)).*r(-rf+f,L) + r(0,L).*conj(r(rf-f,L))...
    -r(f,L).*conj(r(rf,L)) - conj(r(-f,L)).*r(-rf,L);
return;

```

### B.2.3 Demodulated Signal

Here is the in-phase demodulated function.

```

function FPI = fpi(f,phi,varargin)
% ASI with mixing angle phi
% rf = 24481674.998;
rf = 24481323;
if nargin > 2
    L = varargin{1};
else
    L = 3995.05948;
end;
p = (pi / 180) * phi;
FPI = a(f,rf,L).*sin(p) + g(f,rf,L).*(i*cos(p));
return;

```

Here is the quadrature phase demodulated function.

```

function FPQ = fpq(f,phi,varargin)
% ASQ with mixing angle phi
%rf = 24481674.998;
rf = 24481323;
if nargin > 2
    L = varargin{1};
else
    L = 3995.05948;
end;
p = (pi / 180) * phi;
FPQ = a(f,rf,L).*cos(p) - g(f,rf,L).*(i*sin(p));
return;

```

### B.2.4 Data Fitting

Generally within MATLAB I used the “lsqcurvefit” routine to fit data to a theory curve. In this particular instance I was running the fitting routine a number of different times and so wrote a small function to go through the common definitions and function calls needed without the need to remember and type them in again and again. Similar routines were also written which vary only in whether or not I fit to the complex data, real data, or real data with phase info.

```

%function FITFP = fitFP(n,data)
%function for fitting data to theory in matlab
%tmp = n(1) .* (fpi(data,n(2)) + n(3));
%FITFP = [abs(tmp);unwrap(angle(tmp))];
%return;

```

```

function [x,chi2,resnorm,residual] = fitfpmag(freq,data,L,varargin)
% funtion for fitting data magnitude to theory in matlab
% fit already assumes a 1/f dependence,
% remember when plotting results
%         tmp = x(1) .* (fpi(freq,x(2),L) + x(3))
% [abs(tmp);unwrap(angle(tmp))]
%         ~ [abs(data .* freq);unwrap(angle(data.*freq))]
% [x,chi2,resnorm,residual] = fitfpmag(freq,data,L,x0,rf,error)
% any number of outputs allowed [x] or [x,chi2] or ...
% inputs after L are optional (f,d,L) or (f,d,L,x0) or ...
% inputs:
% freq = frequency array of points
% data = complex array of measurement points
% L     = assumed length of FP cavity
% x0    = an array of initial fit parameters [x1,x2,x3]
% rf    = the rf frequency to be used, if default value to be
%         used enter an empty cell {}
% error= 100 * inverse of the percentage error of each data
%         point, to be used to determine chi squared
% outputs:
% x      = the fit parameters in an array [x1,x2,x3]
% chi2   = the chi squared value of the overall fit
% resnorm = the normalized residual (output from lsqcurvefit)
% residual = an array giving the residual between each data
%         point and the fitted point corresponding to it.
rf = 24481674.998;

```



```

error = 54.9;
fun = inline('
    [abs(x(1) .* (fpi(xdata(2:length(xdata))),x(2),xdata(1))+x(3)));
    unwrap(angle(x(1) .*
        (fpi(xdata(2:length(xdata))),x(2),xdata(1))+x(3))))] ',
    'x','xdata');
if nargin > 3
    x0 = varargin{1};
    if nargin > 4
        if size(varargin{2}) > 0
            rf = varargin{2};
        end;
        if nargin > 5
            error = varargin{3};
        end;
    end;
else
    x0 = [8,0,0];
end;
[x,resnorm,residual] =
    lsqcurvefit(fun,x0,[L,freq],
        [abs(data.*freq);unwrap(angle(data.*freq))]);
X = residual(1,:)./(abs(data.*freq)./error);
chi2 = sum(X.^2);

return;

```

Here is the routine which only fit the magnitude of the theory to the magnitude of the data.

```
function [x,chi2,resnorm,residual] = fitfpmag(freq,data,L,varargin)
% funtion for fitting data magnitude to theory in matlab
% fit already assumes a 1/f dependence,
%   remember when plotting results
%       fit = x(1) .* (fpi(freq,x(2),L) + x(3))
%       abs(fit) ~ abs(data .* freq)
% [x,chi2,resnorm,residual] = fitfpmag(freq,data,L,x0,rf,error)
% any number of outputs allowed [x] or [x,chi2] or ...
% inputs after L are optional (f,d,L) or (f,d,L,x0) or ...
% inputs:
%   freq = frequency array of points
%   data = complex array of measurement points
%   L    = assumed length of FP cavity
%   x0   = an array of initial fit parameters [x1,x2,x3]
%   error= 100 * inverse of the percentage error of each data
%           point, to be used to determine chi squared
% outputs:
%   x     = the fit parameters in an array [x1,x2,x3]
%   chi2  = the chi squared value of the overall fit
%   resnorm = the normalized residual (output from lsqcurvefit)
%   residual = an array giving the residual between each data
%               point and the fitted point corresponding to it.
error = 34.03;
fun =
```

```

inline(
    'abs(x(1) .* (fpi(xdata(2:length(xdata)),x(2),xdata(1))+x(3)))',
    'x','xdata');
if nargin > 3
    x0 = varargin{1};
    if nargin > 4
        error = varargin{2};
    end;
else
    x0 = [8,0,0];
end;
[x,resnorm,residual] = lsqcurvefit(fun,x0,[L,freq],abs(data.*freq));
X = residual./(abs(data.*freq)./error);
chi2 = sum(X.^2);

return;

```

### B.2.5 Shaking Response

In section 3.2.1 I discuss the differences in demodulation needed for investigating mirror excitation instead of phase noise injection. Here are the functions which take this difference into account. First is the basic reflectivity of the cavity.

```

function sr = SR(x,L)
%R = FP cavity reflectivity
r1=sqrt(1-0.0281-0.000075);
r2=sqrt(1-0.000005-0.000070);
t1=sqrt(0.0281);

```

```

fsr=299792458/(2*L);
num = (r1*t1^2*r2^2).*exp(-i*pi*x/fsr);
den = (1-r1*r2).*(1 - r1.*r2.*exp(-i*2*pi*x/fsr));
sr = num./den;
return;

```

### B.2.6 Shaking Demodulation Parameters

Here is the  $\alpha'$  parameter.

```

function SA = sa(f,rf,L)
% alpha output
% f = frequency range of interest (in form of an array)
% rf = rf frequency
% nominally rf = 24481674.998;
% L = arm cavity length
% nominally L = 3995.056
SA = feval(@r,-rf,L).*conj(feval(@sr,-f,L))...
    + feval(@sr,f,L).*conj(feval(@r,rf,L))...
    - feval(@sr,f,L).*conj(feval(@r,-rf,L))...
    - feval(@r,rf,L).*conj(feval(@sr,-f,L));
return;

```

And the  $\gamma'$  parameter.

```

function SG = sg(f,rf,L)
% alpha output
% f = frequency range of interest (in form of an array)
% rf = rf frequency

```

```

% nominally rf = 24481674.998;
% L = arm cavity length
% nominally L = 3995.056
SG = feval(@r,-rf,L).*conj(feval(@sr,-f,L))...
    + feval(@sr,f,L).*conj(feval(@r,rf,L))...
    + feval(@sr,f,L).*conj(feval(@r,-rf,L))...
    + feval(@r,rf,L).*conj(feval(@sr,-f,L));
return;

```

### B.2.7 Shaking Demodulation Functions

Here is the in-phase demodulation function for a mirror excitation.

```

function SFPI = sfpi(f,phi,varargin)
% FPI with mixing angle phi
% produced by shaking ITM or ETM
%rf = 24481674.998;
rf = 24481323;
if nargin > 2
    L = varargin{1};
else
    L = 3995.05948;
end;
p = (pi / 180) * phi;
SFPI = sa(f,rf,L).*sin(p) - sg(f,rf,L).*(i*cos(p));
return;

```

And the quadrature phase demodulation function for a mirror excitation.

```

function SFPQ = sfpq(f,phi,varargin)
% FPQ with mixing angle phi
% produced by shaking of ITM or ETM
%rf = 24481674.998;
rf = 24481323;
if nargin > 2
    L = varargin{1}
else
    L = 3995.05948;
end;
p = (pi / 180) * phi;
SFPQ = sa(f,rf,L).*cos(p) + sg(f,rf,L).*(i*sin(p));
return;

```

## B.3 Power Recycled Interferometer

This is a set of functions which were used for the analytic calculation of the full PRIFO response to both phase modulation and mirror excitation. Similarly to the simple FP case, I give the phase modulation routines and then the excitation specific routines.

### B.3.1 Arm Cavity Reflection

This is the same as the reflection for the simple FP but there is no need for an initial distance parameter between the laser and the cavity.

```

function r = R(x,L)
%R = FP cavity reflectivity

```

```

r1=sqrt(1-0.0281-0.000075);
r2=sqrt(1-0.000005-0.000070);
t1=sqrt(0.0281);
c = 299792458;
num = r1 - r2.*(r1^2 + t1^2).*exp(-i*4*pi*x*L/c);
den = 1 - r1.*r2.*exp(-i*4*pi*x*L/c);
r = num./den;
return;

```

### B.3.2 Demodulation Parameters

Here is the  $\alpha$  parameter

```

function A = a(f,rf,varargin)
% alpha output
% f = frequency range of interest (in form of an array)
% rf = rf frequency
% nominally rf = 24481674.998;
A = conj(as(0,varargin{:})).*as(rf+f,varargin{:})...
    + as(0,varargin{:}).*conj(as(-rf-f,varargin{:}))...
    - as(f,varargin{:}).*conj(as(-rf,varargin{:}))...
    - conj(as(-f,varargin{:})).*as(rf,varargin{:})...
    - conj(as(0,varargin{:})).*as(-rf+f,varargin{:})...
    - as(0,varargin{:}).*conj(as(rf-f,varargin{:}))...
    + as(f,varargin{:}).*conj(as(rf,varargin{:}))...
    + conj(as(-f,varargin{:})).*as(-rf,varargin{:});
return;

```

and the  $\gamma$  parameter

```

function G = g(f,rf,varargin)
% gamma output
% f = frequency range of interest (in form of an array)
% rf = rf frequency
% nomially rf = 24481674.998;
G = conj(as(0,varargin{:})) .* as(rf+f,varargin{:})...
    + as(0,varargin{:}) .* conj(as(-rf-f,varargin{:}))...
    - as(f,varargin{:}) .* conj(as(-rf,varargin{:}))...
    - conj(as(-f,varargin{:})) .* as(rf,varargin{:})...
    + conj(as(0,varargin{:})) .* as(-rf+f,varargin{:})...
    + as(0,varargin{:}) .* conj(as(rf-f,varargin{:}))...
    - as(f,varargin{:}) .* conj(as(rf,varargin{:}))...
    - conj(as(-f,varargin{:})) .* as(-rf,varargin{:});
return;

```

### B.3.3 Demodulation Functions

In-phase demodulation output from the anti-symmetric port

```

function ASI = asi(f,phi,varargin)
% ASI(f,phi) dark port output from FullIFO
% ASI with mixing angle phi at frequency f
rf = 24481323.5;
p = (pi / 180) * phi;
ASI = a(f,rf,varargin{:}) .* sin(p)
    + g(f,rf,varargin{:}) .* (i*cos(p));
return;

```

and quadrature phase demodulation output from the anti-symmetric port.



```

function ASQ = asq(f,phi,varargin)
% ASQ(f,phi) dark port output from FullIFO
% ASQ with mixing angle phi at frequency f
rf = 24481323.5;
p = (pi / 180) * phi;
ASQ = a(f,rf,varargin{:})*cos(p)
      - g(f,rf,varargin{:})*(i*sin(p));
return;

```

### B.3.4 Arm Cavity Shaking Response

Essentially the same as the basic arm cavity response with the lack of a prompt reflection (as it is the end mirror being shaken).

```

function sr = SR(x,L)
%R = FP cavity reflectivity
r1=sqrt(1-0.0281-0.000075);
r2=sqrt(1-0.000005-0.000070);
t1=sqrt(0.0281);
c = 299792458;
num = (r1*t1^2*r2^2).*exp(-i*6*pi*x*L/c);
den = (1-r1*r2).*(1 - r1.*r2.*exp(-i*4*pi*x*L/c));
sr = num./den;
return;

```

### B.3.5 Shaking Demodulation Parameters

First the  $\alpha$  parameter:

```

function SA = sa(f,varargin)
% alpha output for shaking
% f = frequency range of interest (in form of an array)
% Parameters set in file:
% rf = non-resonant sideband frequency (Hz)
rf = 24481323.5;
SA = as(-rf,varargin{:})*conj(sas(-f,varargin{:})) + ...
    sas(f,varargin{:})*conj(as(rf,varargin{:})) - ...
    sas(f,varargin{:})*conj(as(-rf,varargin{:})) - ...
    as(rf,varargin{:})*conj(sas(-f,varargin{:}));
return;

```

and then the  $\gamma$  parameter

```

function SG = sg(f,varargin)
% gamma output for shaking
% f = frequency range of interest (in form of an array)
% Parameters set in file:
% rf = non-resonant sideband frequency (Hz)
rf = 24481323.5;
SG = as(-rf,varargin{:})*conj(sas(-f,varargin{:})) + ...
    sas(f,varargin{:})*conj(as(rf,varargin{:})) + ...
    sas(f,varargin{:})*conj(as(-rf,varargin{:})) + ...
    as(rf,varargin{:})*conj(sas(-f,varargin{:}));
return;

```

### B.3.6 Shaking Demodulation Outputs

First the in-phase anti-symmetric port output:

```

function SASI = sasi(f,phi,varargin)
% SASI(f,phi,...) dark port output from FullIFO, shaking input
% ASI with mixing angle phi at frequency f
% further parameters are passed along to sa and sg
% which pass them on to as and sas
p = (pi / 180) * phi;
SASI = sa(f,varargin{:})*sin(p) + sg(f,varargin{:})*(i*cos(p));
return;

```

and now the quadrature phase AS port output:

```

function SASQ = sasq(f,phi,varargin)
% SASQ(f,phi,...) dark port output from FullIFO, shaking input
% ASQ with mixing angle phi at frequency f
% further parameters are passed along to sa and sg
% which pass them on to as and sas
p = (pi / 180) * phi;
SASQ = sa(f,varargin{:})*cos(p) - sg(f,varargin{:})*(i*sin(p));
return;

```

## B.4 Matrix Method Calculations

Here I present the code for the matrix method presented in section 3.2.2. Here I also have both a simple FP cavity and a full PRIFO.

### B.4.1 FP Matrix Code

Here is the root of the matrix method calculation.

```
function tw = tw(f,varargin)
% Butler's continuing modifications of the twiddle
% algorithm in matlab for simple FP
% f = array of input frequencies (can be scalar)
% varargin: optional arguments
% y = input matrix, default is SB injection
% y = [1;0;0;0;0;0;0]; by default
% y = [0;0;0;0;0;-i;0]; for ETM shaking
% z = output matrix, matrix of fields to output
% z = [2] by default
% L = cavity length
%   As ALL FIELDS ARE CALCULATED EVERY TIME
%   it is best to call the program only once
%   and get all the fields of interest
%   eg. if you want field 2 and 3 call
%       tw(f,y,[4;9])
% Define Fields
% 1 = incident on mirror 1 from source (right)
% 2 = reflected from mirror 1 back to source (left)
% 3 = transmitted through mirror 1 (right)
% 4 = incident on mirror 1 from mirror 2 (left)
% 5 = incident on mirror 2 from mirror 1 (right)
% 6 = reflected from mirror 2 to mirror 1 (left)
% 7 = transmitted through mirror 2 (right)

% Define Lengths and frequencies
```

```
if nargin > 3
    L = varargin{3};
else
    L = 3995.05948;
end;
c = 299792458;
ph2 = 2*pi*L.*f./c;
n = length(f);

% Define reflectivities and transmittance
r1=sqrt(1-0.0281-0.000075);
r2=sqrt(1-0.000005-0.000070);
t1=sqrt(0.0281);
t2=sqrt(0.000005);

% Create Matrix
A(1,1,1:n) = 1;
A(2,1,1:n) = -r1;
A(2,2,1:n) = 1;
A(2,4,1:n) = -i*t1;
A(3,1,1:n) = -i*t1;
A(3,3,1:n) = 1;
A(3,4,1:n) = -r1;
A(4,4,1:n) = 1;
A(4,6,:) = -exp(-i.*ph2);
A(5,3,:) = -exp(-i.*ph2);
```

```
A(5,5,1:n) = 1;
A(6,5,1:n) = -r2;
A(6,6,1:n) = 1;
A(7,5,1:n) = -i*t2;
A(7,7,1:n) = 1;

%B = A;
%B(2,1,1:n) = r1;
%B(2,4,1:n) = -t1;
%B(3,1,1:n) = -t1;
%B(3,4,1:n) = -r1;
%B(6,5,1:n) = -r2;
%B(7,5,1:n) = -t2;
%A = B;

% input vector
y = [1;zeros(6,1)];
if nargin > 1
    if length(varargin{1}) == length(y)
        y = varargin{1};
    else
        display('Invalid input matrix');
    end;
end;

for k = 1:n
```

```

    tmp = A(:, :, k) \ y;
    Ebi(:, k) = tmp;
end;

if nargin > 2
    for k = 1:length(varargin{2})
        tw(k, :) = Ebi(varargin{2}(k), :);
    end;
else
    tw = Ebi(2, :);
end;

return;

```

### B.4.2 FP Demodulation Parameters

Here is a single function which returns both the  $\alpha$  and  $\gamma$  parameters for demodulation for both the phase modulation and mirror excitation calculations. As one can easily see this code was written later and is more general, adaptable and complex.

```

function [A,G] = ag(f,rf,varargin)
% alpha gamma output [A;G] = ag(f,rf,varargin)
% f = frequency range of interest (in form of an array)
% rf = rf frequency
% nominally rf = 24481674.998;
% varargin parameters specifying SB injection of mirror excitation
% and further parameters to pass on to tw

```

```

yrf = [1;zeros(6,1)];
if (nargin == 2) | (varargin{1} == yrf)
    % Code Modified to minimize calls to tw subroutine
    car = tw(0,varargin{:});
    prf = tw(rf,varargin{:});
    mrf = tw(-rf,varargin{:});
    pf = tw(f,varargin{:});
    mf = tw(-f,varargin{:});
    pa = tw(rf+f,varargin{:});
    ma = tw(-rf-f,varargin{:});
    pb = tw(rf-f,varargin{:});
    mb = tw(-rf+f,varargin{:});

    A = conj(car).*pa...
        + car.*conj(ma)...
        - pf.*conj(mrf)...
        - conj(mf).*prf...
        - conj(car).*mb...
        - car.*conj(pb)...
        + pf.*conj(prf)...
        + conj(mf).*mrf;
    G = conj(car).*pa...
        + car.*conj(ma)...
        - pf.*conj(mrf)...
        - conj(mf).*prf...
        + conj(car).*mb...

```



```

    + car.*conj(pb)...
    - pf.*conj(prf)...
    - conj(mf).*mrf;
elseif length(varargin{1}) == length(yrf)
    y = varargin{1};
    if length(varargin) > 1
        other = {varargin{2:length(varargin)}};
    else
        other = {};
    end;
    % Code modified to minimize calls to tw subroutine
    mrf = tw(-rf,yrf,other{:});
    prf = tw(rf,yrf,other{:});
    pf = tw(f,y,other{:});
    mf = tw(-f,y,other{:});

    A = mrf.*conj(mf)...
        + pf .*conj(prf)...
        - pf .*conj(mrf)...
        - prf.*conj(mf);
    G = mrf.*conj(mf)...
        + pf .*conj(prf)...
        + pf .*conj(mrf)...
        + prf.*conj(mf);
else
    display('Error input vector length incorrect');

```

```
end;
```

```
return;
```

### B.4.3 FP Demodulation Functions

At this point calculation of the in-phase and quadrature demodulation outputs is rather simple. Here is the in-phase function first.

```
function FPI = fpi(f,phi,varargin)
% FPI = fpi(f,phi,varargin)
% FPI with mixing angle phi
% rf = set in this file
% lengths and other parameters set in tw.m
% f = frequency for analysis
% phi = mixing angle (degrees) between optimum I and Q
% varargin = parameters passed on to tw.m
% note when calling for demodulated outputs you can only
% request one output field at a time.
% To study Simple FP call functions fpi and fpq
% To study Full LH04k call functions asi and asq
rf = 24481323;

p = (pi / 180) * phi;
[alpha,gamma] = ag(f,rf,varargin{:});
FPI = alpha.*sin(p) + gamma.*(i*cos(p));
return;
```

Followed by the quadrature phase function.

```

function FPQ = fpq(f,phi,varargin)
% FPQ = fpq(f,phi,varargin)
% FPQ with mixing angle phi
% rf = set in this file
% lengths and other parameters set in tw.m
% f = frequency for analysis
% phi = mixing angle (degrees) between optimum I and Q
% varargin = parameters passed on to tw.m
% note when calling for demodulated outputs you can only
% request one output field at a time.
% To study Simple FP call functions fpi and fpq
% To study Full LH04k call functions asi and asq
rf = 24481323;

p = (pi / 180) * phi;
[alpha,gamma] = ag(f,rf,varargin{:});
FPQ = alpha.*cos(p) - gamma.*(i*sin(p));
return;

```

#### B.4.4 AS Matrix Code

Here is the root of the matrix method calculation for the full PRIFO. This routine outputs the E field at any point within the configuration, the default is for the AS port.

```

function tw2 = tw2(f,varargin)
% tw2 = tw2(f,varargin)
% algorithm in matlab for Full PRIFO with FP arms

```

```

% f = array of input frequencies (can be scalar)
% varargin: optional arguments (y,xi,asym,z)
% y = input matrix, default is SB injection
% y = [1;zeros(22,1)]; by default (SB injection)
% y = [zeros(13,1);-i;zeros(9,1)]; for ETMX shaking
% y = [zeros(21,1);-i;0]; for ETMY shaking
% y = [zeros(13,1);-i;zeros(7,1);-i;0]; for CM shaking
% y = [zeros(13,1);i;zeros(7,1);-i;0]; for DM shaking
% xi = degrees off perfect dark port conditions
% asym = Michelson Asymmetry
% Ymod = modification to Y-arm length
% z = output matrix, matrix of fields to output
% z = [23] by default (AS port output)
%   As ALL FIELDS ARE CALCULATED EVERY TIME
%   it is best to call the program only once
%   and get all the fields of interest
%   eg. if you want field 2 and 3 call
%       tw(f,y,[4;9])
% Define Fields
% 1 = incident on RM from source      (right)
% 2 = reflected from RM back to source (left)
% 3 = transmitted through RM         (right)
% 4 = incident on RM from BS         (left)
% 5 = incident on BS from RM         (right)
% 6 = transmitted through BS from X  (left)
% 7 = transmitted through BS from RM (right)

```

```
% 8 = incident on BS from X          (left)
% 9 = incident on ITMX from BS       (right)
% 10 = reflected from ITMX to BS     (left)
% 11 = transmitted through IMTX      (right)
% 12 = incident on ITMX from ETMX    (left)
% 13 = incident on ETMX from ITMX    (right)
% 14 = reflected from ETMX to ITMX   (left)
% 15 = reflected from BS to ITMY     (up)
% 16 = incident on BS from ITMY      (down)
% 17 = incident on ITMY from BS      (up)
% 18 = reflected from ITMY to BS     (down)
% 19 = transmitted through ITMY      (up)
% 20 = incident on ITMY from ETMY    (down)
% 21 = incident on EMTY from ITMY    (up)
% 22 = reflected from ETMY to ITMY   (down)
% 23 = transmitted through BS from Y (down)
```

```
% Define Lengths and frequencies
Lx = 3995.05948;          % X-arm length
Ly = 3995.01332;          % Y-arm length
```

```
Ymod = 0;
if nargin > 3
    asym = varargin{3};
    if nargin > 4
        Ymod = varargin{4};
```

```

else
    Ymod = 0;
end;
else
    asym = 0.110;
end;          % Length modifications
Ly = Ly + Ymod;
lx = 6.191 - asym;    % Schematic D970003-00-D says
ly = 6.191 + asym;    % RC Optical length = 9191 mm
lin = 3;             % RC asymmetry    = +- 150 mm
c = 299792458;       % speed of light
Px = 2*pi*Lx.*f./c;  % Propogator X-arm
Py = 2*pi*Ly.*f./c;  % Propogator Y-arm
px = 2*pi*lx.*f./c;  % Propogator BS - ITMx
py = 2*pi*ly.*f./c;  % Propogator BS - ITMy
pin = 2*pi*lin.*f./c; % Propogator RM - BS
n = length(f);       % number of frequency points
if nargin > 2
    xi = varargin{2} * pi / 180;
else
    xi = 0;
end;          % Quality of Lock parameter

py = py - xi/2;     % Easiest and most logical
px = px + xi/2;     % way to insert chi

```

```

% Define reflectivities and transmittance
ritm = sqrt(1-0.0281-0.000075);    % ITM
retm = sqrt(1-0.000005-0.000070); % ETM
titm = sqrt(0.0281);              % ITM
tetm = sqrt(0.000005);            % ETM
rrm  = sqrt(1-0.0281-0.000075);    % RM
rbs  = sqrt(1-0.49995-0.000070);   % BS
trm  = sqrt(0.0281);              % RM
tbs  = sqrt(1-0.49995-0.000070);   % BS

% optional params for lossless optics
%ritm = sqrt(1-0.0281);
%retm = sqrt(1);
%itm  = sqrt(0.0281);
%tetm = sqrt(0);
%rrm  = sqrt(1-0.028);
%rbs  = sqrt(.5);
%trm  = sqrt(.028);
%tbs  = sqrt(.5);

% Create Matrix
for k = 1:23
    A(k,k,1:n) = 1;    % Create n kxk identity matrices
end;                  % Now stick in the propogators
A(2,1,:) = -rrm;     % and refl/trans coefficients
A(2,4,:) = -i*trm;

```

```
A(3,1,:) = -i*trm;
A(3,4,:) = -rrm;
A(4,6,:) = -exp(-i*pin);
A(5,3,:) = -exp(-i*pin);
A(6,8,:) = -i*tbs;
A(6,16,:) = -rbs;
A(7,5,:) = -i*tbs;
A(8,10,:) = -exp(-i*px);
A(9,7,:) = -exp(-i*px);
A(10,9,:) = -ritm;
A(10,12,:) = -i*titm;
A(11,9,:) = -i*titm;
A(11,12,:) = -ritm;
A(12,14,:) = -exp(-i*Px);
A(13,11,:) = -exp(-i*Px);
A(14,13,:) = -retm;
A(15,5,:) = -rbs;
A(16,18,:) = -i*exp(-i*py);
A(17,15,:) = -i*exp(-i*py);
A(18,17,:) = -ritm;
A(18,20,:) = -i*titm;
A(19,17,:) = -i*titm;
A(19,20,:) = -ritm;
A(20,22,:) = -exp(-i*Py);
A(21,19,:) = -exp(-i*Py);
A(22,21,:) = -retm;
```



```
A(23,8,:) = -rbs;
A(23,16,:) = -i*tbs;

% input vector
y = [1;zeros(22,1)]; % default SB injection
if nargin > 1 % if other injection point specified
    if length(varargin{1}) == length(y)
        y = varargin{1};% use it
    else % if specified, but incorrectly
        display('Invalid input matrix');
        tw2 = 0; % assign some value
        return % and return on error
    end;
end;

for k = 1:n % Do the Matrix Inversion
    tmp = A(:, :,k)\y;
    Ebi(:,k) = tmp;
end;

if nargin > 5 % if specific output(s) specified
    for k = 1:length(varargin{5}) % use them
        tw2(k,:) = Ebi(varargin{5}(k),:);
    end;
else
    tw2 = Ebi(23,:); % otherwise give AS port output
```

```
end;
```

```
return;
```

### B.4.5 AS Demodulation Parameters

Again I calculate both the  $\alpha$  and the  $\gamma$  parameter in the same function. Also I enlarged the function so as to eliminate the need for separately calculating the  $\alpha'$  and  $\gamma'$  parameters.

```
function [A,G] = ag2(f,rf,varargin)
% alpha gamma ouput [A;G] = ag2(f,rf,varargin)
% f = frequency range of interest (in form of an array)
% rf = rf frequency
% nominally rf = 24481674.998;
% varargin parameters specifying SB injection of mirror
% excitation and further parameters to pass on to tw2
yrf = [1;zeros(22,1)];
if (nargin == 2) | (varargin{1} == yrf)
    % Code Modified to minimize calls to tw2 subroutine
    car = tw2(0,varargin{:});
    prf = tw2(rf,varargin{:});
    mrf = tw2(-rf,varargin{:});
    pf = tw2(f,varargin{:});
    mf = tw2(-f,varargin{:});
    pa = tw2(rf+f,varargin{:});
    ma = tw2(-rf-f,varargin{:});
    pb = tw2(rf-f,varargin{:});
```

```

mb = tw2(-rf+f,varargin{:});

A = conj(car).*pa...
  + car.*conj(ma)...
  - pf.*conj(mrf)...
  - conj(mf).*prf...
  - conj(car).*mb...
  - car.*conj(pb)...
  + pf.*conj(prf)...
  + conj(mf).*mrf;
G = conj(car).*pa...
  + car.*conj(ma)...
  - pf.*conj(mrf)...
  - conj(mf).*prf...
  + conj(car).*mb...
  + car.*conj(pb)...
  - pf.*conj(prf)...
  - conj(mf).*mrf;
elseif length(varargin{1}) == length(yrf)
y = varargin{1};
if length(varargin) > 1
    other = {varargin{2:length(varargin)}};
else
    other = {};
end;
% Code modified to minimize calls to tw2 subroutine

```

```
mrf = tw2(-rf,yrf,other{:});
prf = tw2(rf,yrf,other{:});
pf  = tw2(f,y,other{:});
mf  = tw2(-f,y,other{:});

A = mrf.*conj(mf)...
  + pf .*conj(prf)...
  - pf .*conj(mrf)...
  - prf.*conj(mf);
G = mrf.*conj(mf)...
  + pf .*conj(prf)...
  + pf .*conj(mrf)...
  + prf.*conj(mf);
else
    display('Error input vector length incorrect');
end;

return;
```

### B.4.6 AS Demodulation Functions

At this point calculation of the in-phase and quadrature demodulation outputs is rather simple. As by the time I wrote this routine I was running sufficiently detailed simulations that computation time was becoming something of an annoyance I merged routines of the two phases of demodulation into one function. As this does not increase the computation necessary for a single demodulated output and cuts in half the computation necessary for two demodulated outputs,

it seemed a prudent step.

```
function [ASI,ASQ] = asiq(f,phi,varargin)
% [ASI,ASQ] = asiq(f,phi,varargin)
% ASI sin demodulation with mixing angle phi
% ASQ cos demodulation with mixing angle phi
% rf = set in this file
% lengths and other parameters set in tw.m
% f = frequency for analysis
% phi = mixing angle (degrees) between optimum I and Q
% varargin = parameters passed on to tw2.m
% note when calling for demodulated outputs you can only
% request one output field at a time.
% To study Simple FP call functions fpi and fpq
% To study Full LH04k call functions asi and asq
rf = 24481323;

p = (pi / 180) * phi;
[alpha,gamma] = ag2(f,rf,varargin{:});
ASI = alpha.*sin(p) + gamma.*(i*cos(p));
ASQ = alpha.*cos(p) - gamma.*(i*sin(p));
return;
```

## B.5 Frame Data Analysis

Frame data from the S3 run was obtained for the channel H1:LSC-AS\_1FSR during a long lock stretch. This data was stored locally on the hard drive and

analyzed.

### B.5.1 Reading in the Data

The time series was converted into frequency representation by use of the MATLAB digital Fourier transform function as implemented in the routine “datamasage.m”. As the data was in frame format (specific to LIGO) a LIGO specific tool was used to read out the data. This was a compiled mexglx file obtained from the LIGO-Tools repository for specifically this purpose, reading frame file data into MATLAB. The help header of that routine is included here:

```
% FREXTRACT - Read time-series data from a frame file
% by B. Mours LAPP   Oct 22, 2002
%
% This Matlab mex file extract from a frame file the data for
%   one ADC channel (this is for Matlab version 5 and later)
%
% The input arguments are:
%   1) file name
%   2) ADC or PROC name
%   3) (optional) first frame (default= first frame in the file)
%   4) (optional) number of frame (default = 1 Frames)
%
% Returned matlab data:
%   1) ADC or PROC data (time serie)
%   2) (optional) time values relative to the first data point
%   3) (optional) frequency values (for FFT's)
%   4) (optional) GPS starting time (in second.nanosec)
```

```

% 5) (optional) starting time as a string
% 6) (optional) ADC comment as a string
% 7) (optional) ADC unit as a string
% 8) (optional) additional info: it is a 9 words vector which
%     content:crate #, channel#, nBits#, bias, slope,
%           sampleRate, timeOffset(S.N), fShift, overRange
%     All this values are stored as double

```

And here is my routine for reading in and manipulating the data as requested prior to analysis.

```

function varargout = datamassage(varargin)
% datamassage -- read data from a local repository on the HD
%     uses standard LIGOTools Fr package tool 'frextract'
% by William Butler, Jan 15th, 2004.
%
% The input arguments are:
% 1) (optional) number of averages to get, default is 1
% 2) (optional) starting frame, default is 1 (first file in the
%           directory)
% 3) (optional) number of frames per average, default is 1
% 4) (optional) baddata threshold, default -1e9 (i.e. none)
% 5) (optional) array of frames to skip must be of
%           length = argument 1
%           default is zeros(1,number of frames to get)
% 6) (optional) array of output strings characterizing data
%
% The output arguments are:

```

```
% 1) time series data
% 2) (optional) time values relative to the first data point
% 3) (optional) frequency values (for FFT's)
% 4) (optional) FFT1
% 5) (optional) phase
directory = '/home/butler/RDS/';
channel   = 'H1:LSC-AS_1FSR';
start     = 1;
num       = 1;
NumPerFFT = 1;
Thresh    = -1e9;
massaged  = 0;
total     = 0;
% default values set, now read in the optional parameters
if nargin > 0
    num = varargin{1};
    if nargin > 1
        start = varargin{2};
        if nargin > 2
            NumPerFFT = varargin{3};
            if nargin > 3
                Thresh = varargin{4};
            end;
        end;
    end;
end;
end;
```



```
if nargin > 4
    skip = varargin{5};
else
    skip = zeros(1,num);
end;
% list all the files in the directory, assume all frame files
files = dir(directory);
% win is a parameter used to downsample the time series info to
% avoid buffer overflow from too many data points
win = num - start + 1;
stop = num + start - 1;
data = [];
time = [];
fftd = 0;
fft1 = 0;
phase = 0;
disp('starting ');
for k = start:stop
    % start averaging
    if skip(k-start+1)
        continue; % unless it's a skipped frame
    end;
    tmp1 = [];
    tmp2 = [];
    tmp3 = [];
    for l = 1:NumPerFFT
```

```

% read in as many files as needed per FFT
s = sprintf('%s%s',directory,files(k+1+1).name);
[tmpa,tmpb,tmpc] = frextract(s,channel);
tmp1 = [tmp1;tmpa];
tmp2 = [tmp2;tmpb+(16*(1-1))];
tmp3 = [tmp3;
        (tmpc + (1-1)*(tmpc(2)+tmpc(length(tmpc)))) ./NumPerFFT];
end;
avg = mean(tmp1);
while min(tmp1) < Thresh
    % set points below threshold to the average value
    massaged = massaged + 1;
    [m,i] = min(tmp1);
    tmp1(i) = avg;
    avg = mean(tmp1);
end;
tmp = tmp1 .* (0.5 * (1-cos(2*pi*tmp2./16)));
        % Hanning window, no overlap
fftd = fft(tmp);
fft1 = fft1 + abs(fftd);
phase = phase + angle(fftd);
total = total + length(tmp2);
if (win > 1)
    % if downsampling is necessary, do it
    tmp1 = filtfilt(ones(1,win)/win,1,tmp1);
    tmp1 = downsample(tmp1,win);

```





```

% output argument
varargout{6} = {string0;string1;string2;string3;
                string4;string5;string6};
return;

```

## B.5.2 Pre-analysis Manipulation

Line noise at multiples of 60 Hz was anticipated and observed, so these lines were removed. This was done with two routines. The first takes a frequency array as an input (and an optional second input) and locates the multiples of 60 Hz (or of the second input) which are located in the frequency array. The second function takes a data set and its corresponding frequency array and masks out data spikes at multiples of 60 Hz.

```

function linemask = linemask(f,varargin)
% linemask = linemask(f,varargin)
% linemask(f,f0) returns frequencies of all multiples of
% f0 in the frequency range f.
% Usefull for creation of a frequency mask
% f0 is an OPTIONAL argument, default is just 60 Hz,
% optionally an array of frequencys (eg [16;60])
% filter = 1 - gauss(f,linemask);
% filterdata = data .* filter

if nargin > 1
    f0 = varargin{1};
else
    f0 = 60;

```

```
end;

temp = [];
for kk = 1:length(f0)
    bottom = fix(f(1) / f0(kk));
    top = fix(f(length(f)) / f0(kk));

    donethat = [];
    for jj = bottom:top
        if length(temp) > 0
            donethat = find(temp == f0(kk)*jj);
        end;
        if length(donethat) > 0
            continue;
        end;
        temp = [temp;f0(kk)*jj];
    end;
end;
temp = sort(temp);

linemask = temp;
return;
```

This function calls the last function as well as making use of the Gaussian function defined previously.

```
function maskdata = maskdata(f,d,varargin)
% maskdata(f,d,varargin)
```

```

% remove the 60 Hz multiple line noise and replace
% with data mean value optional input is f0 an array
% of the base frequencies for which you
% wish to remove the multiples (eg [16;60])

if nargin > 2
    mfreq = linemask(f,varargin{1});
else
    mfreq = linemask(f);
end;
mask = gauss(f,mfreq,0.2);
maskdata = d.*(1-mask);
avg = mean(maskdata);
maskdata = maskdata + avg.*mask;
return;

```

### B.5.3 Data Analysis

Primarily the data fitting is done with the use of the MATLAB `lsqcurvefit` routine. This function is used as the first parameter for `lsqcurvefit`. The section for hard coding specific values was used for changing which parameters were fit with a relative phase and for hard coding specific magnitude values to generate  $\chi^2$  plots.

```

function varargout = FSR_datafit(varargin)
% FSR_datafit (theory for H1:LSC-AS_1FSR channel data):
% A1*exp(i*A1phi*pi/180) + A2*exp(i*A2phi*pi/180)*f
% + A3*exp(i*A3phi*pi/180)*theory(f)

```

```

% + A4*exp(i*A4phi*pi/180)*theory2(f)
% = A + B*f + C*theory(f) + D*theory2(f) + ...
% inputs:
% 1) [[A1,A1phi];[A2,A2phi];[A3,A3phi];[A4,A4phi];...]
% 2) [frequency;theory;theory2;...] must be 1 x N arrays,
%           theory, theory2, ... are optional
% input data is formatted strangely to allow for easy use in
% matlab function lsqcurvefit
% The first parameters are Magnitude and Phase (in degrees)
% of theory arguments (formatted this way to allow for
% real input parameters to generate complex data)
% The second parameters are the theory arguments themselves
% If the length of input #1 < 1 + length input #2 then the
% extra theories are fit with Magnitude 1 and Phase 0
% outputs:
% 1) absolute magnitude of the resulting function

%if nargin ~= 2
% error('Incorrect number of inputs');
%end;

A = varargin{1}(:,1);
B = A(2:length(A));
A = A(1);

Aphi = varargin{1}(:,2) .* (i*pi/180);
Bphi = Aphi(2:length(Aphi));
Aphi = Aphi(1);

```



```

theory = varargin{2}(:, :);
B = [B; ones(size(theory,1) - length(B),1)];
Bphi = [Bphi; zeros(size(theory,1) - length(Bphi),1)];
%[A,Aphi.*(180/(i*pi))] % debug output
%[B,Bphi.*(180/(i*pi))] % debug output

%%%%%%%%%%%%%%%%%%%%%%%%%%%%%%%%%%%%%%%%%%%%%%%%%%%%%%%%%%%%%%%%%%%%%%%%
% hard code specific values here
Aphi = 0;
Bphi(1) = 0;
Bphi(3) = 0;
Bphi(4) = 0;
if nargin == 3
    B(3) = varargin{3}(1);
    B(4) = varargin{3}(2);
end;
%B(3) = 1.5;
%B(4) = 0.5;
%%%%%%%%%%%%%%%%%%%%%%%%%%%%%%%%%%%%%%%%%%%%%%%%%%%%%%%%%%%%%%%%%%%%%%%%

result = A*exp(Aphi) + transpose(B.*exp(Bphi))*theory;
result = abs(result);
varargout{1} = result;
return;

```

Here is a routine written simply to calculate the cross correlation between two different fit parameters. It uses the previous routine as written (specifically

passing the hard coded values as optional parameters to the FSR\_datafit function). This is particularly useful in the context of a contour plot:

```
[xx,yy,zz] = test(f,ntsbi,ntdmi,mi,d2,200);  
contour(xx,yy,zz);
```

```
function [xx,yy,zz] = test(f,ntsbi,ntdmi,mi,d2,varargin)
```

```
if nargin > 6
```

```
    n = varargin{1};
```

```
else
```

```
    n = 20;
```

```
end;
```

```
x = 0:2/n:2;
```

```
y = 0:2/n:2;
```

```
for ii=1:n
```

```
    xx(1+ii,:) = x(1,:);
```

```
    yy(1+ii,:) = y(1,:);
```

```
end;
```

```
yy = transpose(yy);
```

```
clear ii
```

```
sig = 5.9433;
```

```
z2 = [[400,0];[0,0];[40,113];[0,0];[1,0]];
```

```
options = optimset;
```

```
lb = [];
```

```
ub = [];
```

```

for ii = 1:n+1
    for jj = 1:n+1
        [x,resnorm,resid] =
            lsqcurvefit(@FSR_datafit,
                        z2,
                        [f;ntsbi;abs(ntdmi);mi],d2,
                        [],[],
                        options,
                        [xx(ii,jj),yy(ii,jj)]);
        chi2 = sum(abs(resid.*resid))/(sig)^2;
        zz(ii,jj) = chi2;
    end;
end;

return;

```

#### B.5.4 Example Data Analysis

Here is an example of data analysis from reading in through fitting. Comments in command line MATLAB are distinguished the same way as in m-files.

```

% start in the frame analysis directory
[d,t,fq,fd,phase,str] = datamassage(2800,1,1,-900);
clear d t phase
fq = transpose(fq);fd = transpose(fd);
i1 = index(fq,200);
i2 = index(fq,800);

```

```
f = fq(i1:i2);
d = fd(i1:i2);
d1 = maskdata(f,d);
% switch to the matrix method directory
cd ../matrix_method_dir
tsbi = asiq(f+37e3,0,[1;zeros(22,1)],0.1,0.110,0);
    % modify parameters as needed
ntsbi = tsbi ./ max(abs(tsbi));
% continue as necessary to obtain whatever theory curves
% are needed for the fit
% return to frame analysis directory
cd ../frame_analysis_dir
x0 = [[477,0];[-0.07,0];[40,113]];
[x,rn,resid] = lsqcurvefit(@FSR_datafit,x0,[f;ntsbi],d1);
d2 = abs(d1 - x(2,1).*f - x(3,1)*exp(i*pi*x(3,2)/180).*ntsbi);
sig = std(d2);
chi2 = sum(abs(resid.*resid))/(sig)^2
```